

ABSTRACT

DATTA, ARKA. High Resolution Real-Time Neutron Imaging with Dynamic Capability at the PULSTAR Reactor. (Under the direction of Dr. Ayman I. Hawari).

In the present work, a high resolution real time neutron imaging system is developed. The system was characterized and optimized for utilization of static neutron radiography, tomography and for dynamic neutron radiography. Complementary attenuation characteristics with X-ray, make neutron imaging a useful non- invasive investigation modality for a wide range of applications in science and engineering. Advancement in electronic imaging systems makes it possible to obtain neutron radiographs in real-time. The components of the real time neutron imaging system include a neutron source, a collimator, and a detector which includes a scintillator, a lens and a camera. Real time neutron imaging was performed using a ${}^6\text{LiF:ZnS(Ag)}$ scintillator to convert neutrons to optical photons and a Charge Coupled Device (CCD) camera to detect those photons. These components of the real time neutron imaging system have been explored and the resolution contribution has been quantified. A multi-physics Monte-Carlo simulation model was developed to investigate the performance of the thermal neutron imaging system. It has been observed that the resolution contribution of the scintillator screen is correlated to its thickness and the range of the neutron absorption (in lithium) reaction products (i.e., the alpha and triton particles). The results of the simulation were compared to experimental measurements performed at the neutron imaging facility of PULSTAR research reactor of North Carolina State University (NCSU), showing good agreement. The achievable spatial resolution with the developed radiography system was $81 \pm 2 \mu\text{m}$ with $50 \mu\text{m}$ thick scintillator screen.

To explore and expand the capability of the imaging system, a high resolution computed tomography system was developed and characterized. The developed Monte-Carlo Multiphysics simulation model was extended to investigate the performance of the computed tomography (CT) system. The projection data were obtained by simulating various scintillator thickness at two positions from the beam aperture, yielding L/D ratio as 73 and 142. Analytical and iterative

reconstruction algorithms were implemented and characterized for the CT reconstruction. The best performance was obtained with largest L/D ratio and a thinner scintillator as expected. Further, a model based CT reconstruction technique was developed and implemented to improve the spatial resolution of the reconstructed images. The quantified system response function was included in the forward projection model to provide a better estimation of the actual projection, thus improving the spatial resolution of the reconstructed images. Experiments were performed at the neutron imaging facility of the PULSTAR research reactor to corroborate the performance of the developed model-based algorithm. The spatial resolution for tomography with the model based technique was $87 \pm 3 \mu\text{m}$ with $50 \mu\text{m}$ thick scintillator screen, showing an improvement of nearly 40% in achievable spatial resolution as compared to traditional techniques.

In addition, to illustrate the capability of imaging dynamic phenomenon, especially the observation of bubbles in fluids, micro-bubbles were generated and imaged at high resolution. Bubbles of $1300 \mu\text{m}$ diameter were generated by injecting through $50 \mu\text{m}$ orifice to demonstrate the feasibility of such dynamic investigation. The imaging system was characterized with two lens magnification settings and two different positions at the beamline yielding L/D 73 and 142 with $50 \mu\text{m}$ and $250 \mu\text{m}$ thick scintillator. The performance of the neutron imaging system was optimized with spatial resolution, temporal resolution, and SNR, showing the generated micro-bubbles with a spatial resolution of $245 \pm 5 \mu\text{m}$ and a temporal resolution of 50 ms. Additionally, the individual bubbles were identified and segmented to characterize the size distribution of the bubbles.

© Copyright 2019 by Arka Datta

All Rights Reserved

High Resolution Real-Time Neutron Imaging with Dynamic Capability
at the PULSTAR Reactor

by
Arka Datta

A dissertation submitted to the Graduate Faculty of
North Carolina State University
in partial fulfillment of the
requirements for the degree of
Doctor of Philosophy

Nuclear Engineering

Raleigh, North Carolina

2019

APPROVED BY:

Dr. Ayman I. Hawari
Committee Chair

Dr. Igor Bolotnov

Dr. Bernard Wehring

Dr. Paul Huffman

DEDICATION

Dedicated to almighty for finding me the light, whenever it was far away

&

*My beloved soulmate for her support, encouragement, and patience as we sail together through
this great voyage.*

BIOGRAPHY

Arka Datta was born and raised in Kolkata, India. He received his Bachelor of Technology (B. Tech) degree in Electronics and Communication Engineering from West Bengal University of Technology, Kolkata in Spring, 2011. In Fall 2011, he joined the Nuclear Engineering and Technology program at Indian Institute of Technology Kanpur (IITK). During his graduate studies, he started working on radiation imaging and received DAAD scholarship to continue his research work at Helmholtz Zentrum Dresden Rossendorf (HZDR), Germany. His work was focused on image analysis and segmentation to quantify tomographic images from ultrafast X-ray CT scanner (ROFEX) at high scanning rate. He received his Master's of Technology (M. Tech) degree in Nuclear Engineering and Technology in Spring, 2013. He has joined North Carolina State University (NCSU) as a graduate student in Nuclear Engineering Department in Fall, 2013. Pursuing his interest in radiation imaging further, he has started research in the field of neutron imaging at neutron imaging facility of the PULSTAR research reactor, under the supervision of Dr. Ayman I. Hawari. His PhD research focuses on development and characterization of high resolution, real-time neutron radiography, and tomography with dynamic capability at PULSTAR reactor.

ACKNOWLEDGEMENTS

I would like to express my deepest gratitude to my advisor, Dr. Ayman I. Hawari, for his guidance throughout this academic journey. I really like to thank him for his guidance and insight during my research and graduate studies. He has provided me with the resources and tools to be an active contributor in the field of radiation imaging. His steadfast support, integrity and unparalleled expertise have provided me invaluable direction and support.

I would like to thank Dr. Wehring, Dr. Huffman and Dr. Bolotnov for graciously serving on my committee. I am grateful for their valuable inputs, advice and feedback on the research work and thesis.

I express my sincere thanks to Andrew Cook, Scott Lassell, Gerald Wicks, Kerry Kincaid, Ming Liu and Gregory Gibson for the assistance, logistic support and equipment. I would also like to convey my appreciation to all the student reactor operators and staff members of nuclear reactor program (NRP) who assisted during the experiment. I would also like to thank Wendy So, Erwin Miller, Chintan Kanani, Mario Milev, Stefanie Keto and other staff members of nuclear engineering department. Also, I would like to thank my colleagues Ziyu, Jonathan, Yuwei and Andrew for their help during the research.

I am grateful for the constant support of my family and friends I have made along the way – Dev, Priyanka, Ankur, Sonam, Rani, Sanket, Avinav, Baljinder, Lucky, Sushi, Paridhi, Anant, Rudrodip and Ajay.

Finally, I would like to acknowledge the steadfast support of my wife as we sail through this voyage together. Without her support this journey would have been much more difficult.

TABLE OF CONTENTS

LIST OF TABLES	vii
LIST OF FIGURES	viii
ABBREVIATIONS	xix
Chapter 1 Introduction	1
1.1 Introduction to Neutron Imaging	1
1.1.1 Comparison between X-ray and Neutron Imaging	2
1.1.2 History and Trends of Neutron Imaging	6
1.1.3 State of the Art Neutron Imaging Facilities	8
1.2 Neutron Imaging Techniques	12
1.2.1 Neutron Radiography	12
1.2.2 Neutron Tomography	14
1.3 Application of Neutron Radiography and Tomography	17
1.3.1 Energy research	17
1.3.2 Material science and engineering	18
1.3.3 Biomedical and Biological Applications	21
1.3.4 Cultural Heritage	22
1.3.5 Two-Phase Flow	23
Chapter 2 Neutron Imaging at PULSTAR	28
2.1 Introduction	28
2.2 Neutron Imaging Facility	28
2.2.1 PULSTAR Reactor	28
2.2.2 Neutron Beam	31
2.2.3 Characterization of Neutron Source	31
2.2.4 Collimator	34
2.3 Imaging Instrumentations	37
2.3.1 Film	37
2.3.2 Image Plate	38
2.3.3 Real Time Neutron Imaging System	40
2.4 Positioning System	43
2.4.1 Positioning System Controller	45
2.4.2 Data Acquisition and Control for Tomography	49
2.5 Spatial Resolution of Neutron Imaging System	51
Chapter 3 Principles of Real-Time High-Resolution Neutron Imaging	52
3.1 Introduction	52
3.2 Mathematical Model of Image Formation	52
3.3 Simulation Model	55
3.3.1 Introduction to Geant4	57
3.3.2 Functionality and Overview	57
3.4 Geant4 simulation model for the neutron imaging system	63
3.5 Characterization of Neutron Imaging system	71
3.5.1 Image Acquisition and Processing	71
3.5.2 Spatial Resolution	74

3.5.3 Spatial Resolution Model of A Real-Time Neutron Imaging System	76
3.6 Resolution Components of Real-Time Neutron Imaging System	78
3.6.1 Beam Geometry	78
3.6.2 Imaging System	79
3.7 Experimental Results	108
Chapter 4 Development and Characterization of Neutron Tomography System	117
4.1 Introduction.....	117
4.2 CT Reconstruction Techniques.....	118
4.2.1 Analytical Reconstruction Method	119
4.2.2 Iterative Reconstruction Method.....	126
4.2.3 Statistical Reconstruction Method	132
4.2.4 Model-Based Reconstruction Method	134
4.3 Implementation of CT Reconstruction.....	138
4.4 Calculation of Spatial Resolution of CT Reconstruction.....	140
4.5 Phantom Design for CT Performance Evaluation	141
4.6 Monte Carlo Simulation Model of CT System	143
4.7 Simulation Result.....	144
4.8 Experimental Results	160
Chapter 5 Characterization and Implementation of a Dynamic Radiography System ...	173
5.1 Introduction.....	173
5.2 Dynamic Neutron Radiography	173
5.3 Nucleate Boiling and Micro Bubble Formation.....	174
5.3.1 Micro Bubble Generation	176
5.4 CFD Simulation Model for Micro-Bubble Generation.....	178
5.4.1 CFD Simulation Results	182
5.5 Phantom Design	188
5.6 Experimental Results	192
5.7 Bubble Quantification.....	213
Chapter 6 Conclusion and Future Work	217
6.1 Conclusion	217
6.2 Future Work	219
REFERENCES.....	222
APPENDICES	235
Appendix A Neutron Interactions and Geant4 Neutron Data Library	236
A.1 Neutron Interactions	236
A.2 Geant4 Neutron Data Library (G4NDL)	238
Appendix B Convolution of Gaussian PDF: A Brief Note.....	241
Appendix C Number of Projection Requirement for Neutron CT.....	243

LIST OF TABLES

Table 1.1.	Characteristic properties of neutron and X-ray.....	4
Table 1.2.	Neutron source	5
Table 1.3.	State of the art neutron imaging facilities [33-48].....	10
Table 2.1.	Utilization of PULSTAR beam ports.....	30
Table 2.2.	Salient features of iKon L 936 and iXon Ultra 888	42
Table 2.3.	Features of the positioning system.....	45
Table 2.4.	PPU reference	47
Table 3.1.	General purpose Monte-Carlo code [95-101].....	56
Table 3.2.	Typical Geant4 scorer to score quantities during simulation [103].....	62
Table 3.3.	Geant4 physics process used for the simulation	71
Table 3.4.	Scientific CCD specification [118].....	85
Table 3.5.	Specification of Lens	89
Table 3.6.	Spatial resolution contribution from diffraction	91
Table 3.7.	Properties of scintillators used for thermal neutron detection [130-132]	99
Table 3.8.	SRIM validation of range of Alpha and Triton particle inde the scintillator	100
Table 3.9.	The spatial resolution of Lens and CCD.....	110
Table 3.10.	Spatial resolution comparison of the neutron imaging system	115
Table 4.1.	Pseudo-code for the model-based reconstruction algorithm.....	138
Table 4.2.	Pseudo-code for the regular SIRT.....	138
Table 4.3.	Simulation parameters for the generation of projection data.....	144
Table 4.4.	Spatial resolution of CT recosntruction with different FBP filters (simulation results).....	147
Table 4.5.	Spatial resolution components of the CT system.....	149
Table 4.6.	Spatial resolution comparison of FBP, SIRT, and MLEM.....	153
Table 4.7.	Spatial resolution comparison of model-based technique with FBP, MLEM, and SIRT	158
Table 4.8.	Data acquisition settings for CT experiment at PULSTAR neutron imaging facility	165
Table 4.9.	Spatial resolution components of the neutron imaging system	167
Table 4.10.	Spatial resolution comparison of CT reconstruction (experimental result)	169
Table 5.1.	Dimension of the simulation phantom.....	179
Table 5.2.	Mesh description used for the COMSOL CFD simulation.....	180
Table 5.3.	Lens characteristics	192
Table 5.4.	Acquisition parameters for dynamic neutron imaging.....	212

LIST OF FIGURES

Figure 1.1.	Interaction of matter with (a) X-ray, and (b) neutrons.....	2
Figure 1.2.	Mass attenuation coefficients for thermal neutrons and 100 keV x-ray showing a linear increase of attenuation values for an x-ray. [3]	3
Figure 1.3.	Illustration of the essential components of neutron radiography showing neutron source, collimator, an object, and imaging detector consists of an image recorder and converter.....	13
Figure 1.4.	Illustration of tomography showing the formation of projection and sinogram for angle θ	14
Figure 1.5.	Sinogram of an object showing the sinusoid movement of pixel row with different angular position.....	15
Figure 1.6.	The photograph of a lock used to illustrate the neutron imaging technique.....	15
Figure 1.7.	Illustration of neutron imaging techniques showing (a) neutron radiograph of the lock, and (b) tomographic reconstruction of the lock showing the internal structure of the lock.	16
Figure 1.8.	Neutron radiograph of a fuel cell showing formation and movement of water by different concentrations in the neutron radiograph [1].	18
Figure 1.9.	Tomography slices showing the distribution of the Li across the Li-ion battery [31].....	18
Figure 1.10.	Neutron radiography of casting showing the foam degradation, generation of the pyrolysis layer, EPS Foam, Vapor Dissolution area, and molten metal flow [55].....	19
Figure 1.11.	Neutron radiograph of partially dry concrete showing the wet region by dark value illustrating the application of neutron imaging for material science and engineering [57].	20
Figure 1.12.	Neutron radiograph of an unconfined and inflated rat lung illustrating the biomedical and biological application of the neutron imaging [61].	21
Figure 1.13.	Neutron radiograph of an ancient Tibetan metallic Buddha statue (a) photograph of the Buddha sculpture, and (b) neutron image, illustrating the internal organic content of the statue [67].	22
Figure 2.1.	The layout of PULSTAR research reactor (a) Schematic diagram, and (b) PULSTAR reactor bay, showing different beam layout and facilities [84].....	29
Figure 2.2.	Top view of the core and beam ports.....	30
Figure 2.3.	Illustration of PULSTAR neutron imaging facility showing a 3D rendering of the collimator, external shielding, and the imaging area.....	31
Figure 2.4.	Design of the tool to measure the distribution of the neutron flux at the entrance of the neutron beam tube, (a) 3D view, and (b) side view.	32
Figure 2.5.	Top view of the reactor pool showing the arrangement to measure the neutron flux distribution across the entrance of beam tube #5.	32
Figure 2.6.	Neutron flux measurement tool, (a) high voltage (HV) power supply for the miniature fission chamber and electrometer to measure the current, (b) position calibration unit.....	33
Figure 2.7.	Spatial distribution of measured neutron flux across the entrance of beam tube #5 of the PULSTAR reactor (beam tube is shown in dotted line).	34

Figure 2.8.	Schematic of the neutron collimator and beam shutter of the imaging facility, (a) top view, and (b) cross-sectional view.	35
Figure 2.9.	Beam shutter, (a) CAD representation, (b) actual representation.	36
Figure 2.10.	Outside view of neutron imaging cave showing entrance door, beam control interface, dose monitors, tomography controller equipment.	37
Figure 2.11.	Film based neutron imaging equipment showing film cassette, cassette holder at the neutron imaging beam line, dark-room and film developer.	38
Figure 2.12.	IP based neutron imaging equipment showing (a) imaging plate, (b) plate holder cassette inside the imaging beam and, (c) imaging plate eraser..	39
Figure 2.13.	⁶ LiF:ZnS(Ag) scintillator screen, (a) front side of the screen, and (b) aluminum bracket.	40
Figure 2.14.	Lens used for real-time neutron imaging showing (a) micro-Nikkor 55mm, and (b) micro Nikkor 200 mm <i>f</i> /4 IF-ED.	41
Figure 2.15.	Real-time neutron imaging camera iKon-L CCD.	41
Figure 2.16.	Real-time neutron imaging camera iXon-Ultra electronic multiplier (EM) CCD camera.	42
Figure 2.17.	Real time imaging system camera cart assembly showing (a) 3D CAD representation, and (b) camera cart with mounted camera box holding CCD camera, lens and scintillator.	43
Figure 2.18.	CAD representation of the positioning system showing three linear motion and one angular motion to control the object for radiography or tomography experiment.	44
Figure 2.19.	Control logic flow diagram for ACR 9030 connection with a PC.	46
Figure 2.20.	Control logic flow diagram for communication between AR-PE servo driver and ACR 9030 axis controller.	47
Figure 2.21.	Block diagram of positioning system connection showing bidirectional LAN connection between ACR 9030 and AR 04 PE controllers (CB: circuit braker).	47
Figure 2.22.	Control panel for positioning system, (a) ACR 9030 axis controller and (b) AR 04 PE panel containing 4 servo drivers, (c) AR-04 PE controller for axis 4.	48
Figure 2.23.	Control logic flow diagram for automated tomography data acquisition system by control, communicate and synchronize between CCD and ACR 9030.	49
Figure 2.24.	The user interface for an automated data acquisition system showing the user input parameter in left-hand side and the status bar right-hand plane.	50
Figure 3.1.	Schematic of the neutron image formation showing the neutron source, collimator, beam aperture, object, and the imaging detector [1].	53
Figure 3.2.	Geant4 process flowchart showing the building blocks, the interconnection between them for a simulation [103].	58
Figure 3.3.	Illustration of Geant4 basic geometry model showing box, a section of a cylinder, cone, and sphere [94].	60
Figure 3.4.	Geant4 simulation geometry of PULSTAR neutron imaging facility, (a) wireframe rendering of side view, and (b) top view.	64
Figure 3.5.	Geant4 simulation of detailed collimator geometry showing: (1) air, (2) aluminum, (3) lead, (4) RX-277 (concrete with 1.6% boron content),	

	(5) sapphire filter, (6) beam aperture, (7) concrete, (8) beam shutter, and (9) borated polyethylene.	65
Figure 3.6.	Illustration of neutron energy spectrum at the entrance of the beam.	66
Figure 3.7.	Illustration of neutron energy spectrum after filtration with 12'' sapphire filter as produced with Geant4 simulation.	67
Figure 3.8.	Energy-dependent neutron cross section of Li showing the thermal neutron cross section as a function of neutron energy as obtained with Geant4 simulation.	68
Figure 3.9.	Neutron absorption efficiency of the $^6\text{LiF}:\text{ZnS}(\text{Ag})$ scintillator showing absorption probability increases as the ratio of the ^6LiF increases or the scintillator thickness increases.	68
Figure 3.10.	The emission spectrum of the optical photon from $\text{LiF}:\text{ZnS}(\text{Ag})$ scintillator showing peak emission wavelength in the blue region.	70
Figure 3.11.	Illustration of the detector model (top view) used in the Geant4 simulation.	70
Figure 3.12.	Illustration of the image processing of neutron radiography, (a) raw radiograph (b) flat field image, (c) dark field image, and (d) normalized image.	73
Figure 3.13.	Illustration of the modulation transfer function (MTF) of an ideal and practical imaging system.	75
Figure 3.14.	Illustration of spatial resolution calculation of neutron radiographs (a) edge radiograph, (b) edge spread function (ESF), (c) line spread function(LSF), and (d) modulation transfer function (MTF).	76
Figure 3.15.	Illustration of line spread function (LSF) as the image signal transmitted through the neutron imaging system. (used subscript represents the contribution from G: neutron beam geometry, S: scintillator, L: lens, C: CCD, *: convolution operation).	77
Figure 3.16.	The geometric contribution of spatial resolution showing the geometric unsharpness from neutron beam geometry.	79
Figure 3.17.	Illustration of metal-oxide-semiconductor MOS gate for p-doped silicon showing the metal electrode, depletion zone on a p-type semiconductor.	80
Figure 3.18.	Charge shifting process in charge coupled device (CCD) showing the transfer of charge across the horizontal rows (1) to horizontal register followed by readout (2), followed by signal amplification (3), and digitization and storage at the output node (4).	81
Figure 3.19.	Charge transfer between two adjacent pixels of the charge coupled device during the read-out process by controlling the gate potentials.	81
Figure 3.20.	Charge transfer process in 2-phase readout of the charge coupled device by controlling the gate potentials with time.	82
Figure 3.21.	Charge transfer process in 3-phase readout of the charge coupled device by controlling the gate potentials with time [117].	83
Figure 3.22.	Illustration of pixel binning process showing the effective pixel size with the binning process, (a) no binning, (b) 2x2 pixel binning, and (c) 3x3 pixel binning.	84
Figure 3.23.	Illustration of spatial resolution contribution of CCD showing the number of pixels are required for the faithful representation of an image when projected on pixel center (column 1) and pixel vertex (column 3) as the	

	image diameter increases to (a, e) one pixel, (b, f) two pixel, (c, g) three pixel and (d, h) four pixel [119].	86
Figure 3.24.	Illustration of lens aperture (<i>f</i>) number for Nikon Nikkor 55 mm lens (highlighted area is the iris adjustment ring to control the numerical aperture).	91
Figure 3.25.	Illustration of optical aberration showing the optical rays do not merge to a single point after passing through an optical system.	92
Figure 3.26.	Illustration of spherical aberration showing the optical rays do not merge at paraxial focus plane at optical axis due to longitudinal spherical aberration (LA) and transverse spherical aberration (TA) [123].	93
Figure 3.27.	Illustration of Coma effect of the lens showing the oblique optical rays do not merge after passing through the lens due to the variation of magnification with aperture.	93
Figure 3.28.	Illustration of the distortion effect of a lens showing the deformed formation of an image due to image formation at a different distance at the paraxial axis.	94
Figure 3.29.	Illustration of chromatic aberration showing the optical rays of different wavelength do not merge at paraxial axis due to their difference in refraction index (LA: longitudinal axial chromatic aberration, TA: transverse axial chromatic aberration) [123].	95
Figure 3.30.	Representation of a typical lens performance with different lens aperture settings showing the combined effect of diffraction and aberration on the spatial resolution.	95
Figure 3.31.	π -electronic energy levels of organic molecules showing S_0 , ground state S_1 , S_2 , S_3 excited singlet states, T_1 , T_2 , T_3 are excited triplet states and the subscripts are the vibrational states [129].	97
Figure 3.32.	Energy band structure in impurity activated crystal phosphor, showing valance band, conduction band, excited and ground state of activators.	98
Figure 3.33.	Range of Alpha particle with energy 2.05 MeV as obtained with Geant4 simulation.	100
Figure 3.34.	Range of Triton particle with energy 2.72 MeV as obtained with Geant4 simulation.	101
Figure 3.35.	Profile plots for 25 μm scintillator showing, (a) neutron absorption, (b) charge particle generation, (c) energy deposition, (d) optical photon generation, (e) optical photon reception by CCD, and (f) convolution response of optical photon generation and reception (convolution profile is normalized with 400 μm thick scintillator for comparison).	102
Figure 3.36.	Profile plots for 50 μm scintillator showing, (a) neutron absorption, (b) charge particle generation, (c) energy deposition, (d) optical photon generation, (e) optical photon reception by CCD, and (f) convolution response of optical photon generation and reception (convolution profile is normalized with 400 μm thick scintillator for comparison).	103
Figure 3.37.	Profile plots for 250 μm scintillator showing, (a) neutron absorption, (b) charge particle generation, (c) energy deposition, (d) optical photon generation, (e) optical photon reception by CCD, and (f) convolution	

	response of optical photon generation and reception (convolution profile is normalized with 400 μm thick scintillator for comparison).	104
Figure 3.38.	Profile plots for 400 μm scintillator showing, (a) neutron absorption, (b) charge particle generation, (c) energy deposition, (d) optical photon generation, (e) optical photon reception by CCD, and (f) convolution response of optical photon generation and reception (normalized).	105
Figure 3.39.	Illustration of the detector model (top view) used in the Geant4 simulation for the neutron radiograph generation.....	107
Figure 3.40.	Edge radiograph as obtained with Geant4 simulation with 50 μm $^6\text{LiF:ZnS(Ag)}$ scintillator for the calculation of the spatial resolution.	107
Figure 3.41.	Spatial resolution of the scintillator with thickness showing the resolution contribution of the scintillator as obtained with Geant4 simulation.	108
Figure 3.42.	Experimental arrangement to calculate the spatial resolution contribution of lens and CCD by measuring an edge image with light.....	109
Figure 3.43.	Edge images to calculate $RLens + CCD$ obtained with, (a) $f/4$, (b) $f/8$, (c) $f/16$, (d) $f/22$, and (e) $f/32$	110
Figure 3.44.	Spatial resolution components of the Lens and CCD system showing total measured spatial resolution of the Lens and CCD combined ($RLens + CCD$), theoretical contribution of CCD ($RCCD$), and calculated spatial resolution contribution of Lens ($RLens$).	111
Figure 3.45.	Experimental arrangement to calculate the spatial resolution of the detector RD , (a)-(b) neutron imaging equipment, and (c) gadolinium edge as an object.	112
Figure 3.46.	The neutron radiographs for the calculation of RD obtained with $^6\text{LiF:ZnS}$ scintillator of thickness (a) 50 μm , and (b) 250 μm (colour representation of grey scale image for enhanced illustration).	113
Figure 3.47.	Illustration of the Modulation transfer function of the neutron imaging system with 50 μm , 250 μm $^6\text{LiF:ZnS(Ag)}$ thick scintillator screen and Lens- CCD system.	114
Figure 3.48.	Spatial resolution components of the imaging system showing the resolution contribution of lens-CCD, scintillator, total spatial resolution and compared it with the experimental result for 50 μm and 250 μm scintillator.	114
Figure 3.49.	Sketch of resolution bar pattern used in the validation of calculated spatial resolution.....	115
Figure 3.50.	Radiograph of the resolution pattern measured with (a) 250 μm , and (b) 50 μm thick scintillator screen validating the spatial resolution qualitatively with the quantitative measurement.	115
Figure 4.1.	Computed tomography reconstruction methods showing analytical, iterative and model-based technique.....	119
Figure 4.2.	Block diagram of analytical CT reconstruction technique showing the direct application of the technique on the projection data for reconstruction.....	119
Figure 4.3.	Illustration of Fourier Slice Theorem showing 1D Fourier transformation of projection data is equivalent with 2D Fourier transformation of function for the same angle.	120

Figure 4.4.	Fourier space of multiple projections where each line in the polar coordinate represents the 1D Fourier transformation of projection.....	121
Figure 4.5.	Frequency domain representation of a band-limited ramp filter showing the linear increase in the weight as the spatial frequency increases.	124
Figure 4.6.	Frequency response function of the low pass filter used in filtered back projection Shepp-Logan, Hamming, Hann, Cosine.	125
Figure 4.7.	Frequency response function of the filtered back projection filters showing the different weight as the spatial frequency increases.....	126
Figure 4.8.	Workflow of iterative CT reconstruction technique showing the iterative update scheme between the measured projection and calculated forward projection data.....	127
Figure 4.9.	Illustration of Beer-Lambert attenuation law illustrating the reduction in neutron flux as it travels through materials of different attenuation coefficients.....	128
Figure 4.10.	Illustration of data acquisition geometry for computed tomography showing the formation of projection data.	129
Figure 4.11.	Kernel used for calculating forward projection during each iteration of the reconstruction, (a) strip kernel, and (b) line kernel.....	130
Figure 4.12.	Workflow of model-based CT reconstruction technique showing the iterative update scheme between the measured projection and calculated forward projection data.	134
Figure 4.13.	Illustration of the object detector model used for a neutron CT system showing the ideal and actual data acquisition geometry for neutron tomography.....	135
Figure 4.14.	Workflow of model-based reconstruction method showing the inclusion of the system response function within the iterative reconstruction technique.	136
Figure 4.15.	Workflow of regular simultaneous iterative reconstruction technique (SIRT) for computed tomography reconstruction.....	137
Figure 4.16.	Illustration of system response function used for the model-based computed tomography reconstruction.....	137
Figure 4.17.	Memory requirements of the system matrix with different grid size for iterative CT reconstruction.....	139
Figure 4.18.	Calculation process of the spatial resolution from the reconstructed images of R-phantom (a) Reconstructed image, (b) ESF, and (c) LSF.	140
Figure 4.19.	CAD drawings of (a) R-phantom for the quantitative calculation of the spatial resolution, and (b) V-phantom for validating the spatial resolution qualitatively.....	141
Figure 4.20.	Sketch of the resolution bar pattern used in V-phantom. The bar pattern measures the spatial resolution (A) 250 μm , (B) 200 μm , (C) 150 μm , (D) 100 μm , and (E) 50 μm	142
Figure 4.21.	Total cross section of the phantom material as obtained by Geant4 simulation (a) Nickel, and (b) Aluminum.....	142
Figure 4.22.	Neutron absorption probability with the thickness as obtained by Geant4 simulation (a) Nickel, and (b) Aluminum.....	143
Figure 4.23.	Illustration of the object detector model used in the simulation.....	144

Figure 4.24.	(a) Open beam image, and (b) Radiograph of R-phantom, as obtained from Geant4 simulation.	145
Figure 4.25.	Radiographs of V-phantom as obtained from Geant4 simulation for angle (a) 0° , and (b) 45°	145
Figure 4.26.	Radiographs of V-phantom as obtained from Geant4 simulation for angle (a) 90° , and (b) 135°	145
Figure 4.27.	FBP reconstruction of R-phantom for scintillator thickness $50\ \mu\text{m}$ and L/D 142 obtained with (a) Ramp, (b) Hamming, (c) Cosine, (d) Hanning, and (e) Shepp-Logan.	146
Figure 4.28.	MTF of the FBP reconstruction showing the performance of different filters. (Simulation results obtained with $50\ \mu\text{m}$ scintillator screen with L/D 142).	147
Figure 4.29.	FBP reconstruction of R-phantom for scintillator screen thickness (a) $25\ \mu\text{m}$, (b) $50\ \mu\text{m}$, and (c) $250\ \mu\text{m}$ at L/D 142.	148
Figure 4.30.	FBP reconstruction of R-phantom for scintillator screen thickness (a) $25\ \mu\text{m}$, (b) $50\ \mu\text{m}$, and (c) $250\ \mu\text{m}$ at L/D 73.	149
Figure 4.31.	MTF of the FBP reconstruction for L/D 142 showing spatial resolution of CT reconstruction with $25\ \mu\text{m}$, $50\ \mu\text{m}$, and $250\ \mu\text{m}$ scintillator.	150
Figure 4.32.	FBP reconstruction of V-phantom for scintillator thickness (a) $25\ \mu\text{m}$, (b) $50\ \mu\text{m}$, and (c) $250\ \mu\text{m}$. at L/D 142 (color representation for the enhanced illustration of the bar pattern for validation of the spatial resolution).	150
Figure 4.33.	FBP reconstruction of V-phantom for scintillator thickness (a) $25\ \mu\text{m}$, (b) $50\ \mu\text{m}$, and (c) $250\ \mu\text{m}$. at L/D 73 (color representation for the enhanced illustration of the bar pattern for validation of the spatial resolution).	151
Figure 4.34.	Algebraic CT reconstruction (simultaneous iterative reconstruction technique) of R-phantom for scintillator thickness (a) $25\ \mu\text{m}$, (b) $50\ \mu\text{m}$, and (c) $250\ \mu\text{m}$ at L/D 142.	152
Figure 4.35.	Statistical CT reconstruction (maximum likelihood expectation maximization) of R-phantom for scintillator thickness (a) $25\ \mu\text{m}$, (b) $50\ \mu\text{m}$, and (c) $250\ \mu\text{m}$ at L/D 142.	153
Figure 4.36.	MTF comparison of the analytical (FBP), algebraic (SIRT) and statistical (MLEM) CT reconstruction. (project data simulated with $50\ \mu\text{m}$ thick scintillator screen and L/D 142).	154
Figure 4.37.	Algebraic CT reconstruction (simultaneous iterative reconstruction technique) of V-phantom for scintillator thickness (a) $25\ \mu\text{m}$, (b) $50\ \mu\text{m}$, and (c) $250\ \mu\text{m}$. at L/D 142 (color representation for the enhanced illustration of the bar pattern for validation of the spatial resolution).	154
Figure 4.38.	Statistical CT reconstruction (maximum likelihood expectation maximization) of V-phantom for scintillator thickness (a) $25\ \mu\text{m}$, (b) $50\ \mu\text{m}$, and (c) $250\ \mu\text{m}$. at L/D 142 (color representation for the enhanced illustration of the bar pattern for validation of the spatial resolution).	155
Figure 4.39.	Model-based reconstruction of R-phantom for scintillator thickness (a) $25\ \mu\text{m}$, (b) $50\ \mu\text{m}$, and (c) $250\ \mu\text{m}$ at L/D 142.	157

Figure 4.40.	MTF comparison of the analytical (FBP), algebraic (SIRT) and statistical (MLEM), and model-based (MBCT) CT reconstruction.(project data simulated with 50 μm thick scintillator screen and L/D 142).....	158
Figure 4.41.	Model based reconstruction of R-phantom for scintillator thickness (a) 25 μm , (b) 50 μm , and (c) 250 μm at L/D 142 (color representation for the enhanced illustration of the bar pattern for validation of the spatial resolution).	159
Figure 4.42.	Comparison of profile plot through 100 μm bar pattern showing the improvement in the spatial resolution with the model-based reconstruction technique.	160
Figure 4.43.	R-phantom for tomography performance characterization, (a) side view, and (b) top view.	161
Figure 4.44.	V-phantom for tomography performance characterization, (a) side view, and (b) top view.	162
Figure 4.45.	V-phantom assembly during manufacturing process.....	163
Figure 4.46.	Magnified bars of V-phantom validates the spatial resolution [A] 250 μm , [B] 200 μm , [C] 150 μm , [D] 100 μm , and [E] 50 μm	163
Figure 4.47.	Experimental arrangement for tomography showing camera cart, camera box, scintillator, positioning system, and phantom.....	164
Figure 4.48.	The edge images for the calculation of (a) the spatial resolution contribution from lens and CCD, (b) the detector system.	166
Figure 4.49.	MTF of the imaging system as obtained with 50 μm thick ${}^6\text{LiF: ZnS}$ scintillator showing the contribution of lens and CCD, detector and total spatial resolution.	167
Figure 4.50.	Neutron radiograph of R-phantom obtained with ${}^6\text{LiF: ZnS (Ag)}$ scintillator of thickness, (a) 50 μm , and (b) 250 μm	168
Figure 4.51.	CT reconstruction of R-phantom with (a) analytical FBP, (b) algebraic SIRT, (c) statistical MLEM, and (d) model based technique obtained with 50 μm scintillator at L/D 142.....	169
Figure 4.52.	MTF comparison of the analytical (FBP), algebraic (SIRT) and statistical (MLEM), and model-based (MBCT) CT reconstruction.(experimental data obtained with 50 μm thick scintillator screen and L/D 142).	170
Figure 4.53.	CT reconstruction of R-phantom with (a) analytical FBP, (b) algebraic SIRT, (c) statistical MLEM, and (d) model based technique obtained with 250 μm scintillator at L/D 142 (color representation for the enhanced illustration of the bar pattern for validation of the spatial resolution).	170
Figure 4.54.	CT reconstruction of R-phantom with (a) analytical FBP, (b) algebraic SIRT, (c) statistical MLEM, and (d) model based technique obtained with 50 μm scintillator at L/D 142 (color representation for the enhanced illustration of the bar pattern for validation of the spatial resolution).	171
Figure 5.1.	Illustration of bubble formation stages, (a) bubble birth, (b, c) bubble expansion, (d) neck formation, (e) bubble lift-off, and (f) bubble de-attachment [174].	176
Figure 5.2.	Bubble radius with orifice radius 0 μm - 2000 μm	177
Figure 5.3.	COMSOL simulation model (a) 3D phantom, and (b) 2D central slice.	179
Figure 5.4.	Mesh of the geometry (a) 3D phantom, and (b) 2D central slice.	180

Figure 5.5.	Meshed geometry illustrating the hole.....	181
Figure 5.6.	Bubble injection profile (horizontal axis is in microsecond).....	181
Figure 5.7.	Illustration of bubble growth process for time (a) 0.001 s, (b) 0.025 s, (c) 0.075 s, (d) 0.150 s, (e) 0.190 s, and (f) 0.196 s.....	182
Figure 5.8.	Illustration of bubble growth with hole separation 1 mm at (a) 0.001 s, (b) 0.01 s, (c) 0.015 s, (d) 0.021 s, (e) 0.03 s, (f) 0.05 s, (g) 0.06 s, (h) 0.07 s, and (i) 0.08 s.....	183
Figure 5.9.	Illustration of bubble growth with hole separation 2 mm at (a) 0.01 s, (b) 0.02 s, (c) 0.05 s, (d) 0.1 s, (e) 0.2 s, (f) 0.25 s, (g) 0.31 s, (h) 0.39 s, and (i) 0.45 s.....	184
Figure 5.10.	Illustration of bubble growth with hole separation 3 mm at (a) 0.02 s, (b) 0.1 s, (c) 0.2 s, (d) 0.35 s, (e) 0.48 s, (f) 0.52 s, (g) 0.75 s, (h) 0.85 s, and (i) 0.93 s.....	185
Figure 5.11.	Illustration of bubble growth with hole separation 4 mm at (a) 0.01 s, (b) 0.1 s, (c) 0.2 s, (d) 0.3 s, (e) 0.4 s, (f) 0.5 s, (g) 0.6 s, (h) 0.79 s, and (i) 0.97 s.....	186
Figure 5.12.	Illustration of bubble growth with hole separation 5 mm at (a) 0.001 s, (b) 0.1 s, (c) 0.2 s, (d) 0.3 s, (e) 0.4 s, (f) 0.5 s, (g) 0.6 s, (h) 0.7 s, and (i) 0.8 s.....	187
Figure 5.13.	CAD drawing of the aluminum tube with 50 μm holes. The detail view illustrates the holes and the distances between them at 4:1 magnification scale.....	188
Figure 5.14.	CAD drawing of the phantom showing air inlet and outlet and aluminum container for the water column, (a) 3-D drawing of the phantom, and (b) 2-D cross-section of the phantom along the center line.....	189
Figure 5.15.	Designed phantom for dynamic experiment showing air inlet, aluminum body, and an air outlet.....	190
Figure 5.16.	Experimental arrangement to view the 50 μm hole through magnifying lens and camera system.....	190
Figure 5.17.	Visualization of 50 μm hole for air injection into the water column, (a) magnified photographic view, and (b) grayscale threshold for better visualization of the holes.....	191
Figure 5.18.	Light image obtained with Micro-NIKKOR 55 mm lens obtained with bin size (a) 1 x 1, (b) 2 x 2, and (c) 4 x 4 (image size shown is proportional to the pixel number).....	193
Figure 5.19.	Light image obtained with Micro-NIKKOR 200 mm lens obtained with bin size (a) 1 x 1, (b) 2 x 2, and (c) 4 x 4 (image size shown is proportional to the pixel number).....	194
Figure 5.20.	Spatial resolution of the Micro-NIKKOR 55 mm lens for EMCCD bin size 1x1, 2x2 and 4x4 as obtained from light images containing the paper edge.....	195
Figure 5.21.	Spatial resolution of the Micro-NIKKOR 200 mm lens for EMCCD bin size 1x1, 2x2 and 4x4 as obtained from light images containing the paper edge.....	195
Figure 5.22.	Experimental arrangement to calculate the detector spatial resolution by placing a Gadolinium edge on the scintillator.....	196

Figure 5.23.	Experimental arrangement to calculate the total spatial resolution by placing the Gadolinium edge at 1 cm from the scintillator.....	197
Figure 5.24.	Edge radiographs obtained with 250 μm $^6\text{LiF}:\text{ZnS}$ scintillator with Micro-NIKKOR 55 mm lens and aperture $f/2.8$ showing Gadolinium edge for L/D 73 and $d=1$ cm for bin size (a) 1x1, (b) 2x2, and (c) 4x4. (image size shown is proportional to the pixel number).....	198
Figure 5.25.	Edge radiographs obtained with 250 μm $^6\text{LiF}:\text{ZnS}$ scintillator with Micro-NIKKOR 200 mm lens and aperture $f/2.8$ showing Gadolinium edge for L/D 73 and $d=1$ cm for bin size (a) 1x1, (b) 2x2, and (c) 4x4 (image size shown is proportional to the pixel number).....	199
Figure 5.26.	Spatial resolution of the neutron imaging system with Micro-NIKKOR 55 mm lens with 250 μm (left column) and 50 μm thick scintillator screen obtained with lens aperture (a, b) $f/2.8$, (c, d) $f/4$, and (e, f) $f/5.6$	200
Figure 5.27.	Spatial resolution of the neutron imaging system with Micro-NIKKOR 200 mm lens with 250 μm (left column) and 50 μm (right column) thick scintillator screen obtained with lens aperture (a, b) $f/4.0$, and (c, d) $f/5.6$	201
Figure 5.28.	Experimental arrangement for dynamic neutron imaging showing, air-inlet, air-outlet, phantom, camera cart, camera box, shielding (front view).....	202
Figure 5.29.	Experimental arrangement for dynamic neutron imaging showing, air-inlet, air-outlet, phantom, camera cart, camera box, shielding top view.	203
Figure 5.30.	Experimental arrangement for the dynamic imaging showing the setup at two different positions from the neutron beam yielding L/D ratio of 73.....	204
Figure 5.31.	Experimental arrangement for the dynamic imaging showing the setup at two different positions from the neutron beam yielding L/D ratio of 142.....	205
Figure 5.32.	Radiograph obtained with still water column (without air injection) to calculate the exposure and SNR (the highlighted area is used for the calculation).....	206
Figure 5.33.	Exposure time of EMCCD obtained with L/D 73 Nikkor 55 mm lens (L1) and Nikkor 200 mm lens (L2) 250 μm (left column) and 50 μm (right column) thick scintillator for different EM gain and pixel bin (a, b) 1 x 1, (c, d) 2 x 2, and (e, f) 4 x 4.....	207
Figure 5.34.	Exposure time of EMCCD obtained with L/D 142 Nikkor 55 mm lens (L1) and Nikkor 200 mm lens (L2) 250 μm (left column) and 50 μm (right column) thick scintillator for different EM gain and pixel bin (a, b) 1 x 1, (c, d) 2 x 2, and (e, f) 4 x 4.....	208
Figure 5.35.	SNR of EMCCD obtained with L/D 73 Nikkor 55 mm lens (L1) and Nikkor 200 mm lens (L2) 250 μm (left column) and 50 μm thick scintillator (right column) for different EM gain and pixel bin (a, b) 1 x 1, (c, d) 2 x 2, and (e, f) 4 x 4.....	209
Figure 5.36.	SNR of EMCCD obtained with L/D 142 Nikkor 55 mm lens (L1) and Nikkor 200 mm lens (L2) 250 μm (left column) and 50 μm thick scintillator (right column) for different EM gain and pixel bin (a, b) 1 x 1, (c, d) 2 x 2, and (e, f) 4 x 4.....	210
Figure 5.37.	(a) Single frame of the neutron radiograph showing hot pixels, and (b) Processed radiographs to remove the hot pixels whose intensity deviates more than two standard deviations of the mean intensity level.....	214

Figure 5.38.	Bubble edges after applying Sobel edge filter to identify the bubbles within the radiograph and quantify the bubble diameter through subsequent image processing.	215
Figure 5.39.	Close view of the individual detected bubbles in the radiograph after applying the Sobel edge filter showing the shape of the detected bubbles.....	215
Figure 5.40.	Segmented bubbles from the binary image for the calculation of the bubble diameter.....	216
Figure 5.41.	Distribution of bubble diameter from the segmented image showing Gaussian distribution of the bubbles with a mean diameter around 1300 μm	216

ABBREVIATIONS

CAD: Computer Aided Drafting

CCD: Charged Coupled Device

CGLS: Conjugate Least Square

CGS: Constructive Solid Geometry

CT: Computed Tomography

EM: Expectation Maximization

ESF: Edge Spread Function

FBP: Filtered Back Projection

FOV: Field of View

FWHM: Full Width Half Maximum

G4NDL: Geant4 Neutron Data Library

GPU: Graphical Processing Unit

GUI: Graphical User Interface

HPC: High Performance Computing

HV: High Voltage

IAEA: International Atomic Energy Agency

ICNR: International Society for Neutron Radiography

IP: Imaging Plate

LFC: Lost Foam Casting

LSF: Line Spread Function

LSI: Linear Shift Invariant

MBCT: Model Based Computed Tomography

MLEM: Maximum Likelihood Expectation Maximization

MOS: Metal Oxide Semiconductor

MRI: Magnetic Resonance Imaging

MTF: Modulation Transfer Function

NSECT: Neutron Stimulated Computed Tomography

PEM: Proton Exchange Membrane

PET: Positron Emission Tomography

PGNAA: Prompt Gamma-Ray Activation Analysis

PIV: Particle Image Velocimetry

PSF: Point Spread Function

SIRT: Simultaneous Iterative Reconstruction Technique

SNR: Signal to Noise Ratio

SNS: Spallation Neutron Source

SPECT: Single Photon Emission Computed Tomography

TE: Thermo-Electric

UI: User Interface

WMS: Wire Mesh Sensors

Chapter 1 Introduction

Radiation imaging is a useful investigation tool for the examination of the internal structure of objects. It uses penetrating radiative energy to investigate the internal structures and material composition of the optically opaque region non-destructively. As the radiation passes through the object it is attenuated by scattering or absorption. The transmitted beam produces a two-dimensional attenuation map which may be considered the material characteristics of the object. Various types of non-invasive imaging modalities are used, ranging from particles like neutrons, protons, and electrons to electromagnetic waves like X-ray or gamma ray. Depending upon the application requirement appropriate type of imaging modality can be selected. In this work, the focus is on high-resolution neutron imaging, in particular, real-time neutron radiography and tomography.

In the present chapter, an overview to the neutron imaging is presented which includes history and trends in neutron imaging, application of neutron imaging, different neutron imaging facilities across the globe and their characteristics, and image quality parameters. Finally, the purpose and objective of the present work are outlined in the last section of this chapter.

1.1 Introduction to Neutron Imaging

In conventional neutron imaging, image contrast is formed due to absorption and scattering as neutrons interact while passing through the material. Neutrons are more attenuated by light materials like water, hydrocarbons, and some highly absorbing materials like lithium, boron, cadmium. This makes neutron imaging (radiography and tomography) a valuable noninvasive investigations tool for a wide range of applications in science and engineering, e.g., to retrieve structural information of a material which is otherwise difficult to visualize using X-rays [1].

1.1.1 Comparison between X-ray and Neutron Imaging

Unlike X-rays, neutrons interact with the nucleus of the atomic nuclei. The interactions of neutron and X-ray beam with an object depends upon the cross-section properties of materials [2]. X-rays interact with the electronic structure of the materials by photoelectric effect, Compton scattering, and pair production. These interaction probabilities can be correlated with atomic number (Z) resulting in less sensitivity to low Z materials and more sensitivity to high Z materials.

Figure 1.1 illustrates X-ray and neutron interaction with matter.

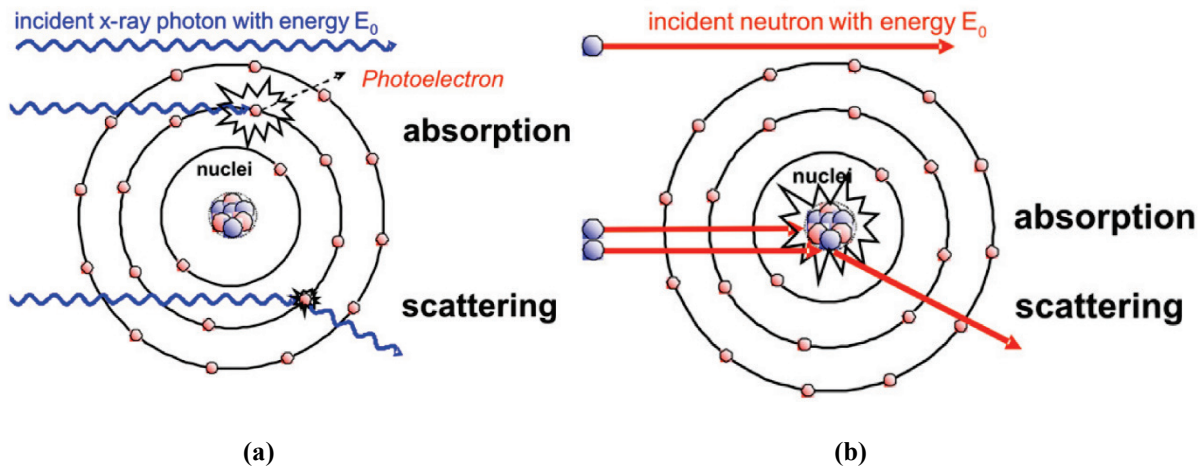


Figure 1.1. Interaction of matter with (a) X-ray, and (b) neutrons.

However, unlike X-rays, it is not possible to form a general trend for neutron interaction in the periodic table. Neutron scattering cross section is relatively constant up to Bragg cut-off energy below which it tends to drop sharply. Figure 1.2 illustrates that the irregular position of neutron interaction probabilities across the periodic table when compared with 100 keV X-rays. The absorption cross section is dependent on neutron energy. The total microscopic cross section can be expressed as shown in Equation 1.1.

$$\sigma_{Total} = \sigma_{scattering} + \sigma_{absorption} \quad (1.1)$$

Where $\sigma_{scattering}$ and $\sigma_{absorption}$ are microscopic scattering and absorption cross section respectively. The neutron scattering cross section can be further broken down into coherent and incoherent components [1]. In conventional neutron imaging the image contrast is formed due to the absorption and scattering as the neutrons interact while passing through material. It can be observed that neutrons are attenuated by light materials like water and hydrocarbons, and some highly absorbing elements like lithium, boron, cadmium and gadolinium.

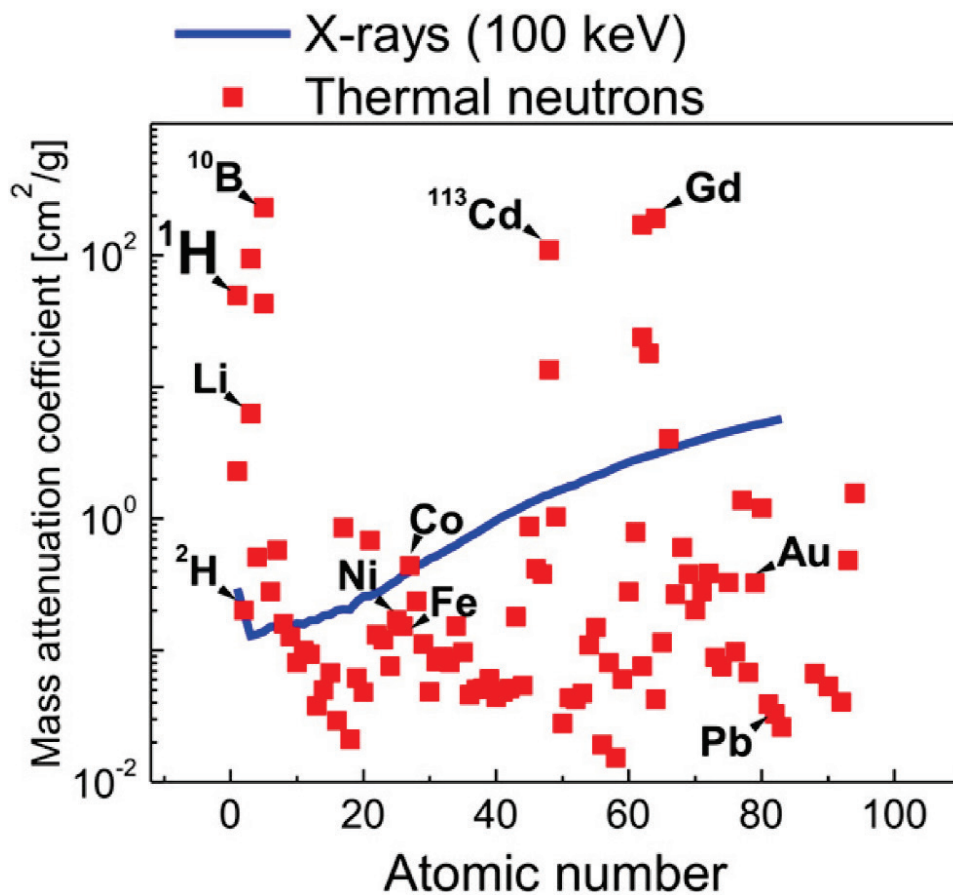


Figure 1.2. Mass attenuation coefficients for thermal neutrons and 100 keV x-ray showing a linear increase of attenuation values for an x-ray. [3]

Depending upon energy, neutrons can be classified as ultra-cold, cold, thermal, epithermal and fast. Similarly, the X-ray can be classified as soft, hard and high energy. The characteristics of neutrons and X-rays is illustrated in Table 1.1.

Table 1.1. Characteristic properties of neutron and X-ray

		Energy (eV)	Temperature (K)	Wavelength (Å)	Speed (m/s)
Neutrons	Ultra-cold	10^{-7}	0.001	750	5
	Cold	0.005	60	4	1000
	Thermal	0.025	300	1.8	2200
	Epithermal	0.5	6000	0.4	10^4
	Fast	10^6	10^{10}	10^{-4}	10^7
X-rays	Soft	10^3	10^7	10	
	Hard	10^4	10^8	1	3×10^8
	High energy	10^5	10^9	0.1	

The fundamentally different characteristics of neutrons as a penetrating probe compared to X-rays open up new possibilities to noninvasive investigations. Neutrons are very sensitive to water or other hydrogen-rich compounds. Many elements with similar atomic numbers can be distinguished. Neutrons can penetrate easily through metals such as aluminum or even lead, in contrast to X-rays. These significant advantages of neutrons over X-rays yield information of internal structure of such objects. Additionally, elements like boron and gadolinium have a very high cross section to thermal neutron energy spectrum, which can be utilized as a tracer element in non-invasive investigation of optically opaque medium.

In spite of such advantages of neutrons, it is difficult to build a small-scale laboratory with sufficient neutron flux. Small radioisotope source like Cf-252 which undergoes constant fission can't produce sufficient neutron flux required for neutron imaging experiment. Therefore, mostly

neutron imaging facilities are developed in research reactor or spallation neutron source (SNS). In a research reactor, neutrons are produced by spontaneous fission whereas, SNS utilizes an ion accelerator to produce neutrons by spallation. Table 1.2 summarizes different neutron sources. Construction and maintenance of such facilities are very costly and time-consuming. On the contrary X-ray source can be manufactured easily and not very expensive.

Table 1.2. Neutron source

Neutron source	Reaction type	Reaction
α – Beryllium	(α, n)	$Be^9 + He^4 \rightarrow C^{12} + n$
		$Be^{11} + He^4 \rightarrow N^{14} + n$
Spontaneous neutron source	Fission	$Cf^{252} \rightarrow \begin{cases} \alpha + Cm^{248} \\ fission\ fragments + \sim 4n \end{cases}$
Accelerator	(d, n)	$H^3 + H^2 \rightarrow He^4 + n$
		$H^2 + H^2 \rightarrow He^3 + n$
	(p, n)	$H^3 + H^1 \rightarrow He^3 + n$
		$Li^7 + H^1 \rightarrow Be^7 + n$
Reactor	Fission	$n + U^{235} \rightarrow fission\ fragments + \sim 2n$

Apart from source, neutrons also have some undesirable properties. Neutron imaging is mostly performed with thermal or cold neutrons due to their high interaction probabilities with materials. But neutrons produced by research reactors, usually have a broad energy spectrum. Therefore,

neutrons must be moderated and filtered properly before they can be used for imaging applications. Since neutrons are a neutral particle, a converter material is required in the detector to convert neutrons to detectable secondary radiations. This process reduces detection efficiency and also increases un-sharpness of the resulting image. Additionally, neutron absorption by some materials transmutes them into new isotopes. Although many of these isotopes have a very short half-life, some of them have prolonged high activity period after exposure with neutrons. Since neutrons have high penetrating capabilities, heavy shielding is also required for safe operation of neutron imaging facilities.

However, advantages of neutron imaging circumvent the challenges and other shortcomings. There are many applications where neutron imaging is only viable imaging modality that can be used for non-invasive investigations. Such usefulness of neutron imaging can explain the growth rate in the development of such neutron imaging facilities in recent times.

1.1.2 History and Trends of Neutron Imaging

Ernest Rutherford was the first to predict the existence of neutrons in 1920. However, in 1932 James Chadwick discovered neutron by using scattering data to calculate the mass of the neutral particle that resides inside the nucleus. Neutron imaging began with the work of Kallmann and Kunn after 3 years of its discovery [4]. The initial experiment was performed using a Ra-Be source and a small (*d. n*) generator, radiographic converter film, and vacuum cassette. The availability of sufficient neutron flux was a major challenge in the early days of neutron imaging. The first reactor based neutron imaging was performed by Thewlis in 1956 using a neutron beam port at BEPO reactor [5]. Availability of high-intensity neutron flux begins the neutron imaging as a practical noninvasive investigation tool. Scientific interest was gradually growing for this imaging modality. It can be seen from research on parallel and divergent collimators to improve neutron radiography

[6], [7]. Starting from 1965 many nuclear research centers started developing and began to offer neutron radiography as commercial services. Apart from thermal neutrons investigation using other neutron energies was also started during that time. In 1966, Berger reported initial investigation of dynamic neutron imaging [8]. The detector consisted of a neutron sensitive image intensifier tube coupled with a television camera and the system was described as neutron television system. Kawasaki and Hendry developed a multistage image intensifier detector system. The use of image intensifier increases optical photon output, thus reduces the acquisition and development time [9], [10]. Research to improve neutron detector system can be seen during 1970 [11], [12]. Apart from neutron radiography, growing interest to visualize the internal structure of an object with neutrons began to drive the development of neutron tomography around 1980 [13]. At early stages, the feasibility of neutron tomography was mainly limited to the availability of digital sensors and computers with limited resources for reconstruction [14]. But those limitations were resolved with development of real-time imaging systems and rapidly growing computational capabilities. Real-time neutron imaging systems are commercially available from 1983 [15]. These systems are based on an electrostatic image intensifier, gadolinium oxy-sulfide scintillators and video camera [16]. The photo-stimulable phosphor was introduced in 1990 as an alternative method for imaging film. Although imaging plates (IP) had a moderate spatial resolution as compared to film, it had a better linear response, reusable, and no chemical processing was required for image development [17-19]. Advancement of digital imaging technique like charged couple devices (CCD) further reduced the image development time. Scintillator coupled with CCD became a popular method for neutron imaging as the image can be read in real-time and grey values can be used for quantitative assessment. Although, early stages of digital imaging systems provided coarser spatial resolution than film, simplifications associated with recording, handling,

and treatment of digital data increased the development rate of such digital imaging system for neutron imaging. Five new neutron imaging facilities became operational between 1994 to 2004 as research and development in computational resources, digital imaging devices opened up a new opportunity in neutron imaging [20-23].

While majority of applications of neutron imaging focuses on neutron attenuation other advanced neutron imaging techniques were explored from early 2000. Polarized neutron imaging visualizes magnetic field inside and around the sample by measuring the polarization changes in transmitted beam [24]. Phase contrast method improves image visualization by edge enhancement which depends upon the neutron coherent scattering lengths of materials and the degree of spatial coherence of the neutron beam [25], [26]. Energy-selective neutron imaging uses a mono-energetic neutron beam to visualize the energy dependence attenuation properties of an object [27]. Neutron grating interferometry uses simultaneous information of transmission, differential phase, and dark-field image to provide spatially resolved information on anisotropy and shape of microstructure of the sample [28]. Diffractive neutron imaging combines transmission and scattered components to obtain micro-structural information [29]. Data fusion between X-ray and neutron is also used to improve quantitative evaluation and material characterization [30].

1.1.3 State of the Art Neutron Imaging Facilities

Neutron imaging beamlines have traditionally been installed as reactor based facilities, although few are associated with the spallation source. Most of the beamline uses thermal neutrons with a Maxwellian spectral distribution. Although, few cold neutron facilities for neutron imaging applications have started their operation recently. In spite of having higher cost and maintenance the number of neutron imaging facilities is growing. According to a recent survey by the International Society for Neutron Radiography (ICNR) and International Atomic Energy Agency

(IAEA), there are 48 registered facilities around the globe. But among them, only 15 can be classified as state-of-the-art [31]. The criteria for evaluating such state-of-the-art neutron facilities can be summarized below. Table 1.3 summarizes such facilities across the globe. It can be observed that neutron imaging facilities developed at university-based research reactor have comparatively low power, thermal spectrum, and moderate collimated beam, whereas specialized facilities have higher flux, cold neutrons, and high beam collimation.

Evaluation criteria for neutron imaging system[32]

- Dedicated high-intensity beamline
- Well defined thermal or cold spectrum
- High beam collimation ($L/D > 100$)
- Uniformly illuminated reasonable large field-of-view (diameter $> 10\text{cm}$)
- The advanced digital imaging system
- Experimental infrastructure
- Capable of hosting internal and external user

Table 1.3. State of the art neutron imaging facilities [33-48]

Country	Organization	Facility Name	Reactor Power (MW)	Spectrum	Flux ($n\text{ cm}^{-2}\text{ s}^{-1}$)	L/D	Spatial Resolution (μm)	Imaging Technique [§]
Australia	ANSTO	OPAL	20	Thermal	5.3×10^7	500 - 1000	-	R, T
Austria	Atom Institute	TRIGA	0.250	Thermal	1.3×10^5	135	-	R, T
Brazil	IPEN	IEA-R1M	5	Thermal	8×10^6	70	263	R, T
China	CIAE	CARR	60	thermal	5×10^7	293 - 585	200	R, D
Germany	MLZ	ANTARES	20	Cold	4×10^8	200 – 8000	30	R, T, D
		NECTAR		Thermal	7.92×10^6	240	88	R, T
	HZB	CONRAD-2	10	Cold	7.2×10^7	170- 350	-	R, T
Hungary	KFKI	NORMA	10	Thermal	2.7×10^7	233	223	R, T
Japan	SHI	ATEX	18	Thermal	2×10^5	44	-	-
	JAEA	JRR-3M	20	Thermal	1.5×10^8	154 - 185	-	R, T
	RADEN	J-PARC	1	Cold	9.8×10^7	180 – 230	100	R, T

[§] R: radiography, T: tomography, D: dynamic

Table 1.3. (continued).

Country	Organization	Facility Name	Reactor Power (MW)	Spectrum	Flux (n cm⁻² s⁻¹)	L/D	Spatial Resolution (μm)	Imaging Technique[§]
South Korea	KAERI	HANARO	30	Thermal	1.17 x 10 ⁷	266	100	R
South Africa	NECSA	SAFARI	20	Thermal	1 x 10 ⁷	125 - 525	-	R, T
Switzerland	PSI	ICON	1	Cold	5.8 x 10 ⁶	90 – 12000	7.6	R, T, D
		NEUTRA		Thermal	1.6 x 10 ⁷	200-550	-	R, T
USA	Penn State	BREAZEALE	1	Thermal	1.7 x 10 ⁷	150	145	R, T, D
	Mc Clellan	TRIGA	2	Thermal	5.6 x 10 ⁶	200	-	R, T
	NCSU	PULSTAR	1	Thermal	7 x 10 ⁶	70 – 150	81	R, T, D
	University of Texas at Austin	TRIGA	0.5	Thermal	5x10 ⁶	110	200	R, T
	ORNL	HFIR CG -1D	85	Cold	2 x 10 ⁷	400 – 800	50	R, T, D
	NIST	NBRS	20	Cold	5.1 x 10 ⁷	100 - 6000	13	R, T, D

[§] R: radiography, T: tomography, D: dynamic

1.2 Neutron Imaging Techniques

Neutron imaging is a powerful non-invasive examination tool that produces a two-dimensional map of the object being investigated. The map is proportional to attenuation characteristics of the object. Currently, neutron imaging is extensively used for nondestructive investigation of various applications of science and engineering, ranging from inspection of turbine blades, study of two-phase flow, energy research etc. Neutron imaging technique can be classified into neutron radiography and tomography for such noninvasive investigations.

1.2.1 Neutron Radiography

Neutron radiography is the production of the two-dimensional image and can be interpreted as the integrated attenuation properties of the object. The information about the composition of material can be inferred from the image. Typically, neutron radiography system consists of a source, moderator, collimator with aperture and detector. The source may include a research reactor, accelerator, and radioisotope neutron sources. The moderator moderates high energy neutrons for conventional neutron radiography. Next, the collimation of the moderated neutrons are required, to concentrate them at image plane. However, neutrons are a neutral particle and can't be focused like charged particles. A beam tube adjacent to moderator allows neutrons in direction of the beam axis to image plane. One of the popular types of collimator is convergent-divergent type, where the collimator exit area is larger than entrance area, thus allowing a larger imaging area. A higher collimation reduces the beam spread at cost of neutron flux and low collimation, may maintain high neutron flux at image plane but high spread of the neutron beam affects image spatial resolution. The neutrons that reach the detector after penetrating the object must be detected for the production of the radiograph. The detector generally uses a converter to convert neutrons in some form of detectable signal. The most common type of detector used in neutron radiography

is an image film which uses gadolinium foil as converter. Another type of detector is the scintillator detector, where absorbed neutrons produce charged particles. The charged particle deposits their energy in the scintillator resulting scintillation event. Escaped optical photons are captured in photo-sensitive medium for production of the neutron radiograph. The schematic of the production of neutron radiograph is shown in Figure 1.3.

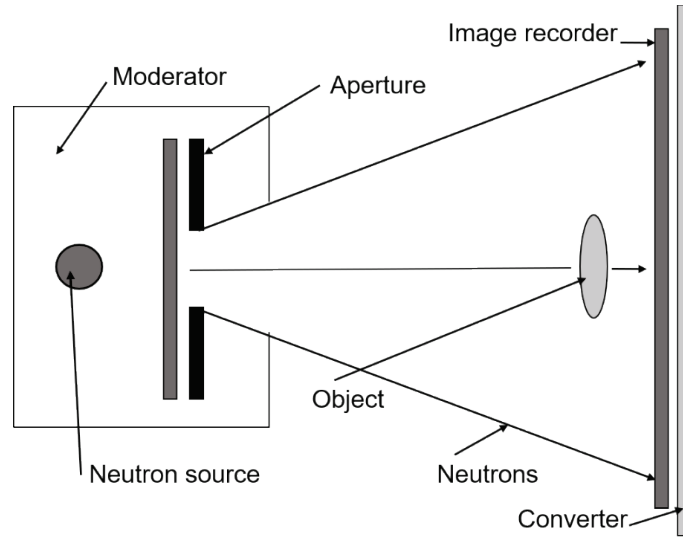


Figure 1.3. Illustration of the essential components of neutron radiography showing neutron source, collimator, an object, and imaging detector consists of an image recorder and converter.

The transmission ratio can be expressed as the ratio of the transmitted beam intensity, I , to the incident beam intensity I_0 ,

$$Transmission = \frac{I}{I_0} . \quad (1.2)$$

The transmission of radiation can be described by the exponential attenuation law as,

$$I = I_0 e^{-\int \mu(x) dx} , \quad (1.3)$$

where, $\mu(x)$ is local attenuation coefficient at location x , and dx is the differential propagation length. The attenuation phenomenon includes both the absorption and scattering. While, scattering attenuates the intensity of transmission of the neutron beam it is not an ideal attenuation process, since it changes the actual propagation direction. Although, simple attenuation holds in simple

cases, other modification needs to be consider when material consists of strong absorbing or scattering material.

1.2.2 Neutron Tomography

Although neutron radiography provides insight into an object, two-dimensional representation of three-dimensional object results loss in the information retrieval of the object. However, it can be overcome by a technique known as the computed tomography. It is achieved by reconstructing image slice, of an object by acquiring multiple radiographs at successive interval angle. The aim of tomography is to reconstruct the attenuation values of an object from projection. The schematic is shown in Figure 1.4. All projections are first converted to sinogram by arranging the n^{th} pixel row for all angles as illustrated in Figure 1.5. Each sinogram contains all the attenuation information of the particular section of the object at the different angular interval. The sinograms are processed to reconstruct the attenuation coefficients for the section of the object.

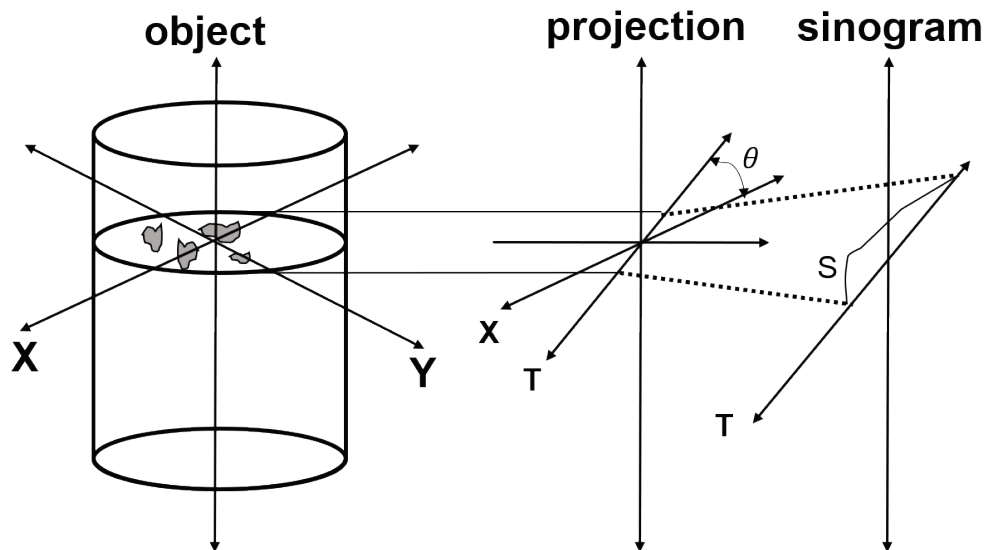


Figure 1.4. Illustration of tomography showing the formation of projection and sinogram for angle θ [1].

By stacking multiple two-dimensional image slices in image stack, three-dimensional attenuation map of the object can be retrieved. The three-dimensional image stack can be further rendered or

processed to extract useful information. Many reconstruction algorithms exist for tomographic reconstruction and detail discussion can be found in Chapter 4.

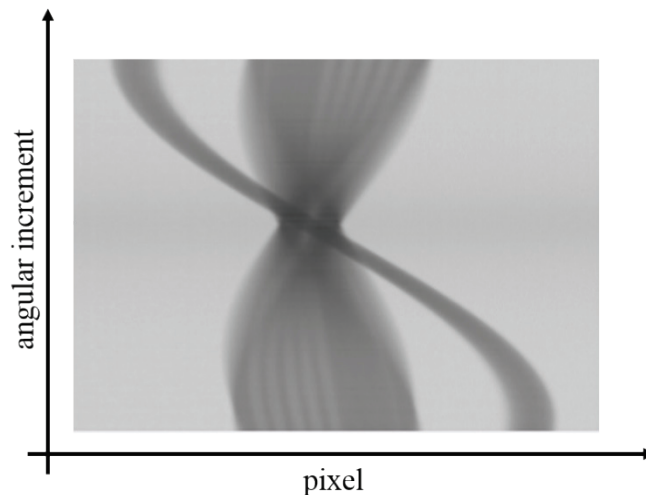
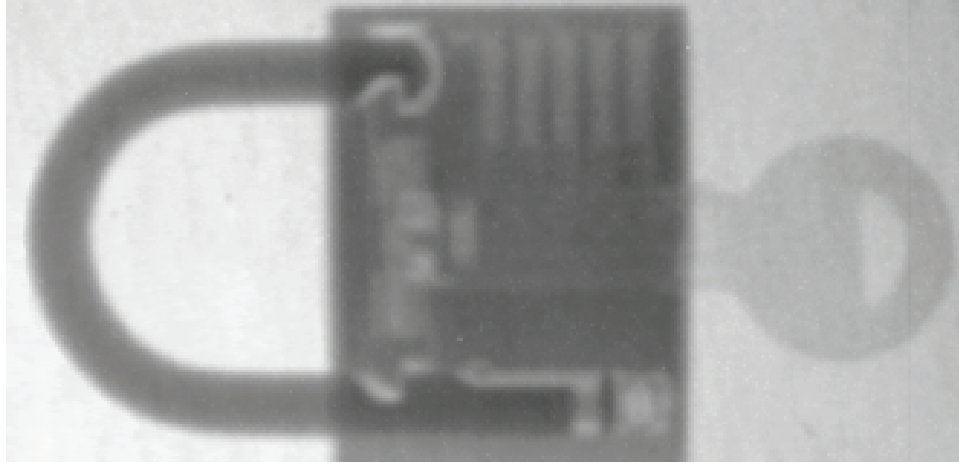


Figure 1.5. Sinogram of an object showing the sinusoid movement of pixel row with different angular position.

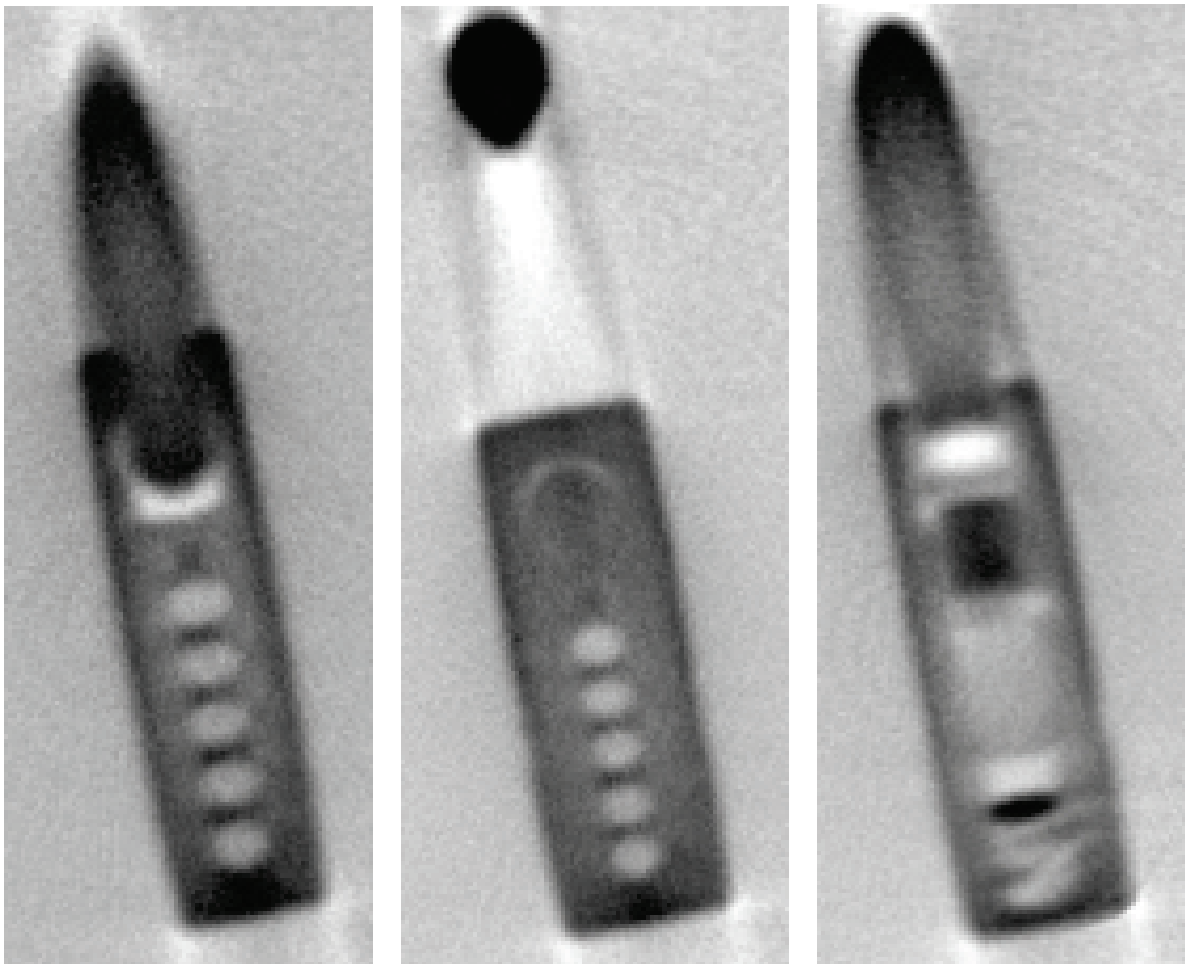
The photographic image of the object is shown in Figure 1.6. Neutron radiography and tomography techniques are shown in Figure 1.7, (b) and Figure 1.7, (c). Neutron radiography of the lock showing the internal structure of a lock in two dimension non-invasively which is otherwise not visible. However, three-dimensional structural information can't be obtained from the radiograph alone. The tomographic reconstructed slices are shown in Figure 1.7 (c) illustrating the internal structure of the lock at a different position.



Figure 1.6. The photograph of a lock used to illustrate the neutron imaging technique.



(a)



(b)

Figure 1.7. Illustration of neutron imaging techniques showing (a) neutron radiograph of the lock, and (b) tomographic reconstruction of the lock showing the internal structure of the lock.

1.3 Application of Neutron Radiography and Tomography

Over the past decade, neutron imaging (radiography and tomography) already proved to be useful in many different areas of science and technology. The advancement of digital techniques along with the high-resolution real-time imaging detectors extended application towards archaeology, geology, aerospace, material science etc. We will briefly discuss few unique applications to highlight the diversity of neutron imaging application areas and importance of neutron as an imaging probe.

1.3.1 Energy research

Proton Exchange Membrane (PEM) fuel cells are an efficient and non-polluting source of clean energy. PEM convert the chemical energy into electricity in presence of a catalyst without combustion. The efficiency of PEM is high as compared to traditional heat engines as it eliminates intermediate heat generation process required for electricity production. Thus, it has the potential for delivering cost-efficient power for everyday use in the near future. Sufficient membrane hydration is required for efficient high power operation as it impacts ionic conductivity and mechanical properties. Change of hydration content in the fuel cell impedes the reactant flow thus resulting in degradation inefficient operation [49], [50]. So, it is important to visualize these dynamics by non-destructive methods. Figure 1.8 shows water content in channels of a fuel cell [1]. Due to high hydrogen content neutron imaging is the best non –destructive investigation tool for high contrast imaging.

Lithium batteries are another source of clean energy that is used extensively in automotive applications. The performance of these type of batteries like capacity, charging speed and aging behavior depends upon the concentration of the lithium concentration and state of the electrodes. Nondestructive technique is a viable method for understanding the batteries under operations [51],

[52]. By visualizing and measuring these quantities by neutron imaging the performances can be investigated and improved during operation. Figure 1.9 shows the cross-section of such battery indicating Li concentration.

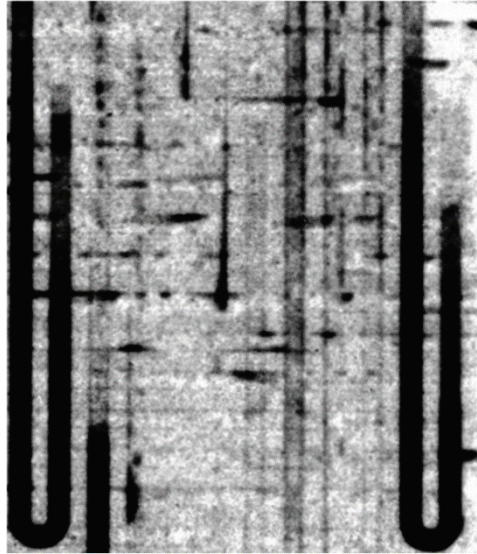


Figure 1.8. Neutron radiograph of a fuel cell showing formation and movement of water by different concentrations in the neutron radiograph [1].

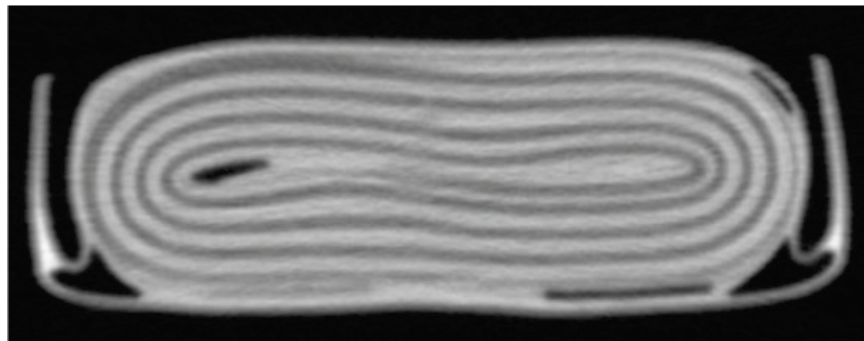


Figure 1.9. Tomography slices showing the distribution of the Li across the Li-ion battery [31].

1.3.2 Material science and engineering

Casting is one of the common and popular methods to produce a compound object from multiple small objects. One type of such casting technique known as lost foam casting (LFC) method. LFC is widely used today due to the advantage of producing near net shaped casting products without any size limits. The first step is to produce a polymeric foam pattern and the next

step is replacing the polymer pattern by molten metals. The molten metal fills the space by decomposing the polymer foam. During this process, a gas layer known as pyrolysis front exists between the metal and the polymer. The quality of casting significantly depends upon the behavior of the pyrolysis front [53], [54]. Neutron imaging provides useful insight of such casting products to identify different flaws to ensure integrity of the products. Figure 1.10 illustrates the foam degradation and generation of pyrolysis layer.

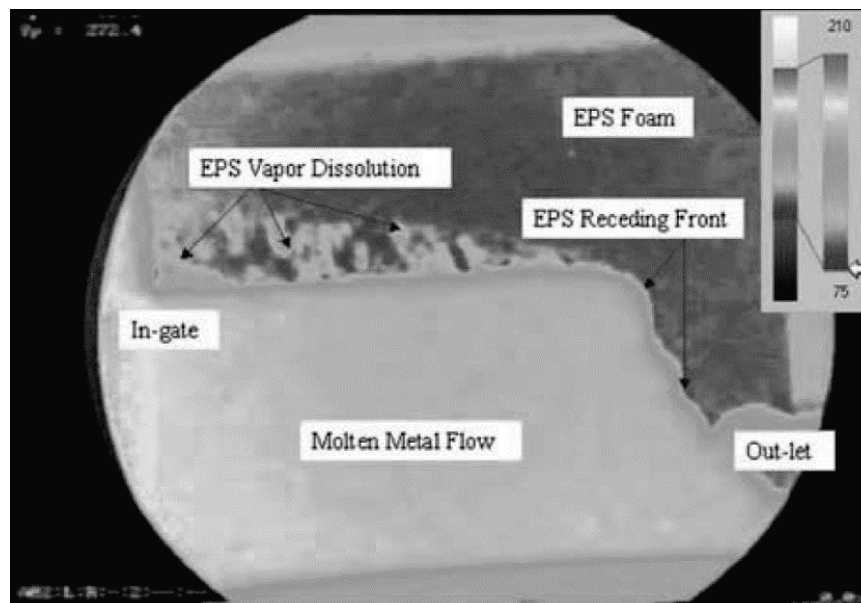


Figure 1.10. Neutron radiography of casting showing the foam degradation, generation of the pyrolysis layer, EPS Foam, Vapor Dissolution area, and molten metal flow [55].

Residual stress is one of the phenomena arises during a process such as grinding, machining, welding, rolling and heat treatment. It can be defined as self-equilibrating internal stress existing in a free body without constraints or external force added on the boundary, or as an elastic response of the material to an inhomogeneous distribution of inelastic strains such as plastic strains, precipitation, phase transformation, misfit, or thermal expansion strain. It type of deformation is a slow process and need significant time before showing symptoms. Residual stress is very difficult to predict but has a significant effect on the durability of material. Neutron imaging especially

neutron diffraction is an important tool to measure the inter-planar spacing from which the lattice strain can be determined [56].

The durability of concrete is determined by porosity, sorptivity, and permeability. Water and moisture affect concrete as it can result in severe freeze damage if not properly drained or vulnerable to shrinkage after drying [57]. Corrosion is another problem in steel structures of reinforced concrete due to moisture. Thus, understanding of water transport through the pores structure of concrete can correlate durability of concrete [58]. Moisture content of concrete can be visualized by neutron imaging as illustrated by Figure 1.11. Neutron imaging is a useful investigation tool for such investigation as it can provide an accurate indication and quantification of the pore structure of concrete [59].

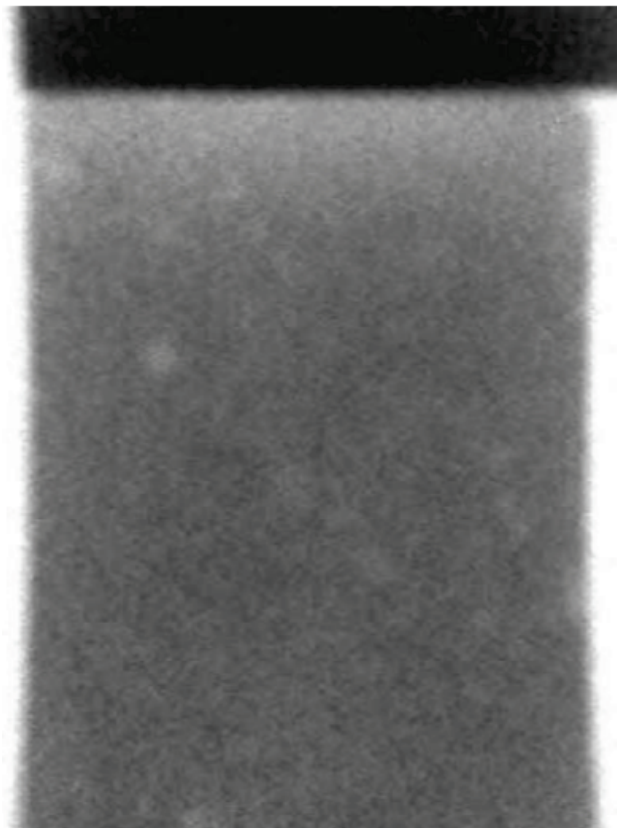


Figure 1.11. Neutron radiograph of partially dry concrete showing the wet region by dark value illustrating the application of neutron imaging for material science and engineering [57].

1.3.3 Biomedical and Biological Applications

Although neutrons are potentially more damaging than photon to biological specimen. Epithermal neutrons have lower dose as compared to thermal neutrons for same exposure time. Depending upon the nature of the sample, neutron imaging provides complementary information which otherwise cannot be visible with X-ray. Currently, study of neutron imaging on a biological sample is ongoing for pharmaceutical research [60]. Figure 1.12 shows neutron radiograph of rat lung.



Figure 1.12. Neutron radiograph of an unconfined and inflated rat lung illustrating the biomedical and biological application of the neutron imaging [61].

Neutron stimulated emission computed tomography (NSECT) has been developed recently to detect the presence and quantify the spatial distribution of elements in a biological sample. This technique uses fast neutrons to excite the target nucleus. By measuring the emitted gamma signature from the excited nucleus, elements can be identified. Tomographic reconstruction of such gamma signatures can provide the spatial distribution of such elements across the sample.

These characteristics of NSECT are used to find and diagnose a disorder of the human body like detection of malignant tissue of cancer [62], [63].

1.3.4 Cultural Heritage

Noninvasive investigation of cultural heritage is often required for accurate determination of elemental composition, structural condition for restoration and preservation. X-ray imaging doesn't provide sufficient contrast when a metal object needs to be examined with organic matter like religious relics, bones in chalk rock or ferrous clastic terrestrial deposit [64]. Prompt gamma-ray activation analysis (PGNAA) coupled with neutron tomography is used to map three-dimensional elemental compositions across the object. Thus neutron imaging technique combined with advanced image analysis leads to a characterization of cultural heritage objects [65], [66]. Figure 1.13 illustrates neutron radiograph of an ancient Tibetan metallic Buddha statue.

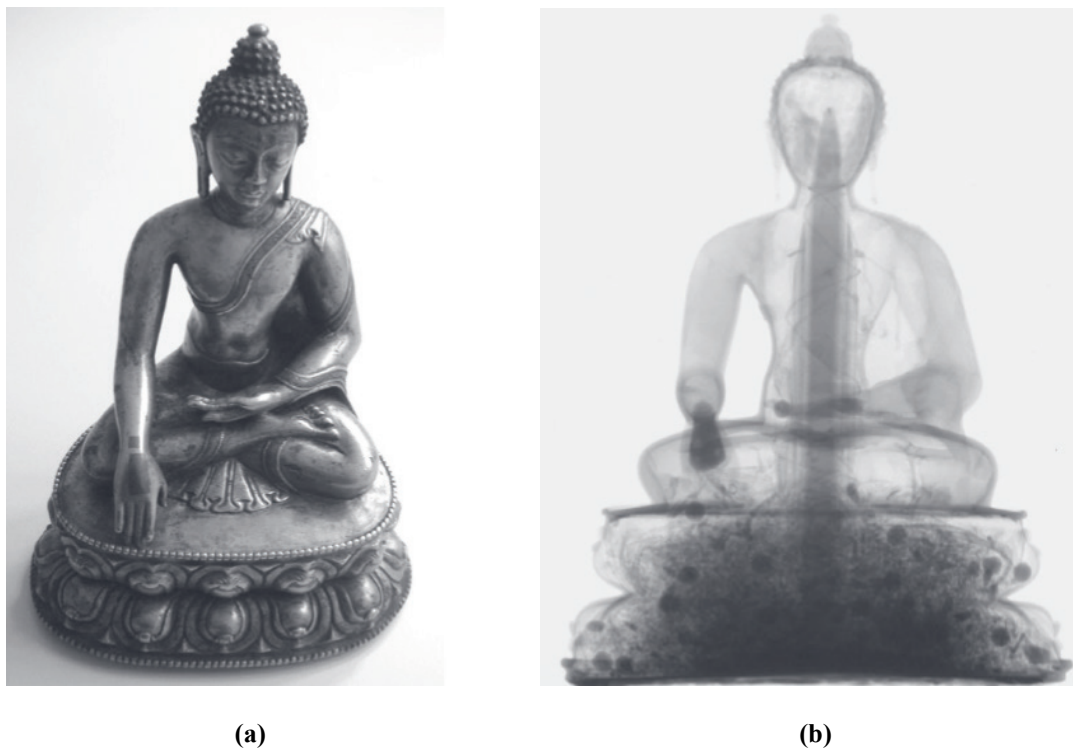


Figure 1.13. Neutron radiograph of an ancient Tibetan metallic Buddha statue (a) photograph of the Buddha sculpture, and (b) neutron image, illustrating the internal organic content of the statue [67].

1.3.5 Two-Phase Flow

Flow pattern visualization is important in two-phase flow to study, analyze and understanding the thermal hydraulics. The observation serves as a tool to understand the mechanism of multiphase flows for formulating the constituent equations. Observing and measuring bubbles that are formed during nucleate boiling can be used for validating the existing model and predicting the bubble dynamics accurately [68]. Such models can be used to calculate the heat transfer coefficient more precisely which may help us for safe and efficient utilization of nuclear reactors. Visible ray is sufficient for these type of study for fluids enclosed in transparent tube or vessels but occasionally requirement arises to observe the flow inside an optically opaque metal enclosure [69]. Neutron imaging is a viable tool to investigate such situations due to their unique interactions type unlike other imaging modalities [70]. In this section, we will briefly discuss few non-invasive and invasive techniques for such investigation of two-phase flow and discuss the importance of neutron imaging to overcome their limitations.

1.3.5.1 Non-Invasive Technique

Ultrasonic Technique

It uses a piezo-electric transducer and AC pulsed signal to generate ultrasonic sound for characterization of two-phase flow. When AC pulsed signal is applied to a piezoelectric crystal, it causes vibration to generate ultrasonic sound. The transmitted sound pulse interacts differently with each phase and the interfaces between phases with different acoustic impedances reflect sound pulses back towards a transducer [71]. Pulse-echo method is mainly used for measurement of film thickness and the transmission method is used for measurement of void fraction, phase distribution, interfacial areas, and bubble diameter. Although this technique has excellent time response, the major limitations are the transducer curie point and false echo. The Curie point is the maximum operating point of the transducer and a false echo can be generated from any obstacle

within the flow. As an example, a false echo can be generated from the fuel rod bundle interfaces, which can be detected as an incorrect void fraction in the two-phase flow. Typical spatial resolution of this technique is around 14 mm [72].

Gamma and X-ray

This technique uses gamma radiation and gamma sensitive detector. In the case of two-phase flow, a gamma flux is exponentially attenuated by the mass of the liquid. Similar to other radiation modalities, a gamma beam also attenuates by exponential attenuation law. The void fraction can be calculated as,

$$\alpha = -\frac{\ln\left(\frac{I_{2\phi}}{I_l}\right)}{\ln\left(\frac{I_g}{I_l}\right)} \quad (1.4)$$

where α is the void fraction, $I_{2\phi}$ is detected gamma flux after attenuated by two phase flow, I_l and I_g is detected gamma flux after passing through the liquid and the gas respectively [73]. Usually, ionization chambers and photo-multiplier tube are used as the detector. When radiation interacts with these types of detector, the charged particles generated and multiplied by the photo-multiplier tube before detection. The main limitation with these type of investigation is the low contrast and coarse spatial resolution. Additionally, gamma densitometer is applicable only to small homogeneous channel. The calculated void fraction by this method assumes one-dimensional model and can results in a strong flow regime effect. X-ray also operates in a similar principle as gamma-ray [74]. With the advancement of fast electronics, X-rays are often utilized for such characterization due to the easy access of the required hardware. Similar to gamma rays, the imaging with X-rays also limited with low resolution. However, X-rays produce better spatial resolution compared with the gamma rays due to the improvement in the X-ray detector technology. The modern X-ray tube can generate smaller spot size as compared with the gamma

source of equal strength, thus improving spatial resolution. Typical spatial resolution of gamma and X-ray techniques for such type of investigation is around 2 mm and 1 mm [75], [76].

Optical Method

An easy way to observe and characterize two-phase flow is the optical method. This technique used a fluorescent lamp and a high-speed camera to capture an image. However, applicability of this method is limited when vessel is optically opaque and thickness of liquid allows the light to be transmitted inadequately. Typical spatial resolution of this method is around 50 μm [77]. Sometimes, a tracer agent is mixed with liquid to observe velocity field within the liquid. Particle image velocimetry (PIV) is a method for flow visualization, where suspended particles are illuminated and path followed by these particles are studied to characterize the flow properties [78]. Many multiphase flows are optically opaque and often enclosed within a metal enclosure, which limits the feasibility of this technique.

Magnetic resonance imaging (MRI)

MRI is a technique that utilizes the interaction between the nuclear spin of certain nuclei with an externally applied magnetic field. MRI investigation can provide information like coherent fluid velocities, molecular diffusive rates, etc. MRI utilizes the fact that frequency of precession of nuclear spins in a magnetic field is directly proportional to magnetic field strength and when magnetic field is turned off, they relax back to equilibrium with longitudinal field. The precession of these nuclear spins with and without field induces a time-dependent complex signal in a receiver coil. This signal is decoded and reconstructed to extract positional information about object [79], [80]. Bubble size can be measured either from a projected bubble shape in the rendered image or can be extracted from a local signal intensity in the image. However, positional information can be obtained if the whole bubble is contained within the region of excited fluid. The typical spatial

resolution of this technique is around 500 μm [81]. However, applicability of this technique is limited from the high void fraction and pressure fluctuation caused by bubble interactions.

1.3.5.2 Invasive Technique

Wire Mesh Sensors (WMS)

The WMS is an invasive technique to characterize the two-phase flow. This technique uses a grid structure of electrodes that measure the electrical conductivity or capacitance properties to extract the positional information, when the fluid and bubble crosses the grid. Since conductivity of fluids changes with temperature variations, capacitance property is used to measure the changes to detect time-varying cross-sectional void fractions across the grid. The accuracy of this method depends on accurate correlation between measured electrical parameters to local void fractions and exact handling of positional information at sensor. The spatial resolution of this technique depends upon density of the measurement grid and typical spatial resolution is around 3 mm [82]. However, intrusive nature of this technique disrupts the flow pattern which affects the measured quantities.

Electrical Conductivity Probe

This technique uses electrical conductivity probes for the determination of local void fraction of the two-phase flow systems. It is possible to measure the bubble sizes in two-phase flow using multiple probes at the same time. Usually, a small portion of the wire tip is exposed for measurement and rest part is insulated. Twin probe is an advanced version of the single wire probe, which can measure the bubble size and velocity in a three-phase fluidized bed. Similar to WMS, this technique also disrupts the flow pattern and can measure the parameters of a small localized region [83].

These limitations of preceding imaging methods for two-phase flow can be overcome by the high-resolution neutron imaging. Unlike WMS or electrical conductivity probe, neutron imaging is a non-invasive imaging technique, thus it doesn't disrupt the flow pattern during the

investigation. In addition, neutrons are more sensitive to hydrogenous material like water, thus good contrast can be obtained compared with gamma and X-ray. Ultrasonic sensors are usually mounted around a surface of a metallic enclosure and limited by temperature of the surroundings, thus limiting its applicability in high-temperature scenarios. The application of MRI is limited for the observation of steady-state flow, as pressure fluctuation due to bubble interaction results in the interpretation of false information. The investigation of two-phase flow with neutrons doesn't affect by bubble interaction, thus accurate information regarding bubble dynamics can be obtained. So, high resolution neutron imaging technique is a viable technique to overcome the preceding limitations for the investigation of two-phase flows specifically microbubbles.

The outcome of this work will not only provide a better understanding of neutron imaging system, but also by examining the characterization of such systems with advanced image processing techniques, a path can be envisioned for the development of high-resolution real-time neutron imaging system. After giving an overview of the PULSTAR neutron imaging facility in the next chapter, the details of this work will be presented in subsequent chapters.

Chapter 2 Neutron Imaging at PULSTAR

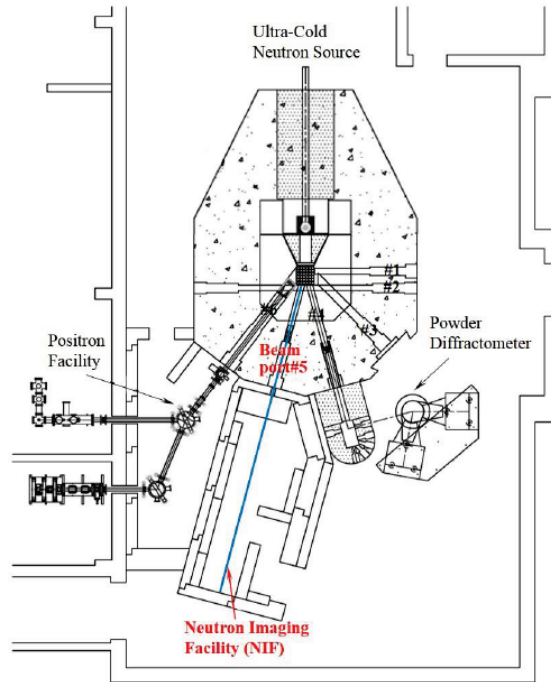
2.1 Introduction

The PULSTAR research reactor is located at North Carolina State University and dedicated for scientific research in various multidisciplinary areas. The reactor went critical in 1972 and has been operational at 1MWth for last 45 years. Utilizing different beam ports of the PULSTAR several unique high-performance instruments have been developed for advanced research and industrial applications. These facilities include intense positron beam, an ultra-cold neutron source, advanced neutron imaging system, a neutron powder diffractometer, and a fission gas release and measurement loop. Apart from the advanced research, PULSTAR has been utilized for education and training through Internet Reactor Laboratory. Design and analysis of imaging detector system require understanding of the imaging facility and their characteristics. This chapter presents description and characteristics of the neutron beam and the state of the art instrumentation of the imaging facility at PULSTAR.

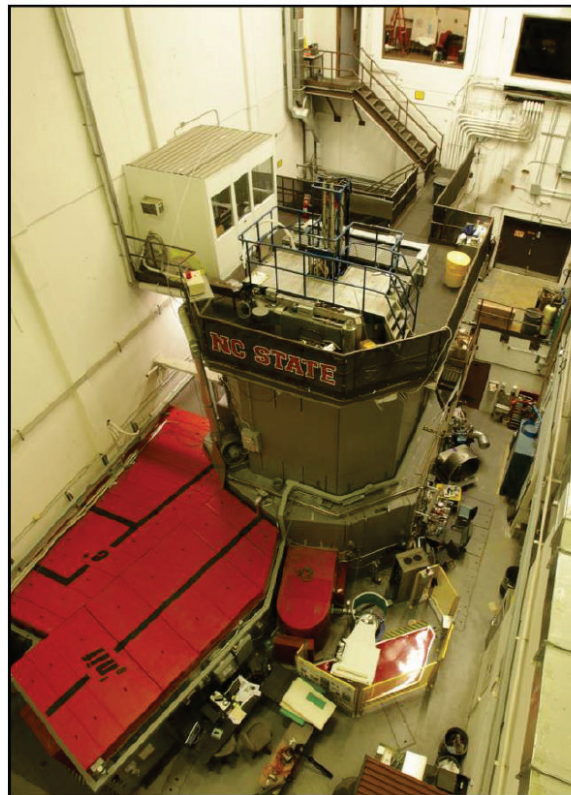
2.2 Neutron Imaging Facility

2.2.1 PULSTAR Reactor

The PULSTAR reactor is an open swimming pool type and reactor core is housed inside a 15,000-gallon water. The water acts as coolant and the moderator. The core has a size of 15 x 13 x 25 and contains 6% enriched UO₂ fuel. An upgrade to the current capacity of 1 MWth to 2 MWth has been started. It is loaded with 5x5 rectangular fuel assembly and 25 UO₂ fuel pin each assembly. There are total 6 beam tubes to address the needs of multidisciplinary research. The layout of PULSTAR is illustrated in Figure 2.1 and the details of the beam port are in Table 2.1. Top view of the beam ports is shown in Figure 2.2.



(a)



(b)

Figure 2.1. The layout of PULSTAR research reactor (a) Schematic diagram, and (b) PULSTAR reactor bay, showing different beam layout and facilities [84].

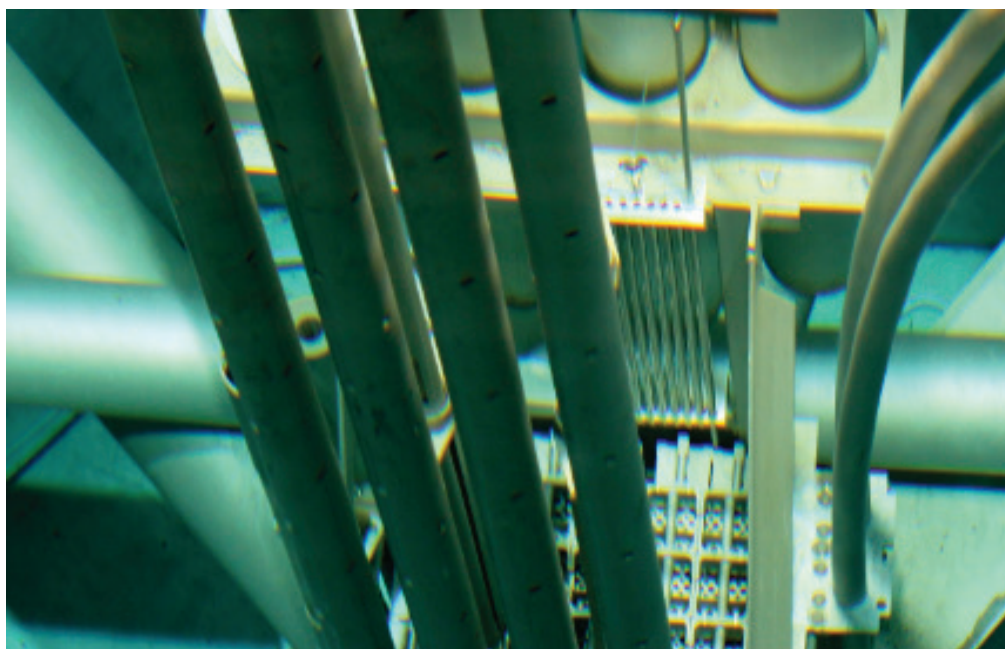


Figure 2.2. Top view of the core and beam ports

Table 2.1. Utilization of PULSTAR beam ports

Beam port	Utilization	Description	Intensity (n/cm²/sec)
1	Fission Gas Release Measurement	6-inch diameter radial tube	1×10^{12} thermal at core end
2	Ultra-Cold Neutron Source	6-inch diameter tangential tube	1×10^{12} thermal at center point
3	-	8-inch diameter radial tube	1×10^{12} thermal at core end
4	Powder neutron diffractometer	6-inch diameter radial tube	$\sim 0.5 \times 10^5$ thermal 1.4 Å on target
5	Thermal neutron imaging	6-inch diameter radial tube	$\sim 5 \times 10^6$ thermal at imaging plane
6	Intense positron beam facility	12-inch x 12-inch square radial tube	6×10^8 positrons/second at target

2.2.2 Neutron Beam

The thermal neutron imaging facility is located at beam tube number 5 at PULSTAR. The port has been strategically selected due to its available distance from core to image plane. Details of the design have been already documented in ref. [85]. The major components of the thermal neutron imaging facility are filters, collimator, and detection system. The overview of the neutron imaging facility is illustrated in Figure 2.3.

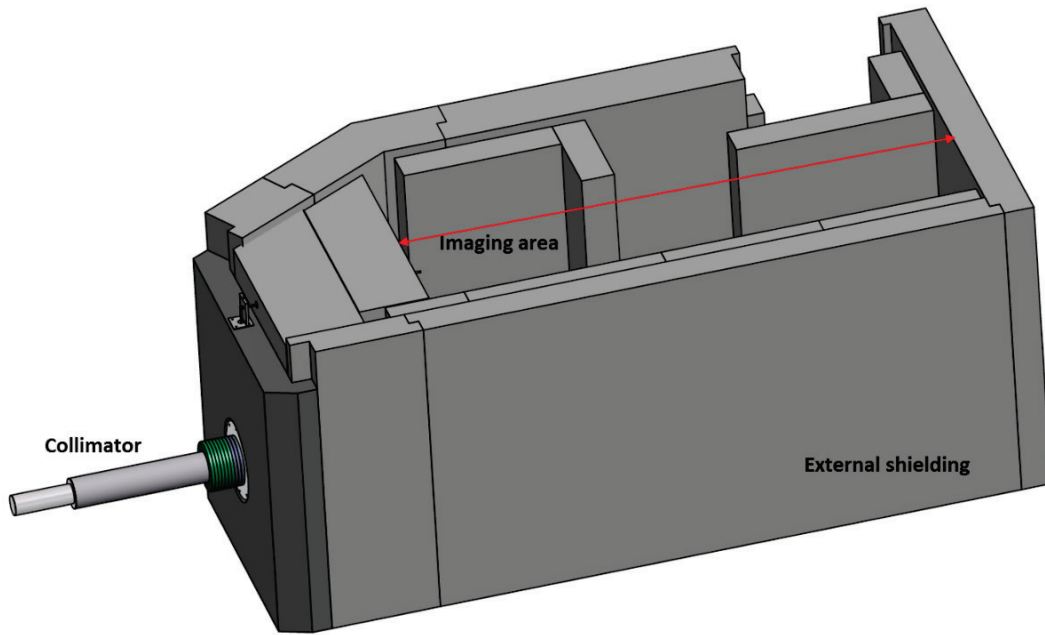


Figure 2.3. Illustration of PULSTAR neutron imaging facility showing a 3D rendering of the collimator, external shielding, and the imaging area.

2.2.3 Characterization of Neutron Source

The measured neutron flux at beam port entry is $\sim 3.7 \times 10^{12} \text{ n/cm}^2\text{s}^{-1}$. The uniformity in spatial distribution of neutron flux around inlet area is experimentally measured. The flux is measured with a miniature fission chamber at a different position around the port entry. The principle of the neutron flux measurement with fission chamber is based on the creation of electrical signal under influence of neutrons. By measuring the change in electrical parameters, the flux can be calculated with the calibrated fission chamber.

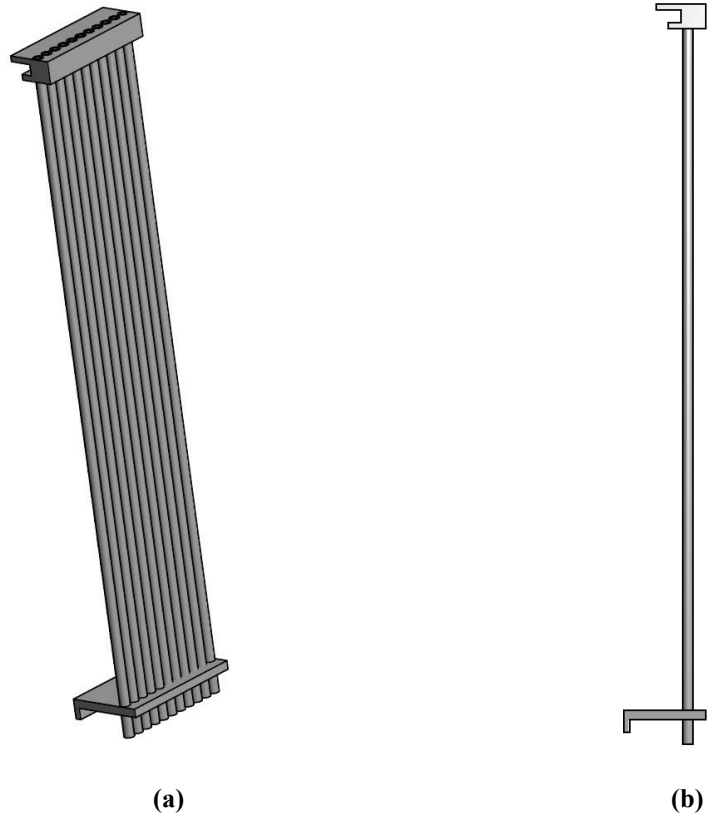


Figure 2.4. Design of the tool to measure the distribution of the neutron flux at the entrance of the neutron beam tube, (a) 3D view, and (b) side view.

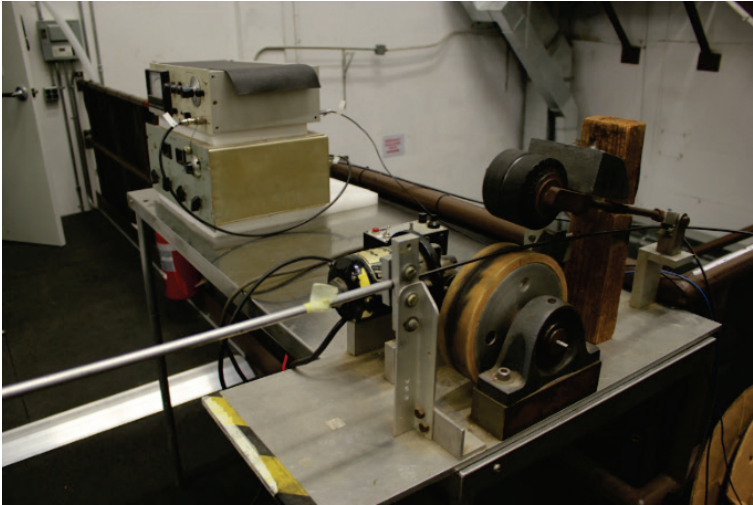


Figure 2.5. Top view of the reactor pool showing the arrangement to measure the neutron flux distribution across the entrance of beam tube #5.

The position across the tube is controlled by an aluminum jig as shown in Figure 2.4. The pin diode is pulled through the tube with a calibrated stepper motor to measure the flux along the tube. The experimental arrangement for the measurement is shown in Figure 2.5 and Figure 2.6. The spatial distribution of the neutron flux is shown in Figure 2.7.



(a)



(b)

Figure 2.6. Neutron flux measurement tool, (a) high voltage (HV) power supply for the miniature fission chamber and electrometer to measure the current, (b) position calibration unit.

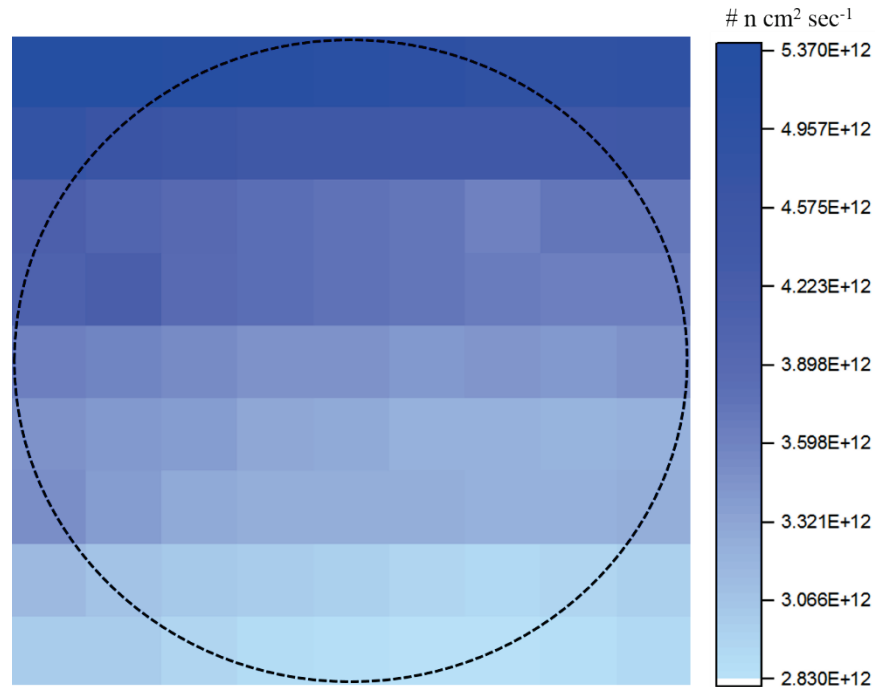


Figure 2.7. Spatial distribution of measured neutron flux across the entrance of beam tube #5 of the PULSTAR reactor (beam tube is shown in dotted line).

2.2.4 Collimator

The collimator is a cylindrical tube and starts after the reactor core as illustrated in Figure 2.8. The collimator is a convergent and divergent type and has three different thicknesses along the length. It can be divided into pre-collimator, beam filters, and main collimator. It starts with a 6 inches diameter near the reactor core then increases to 9 inches after 65 inches. The final diameter of the collimator is 10 inches long with a 15 inches diameter. First part of the collimator is pre-collimator and its convergent shape leads the neutron towards the filters. The beam tube has a direct view of the reactor core. So the beam contains high gamma flux as well as fast neutrons. To improve the beam quality for thermal neutron imaging, proper filtration was required. Single crystal beryllium, silicon, quartz, sapphire, bismuth, and lead are known for fast neutron filters. But sapphire has a significant advantage over other material as properties of sapphire remains constant after prolonged operation at high activity environment. Thermal neutron transmission is not very sensitive with temperature as compared to other material. Thus making it as a viable

choice as a fast neutron filter. Additionally, Gamma can be filtered effectively with bismuth. However, bismuth also have high cross section towards thermal neutron, which reduces thermal neutron flux. The filter selection and length optimization for this facility can be found in Ref. [85], [86]. Currently, two six inches single sapphire crystals are used to remove fast neutrons and gammas while sustaining adequate thermal neutron flux. The neutron and gamma energy spectrums can be found in ref. [85]

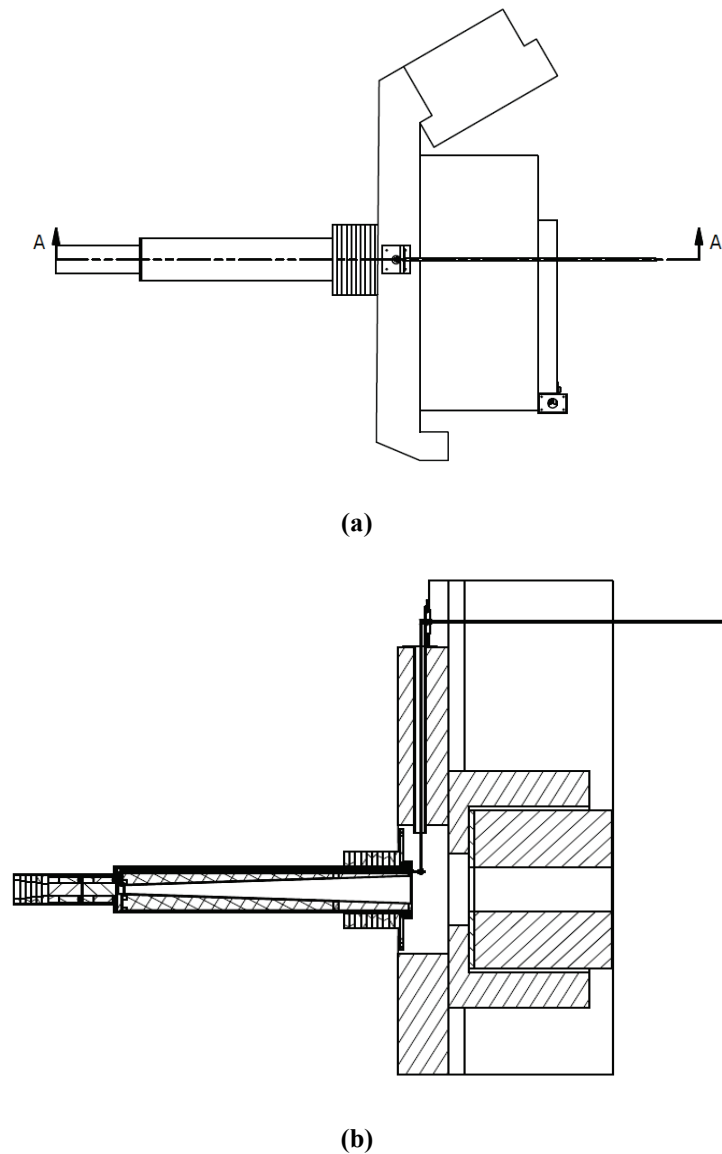
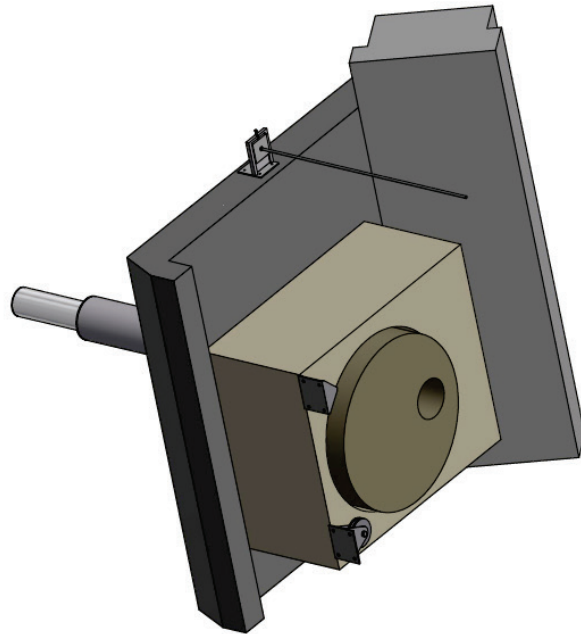


Figure 2.8. Schematic of the neutron collimator and beam shutter of the imaging facility, (a) top view, and (b) cross-sectional view.

After the filter section, the collimator is the divergent type with a 2-degree divergence. Inner walls are shielded with 0.1 inch thick Boral to reduce scattered neutron. Rest of the divergent section is filled with heavy concrete shielding. Next section of the beam is 25.5-inch-thick rotating drum type beam shutter. The shutter and the imaging facility are shown in Figure 2.9 and Figure 2.10 respectively.



(a)



(b)

Figure 2.9. Beam shutter, (a) CAD representation, (b) actual representation.

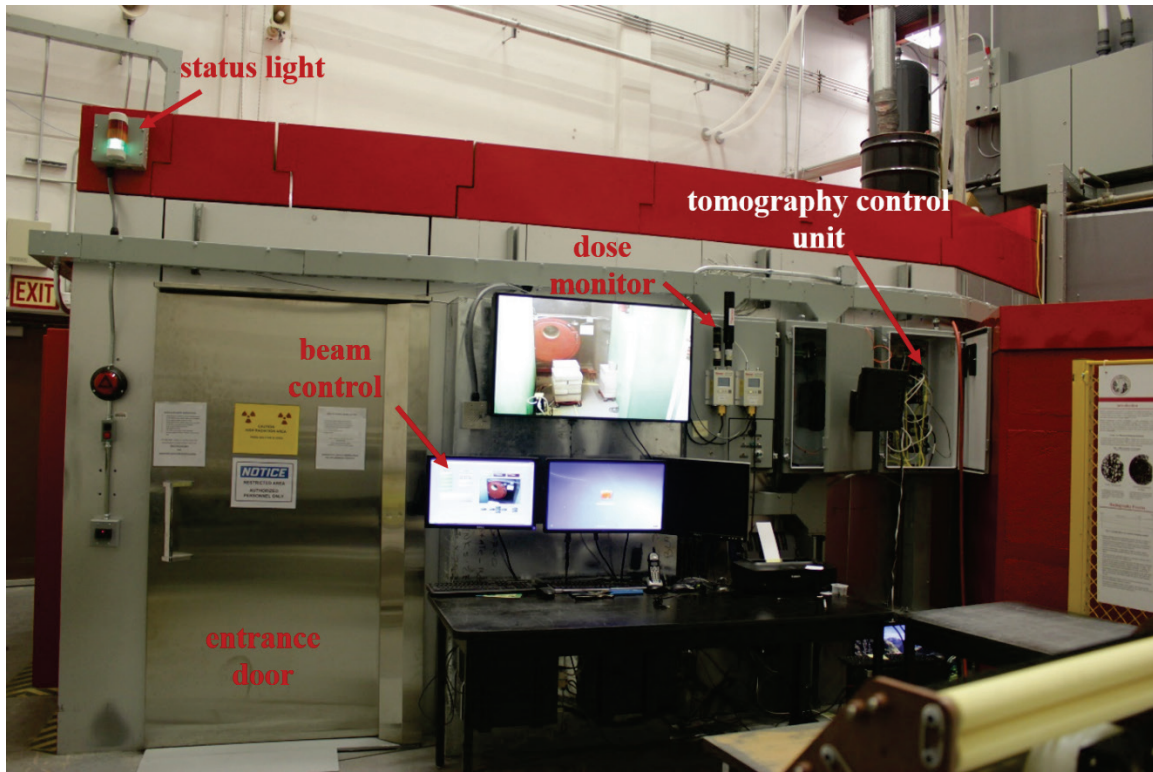


Figure 2.10. Outside view of neutron imaging cave showing entrance door, beam control interface, dose monitors, tomography controller equipment.

2.3 Imaging Instrumentations

2.3.1 Film

Since neutrons interact with the atomic nucleus only, neutron needs to be converted to some secondary particle for detection. Similar to X-ray radiograph, films with a neutron absorbing converter screen has been used for neutron imaging. Although, this technique achieves comparatively good spatial resolution, their performances are limited with the scanner hardware to read and digitize the neutron radiograph. Most neutron films use a gadolinium conversion screen due to its high absorption cross-section, followed by an image recorder screen. Secondary radiations are emitted when neutrons are absorbed in the converter screen. An image is formed when these secondary radiations are detected in a recorder screen. The image recorder screen contains silver halide. A latent image is formed on the film when it is exposed to the neutrons and visible later when the film is developed. Development process in the exposed region results in a

high optical blackening due to more precipitated silver from exposed silver halide. The degree of blackening is known as optical density and represents the characteristic performance of the film based neutron imaging system. The exposure time for this type of detector can be typically up to several minutes. Films are still used as a regular method for non-destructive technique on a routine basis. The equipment for film-based system is illustrated in Figure 2.11.

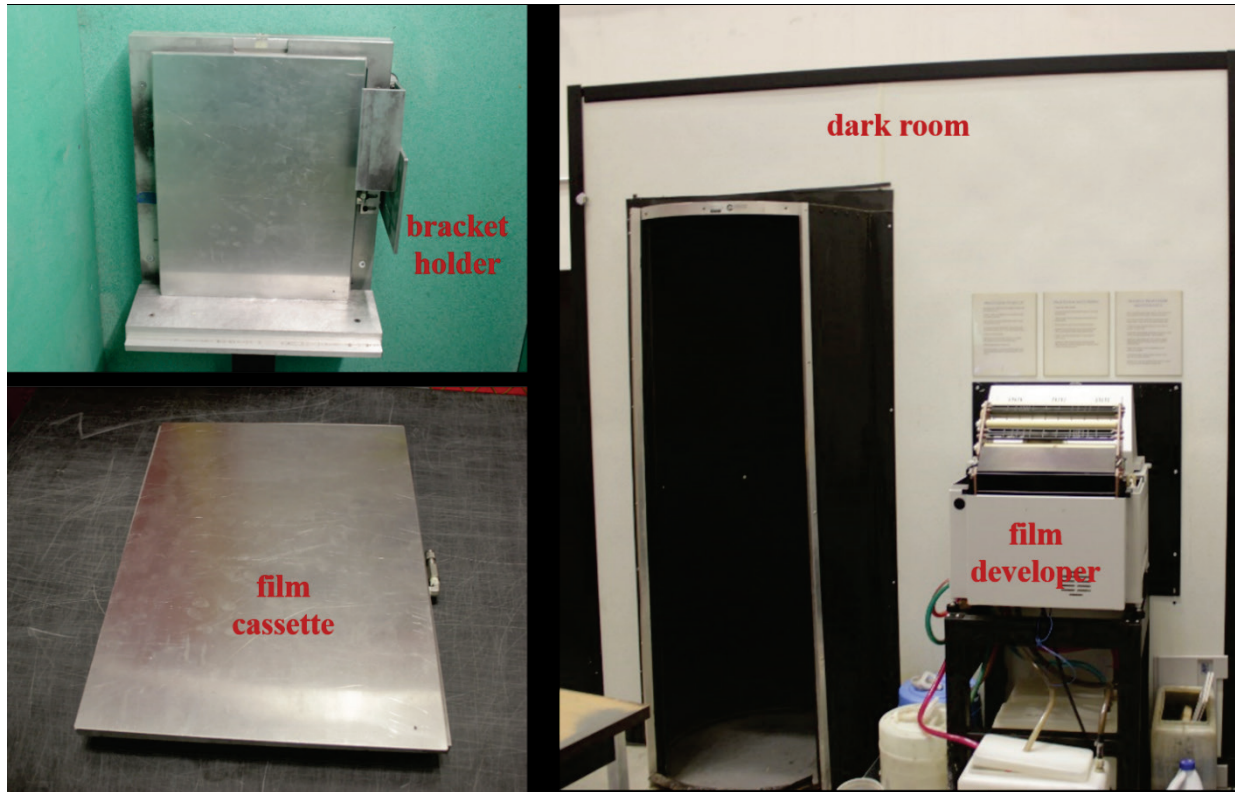


Figure 2.11. Film based neutron imaging equipment showing film cassette, cassette holder at the neutron imaging beam line, dark-room and film developer.

2.3.2 Image Plate

The overall development process of the film based imaging systems is slow. The dynamic ranges and linearity of the films are limited and films can't be reused once it has been exposed to neutrons or optical light. Image plates (IP) have traditionally been used in X-ray imaging but their use in neutron imaging is comparatively recent. IP consists a mixture of neutron absorber material and storage phosphor. When neutrons are absorbed in the IP, secondary radiations are emitted and

absorbed in the storage phosphor. Subsequently, electron-hole pairs are created at the storage locations. A conventional He-Ne laser is used to readout the IP, point by point after the neutron exposure. The laser light causes photostimulation of the electron storage center causing them to recombine and transfer the stored energy to the dopant ion. Released energy is detected by its characteristic luminescence by a photomultiplier tube through a light guide and later converted into an electrical signal. The digital output of the IP scanner can be stored for further processing. IP based detection system are listed shown in Figure 2.12.

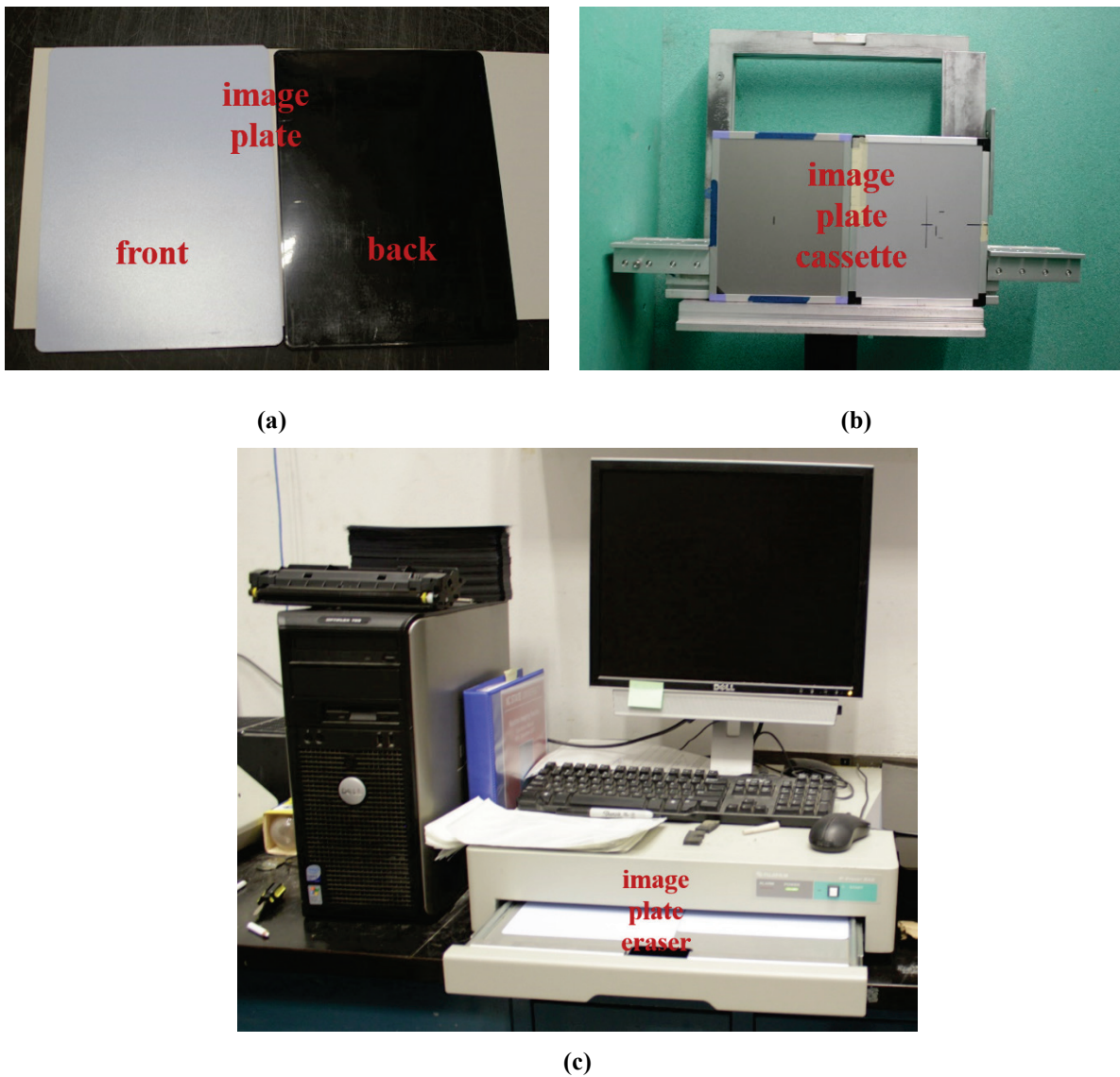


Figure 2.12. IP based neutron imaging equipment showing (a) imaging plate, (b) plate holder cassette inside the imaging beam and, (c) imaging plate eraser.

2.3.3 Real Time Neutron Imaging System

Films and IP based neutron imaging system can't be used to investigate in real time applications. Scintillator combined with charged couple device (CCD) can overcome that limitation while maintaining good spatial resolution. Unlike IP this type of scintillator works on neutron capture followed by phosphorescence phenomenon. A scintillator screen is typically made of materials with high cross sections for thermal neutrons. When neutrons are absorbed in a scintillator charged particles are generated. These charge particles deposited their energy inside the scintillator and optical photons are generated. The optical photons are transported through the scintillator and guided through lenses and finally captured by CCD. Electrons are generated from the captured optical photons inside the pixel well of the CCD chip. Charges are read by serial register row by row and converted to a digital value by an analogue to digital (A/D) converter. Details discussion on this type of imaging system will be presented in Chapter 3. The scintillator screen, lenses, CCD cameras and imaging system cart assembly are illustrated in Figure 2.13, Figure 2.14, Figure 2.15, Figure 2.16 and Figure 2.17 respectively. The salient features of the CCD are illustrated in Table 2.2.



Figure 2.13. ${}^6\text{LiF:ZnS(Ag)}$ scintillator screen, (a) front side of the screen, and (b) aluminum bracket.



(a)



(b)

Figure 2.14. Lens used for real-time neutron imaging showing (a) micro-Nikkor 55mm, and (b) micro Nikkor 200 mm $f/4$ IF-ED.



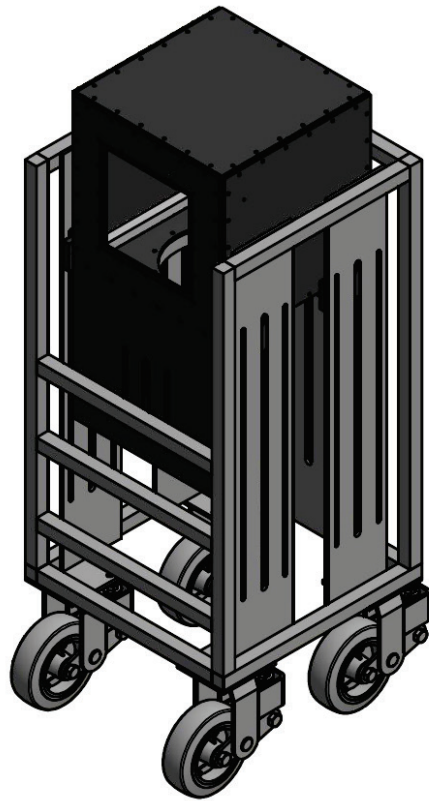
Figure 2.15 Real-time neutron imaging camera iKon-L CCD.



Figure 2.16. Real-time neutron imaging camera iXon-Ultra electronic multiplier (EM) CCD camera.

Table 2.2. Salient features of iKon L 936 and iXon Ultra 888

Parameter	ANDOR iKON-L 936	ANDOR iXon ULTRA 888
CCD Sensor size (cm x cm)	2.76 x 2.76	1.33 x 1.33
Pixel size (μm)	13.5	13
pixels (horizontal x vertical)	2048 x 2048	1024 x 1024
Pre-amp Gain	1,2,4	1,2
EM Gain	NA	1 – 900
Readout clock rate (MHz)	0.05, 1, 3, 5	0.1, 1, 10, 20, 30
Pixel well capacity (electrons/pixel)	89064	74900
Minimum dark current achievable	3.72E-04	6.8E-05
Sensor temperature	-78.6	-100.76
Digitizer (bit)	16	16
Communication	USB 2.0	Camera Link, USB 3.0
Frames per second	0.414	10



(a)



(b)

Figure 2.17. Real time imaging system camera cart assembly showing (a) 3D CAD representation, and (b) camera cart with mounted camera box holding CCD camera, lens and scintillator.

2.4 Positioning System

A positioning system is required to move and position an object during radiography or collect data for different angular position during a tomography experiment. The sample positioning system has 4 degrees of motion and capable of handling 200 lbs. of load. Three of them are linear and control x - y - z motion and another one is angular. The design of the table is shown in Figure 2.18 and characteristics are summarized in Table 2.3. The positioning system was designed in several modules and can be assembled by the following process. Mechanical assembly of the positioning system starts with a 406XR base platform. The 406XR clamped with a base platform with 4 toe clamp. Next 406XR to 404XR (x - z axis) clamps are mounted top of a 406XR table next such that the face of the bracket should be in the direction of the motor.

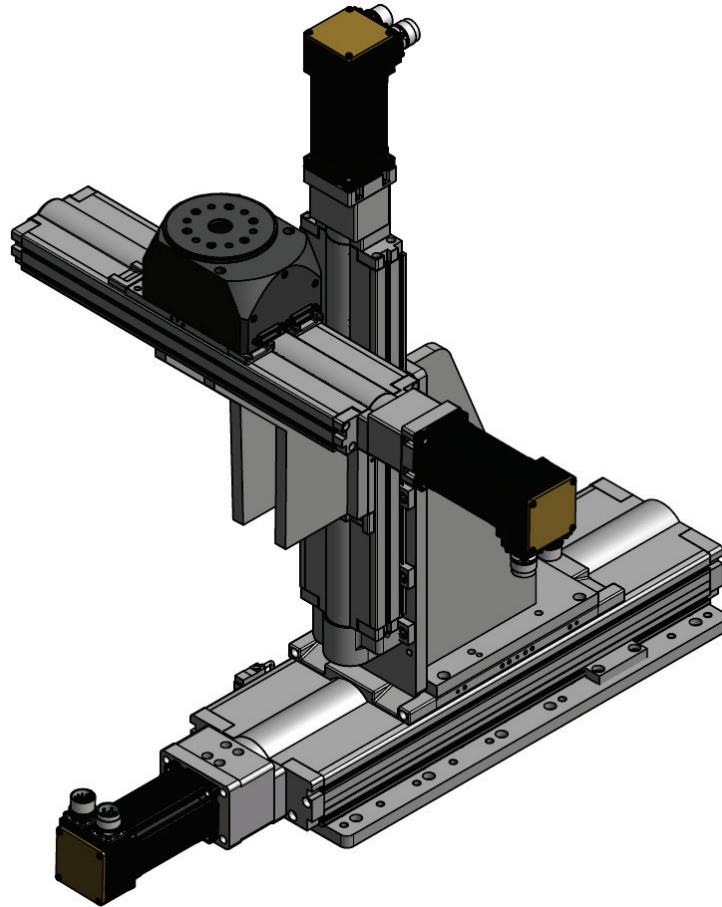


Figure 2.18. CAD representation of the positioning system showing three linear motion and one angular motion to control the object for radiography or tomography experiment.

The 404XR is mounted on the vertical clamp with the support of 4 toe clamp. The z -axis to y -axis clamp holds and supports the rotational table. The dimensions are calculated such that the centerline of the beam should intersect the object center and the inline motor of the 404XR vertical table is outside of the neutron beam. Orientation of the positioning table can be later adjusted to accommodate different object as per application requirements. The interface plate between y -axis and rotary table, RD100 act as pinning device between 404XR table and RD100. The connector of RD100 is aligned in the x -axis direction. A control software handles the interface between a user and all the hardware for the data acquisition system. The user interface (UI) is designed with the LabVIEW (Laboratory Virtual Instrumentation Engineering Workbench). It is a platform and

development environment for a visual programming language from National Instruments. Originally released for the Apple Macintosh in 1986, it is commonly used for data acquisition, instrument control, and industrial automation on a variety of platforms. The UI has been designed to control the positioning system, control and CCD camera in synchronization.

Table 2.3. Features of the positioning system

Parameter	Stages			
	Horizontal x	Horizontal y	Vertical z	Angular
Load Capacity(lbs)	200	100	100	150
Travel Distance	9"	9"	9"	360°
Position Accuracy	$\pm 0.0002 \mu\text{m}$	$\pm 0.0003 \mu\text{m}$	$\pm 0.003 \mu\text{m}$	$\pm 2.73 \text{ arc sec}$
Position repeatability	$\pm 0.0004 \mu\text{m}$	$\pm 0.0004 \mu\text{m}$	$\pm 0.0004 \mu\text{m}$	$\pm 8.4 \text{ arc sec}$
Flatness Accuracy	$\pm 0.003 \mu\text{m}$	$\pm 0.003 \mu\text{m}$	$\pm 0.003 \mu\text{m}$	-
Control	Closed loop			

2.4.1 Positioning System Controller

The primary connection between UI and the positioning system is made through Ethernet Powerlink communication. Parker ACR 9030 acts as a standalone server to control multiple positioning system axis. The system is scalable through a daisy chain and can control up to eight independent axis. ACR 9030 is called controller managing node (MN) and command position, velocity, drive enable and reset signal to servo drive controller node (CN). The closed feedback loop architecture ensures that the servomotor drive operates as expected. The CN reads the command and drives the servomotor accordingly. Parker Aries EPL can run rotary or linear servomotors with a wide range of feedback device. AR 04 PE is used in our positioning system control hardware to run the servomotor and control the positioning table. ACR server can be

accessed by Ethernet, USB, Serial or Parallel port. The flowchart is shown in Figure The server has fixed IP address and can be accessed via Ethernet switch. It is a good practice to connect the ACR 9030 server without any peripherals and test the initial communications. The comACRServer.exe is based on the previous generation of ACR communication server known as ComACRsrvr.dll. The bstrIP and connect method resides in a shared properties of the IChannel object for the connection. The successful connection can be verified either through via user interface or status LED. The process is illustrated in Figure 2.19.

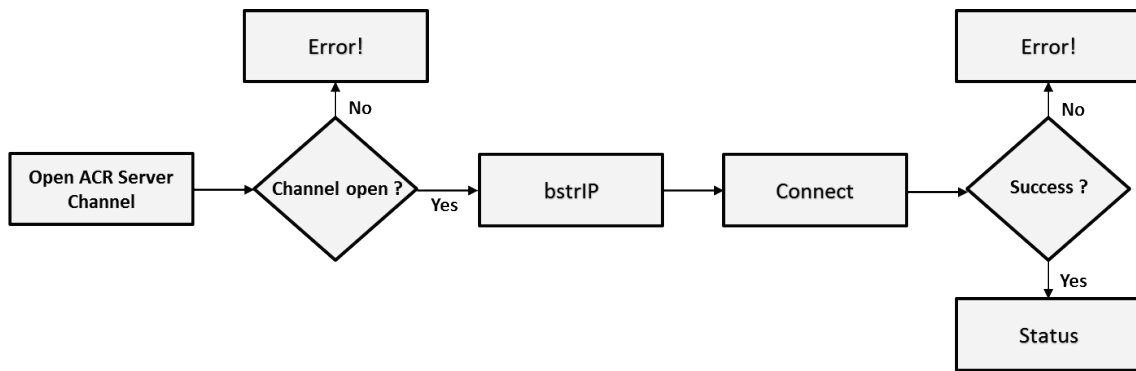


Figure 2.19. Control logic flow diagram for ACR 9030 connection with a PC.

ACR server 9030 is further connected with the AR PE servo drive. Each of the four axis has a separate servo driver and they are connected with the server. After a successful connection, the server checks whether the connected drive is enabled. If the drive is enabled and there is no drive fault then drive, axis and error status are monitored in every 10 ms. Channel once opened by server, IChannel continuously monitor all the connection to ensure proper connectivity among all the hardware components. Unlike IChannel, error channel carries common error messages from one block to another. Each of the axis can be addressed and controlled by appropriate PPU code. PPU is the axis parameter that defines which axis or servo motor is addressed by the controller. PPU code starts with P followed by bit reference. The PPU code for ACR controller is shown in Table

2.4 and the process is illustrated in Figure 2.20. The block diagram and control panel for electrical connection are shown in Figure 2.21 and Figure 2.22 respectively.

Table 2.4. PPU reference

Axis	x	y	z	rotational
PPU	4360	4361	4362	4363

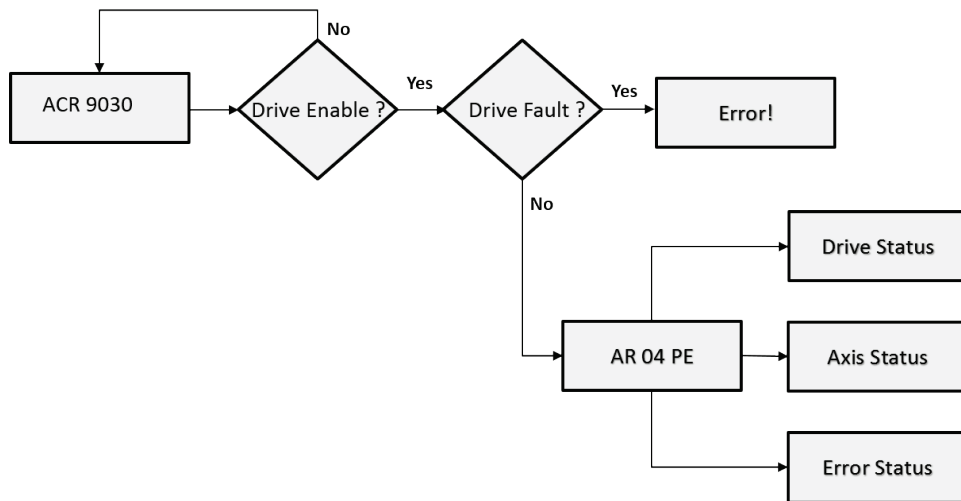


Figure 2.20. Control logic flow diagram for communication between AR-PE servo driver and ACR 9030 axis controller.

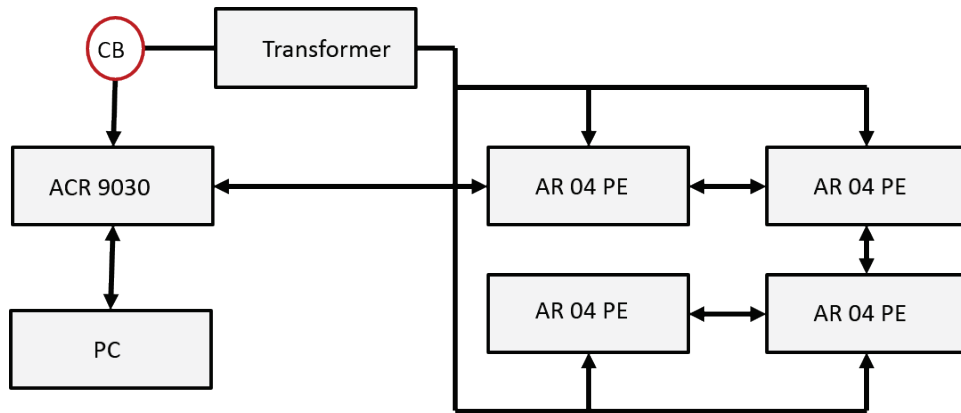
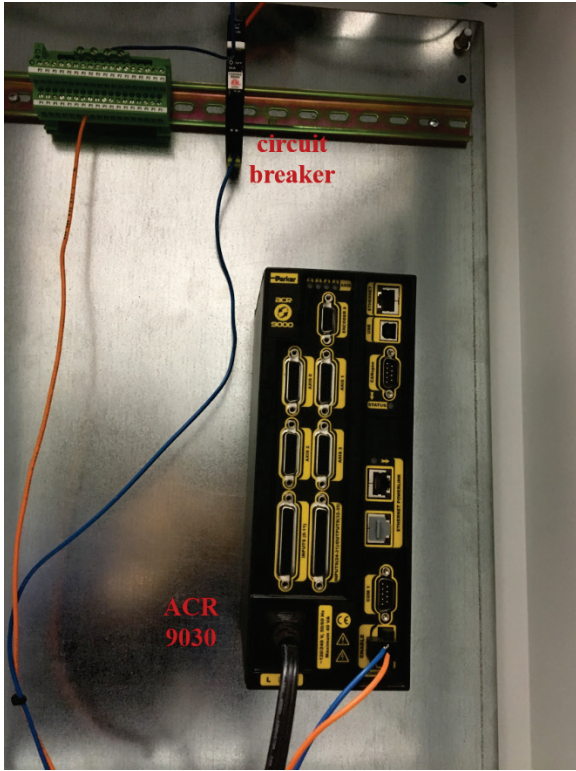
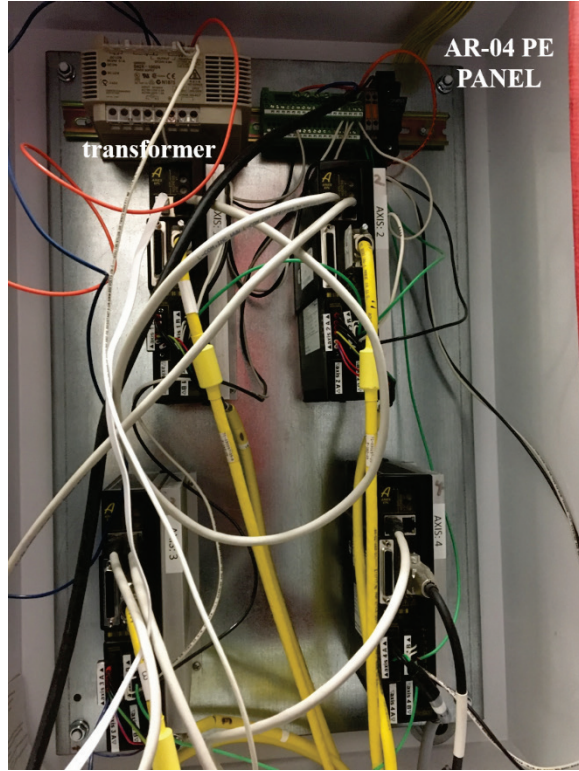


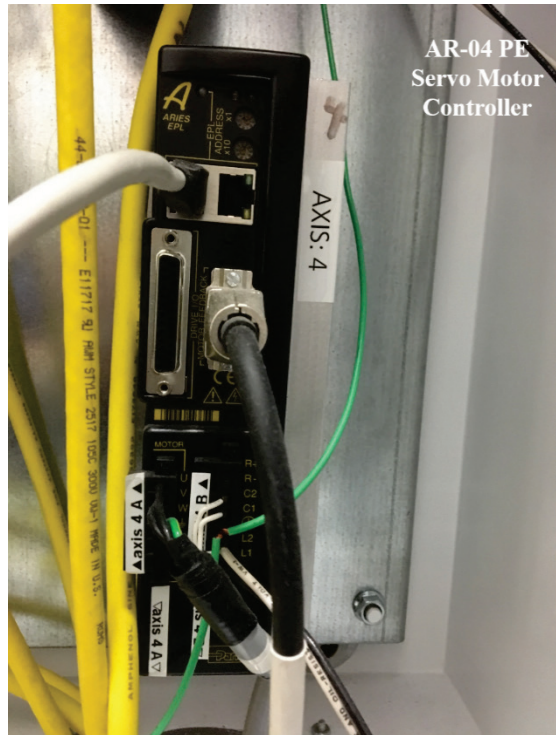
Figure 2.21. Block diagram of positioning system connection showing bidirectional LAN connection between ACR 9030 and AR 04 PE controllers (CB: circuit braker).



(a)



(b)



(c)

Figure 2.22. Control panel for positioning system, (a) ACR 9030 axis controller and (b) AR 04 PE panel containing 4 servo drivers, (c) AR-04 PE controller for axis 4.

2.4.2 Data Acquisition and Control for Tomography

The flow diagram for an automated data acquisition system is shown in Figure 2.23. To reduce dark current, the CCD needs to be cool before it starts operation. The ANDOR CCD camera has an inbuilt thermos electric (TE) Peltier cooling. First, the code will initialize the camera and wait until the temperature reaches -70° C. After that, it will initialize user defined acquisition parameters like exposure time, type of images etc. and check the axis busy flag of the positioning system. If the positioning system busy flag is idle then the CCD will start data acquisition and save the data at predefined disk location.

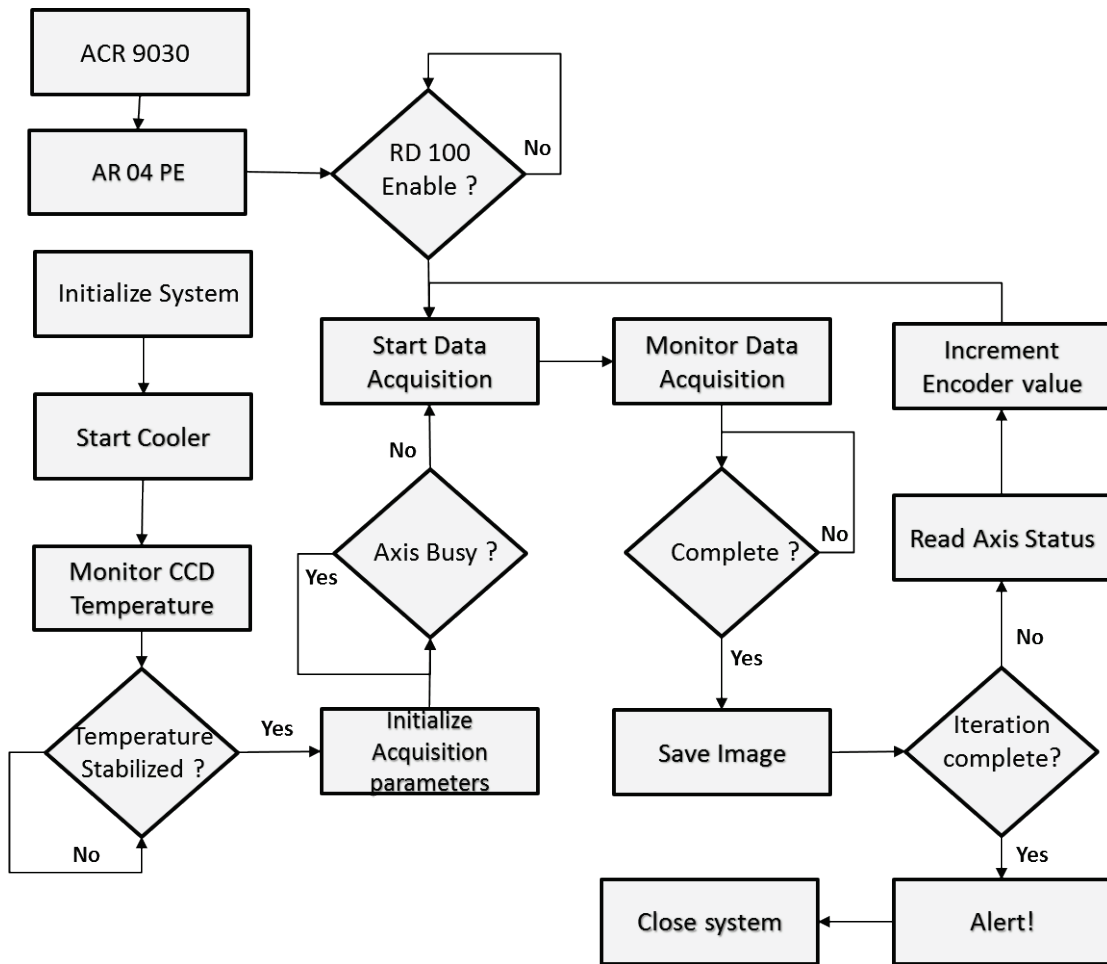


Figure 2.23. Control logic flow diagram for automated tomography data acquisition system by control, communicate and synchronize between CCD and ACR 9030.

After each data acquisition, the encoder value of RD100 is incremented for the required angular step. This process continues until the iteration is complete for all images. After the data acquisition process complete, the system will automatically send an email alert and initiates shutdown process.

The user interface for the data acquisition system is shown in Figure 2.24.

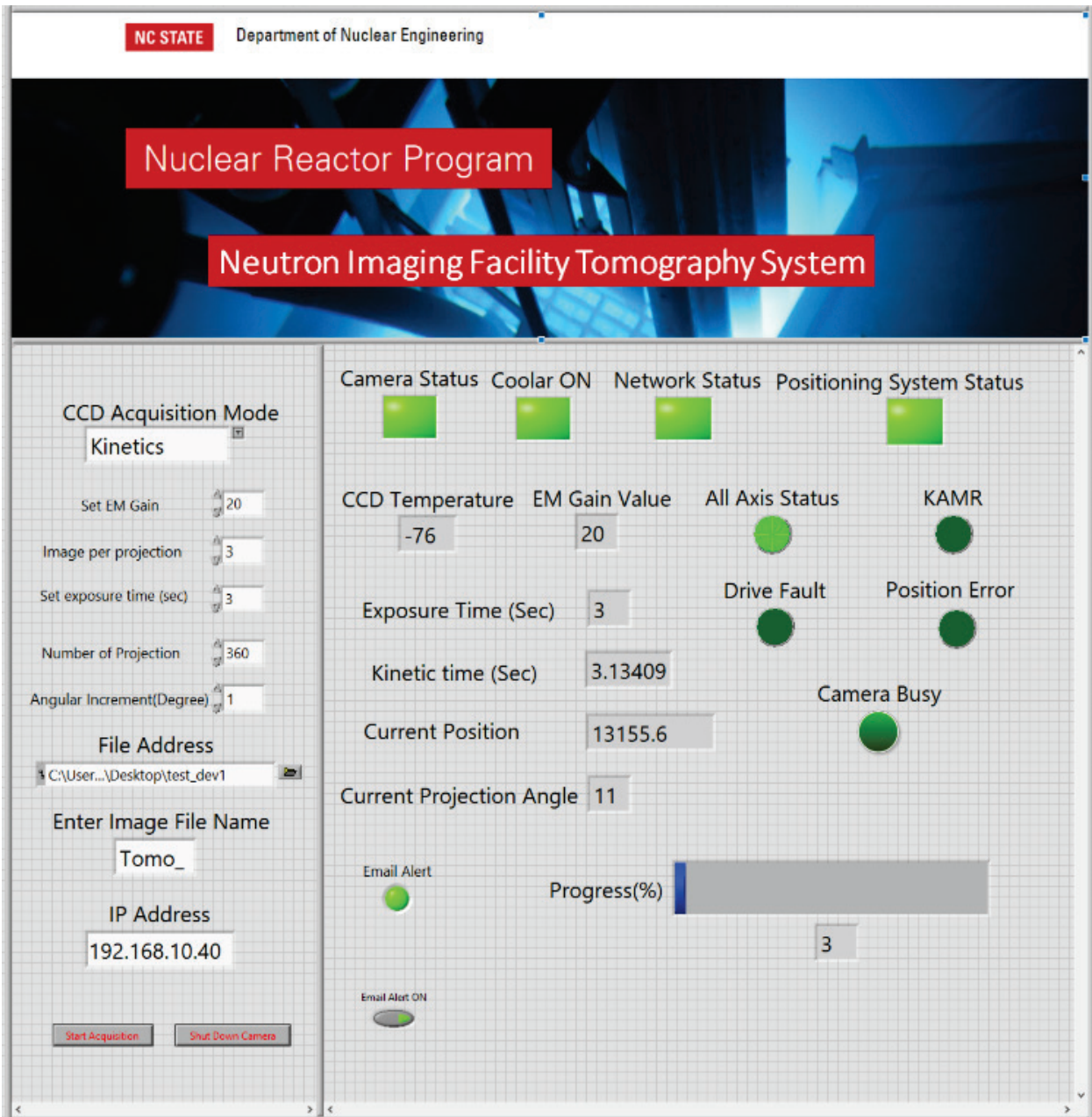


Figure 2.24. The user interface for an automated data acquisition system showing the user input parameter in left-hand side and the status bar right-hand plane.

2.5 Spatial Resolution of Neutron Imaging System

Spatial resolution is defined as the closest distinguishable points in the plane of interest. High spatial resolution is always desirable in examining the fine details of an object. Typical spatial resolution of film and IP based neutron imaging system are 33 μm and 110 μm [87]. However, the spatial resolution of scintillator/CCD based neutron imaging system varies with individual components as well as scintillator thickness [88]. Although, film and IP have acceptable spatial resolution, post-processing is required to develop the image, which makes them inappropriate for real time applications. However, direct digital output of the CCD eliminates the need for intermediate processing, making it an ideal system for investigating real time phenomenon. For the scintillator/CCD camera option, the components i.e., CCD, lens and scintillator plays an important role in setting the spatial resolution for real-time neutron imaging systems that can be used in visualizing dynamic phenomenon. Therefore, understanding and characterization of the components are required for the development and performance prediction of high spatial resolution applications. In the next chapter, individual components of the real time imaging system has explored and quantified. Additionally, a multi-physics simulation approach was performed to understand a correlation between scintillator thickness and spatial resolution.

Chapter 3 Principles of Real-Time High-Resolution Neutron Imaging

3.1 Introduction

High resolution is always a desirable feature of an imaging system for observing fine details of an object. In the non-destructive investigation, ability to observe a real-time event at high resolution will increase the utility in the various application as outlined in the earlier section. Historically the development of neutron imaging can be closely linked with X-ray field. In fact, earlier imaging devices like films and IP are modified for use with neutrons. Although thin film or digital image plates have an acceptable spatial resolution, post-processing is required to develop image, which makes them inappropriate for real-time applications. Digital neutron imaging systems may include scintillator screens combined with charge- coupled device (CCD) camera, gas electron multipliers, time projection chambers, and semiconductor converters combined with application-specified integrated circuit readout.

3.2 Mathematical Model of Image Formation

In neutron imaging, neutrons are used to investigate the internal structure and material composition of an object by measuring the attenuation. Attenuation depends on the thickness and material of the sample thickness along the path. This produces a two-dimensional distribution of grey scale image that is proportional to the integrated attenuation properties of the object. The model can be illustrated with the Figure 3.1. The collimated neutrons carry attenuation information as it passes through the object. Neutrons are converted to secondary particle in converter screen for detection. Secondary particles are detected and positional information is extracted. This information can be further processed to characterize and quantify the object under investigation.

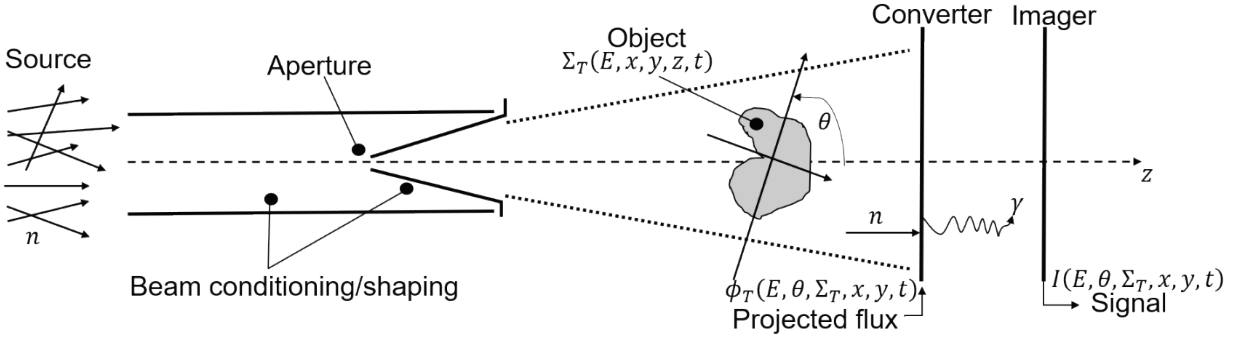


Figure 3.1. Schematic of the neutron image formation showing the neutron source, collimator, beam aperture, object, and the imaging detector [1].

Generated neutrons are usually directed towards object with collimator. Neutron flux incident on object depends on the distance of the object from aperture and aperture size. In divergent type collimator, incident flux can be expressed as,

$$\phi_0 \propto \frac{D^2}{L^2}, \quad (3.1)$$

where, D is the diameter of the aperture and L is distance between aperture and object [89]. Transmission through object can be expressed as the ratio of transmitted beam to incident beam and given as,

$$T = \frac{\phi}{\phi_0}, \quad (3.2)$$

where, ϕ is intensity of transmitted beam and ϕ_0 is the intensity of the incident beam. Neutrons are electrically neutral particle and interact with the nuclei of the material. The probability of the neutron interaction with material depends upon cross-sectional properties of material and neutron energy. Interaction of neutrons through material can be described by Beer-Lambert exponential attenuation law [90] as expressed by the following equation,

$$\phi = \phi_0 e^{-\Sigma_{Total} t}, \quad (3.3)$$

where Σ_{Total} is total macroscopic is cross section and t is the thickness of the material. Further, Σ_{Total} can be expressed by,

$$\Sigma_{Total} = \sigma_T \frac{\rho N_A}{M}, \quad (3.4)$$

where, σ_T is total microscopic cross section, ρ is the density of the material, N_A is Avogadro's number, and M is molar mass [91]. If neutrons are passing through N different material, Σ_{Total} can be expressed as,

$$\Sigma_{Total} = \sum_{i=1}^N \sigma_i \frac{\rho_i N_A}{M_i}. \quad (3.5)$$

Interaction of neutrons with material can be scattering, absorption or combination of both. In the case of scattering, radiations are dispersed into a range of direction after interaction with material. Whereas, direction of the neutrons is retained after interaction within material. Absorption may be coupled with emission of secondary radiation from excited state of the material. While absorption is ideal attenuation process, scattering introduces uncertainty in the process since it alters propagation direction.

Transmitted neutrons are first converted to any form of secondary radiation for detection. Either secondary radiations are detected directly or converted further for detection. Films and imaging plates (IP) are the examples of first type of detectors where secondary radiations are stored and developed as film or digitized readout through an image scanner. The scintillator/CCD based imaging system can be categorized as second type of the detection system where the optical photons are detected through a photo-sensitive CCD. Assuming the acquisition process is a linear shift invariant, mathematical model of the imaging system can be expressed as,

$$g(x, y) = o(x, y) * h(x, y) + n(x, y), \quad (3.6)$$

where, $o(x, y)$ is the spatial representation of the object function, $h(x, y)$ is the spatial distribution of the response function, $g(x, y)$ is the obtained image, $n(x, y)$ is the spatial distribution of noise function and $*$ is convolution operator [92]. The obtained image is two-dimensional convolution of system response function with object function. In a discrete domain, the model can be represented as,

$$g(x, y) = \frac{1}{MN} \sum_{m=0}^{M-1} \sum_{n=0}^{N-1} o(x, y)h(x - m, y - n) + n(x, y). \quad (3.7)$$

Using the convolution theorem, frequency domain representation of the model can be expressed as,

$$G(u, v) = O(u, v)H(u, v) + N(u, v). \quad (3.8)$$

Where, $H(u, v)$ can be interpreted as impulse response function of an imaging system. The scintillator/CCD based imaging system consists of a scintillator screen, followed by a mirror, lens and CCD. After neutrons absorbed in scintillator material, charge particles are generated and deposits their energy. Consequently, optical photons are generated and transported through the scintillator. Further, the escaped optical photons are captured in the photo-sensitive CCD, forming neutron radiograph. The system response function of scintillator/CCD based imaging system was explored. Spatial resolution contribution of different imaging components i.e., CCD, lens and scintillator were characterized. A multi-physics Monte-Carlo simulation model was developed to understand and predict the performance of such an imaging system.

3.3 Simulation Model

Monte-Carlo is a statistical approach to determining solution by random sampling of probability distribution function that describes the problem [93]. In radiation transport simulation, particles travel in discrete steps while undergoing various types of interaction. Step length and

interaction probabilities are sampled from cross-section data. The energy and direction of the resultant particle are determined by sampling appropriate differential cross section. Stochastic nature of the particles is simulated by a random number generator. A number of Monte-Carlo codes are used for solving radiation transport problems as illustrated in Table 3.1. It can be observed, Geant4 has the capability to simulate the interaction of neutrons with matter, formation, and interaction of charged particles, and generation and propagation of optical photons inside scintillating layers [94]. In addition, object-oriented implementation has greater flexibility and scalability compared to other FORTRAN based code. Thus, the Geant4 framework is selected and a computer subroutine has been developed for the modeling and simulation of the real-time thermal neutron imaging system.

Table 3.1. General purpose Monte-Carlo code [95-101]

Monte-Carlo Code	Particle	Programming Language
MCNP	Electron, gamma photon, neutron	FORTRAN
MCNPX	All particle (except optical photon)	FORTRAN
ERTAN/ITS	Electron, gamma photon	FORTRAN
EGS4	Electron, Gamma photon	FORTRAN
PENELOPE	Electron, Gamma photon	FORTRAN
Geant3	All particles	FORTRAN
Geant4	All particles	C++

3.3.1 Introduction to Geant4

The acronym ‘GEANT’ was invented in the 1970’s to name a code that simulated ‘GE’ometry ‘AN’d ‘T’racking for particle physics experiments. First widely-used released version of the code, GEANT3, was written in FORTRAN [102]. Object-oriented approach was opted for to manage the increasing complexity without compromising performance. In 1998, this new phase of development led the first production release of Geant4, a C++ program that nowadays begins to be adopted by particle physics [94]. Initial work of two independent work by KEK and CERN were merged in 1994 and a new program-based object-oriented code was developed. Initial code was known as RD44 and it has the flexibility and functionality to accommodate advanced physics. RD44 was later upgraded, re-designed and later released as the first version of Geant4 in 2004 [101].

3.3.2 Functionality and Overview

Geant4 is written in object-oriented C++ programming language thus its structure is completely different than other widely used Monte-Carlo simulation tool like MCNP. In an MCNP simulation user provides an input deck which contains the parameters of simulation. During execution, input parameters like geometry and particle sources are read and simulation results are produced. Unlike MCNP, Geant4 is a toolkit not an executable. Thus, user must install and create a Geant4 environment for compiling before invoking the executables. General structure of Geant4 is explained as follows and illustrated in Figure 3.2. Geant4 categories are as follows,

- Global categories includes global definition of units, constants, and random number generation (seed) handling and output control.
- Material categories describe physical properties of used materials. New material can be defined, or material can be used from Geant4 library.

- Geometry describes geometrical description or dimension of the simulation model.
- Track category contains classes for tracking the particle
- Process category contains model implementation

The other categories contain classes for tracking the particle interaction and controlling output

- Tracking category manages the track of the particle until it disappears from the global geometry.
- Run category manages the collection of all single events for the same geometry and same particle type.
- Readout category contains classes for print output.

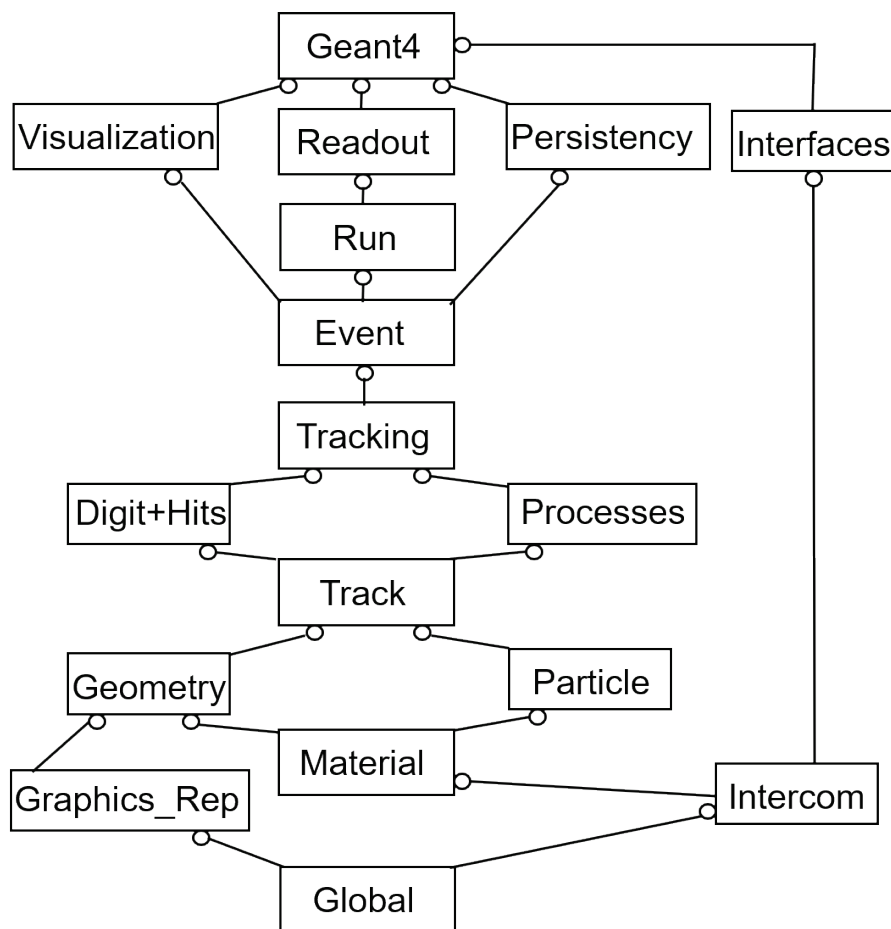


Figure 3.2. Geant4 process flowchart showing the building blocks, the interconnection between them for a simulation [103].

All Geant4 categories follows same class architecture. All source files are compiled together to generate executable for a single project. One Geant4 application structure contains at least one main function, a particle source file, geometry, and physics. Usually, one complex application can contain multiple source file to implement different functions. Modular structure of Geant4 assists developer to develop and debug easily. The main class is an abstract layout of program that links the all classes with executables, provide the framework for MPI libraries and invoke scorer libraries.

3.3.2.1 Primary Particle Source

Primary generator specifies the source types, shape, and energy distribution with direction distribution. There are many predefined particle types are available in Geant4, including photons, leptons, mesons, baryons etc. Each type of particle can be derived from *G4ParticleDefinition* class. It contains the properties of the particles, such as name, mass, spin, lifetime and decay mode. *G4ParticleDefinition* contains static properties of the particle, whereas *G4DynamicParticle* describes dynamic properties of the particle, like energy, momentum, and polarization. User must define a derived class form *G4UserPrimaryGeneratorAction* method to define parameters associated with the source. Source parameters like energy, position or type of the particle can be constant or they can be generated dynamically during the simulation. Easier way to generate primary particle is *G4GeneralParticleSource* method but this method doesn't work well in MPI environment. Current information about a particle, such as position, energy, momentum, and direction can be extracted by the *G4Track* method [103].

3.3.2.2 Geometry

Geometry class specifies the dimension, material and location information. The outermost geometry is known as World which must be specified at the beginning. All other geometry must reside within the World. Mandatory class for defining geometry is derived from

G4UserDetectorConstruction and in the *Construct* method, the user should define all necessary materials, volumes, and geometry. Conceptually, geometry class can be divided into three layers: solid volume, logical volume, and physical volume. Solid volumes manage the representation of the shape and size, logical volume determines the material visibility and sensitivity. All solid must be allocated by *G4SolidStore* method during construction. User can define a material as sensitive and add a scorer to read the output data from that area. The physical volume defines the orientation of the volume geometry. There are three types of solids that are available for the model. They are Constructive Solid Geometry (CSG), Boundary Represented Solid (BREP), and Boolean solid. CSG solid includes geometrical primitives like boxes, cylinders, cones, and spheres, BREP solids can be defined by their boundary surfaces. Complex solid can be constructed by Boolean operation between two objects. Typical classes for defining CSG solids are *G4Box*, *G4Cylinder*, *G4EllipticalTube*, *G4Polyhedra* [104]. Few geometries are illustrated in Figure 3.3.

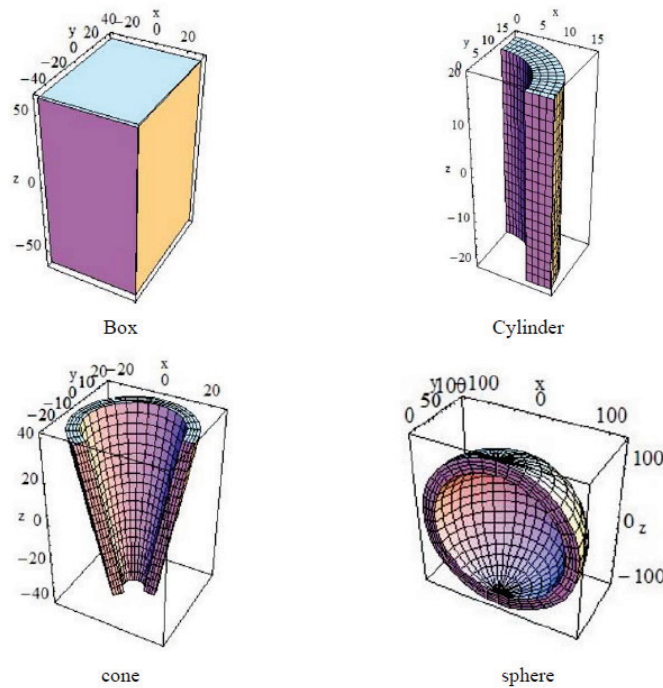


Figure 3.3. Illustration of Geant4 basic geometry model showing box, a section of a cylinder, cone, and sphere [94].

Repeated structure can be created as parameterized volume and different materials can be assigned to it. Multiple copies of similar structure can be placed into a mother volume which can be referenced as a single entity. User can use any number of parameterized volume, but memory consumption and simulation time increases with the higher number of parameterized volume.

3.3.2.3 Physics Process

Unlike MCNP, Geant4 doesn't invoke any physics process automatically. User should derive a class from *G4UserPhysicsList* and define all necessary physics list to invoke the necessary process for simulation. Physics process in Geant4 can be categorized into seven groups: hadronic, electromagnetic, optical, decay, photo-lepton, parameterization, and transportation. All physics processes are derived from *G4VProcess* and must process continuous, discrete and rest condition. *GetPhysicalInteractionLength* (GPIL) and *DoIt* method determine necessary action for those conditions. *GPIL* method gives step length from current space-time point to next and determines when the interaction will occur by calculating the probability of interaction based on processes cross-section information. The *DoIt* method generates the final state of the particle. A brief discussion on the Geant4 physics can be found in Appendix A [105].

3.3.2.4 Tracking and Absorption

Status of the optical photon can be defined by photon momentum and photon polarization. Optical photons are subjected to scattering, boundary actions, and absorption. Scattering phenomenon can be simulated by Mie scattering or Rayleigh scattering. The boundary action depends on the reflection, refraction angle, and probability of reflection or refraction. Optical photons are tracked until they are absorbed or disappear from the geometry. An optical photon can be detected if absorbed in the dielectric material or undetected if absorbed in the black material. At the interaction location, the type of interaction can be determined by the relative probability of

absorption and scattering effects. Additionally, optical photons can also be terminated by specifying absorption length in the material property table [103].

3.3.2.5 Scoring and Analysis

The purpose of running a Monte-Carlo simulation is to extract certain quantities from simulation. In Geant4, it can be achieved by specifying a certain region of geometry as a scoring region. This region can be specified by an external scorer or it can be defined as a sensitive region with *G4VSensitiveDetector* scorer. However, it is often preferable to define the sensitive region same as the scorer. In addition to collecting the information at the detector region, the user can choose to extract information by specifying various user data hook at *G4UserTrackingAction* or *G4UserSteppingAction*. By default, Geant4 doesn't store any information while tracking. Several primitive scorers are defined in Geant4 to score the commonly used physical quantities as illustrated in Table 3.2.

Table 3.2. Typical Geant4 scorer to score quantities during simulation [103]

Physical attributes	Scorer
Track length	<i>G4PSTrackLength, G4PSPassageTrackLength</i>
Energy deposit	<i>G4PSEnergyDeposit, G4PSDoseDeposit, G4PSChargeDeposit</i>
Current Flux	<i>G4PSFlatSurfaceCurrent, G4PSSphereSurfaceCurrent, G4PSFlatSurfaceFlux, G4PSCellFlux, G4PSPassageCellFlux</i>

The quantities from each step can be retrieved with the *ProcessHits()* method. A hit can be defined by *G4Hit* class and can collect information of a single track or collection of multiple tracks. For example, a user can retrieve information of energy deposition by a single particle or a collection of particles by defining a hit object at the sensitive detector region. Multiple information can be retrieved for same or different particle by defining particle filter. The information can be

retrieved in .ascii or .csv format. Spatial information can also be retrieved by defining a mesh in the scorer. However, requirement of computational resources increases with the mesh size.

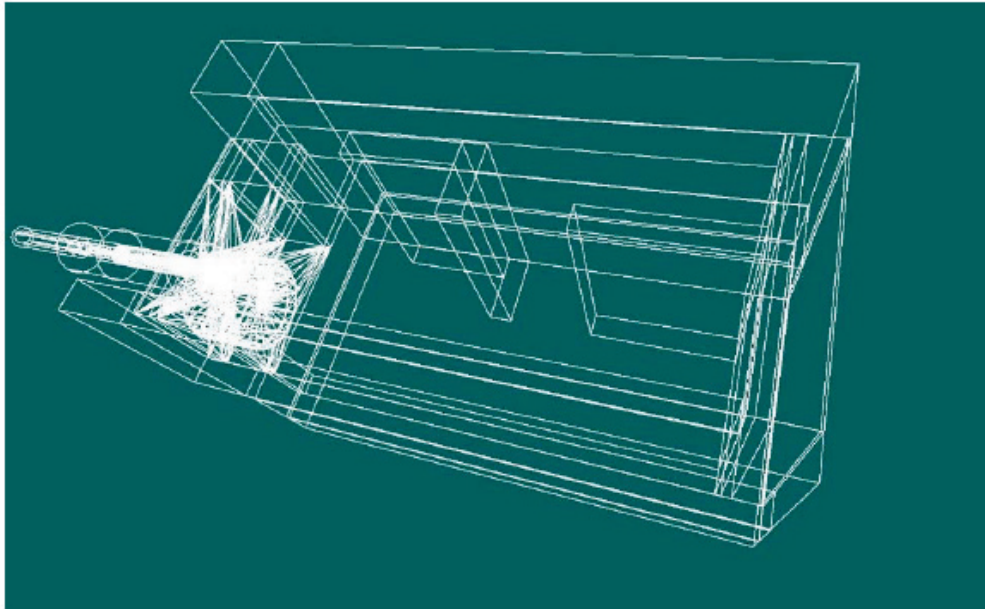
3.3.2.6 Running and Compiling

One Geant4 project consists of several source and header files. They can be compiled with GNU compiler to create an executable. Computation can be parallelized on several nodes with MPI parallelization. Modeling and simulation of the neutron imaging system includes neutron transport, charged particle transport, and optical photon transport. All of them requires significant computation resources. Thus, the computations were performed on a Linux platform at High-Performance Computer (HPC) cluster at North Carolina State University. Computation time depends on the number of particles, scintillator thickness, and mesh size. With thick scintillator number of optical photons generated is more, thus increases computation time. On average, simulation time with 10 million neutrons and 250 μm scintillator requires around 500 CPU hours. The visualization is performed with the HepRep browser [106]. The visualization is turned off during intensive computation task but can be turned on with a user interface (UI) command.

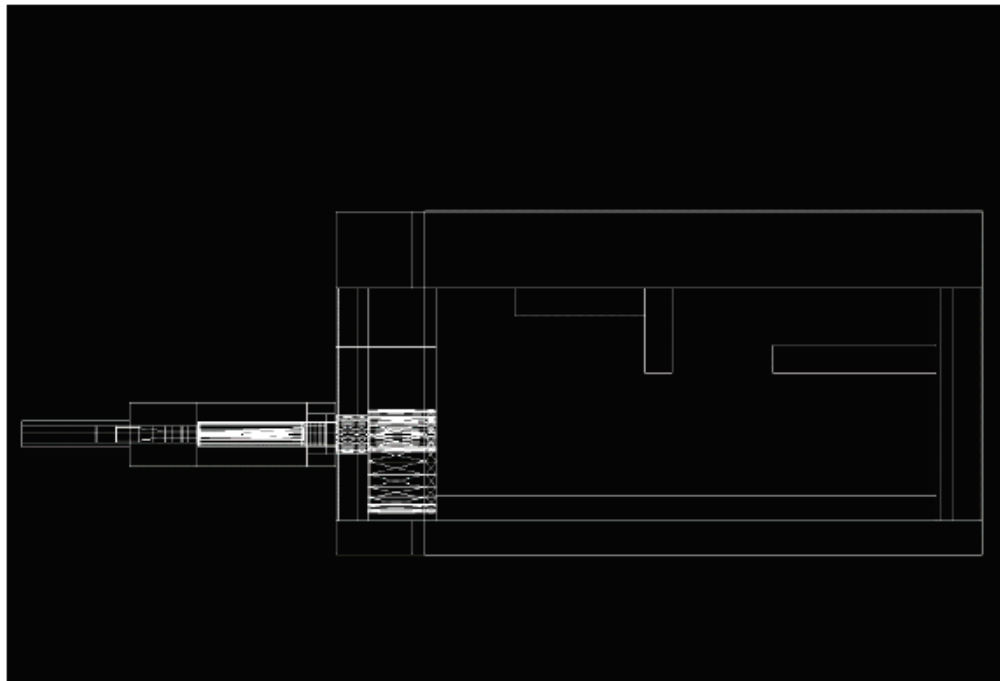
3.4 Geant4 simulation model for the neutron imaging system

In order to study the effect of different parameters of the neutron imaging system, the PULSTAR neutron imaging facility is modeled in Geant4. The model includes a detailed description of the facility including collimator, filters, beam shutter, and shielding. The development was performed in three steps. At first, geometry was constructed, and materials were assigned to volumes. Redundancy and overlapping check were performed after placing each geometry to ensure the integrity of the simulation model. The view of the facility is shown in Figure 3.4 and Figure 3.5. These figures were generated by wire-frame rendering with HepRep browser. The materials are described in ref.[107], [108] and defined from *G4Nist* material store

[103]. Geometry of the model was developed in the Windows computational environment as easier visualization. The model was later ported to Linux environment for intensive computation and parallelization requirements.



(a)



(b)

Figure 3.4. Geant4 simulation geometry of PULSTAR neutron imaging facility, (a) wireframe rendering of side view, and (b) top view.

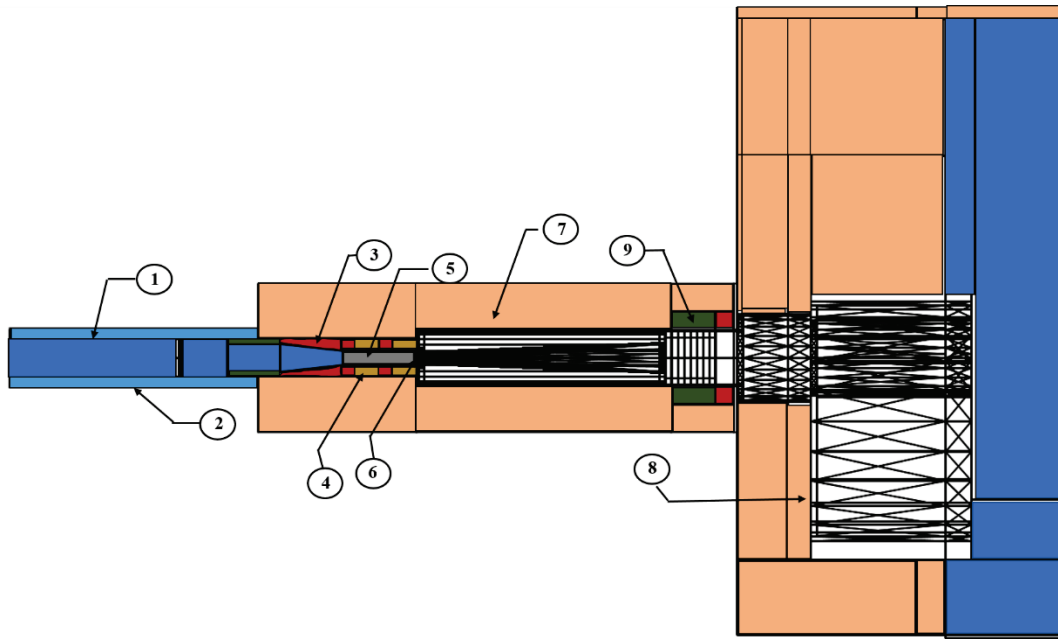


Figure 3.5. Geant4 simulation of detailed collimator geometry showing: (1) air, (2) aluminum, (3) lead, (4) RX-277 (concrete with 1.6% boron content), (5) sapphire filter, (6) beam aperture, (7) concrete, (8) beam shutter, and (9) borated polyethylene.

The physics list was prepared and added to the simulation model. The neutron physics was added first, followed by charged particle physics and optical physics. The physics list was developed in a modular fashion. So, user can select a module and modify it when necessary. A brief discussion on the available Geant4 physics list can be found in Appendix A. The *G4NeutronHP* (high precision) model is the appropriate transport code for simulating neutron transport below 20 MeV and it relies on Geant4 Neutron Data Library (G4NDL). In general, it contains similar cross-sectional information that is found in standard ENDF-VI data files but in a different format. This makes it difficult to include cross-section for a new material such as sapphire. The cross-section of the sapphire was not available in the G4NDL library. Sapphire filter is used in thermal neutron imaging to remove high energy neutrons while maintaining reasonable thermal neutron flux. Thermal neutron scattering cross section libraries for sapphire was processed from LEAPR calculation using the THERMR module [86]. An in-house code was developed in

C++ platform to process the THERMR output and converted to G4NDL format. The generated data library for sapphire was zipped with *zlib* and imported in Geant4. Geant4 source code was compiled again to include the sapphire cross-section after the addition. Details can be found in Appendix A. The simulation was performed with the input energy spectrum as shown in Figure 3.6. The input neutron energy spectrum was generated with full reactor core simulation as described in ref. [107]. The energy spectrum was included as a tabulated energy function in *PrimaryGeneratorAction*. A planner neutron source was created by randomizing the position of the neutron at the input surface of the collimator. Energy of the neutrons, coming out of the other side of the filter was scored and output spectrum was generated with histogram as shown in Figure 3.7. It can be observed that sapphire filter removes the high energy neutrons. Thus, making it suitable for thermal neutron imaging. To reduce computational resources, filtered neutron spectrum was placed at the at the beam aperture and used as neutron source for all future simulations.

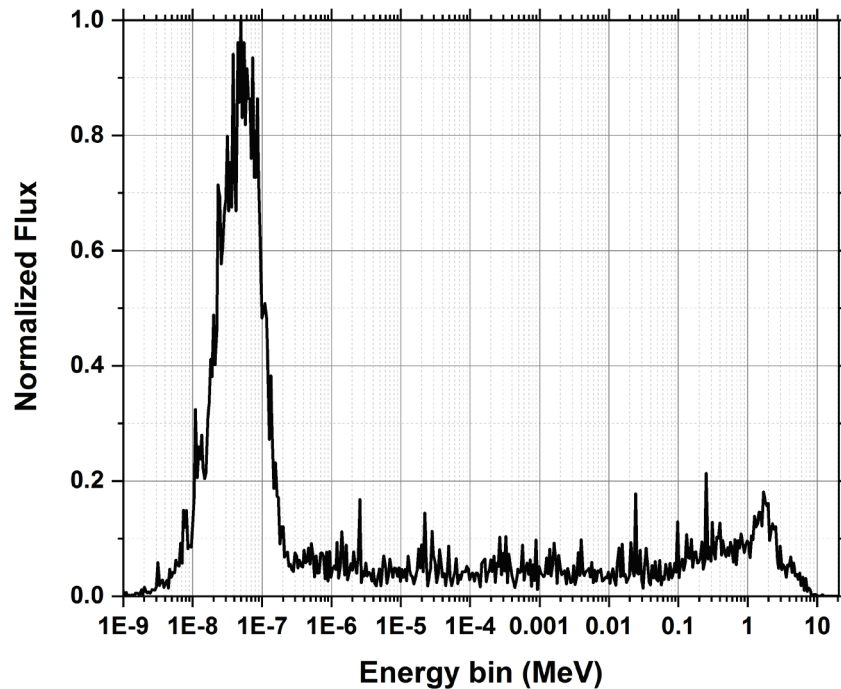


Figure 3.6. Illustration of neutron energy spectrum at the entrance of the beam.

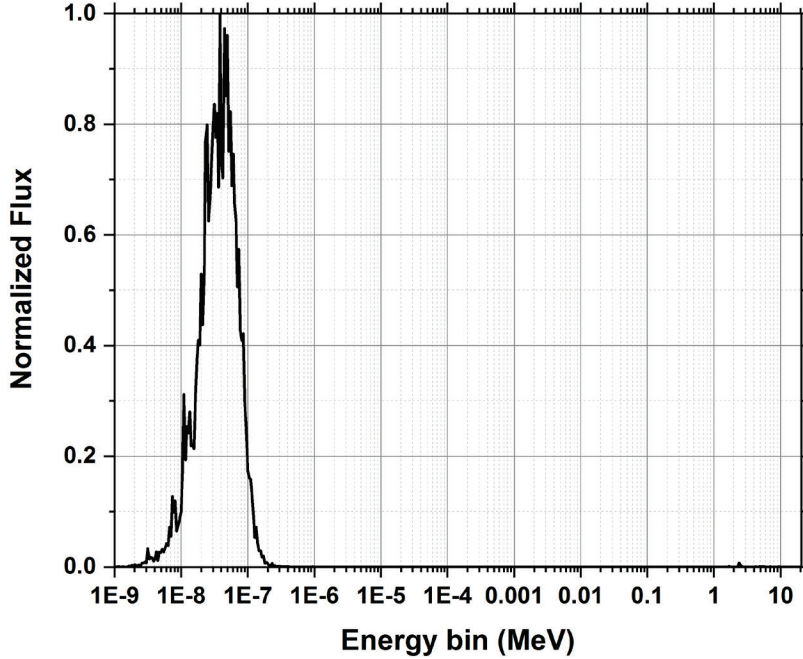


Figure 3.7. Illustration of neutron energy spectrum after filtration with 12'' sapphire filter as produced with Geant4 simulation.

The scintillator screen is assumed to be a homogeneous mixture of its constituents. The probability of capture of the neutron depends on the incoming neutron energy and ${}^6\text{Li}$ concentration. Energy dependence can be illustrated in Figure 3.8. It can be observed that as neutron energy reduces, cross-section of ${}^6\text{Li}$ increases. For thermal neutrons with energy 0.025 eV, the cross-section is around 940 barns. When a neutron is captured by a ${}^6\text{Li}$ nucleus, track is terminated from the Geant4 stack and an Alpha and a Triton particle are created as secondary particles. These particles travel through the scintillator screen and deposit their energy along their path. Neutron absorption efficiency inside the scintillator was calculated as,

$$\varepsilon_n = \frac{I_0 - I}{I_0} \times 100, \quad (3.9)$$

where, I_0 is the number of neutrons arriving the scintillator, and I is the number of neutrons leaving the scintillator. The simulation were performed for different thickness and a different ratio of LiF:ZnS(Ag) and shown in Figure 3.9.

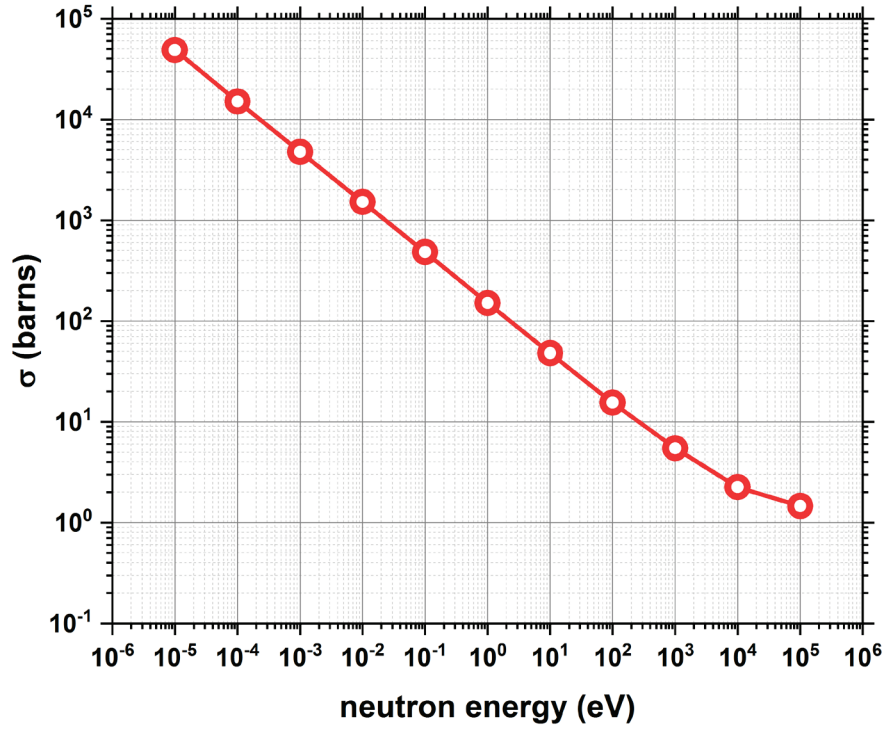


Figure 3.8. Energy-dependent neutron cross section of Li showing the thermal neutron cross section as a function of neutron energy as obtained with Geant4 simulation.

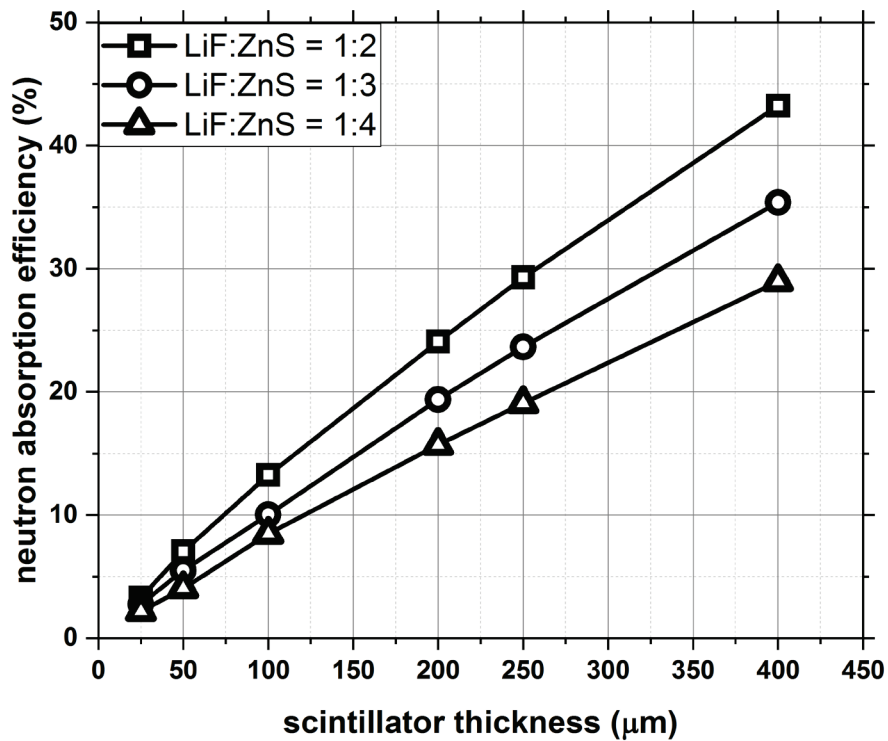


Figure 3.9. Neutron absorption efficiency of the ⁶LiF:ZnS (Ag) scintillator showing absorption probability increases as the ratio of the ⁶LiF increases or the scintillator thickness increases.

The light output response of an inorganic scintillator carries a nonlinear relationship with deposited energy. According to Birks assumption, the amount of luminance per unit length decreases by quenching effect in high stopping power region. The non-linearity can be expressed as,

$$\frac{dL}{dx} = \frac{S\left(\frac{dE}{dx}\right)}{1+kB\left(\frac{dE}{dx}\right)}, \quad (3.10)$$

where, S is the scintillation efficiency, and kB is the Birks parameter [109]. The Birks parameter for LiF:ZnS(Ag) scintillator is calculated from the following approximation as shown in ref. [110]

$$Q_i \approx \frac{1}{kB\left(\frac{dE}{dx}\right)}, \quad (3.11)$$

where, Q_i is quenching factor and can be expressed as and $\frac{\alpha}{\beta}$ is the ratio for the alpha particle.

Using, $\frac{\alpha}{\beta} = 0.44$ [111] for ${}^6\text{LiF:ZnS(Ag)}$ scintillator and $\frac{dE}{dx} = 2.102 \times 10^2$ MeV/mm for the alpha particle, the Birks parameter for ${}^6\text{LiF:ZnS(Ag)}$ scintillator can be calculated as 0.0108 mm/MeV, which is of the same order of similar inorganic scintillators [110]. The optical photon emission spectrum for ${}^6\text{LiF:ZnS(Ag)}$ scintillator is shown in Figure 3.10. The simulation model accounts for self-absorption and scattering of optical photons in the scintillator. The ability to accurately specify the optical photon absorption length in LiF:ZnS scintillator screen is challenging as it can vary significantly with screen characteristics. In the simulation model, the optical photon absorption length is selected as 31 μm [112]. Scattering of optical photons inside a granular medium can be approximated by Mie scattering [113]. The solution was approximated by Henyey-Greenstein (HG) and incorporated in Geant4. The scattering process of an optical photon is included in the simulation model by invoking the *G4OpMieHg* method. The boundary of the scintillator is assumed to be polished. Silicon is modeled as a pixilated photosensitive detector and placed after the scintillator as shown in Figure 3.11. The optical photons those are escaped from

the scintillator are captured by the photosensitive pixel. Physics process used in the simulation is shown in Table 3.3. Pixel size can be adjusted by user. A scorer counts the total number of captured optical photons at each pixel and produced an ASCII file after a run has been completed. A MATLAB script was written to extract the data and converted the data to the 16-bit image file for further analysis.

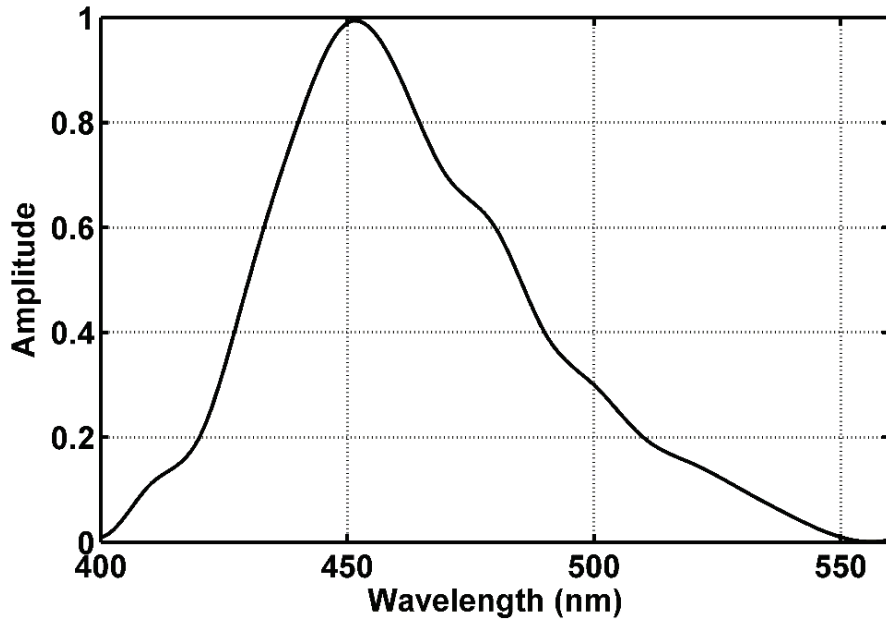


Figure 3.10. The emission spectrum of the optical photon from LiF:ZnS(Ag) scintillator showing peak emission wavelength in the blue region.

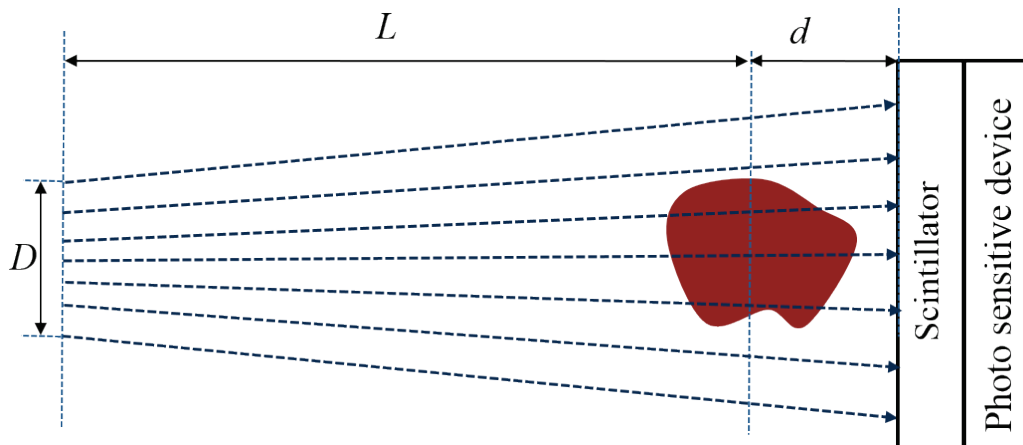


Figure 3.11. Illustration of the detector model (top view) used in the Geant4 simulation.

Table 3.3. Geant4 physics process used for the simulation

Particle	Physics Process
Neutron	G4HadronElasticProcess, G4NeutronInelasticProcess, G4HadronCaptureProcess
Charge Particle	G4HadronElasticProcess, G4AlphaInelasticProcess, G4TritonInelasticProcess, G4VMultipleScattering, G4hIonisation, G4NuclearStopping, G4eIonisation, G4Scintillation
Optical Photon	G4OpAbsorption, G4OpMieHG, G4OpBoundaryProcess

3.5 Characterization of Neutron Imaging system

3.5.1 Image Acquisition and Processing

Neutrons are a neutral particle and only interact with the atomic nuclei. Thus, neutrons are converted to some secondary forms of radiations which can be detected. The popular neutron imaging instruments are films, image plate, and scintillator-charge couple device based detection system. Most neutron films use a gadolinium conversion screen due to its high absorption cross-section followed by an image recorder screen. Secondary radiations are emitted when neutrons are absorbed in a converter screen and image is formed when they are detected in a recorder screen. Imaging plate (IP) consists of a mixture of neutron absorbers, storage phosphor. When neutrons are absorbed in the IP, secondary radiations are emitted and absorbed in a storage phosphor which creates electron-hole pairs are created. Subsequently, laser is used to readout the locations by detecting characteristic luminescence. Although thin film or digital image plates have an acceptable resolution, post-processing is required to develop the image for films and image plate, which makes them inappropriate for the real-time applications. However, scintillator coupled with CCD device can be used for visualizing such dynamic applications. In the real-time scintillator-

CCD based system, neutrons are absorbed in scintillator and neutron absorption products (i.e., Alpha and Triton) deposit their energy along the track inside the scintillator. The deposited energy generate optical photons and the photons are transported through scintillator. The optical photons that are able to escape the scintillator reflected from a mirror and focused through a lens. The optical photons are captured with a pixelated charged device in reverse bias. Electrons are generated through photo-electric process and shifted from one pixel to another before reading through an analog to digital (A/D) converter. The A/D converter converts analog voltage to a quantized digital value and stored as an image file. The optical photons that are escaped from the scintillator are accumulated to produce the radiographs. Another advantage of the scintillator-CCD based detection system is the linearity of the optical density with exposure time.

Similar to other electronic equipment that operates in a radiation environment is susceptible to noise. Raw neutron radiographs are mainly suffered from two type of noise and can be corrected easily. One is the fluctuations in gray value in the radiograph related with the electronics of CCD camera. The fluctuation occurs due to dark current, conversion during analog to digital conversion and during readout of the registers. Sometimes high energy radiation also penetrates the shielding and interacts with CCD which results in the saturation of pixel and appears as a white spot in radiograph. Another source of fluctuation is related with inhomogeneity in the neutron beam itself. The white spot can be removed by a median filtering where saturated pixel value can be replaced with the median value of neighboring pixel. Although, this filtering approach remove the white spot, but reduces spatial resolution. Adaptive median filtering can retain the spatial resolution while removing the saturated pixel [92]. Grey level fluctuation due to the electronics, as well as neutron beam, can be corrected by an image normalization. To correct the radiograph by the

normalization, three images are required, the radiograph itself, one dark image, and one open beam image as shown in Figure 3.12.

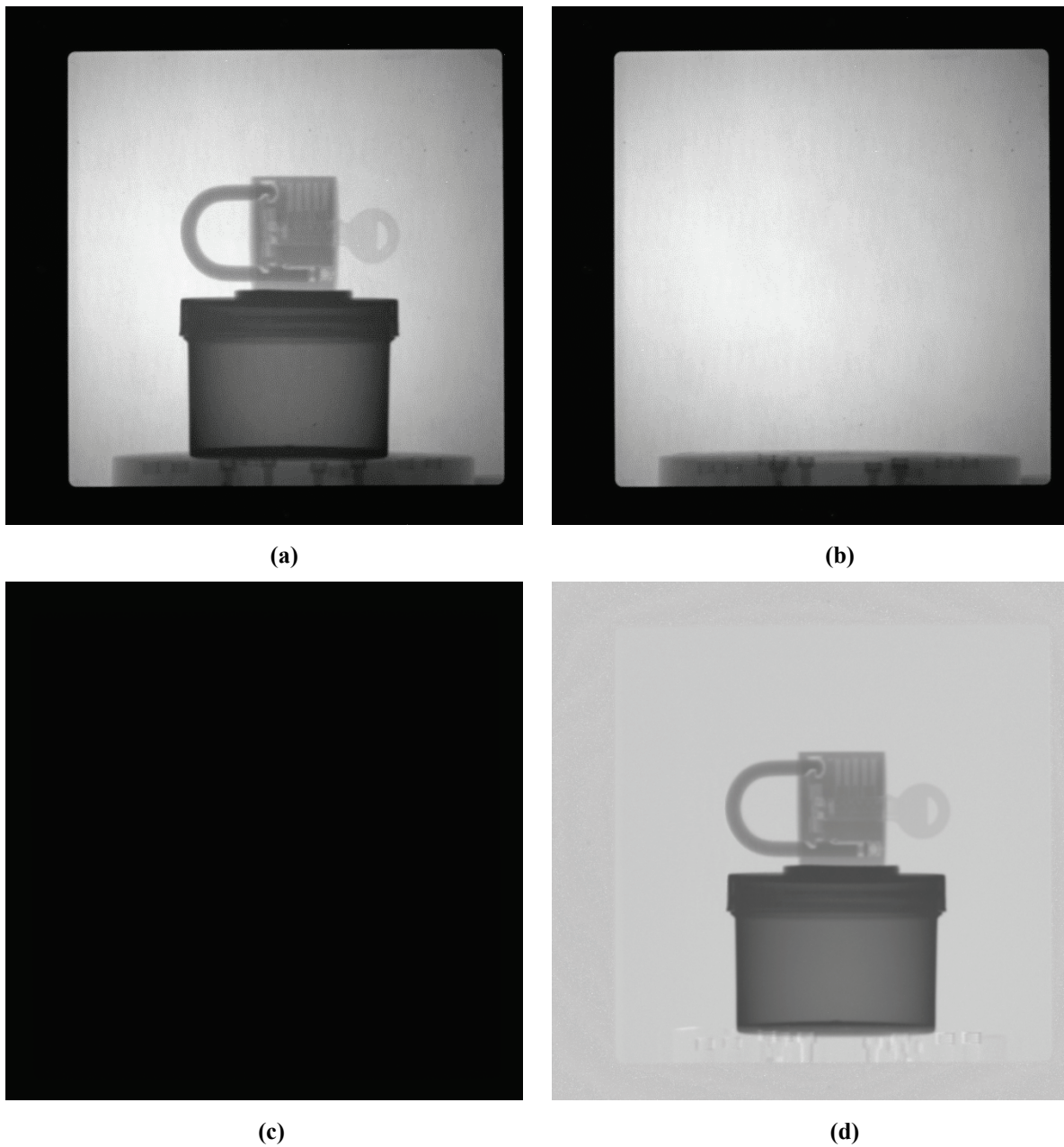


Figure 3.12. Illustration of the image processing of neutron radiography, (a) raw radiograph (b) flat field image, (c) dark field image, and (d) normalized image.

The dark image is a radiograph obtained without neutron source and the open beam image is a radiograph obtained with the unperturbed neutron beam, i.e. without the object. The normalized image is calculated as,

$$I_N = \frac{I_{radiograph} - I_{dark_image}}{I_{open_beam} - I_{dark_image}} \quad (3.12)$$

where, $I_{radiograph}$ is the neutron radiograph image, I_{dark_image} is the dark image, and I_{open_beam} is the open beam image. Subtraction of the dark image reduces the fluctuation due to electronics while normalization with open beam image reduces the variation in the grey value due to the fluctuation in neutron beam. Generally, multiple dark images and open beam images are acquired and averaged to produce I_{dark_image} and I_{open_beam} respectively.

3.5.2 Spatial Resolution

Spatial resolution is often described as the ability to discern two objects at a image. The modulation transfer function (MTF) is a basic performance measure of an imaging system. It describes the signal transfer characteristics as a function of spatial frequency when the signal passes through the system. Ideally, the system response function should be delta function such that it passes all the frequency equally. But actually, the imaging system degrades the spatial frequency as the signal passes through the system. High spatial frequency is attenuated more than the low-frequency components, thus resulting in the shape of MTF for any practical imaging system. Figure 3.13 illustrates the MTF for an ideal and practical imaging system. Spatial resolution can also be described in spatial domain by point spread function (PSF), edge spread function (ESF) and line spread function (LSF). PSF is a representation of an impulse response function of an imaging system and represents the broadening of a 2D delta Dirac function when passing through an imaging system.

The full width at half maximum (FWHM) of PSF can be used for the representation of the spatial resolution. When an image signal passes through one imaging component to another, the image is blurred by the frequency response of each system. Assuming linear shift-invariant (LSI) system the total blur is the convolution of each component. Mathematically, the total MTF is the

product of the individual components as the convolution in the spatial domain is equivalent to the multiplication in the frequency domain.

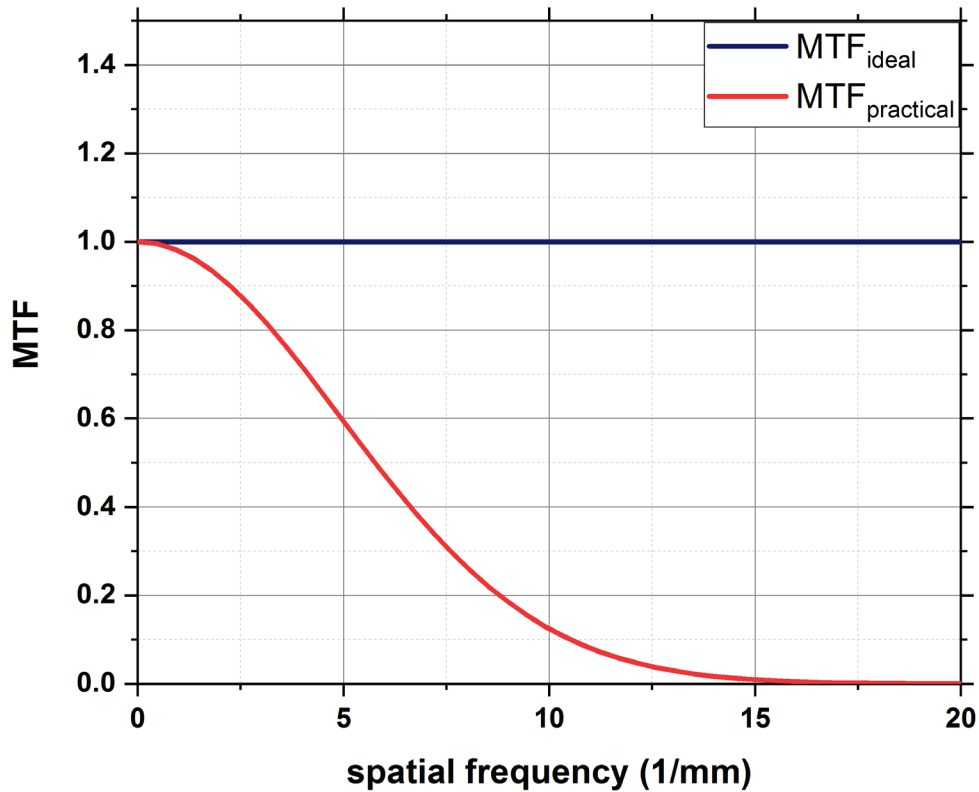


Figure 3.13. Illustration of the modulation transfer function (MTF) of an ideal and practical imaging system.

Ideally, PSF represents the broadening of a single point-like object but difficult to implement. In practice, a sharp edge is imaged and the grey level of the edge is plotted to calculate the ESF. Sometimes spatial resolution is also reported by measuring the broadening of ESF in between 10% and 90% of the normalized image [114]. The ESF is differentiated to generate the LSF. Spatial resolution is often reported from the FWHM of the normalized LSF [114]. The Fourier Transformation of the LSF is known as modulation transfer function (MTF) and the spatial resolution is calculated from the spatial frequency at the 10% of the normalized MTF [115]. The process of calculating MTF from an edge for radiography is illustrated in Figure 3.14.

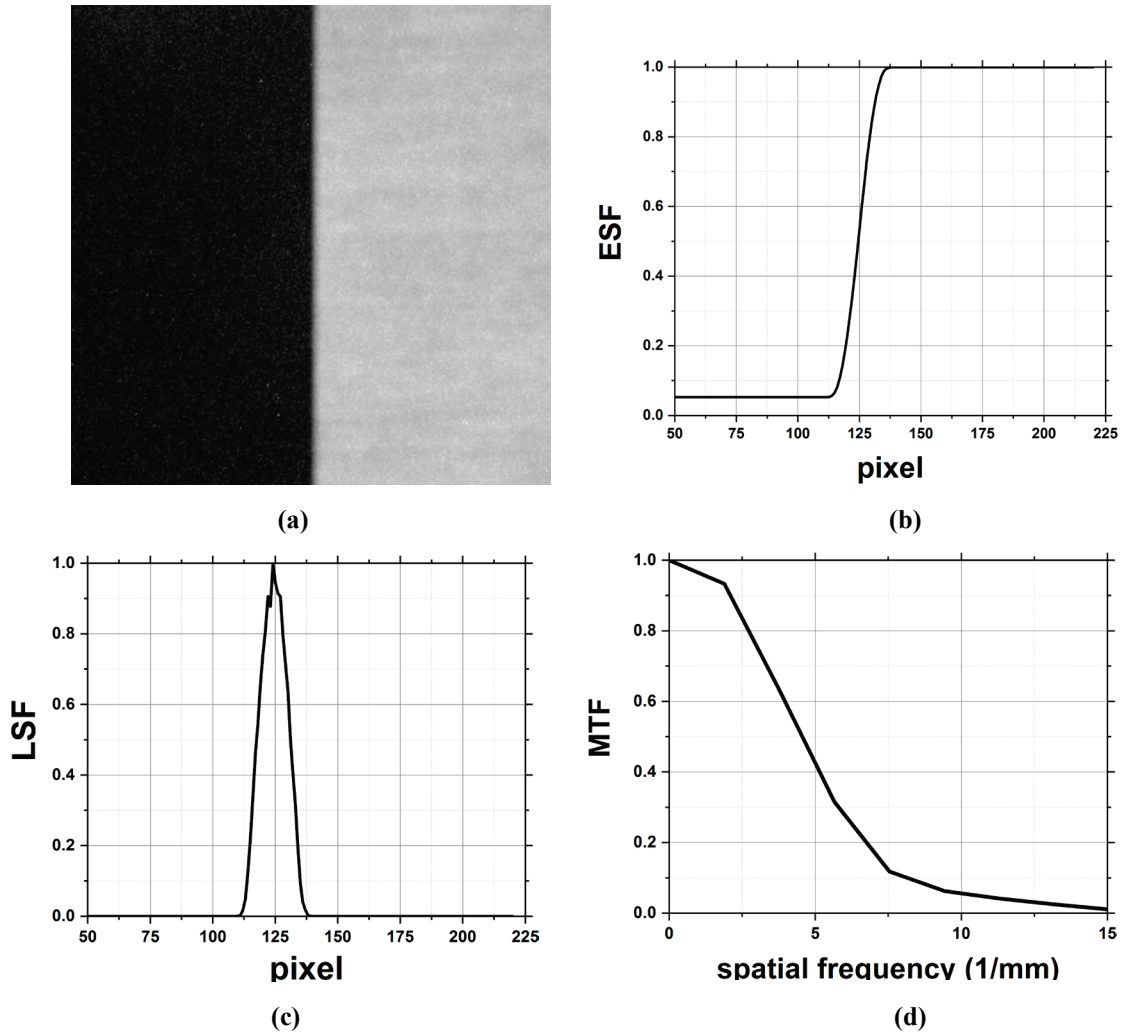


Figure 3.14. Illustration of spatial resolution calculation of neutron radiographs (a) edge radiograph, (b) edge spread function (ESF), (c) line spread function(LSF), and (d) modulation transfer function (MTF).

3.5.3 Spatial Resolution Model of A Real-Time Neutron Imaging System

Each component of the real-time neutron imaging system like beam geometry, scintillator, lens, and CCD, contributes to a spatial resolution which limits the achievable spatial resolution of the system. The objective of the spatial resolution modeling is to understand and quantify the spatial resolution contribution of the different components of the system. Assuming, a linear and shift-invariant system the total system response function, $h_T(x, y)$ can be expressed as the convolution of individual response function as given by,

$$h_T(x, y) = h_G(x, y) * h_{Sc}(x, y) * h_m(x, y) * h_{Lens}(x, y) * h_{CCD}(x, y) , \quad (3.13)$$

where, $h_G(x, y)$ is the geometry contribution, $h_{Sc}(x, y)$ is the scintillator contribution, $h_m(x, y)$ is the mirror contribution, $h_{Lens}(x, y)$ is the lens contribution and $h_{CCD}(x, y)$ is the contribution of CCD. In the spatial domain, the PSF characterize the imaging system and determine the spatial resolving capability of an imaging system. Gaussian is a self-similar function and convolution with a Gaussian is a linear operation. So a convolution with a Gaussian kernel with another Gaussian kernel results in a Gaussian kernel with a broader variance which is illustrated in Appendix B. The total spatial resolution can be expressed as,

$$R_T = \sqrt{(R_G)^2 + (R_{Sc})^2 + (R_m)^2 + (R_{Lens})^2 + (R_{CCD})^2}, \quad (3.14)$$

where, R_G is the resolution contribution of the geometry, R_{Sc} is the resolution contribution of the scintillator, R_m is the resolution contribution of the mirror, R_{Lens} is the resolution contribution of the lens and R_{CCD} is the resolution contribution of the CCD. This can be illustrated in Figure 3.15.

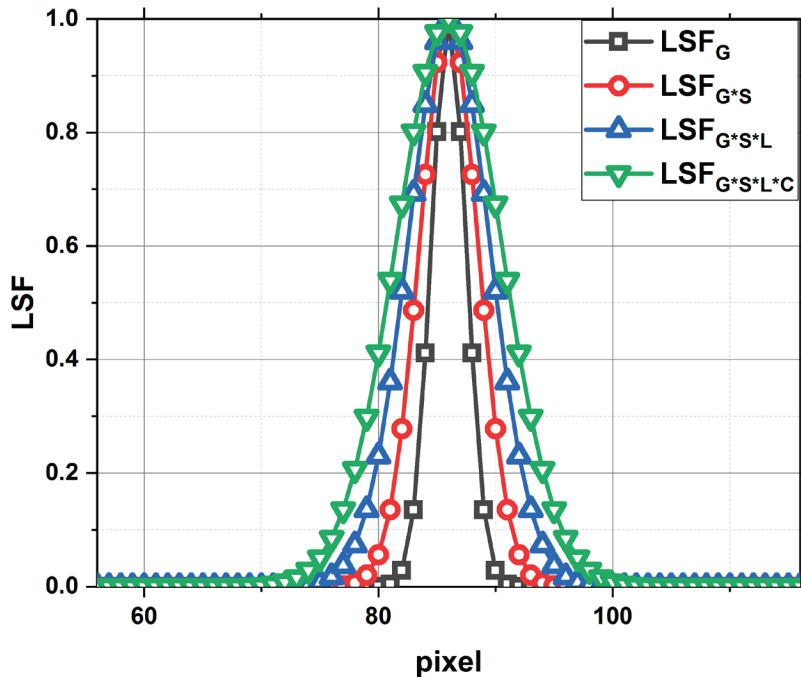


Figure 3.15. Illustration of line spread function (LSF) as the image signal transmitted through the neutron imaging system. (used subscript represents the contribution from G: neutron beam geometry, S: scintillator, L: lens, C: CCD, *: convolution operation).

3.6 Resolution Components of Real-Time Neutron Imaging System

In scintillator-based detection system consists of a scintillator screen, followed by a mirror, lens, and CCD. After neutrons transmitted through the object, it reaches the scintillator. The scintillator screen usually contains highly neutron absorptive material like ${}^6\text{Li}$ and Gd whose neutron cross section is high. After neutrons are absorbed inside the scintillator charge particles are generated. Charged particles are transported inside the scintillator and deposit their energy along the track. Optical photons are generated, and they transport and scatter through the scintillator. Optical photons those are able to escape the scintillator reflected through the mirror and focused through the lenses. Then the optical photons reached the CCD and converted to electrons by photo-electric process. Electrons are shifted row by row and quantized to digital values by analog to digital (A/D) converter. Finally, the digital values are represented as a two-dimensional matrix. The two-dimensional array is the image which is proportional to the integrated attenuation properties of the object. At each of this image development stages, spatial resolution of the image is reduced. In this section, the spatial resolution contribution of each component has been investigated and quantified for the real-time neutron imaging system.

3.6.1 Beam Geometry

The image un-sharpness from a neutron beam depends on the neutron beam collimation ratio. The beam collimation ratio can be expressed as L/D . Where L is the distance between a beam aperture and an object, D is the size of beam aperture. Geometric blurring also depends on the distance between the object and the image plane. This un-sharpness arises due to the finite size of a neutron source as illustrated in Figure 3.16. Mathematically, it can be expressed as,

$$R_G = \frac{d}{L/D}, \quad (3.15)$$

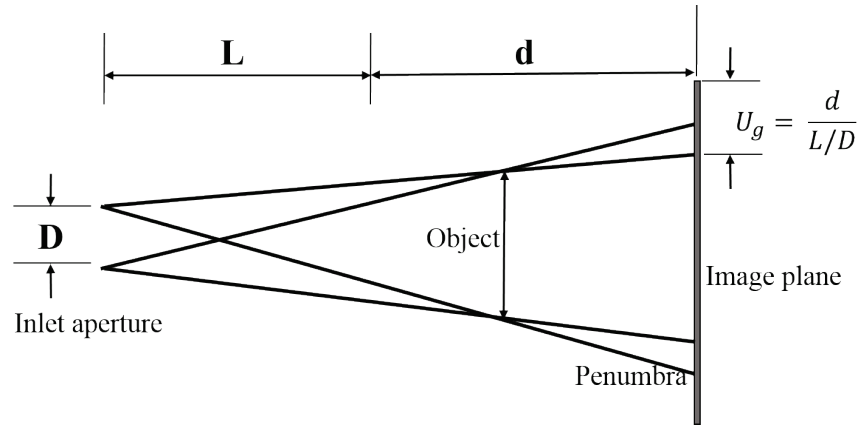


Figure 3.16. The geometric contribution of spatial resolution showing the geometric un-sharpness from neutron beam geometry.

Geometric resolution R_G can be improved by increasing L or reducing D . But increasing the distance between an aperture and an object or reducing a aperture diameter decrease neutron flux at image plane. In addition, reducing aperture also reduces field of view (FOV) or area available at the imaging plane. Further reducing the distance between object and image plane improves spatial resolution but limited with dimension of the object. Thus there are a practical limit for selection of L , D , and d . So designing a neutron imaging facility is a trade-off between neutron flux , field of view at imaging plane while maintaining reasonable spatial resolution.

3.6.2 Imaging System

3.6.2.1 Charged Coupled Device

A Charge Coupled Device (CCD) is a sensitive integrated circuit for detection of optical photons. CCD is composed of many small square light-sensitive units, known as pixels. The working principle of CCD sensors is based on the Metal Oxide Semiconductor (MOS) capacitor as shown in Figure 3.17 [116]. When an optical photon whose energy exceeds the energy of the band gap and absorbed in the depletion area, creates an electron-hole pair. The ratio of this conversion is known as quantum efficiency and can be expressed as,

$$\text{Quantum efficiency} = \frac{\text{number of electron hole pair generated}}{\text{number of optical photon reached at CCD}} \quad (3.16)$$

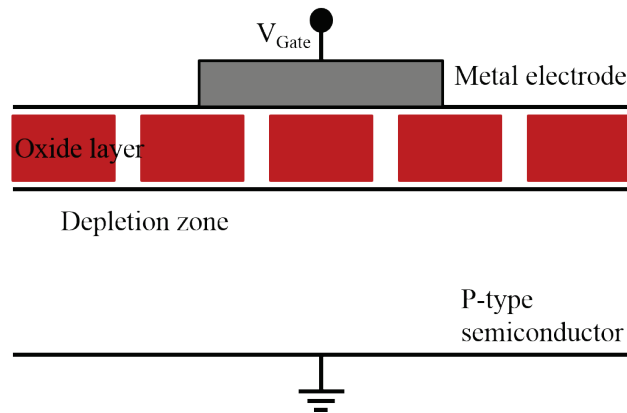


Figure 3.17. Illustration of metal-oxide-semiconductor MOS gate for p-doped silicon showing the metal electrode, depletion zone on a p-type semiconductor.

Due to a negative bias, hole starts moving towards the ground gate. Electron stays in the depletion region and the number of electrons collected are proportional to the applied voltage and oxide layer thickness and surface area [116]. The total number of electrons that can be stored per pixel is known as well capacity. During an exposure, each pixel fills up with optical photon as per their well capacity and proportional with the quantum efficiency. Thus, the signal is acquired for a time period to fill up the electron well below its full capacity to prevent overexposure. The time is known as exposure time and can be controlled by the camera shutter. In general, CCD is consisting of a number of pixels arranged in a two-dimensional matrix structure. The size of the CCD sensor depends on the size of an individual pixel and the total number of pixels. Electrons are accumulated after each exposure, and shifted from one pixel to another by row then shifted to horizontal register before digitized by analog to digital converter as shown in Figure 3.18.

The transfer of charges from one row to another is achieved by handling of a gate voltage in systematic and sequential way. Gate voltage is square wave clock signal, applied to one-pixel row at a time as illustrated in Figure 3.19. Photoelectrons are collected from well 1 when gate 1 voltage is applied. Then, the electrons move to well 2 as the voltage applied to gate 2 and the collected

charge is distributed between two well. Gate1 voltage is reduced which results in the well 2 to fill up with the charge from well 1. This transfer process continues until all the charge from the pixel rows shifted. Depending upon the number of the pixel rows that participates in charge transfer process, phase of the system can be defined. It can be observed, that only one-pixel participated in the charge transfer process in Figure 3.19. So, it can be defined as single-phase CCD.

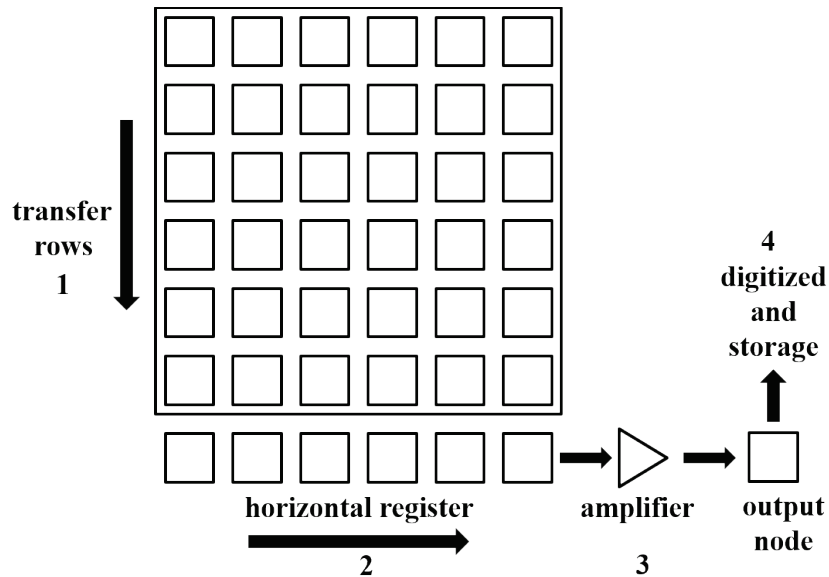


Figure 3.18. Charge shifting process in charge coupled device (CCD) showing the transfer of charge across the horizontal rows (1) to horizontal register followed by readout (2), followed by signal amplification (3), and digitization and storage at the output node (4).

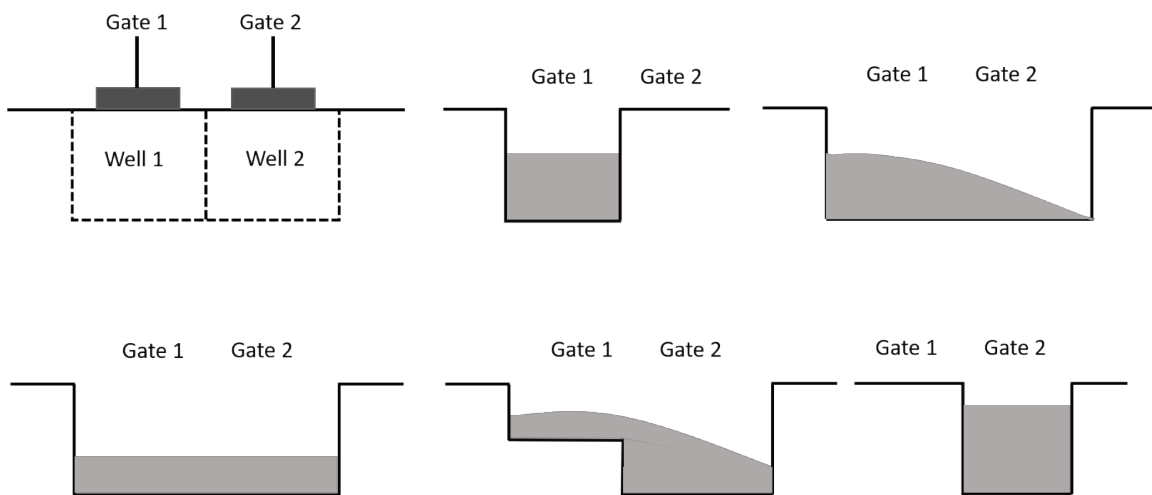


Figure 3.19. Charge transfer between two adjacent pixels of the charge coupled device during the read-out process by controlling the gate potentials.

It can be observed that for the multi-phase system, charge transfer rate is higher than a single-phase system since multiple pixels participate in the charge transfer process. However, a multiphase system reduces the well capacity, which may reduce the dynamic range of the CCD. When the CCD is exposed to the optical photons, electrons are generated in depletion region of the pixel area. The charges are transferred from one row to another by intra-pixel gate jump. At the end of each column, the charges are transferred from one pixel to another by a serial register and an output amplifier. A complete charge transfer process requires two clocks to shift the charges from pixel to output A/D converter. Vertical clock transfers the charge from one row to another and horizontal clock transports the charge packet in serial mode to an output register. The charge transfer process in 2-phase and 3-phase readout process is shown in Figure 3.20 and Figure 3.21. The phases of each pixel are shown as a function of the applied clock time cycle. It can be observed that 2 pixel and 3 pixels are used for a charge transfer process

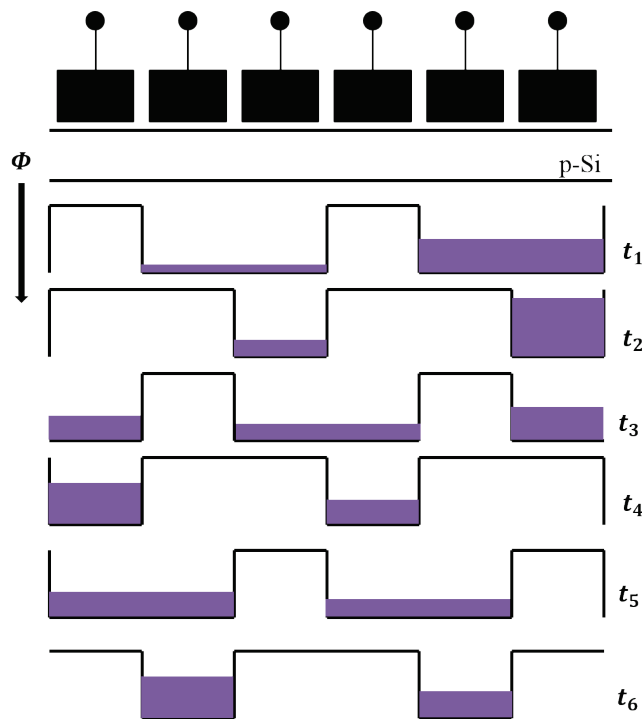


Figure 3.20. Charge transfer process in 2-phase readout of the charge coupled device by controlling the gate potentials with time.

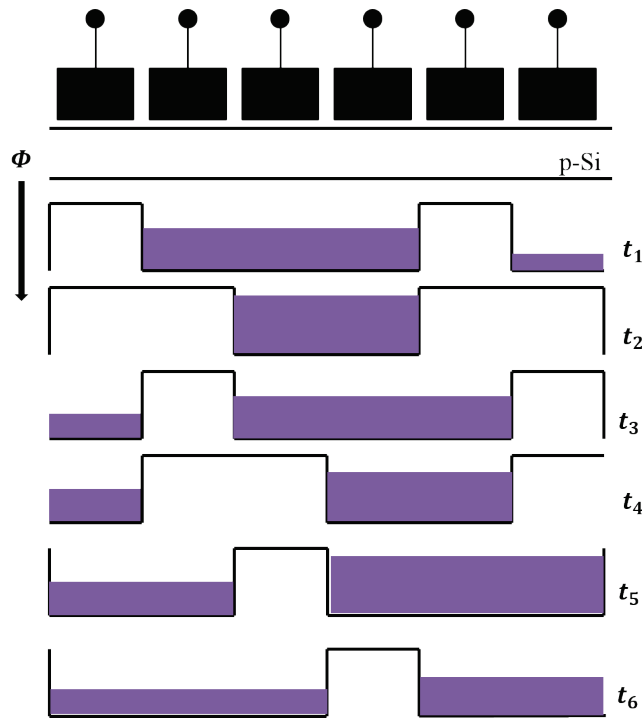


Figure 3.21. Charge transfer process in 3-phase readout of the charge coupled device by controlling the gate potentials with time [117].

At the end of the transport process, charge packets are converted into a voltage. An output amplifier mainly consists of a diode, generate a voltage proportional to number of electrons accumulated for each pixel. Signal can be amplified with a preamplifier and then digitally converted by an analog to digital converter (A/D) for further processing. A multi-phase system can be implemented with a binning method. Binning is a technique where a number of pixels is combined to increase the output signal and reduce exposure time at the expense of spatial resolution of the image. Binning allows the combination of charges from adjacent pixel resulting faster readout speed. In binning mode, a multiphase system is used with 2, 4, 8 pixels participated in the charge collection process.

At the end of the charge collection, more than one element from serial register is moved into a summing gate before the output node. Binning process is illustrated in Figure 3.22. Binning process increases an effective pixel size thus reducing spatial resolution. Thus, a small pixel size

increases. But the high pixel size reduces the achievable spatial resolution. The dynamic range can be expressed in decibels (dB) and can be calculated as,

$$dynamic\ range(dB) = 20 \log_{10} \left(\frac{Full\ well\ capacity}{read\ out\ noise} \right). \quad (3.17)$$

Table 3.4. Scientific CCD specification [118]

CCD	Full well capacity	Read noise	Pixel	Pixel Size (μm)	Bits
iXon 885	30000	1	1004 x 1002	8	14
iXon 887	180000	1	512 x 512	16	16
iXon 888	80000	1	1024 x 1024	13	16

Spatial resolution contribution from a CCD can be calculated by the number of pixels required in reconstruction of image signal. In the case of the 1D signal, it can be associated with the Nyquist sampling theorem. Which states that, the sampling rate must be at least two times of the maximum frequency present in the signal for the accurate representation of the original signal. In the case of a 2D image, the number of the pixel required for the representation of the image may require more than two pixel [119]. This is illustrated in Figure 3.23. The image is assumed to be a circle and recording position of the CCD in centered on a pixel for Figure 3.23, (a-d) and the vertex of a pixel for Figure 3.23, (e-h). The diameter of the circle is varied from 1 pixel to 4 pixel. It can be observed that, even if the diameter of the circle is two pixel the projected image still look like a square which is not an accurate representation of the circle image. As the object image start covers around 3 pixels, the CCD representation of the image closely resembles with the object. This phenomenon can be observed for both the cases, regardless the position of the projected image on a CCD sensor.

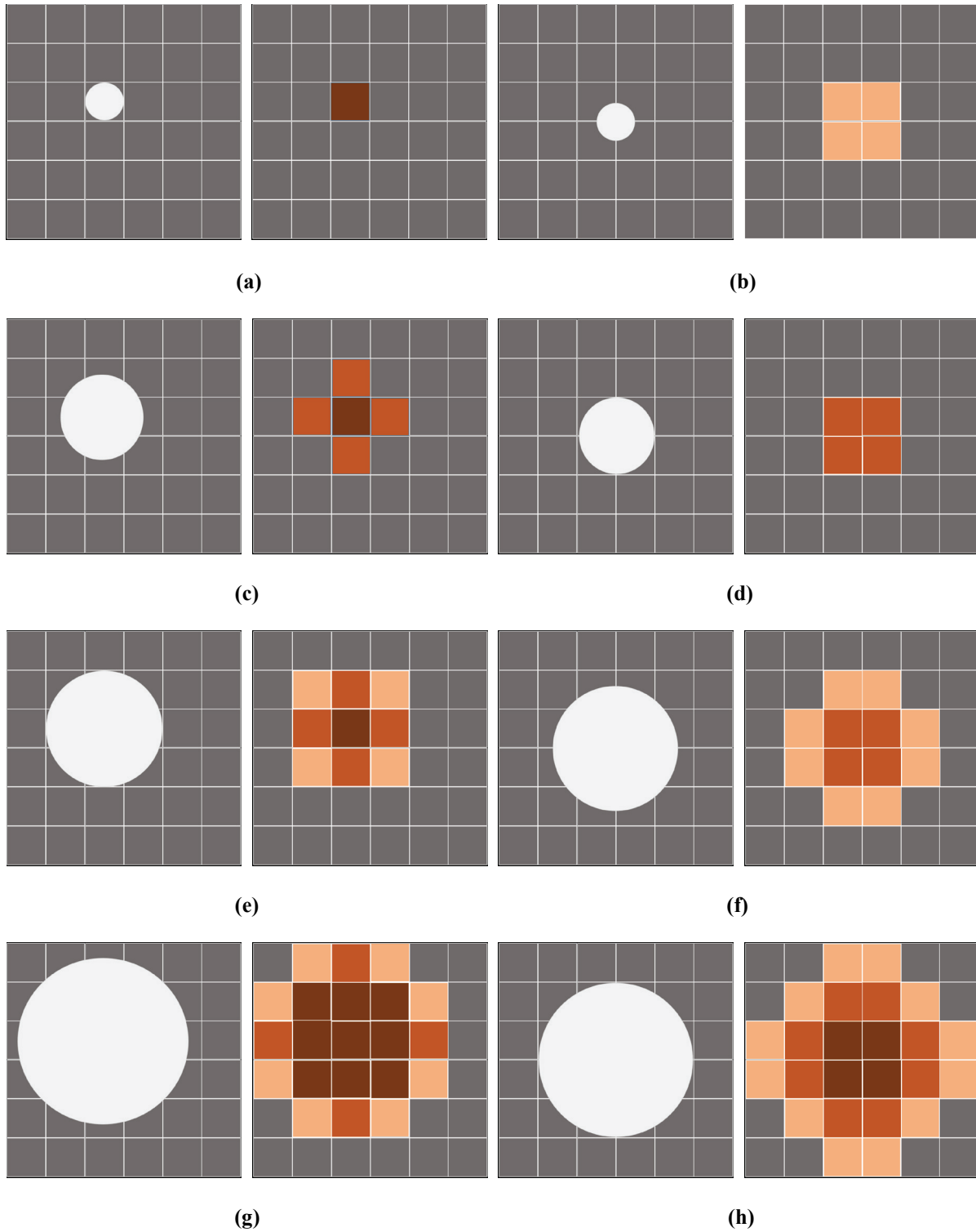


Figure 3.23. Illustration of spatial resolution contribution of CCD showing the number of pixels are required for the faithful representation of an image when projected on pixel center (column 1) and pixel vertex (column 3) as the image diameter increases to (a, e) one pixel, (b, f) two pixel, (c, g) three pixel and (d, h) four pixel [119].

Some manufacturer reports the spatial resolution as 2.5 times of the pixel size. For the high-resolution imaging, an interval of 2.5 to 3 samples for the pixel size is often suggested [119], [120]. Mathematically, the FWHM can be shown as [121],

$$FWHM = 2 \times \sqrt{2 \ln 2} \sigma, \quad (3.18)$$

where σ is the pixel pitch. For a 2D Gaussian, spatial resolution is measured across the diagonal of the a square pixel, and can define the theoretical spatial resolution of CCD [121].

$$R_{Th_{CCD}} = \sqrt{2} \times 2.355 \times \sigma = 3.33 \times \sigma. \quad (3.19)$$

From Figure 3.23, it can be observed that at least 3 pixels are required for the faithful representation of the image, which in well agreement with the theoretical limit. A small pixel size is desirable because it improves the spatial resolution. However, smallest pixel size is limited by the chip fabrication technology. Also reducing the pixel size reduce charge collection capabilities of a single pixel and it reduces the achievable dynamic range. So large pixel size is desirable as it results in better dynamic range and fast readout. Therefore, the commercial manufactures agree on certain pixel sizes that optimize between spatial resolution, dynamic range, readout speed and field of view.

3.6.2.2 Optical Lens

A camera lens is an assembly of a transmissive optical device that focuses the incoming light beam on the photographic sensor. Depending upon, focus length, field of view, angular area there are different types of lens available. Focal length is a basic characteristic of a lens and represents the distance from the point where light rays converge to form a sharp image of an object to the digital sensors when the lens is focused at infinity [122]. Usually, focal length is represented in mm. Focal length also represents a field of view. The longer the focal length, the narrower the field of view. Depending upon the focal length, lenses are categorized as fixed focal length and variable focal length lenses. First type of lenses are known as prime lenses and the second type of lenses

are known as zoom lenses. Main advantage of prime lenses are their size, weight, and maximum aperture. Prime lenses are lighter in weight and compact. Prime lenses can also reach a larger aperture which allows image acquisition in low light condition. Macro lenses are one type of prime lenses that are generally used in close up photography and allows to achieve life-size magnification (1:1). Zoom lenses are more versatile and generally used in wide variety of subjects such as landscapes and portraits [123]. However, zoom lenses can't reach life-size magnification or high aperture opening. Depending upon focal length, lenses can be grouped as shown in Table 3.5. Thus a single lens is not sufficient for all the photographic requirement. However, it is possible to list the parameter of an ideal lens for neutron imaging. The parameters are listed as follows.

- Long focal length (200 mm or larger)
- Can achieve life-size photography (1:1 magnification)
- Can reach the maximum aperture ($f/1$)
- Variable focus length (zoom lens)
- Manual focus

Longer focal length is required to achieve maximum distance from the focal length. In neutron imaging, the scintillator is placed at the focal plane of the lens. Thus, high focal length will reduce the shielding required to protect the CCD electronics. Life size (1:1) magnification is desired to achieve high spatial resolution. Maximum aperture of the lens reduces the exposure time thus making the system suitable for dynamic imaging and zoom lenses allow selection of a various field of view. However, in practice, all of the criteria doesn't meet simultaneously due to design constraint. However, a few lenses actually satisfy some requirements simultaneously. Nikon 200 mm $f/4D$ is a telephoto lens with long focal length and can achieve 1:1 magnification with a maximum aperture up to $f/4$. In fact, this is the only lens that is a telephoto macro lens and available

commercially. Generally, a camera lens is made of multiple lenses to correct the optical aberration. But in any lens system, some optical aberration will always present. Diffraction and aberration are the two phenomenon that limits spatial resolution of the lens.

Table 3.5. Specification of Lens

Focal Length	Lens Type	Typical Use
8mm -24mm	Ultra-wide angle	Wide angle photography
24mm – 35 mm	Wide angle	Interiors, architecture, landscapes
35mm – 85mm	Standard	General purpose
85mm – 135mm	Short telephoto	Portraits
135mm – 300 mm	Medium telephoto	Distance photography
300mm – 700 mm	Super telephoto	Astronomy, wildlife

Diffraction

In optical lens, light that forms an image are limited by the angularity of an aperture stop. For a glass-based lens system, spatial resolution is limited by the diffraction phenomenon of visible light. Light wave diffracted at the edge of the aperture as the light wave passes through the lens, effectively spreading the wave-fronts to broaden the point source. Thus, if an infinitely small emission point passed through an objective lens, it doesn't produce another infinitely small point, but a diffraction image with a finite spread. An Airy diffraction pattern is formed by the lens aperture from which spherical wave converge to the focal point [124]. The intensity distribution of the diffraction image can be expressed as,

$$I(\gamma) = I_0 \left(\frac{2J_1(\gamma)}{\gamma} \right)^2, \quad (3.20)$$

where, $J_1(\gamma)$ is first order Bessel function and γ is the proportional angle and can be expressed as,

$$\gamma = 2\pi \frac{NA}{M\lambda} r_i, \quad (3.21)$$

where NA is the numerical aperture, M is the magnification, λ is the wavelength of the light and r_i is the radial distance. The radius of the Airy disk pattern in the object plane define the limit of resolution and can be expressed as,

$$r_{Rayleigh} = 0.61 \times \frac{\lambda}{NA}. \quad (3.22)$$

The condition is known as Rayleigh's criteria for diffraction limited spatial resolution [125]. However, the criteria may not be applicable if diffraction pattern has no well-defined zeros or these are far from the central maximum. An alternative approach was proposed by Sparrow and can be expressed as,

$$r_{Sparrow} = 0.47 \times \frac{\lambda}{NA}. \quad (3.23)$$

In practical optical systems, lens usually works with partially coherent illumination due to the dimension of the object. Abe's theory is usually used to describe the spatial illumination imposed by the diffraction phenomenon and can be expressed as,

$$r_{Abbe} = \frac{\lambda}{2n \sin \alpha} = 0.5 \times \frac{\lambda}{NA}, \quad (3.24)$$

where n is the refractive index of the medium and α is the angle between an axis and the light travelling direction [125]. The limit is known as Abbes resolution limit and represent the best resolution that can be achieved by a lens with given numerical aperture and wave length of light. Numerical aperture can be represented by the f -number of the lens by the following equation,

$$NA = \frac{1}{2 \times f\#}. \quad (3.25)$$

In most lenses, f - number is set by turning the iris adjusting ring as shown in Figure 3.24, thereby opening and closing the iris diaphragm inside [126]. Table 3.6 illustrates spatial resolution contribution of lens from Abe’s diffraction limit for a 200 mm lens.



Figure 3.24. Illustration of lens aperture (f) number for Nikon Nikkor 55 mm lens (highlighted area is the iris adjustment ring to control the numerical aperture).

Table 3.6. Spatial resolution contribution from diffraction

f -number	NA	Aperture diameter (mm)	Opening area (mm ²)	r_{Abe} (μ m)
$f/4$	0.125	50	1963.5	1.8
$f/8$	0.0625	25	490.8	3.6
$f/16$	0.0312	12.5	122.7	7.2
$f/22$	0.0227	9.5	70.88	9.9
$f/32$	0.0156	6.25	30.67	14.4

Aberration

In general, a practical optical system doesn't perform ideal imaging. As illustrated in Figure 3.25, optical rays don't converge into a single point after transmission through a system. This phenomenon is known as an optical aberration of a lens. The types of aberration that affect the performance of the lens systems are spherical aberration, coma, astigmatism, distortion and chromatic aberration [123].

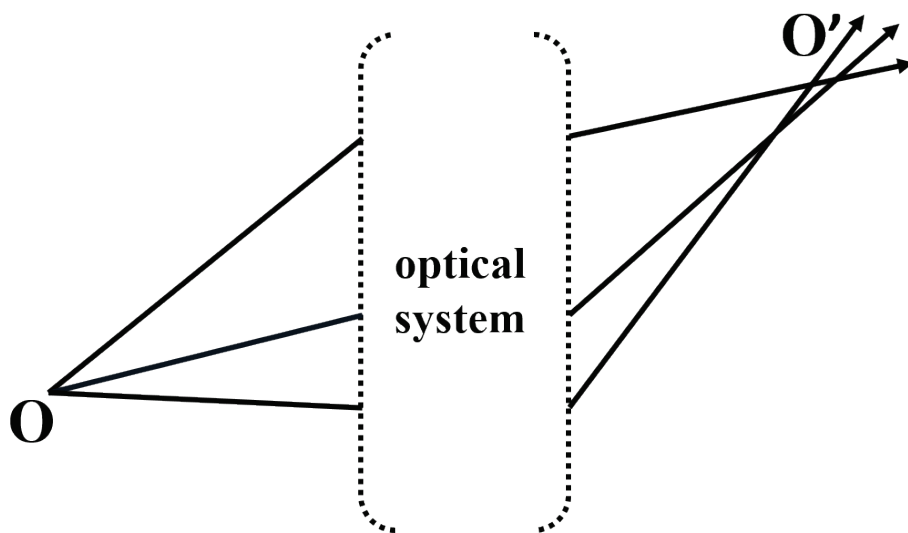


Figure 3.25. Illustration of optical aberration showing the optical rays do not merge to a single point after passing through an optical system.

Spherical aberration can be defined as a variation of the focus with an aperture as illustrated by Figure 3.26. Rays that are close to the optical axis intersect an axis close to paraxial focus compared with other rays. As the distance of the ray from the axis increases, an intersection with the optical axis moves further. Spherical aberration depends on the shape or bending of the lens [123]. It can be observed that the transverse measure of an aberration is directly related to the size of the blur. This can be corrected ideally by a perfectly spherical lens surface. Transverse spherical aberration (TA) can be expressed as a distance between the optical axis and the intersection of the farthest optical ray at the paraxial focal plane and the longitudinal spherical aberration (LA) can

be expressed as the distance between the intersection of optical rays with the optical axis and paraxial focus plane.

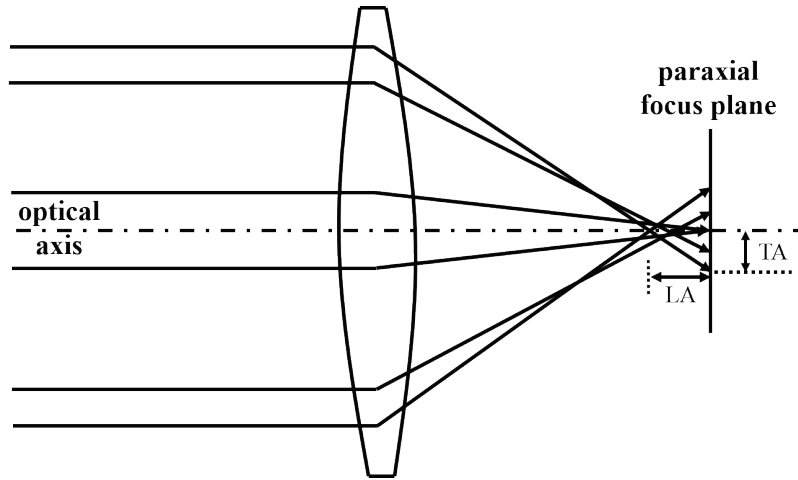


Figure 3.26. Illustration of spherical aberration showing the optical rays do not merge at paraxial focus plane at optical axis due to longitudinal spherical aberration (LA) and transverse spherical aberration (TA) [123].

Coma can be defined as the variation of magnification with aperture. When multiple oblique rays pass through a lens, rays transmitted near the edge of the lens may image at a different height as compared with the ray passes through the center of the lens, the appearance of the point image formed by the comatic lens is shown in Figure 3.27.

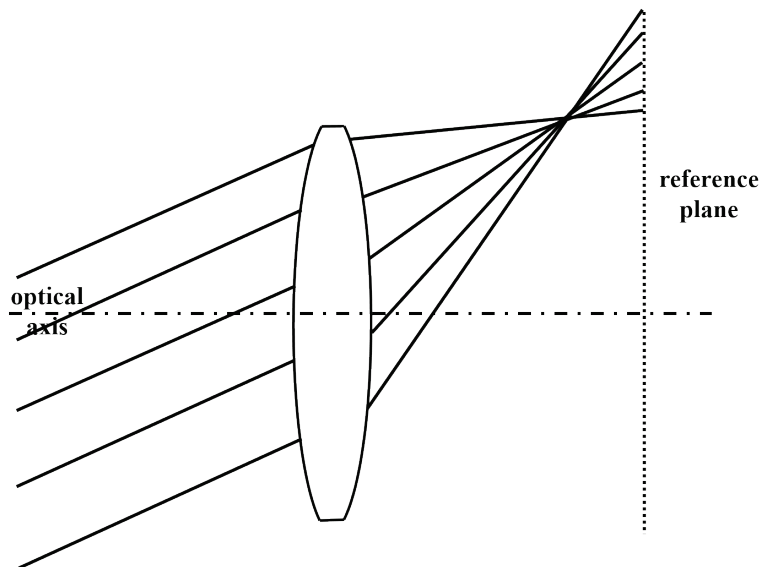


Figure 3.27. Illustration of Coma effect of the lens showing the oblique optical rays do not merge after passing through the lens due to the variation of magnification with aperture.

Coma varies with the shape of the lens and the position of an aperture and minimal for a symmetrical system. When coma is extended, such that tangential and sagittal image doesn't coincide, it is known as astigmatism [123]. If a lens has astigmatism, then a point takes the form of two separate lines at the focal plane. Astigmatism of a lens depends on the power, shape, and distance from an aperture of a lens. When an image is formed at a different distance at paraxial axis, actual shape of the image is distorted. The distortion may be different and depending on the position of the object, image may be extended or shrunken. Distortion can be expressed directly or as a percentage of the ideal image. Distortion can be illustrated by Figure 3.28. This type of distortion is also known as Barrel distortion [123].

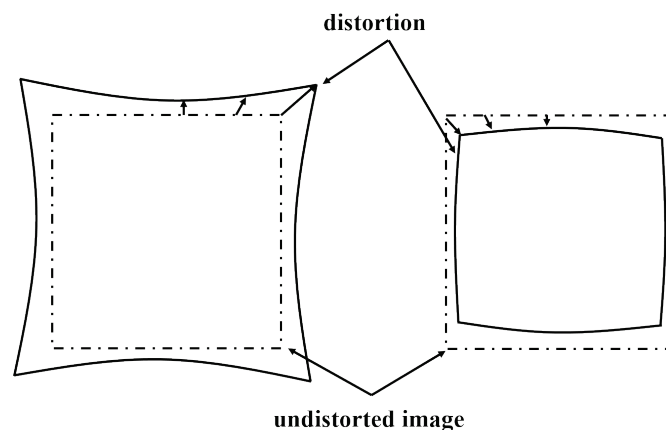


Figure 3.28. Illustration of the distortion effect of a lens showing the deformed formation of an image due to image formation at a different distance at the paraxial axis.

The index of refraction depends on the wavelength of the light. In general, the refraction index is high for short wavelength and low for the longer wavelength of the light. Thus, light with short wavelength like blue light ray refracted more, thus intersect the optical axis before the red light which has the longer wavelength as illustrated in Figure 3.29. In presence of chromatic aberration, a point object image represented by a bright dot surrounded by a halo. A bright dot is formed by light which is at focus and halo is formed by out of focus rays. For monochromatic ray, variation in refractive index also results in similar aberration effect.

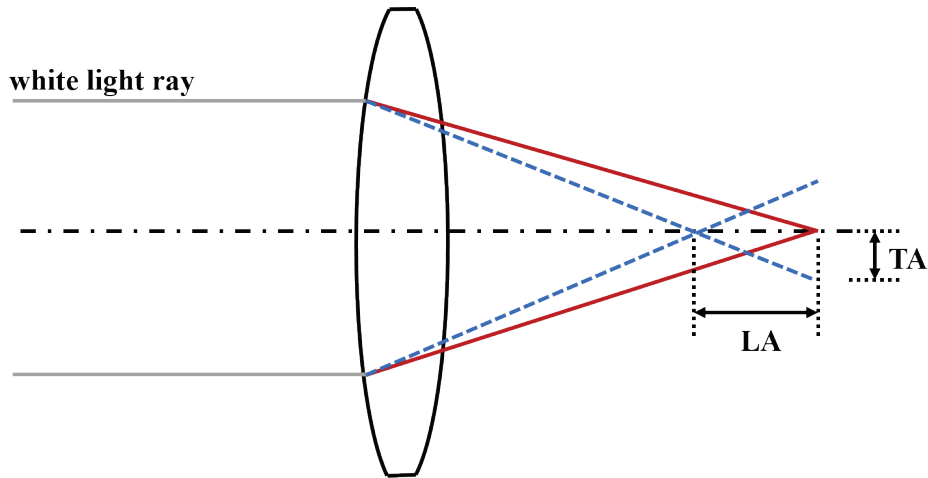


Figure 3.29. Illustration of chromatic aberration showing the optical rays of different wavelength do not merge at paraxial axis due to their difference in refraction index (LA: longitudinal axial chromatic aberration, TA: transverse axial chromatic aberration) [123].

Typical performance of an optical lens is shown in Figure 3.30. Thus, spatial resolution of a lens is limited by diffraction and aberration. Diffraction is a fundamental physical limit caused by the diffraction of the light, and aberration depends on the lens design. Thus, to allow more light a lens aperture must be as open as possible.

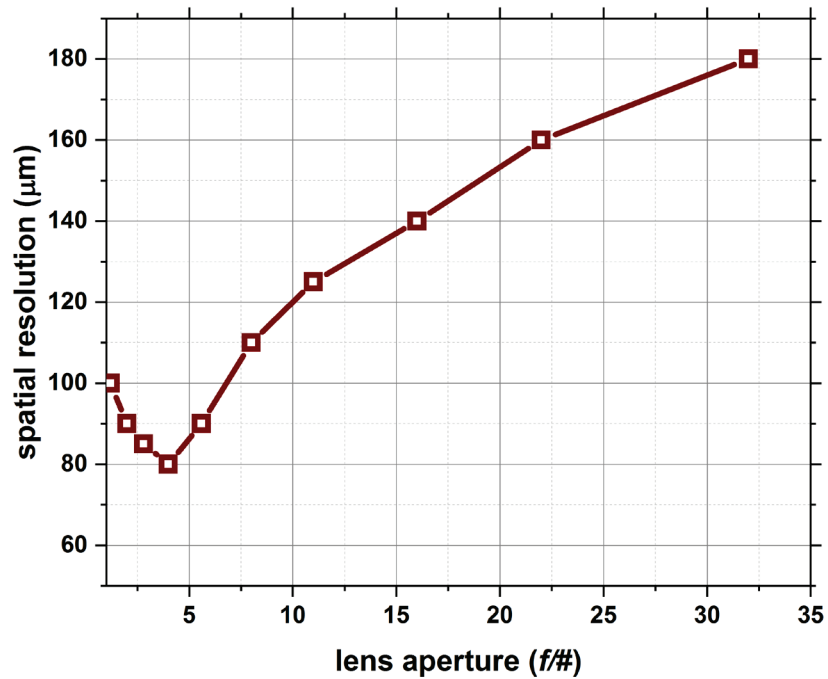


Figure 3.30. Representation of a typical lens performance with different lens aperture settings showing the combined effect of diffraction and aberration on the spatial resolution.

But as the lens aperture is more open, aberration affects more. At very small aperture, all lenses produce similar results whereas at large aperture high-quality lenses perform better. Thus, the effect of aberration can be minimized by designing better lens design practices whereas, the effect of diffraction cannot be eliminated.

3.6.2.3 Scintillator

Scintillator is a material, which is able to convert radiation energy to visible optical photons by a direct or indirect mechanism. The use of scintillator material can be found as early as the discovery of X-rays. In fact, in early stages of X-ray registration with the photographic film used CaWO_4 . Later, ZnS-based powder phosphor was introduced by Crookes and Regener and mixed with CaWO_4 to improve the efficiency [127]. Based upon scintillation mechanism, scintillator can be broadly classified into inorganic scintillator and organic scintillator. The inorganic scintillator usually has better light output and linearity but slower response time. However, organic scintillator generally has faster response time but lower light output [128]. In this section, we will briefly discuss the scintillation mechanism for organic and inorganic scintillator and introduce popular inorganic scintillators used for neutron imaging applications.

Organic Scintillator

Organic scintillators is based on organic molecules with certain symmetry properties of the π -electron structure. The structure is illustrated in Figure 3.31. Singlet and triplet states are labeled as S_0, S_1, S_2, S_3 and T_1, T_2, T_3 . The vibrational states are labeled with the second subscript. As the kinetic energy absorbed from the charged particles, the molecule are excited as shown with the arrow pointing upward direction. The higher singlet states *i.e.*, S_2 and S_3 de-excites quickly to the S_1 through the internal conversion process. Thus, after the excitation process of an organic scintillator, the excited molecules are majorly in S_1 excited state. Scintillation event occurs during the transition of S_{10} to any vibrational states S_0 is known as prompt fluorescence. The organic

scintillators have decay time on the order of nano-seconds for the transition in between singlet states and longer decay times observed between the transitions between triplet states. The scintillation event occurs due to the de-excitation process of triplet states are known as phosphorescence. Sometimes, molecules at T_1 may excited back to S_1 and de-excited through normal fluorescence [129].

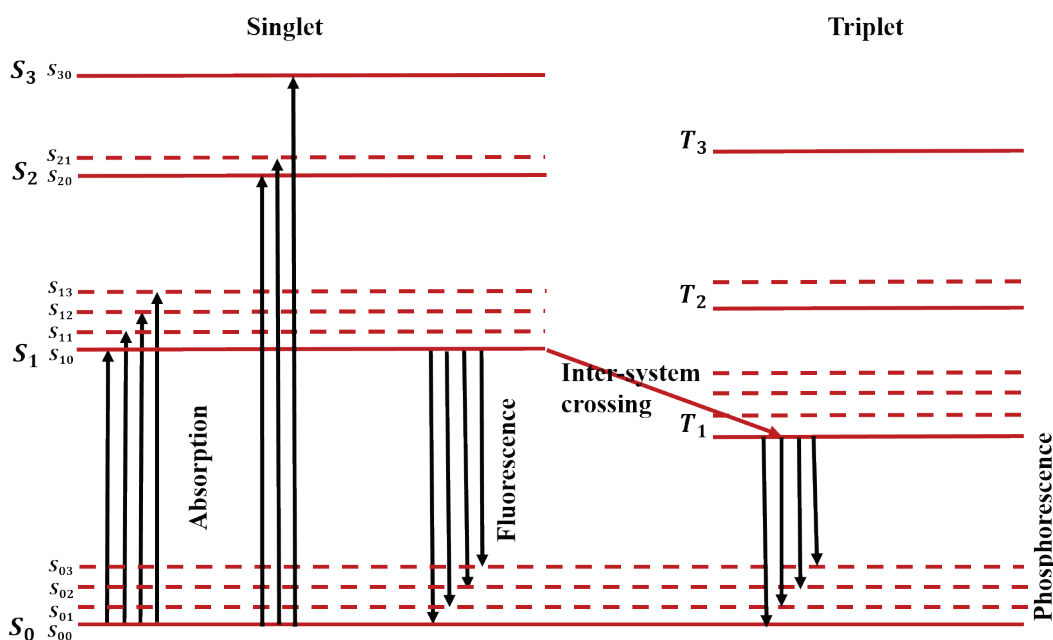


Figure 3.31. π -electronic energy levels of organic molecules showing S_0 , ground state S_1 , S_2 , S_3 excited singlet states, T_1 , T_2 , T_3 are excited triplet states and the subscripts are the vibrational states [129].

Inorganic Scintillator

Luminescence property of an inorganic scintillator is a crystalline property and unlike inorganic scintillator may not normally exhibit in any other phases like liquid or vapor. The scintillation mechanism in an inorganic scintillator depends on an energy states of a crystalline material as shown in Figure 3.32. The details of the collective electron model for inorganic scintillator can be found in. The energy state of an individual atom or molecules comprises of distinct energy levels as defined by Schrodinger equation. In crystal lattice, distinct energy levels

of multiple atoms mutually interact and broadened into a series of continuous energy bands. In a normal state, lower energy bands are completely filled while higher bands are empty. The lower energy band is known as valence band and the higher energy band is known as conduction band. These bands are separated by few eV energy gaps known as bandgap energy [129].

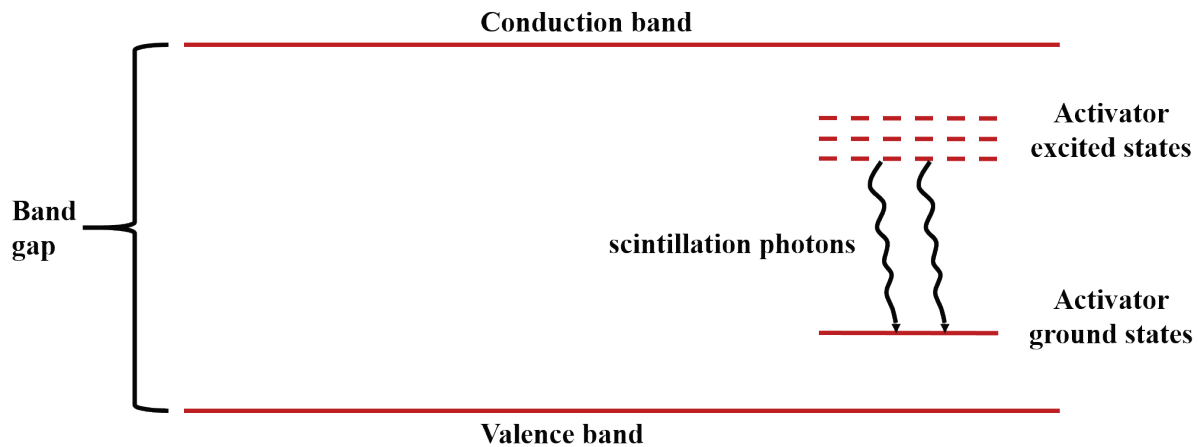


Figure 3.32. Energy band structure in impurity activated crystal phosphor, showing valence band, conduction band, excited and ground state of activators.

When absorbed energy is more than band gap energy, an electron is elevated from valence band to conduction band leaving a hole in the valence band. In pure crystal, the electron in conduction band and hole in valence band may combine to form excitons. Additionally, de-excitation may produce a photon with a wavelength outside of the visible optical spectrum. To improve scintillation efficiency, often impurity is added which is known as activators. Added impurities modify the electronic band structure as shown in Figure 3.32. The excited electrons in the conduction band can drop into the activator excited states and de-excited as it transits through the activator ground states resulting scintillation light.

Typical neutron scintillators require two processes to follow. They are neutron capture within the scintillator and transfer of the energy to the scintillator material. The scintillator for thermal neutron detection consists of a material with a high neutron capture cross section along with the

scintillating material. Typical, choice of materials for thermal neutron capture are ^6Li , ^{10}B , ^{158}Gd . These materials are used in compound forms for the stability and mixed with scintillating materials. Table 3.7 shows few scintillators for thermal neutron detection.

Table 3.7. Properties of scintillators used for thermal neutron detection [130-132]

Scintillator	Density (g/cm^3)	λ_{em} (nm)	Optical photon per neutron
LiF/ZnS:Ag	2.6	450	160000
LiI:Eu	4.1	470	50000
Li(glass):Ce	2.5	395	7000
$\text{Cs}_2\text{LiYBr}_6\text{:Ce}$	4.1	390	110000
$\text{Rb}_2\text{LiLaBr}_6\text{:Ce}$	3.9	363	54000
$\text{LiCaAlF}_6\text{:Eu}$	2.9	370	29000
$\text{Cs}_2\text{LiYCl}_6\text{:Ce}$	3.31	373	73000
$\text{Li}_3\text{Cs}_2\text{I}_5\text{:Tl, Eu}$	4.5	450	57400
$\text{Li}_x\text{Na}_{1-x}\text{I}$	3.6	420	102500
$\text{GdI}_3\text{:Ce}$	5.2	550	5000
$\text{Gd}_2\text{O}_2\text{S:Tb}$	7.3	545	1000

A high optical photon yield of $^6\text{LiF:ZnS:Ag}$ scintillator makes it a popular choice for thermal neutron imaging. For the real-time neutron imaging application scintillator plays an important role in setting spatial resolution for a real-time neutron imaging systems. Therefore, understanding and characterization of the scintillator are required for the development and performance prediction of high spatial resolution application. A Geant4 multi-physics model of the scintillator was developed

to characterize and correlate the resolution performance with the scintillator thickness. Thermal neutrons are absorbed in ${}^6\text{Li}$ and consequently Alpha and Triton particles are emitted as,



Alpha is generated with 2.05 MeV and Triton is generated with 2.72 MeV energy. Both charge particles are generated at a same position but in opposite direction to conserve momentum. The charged particle deposits their energy along their track inside the scintillator. Stopping power of Alpha and Triton is shown in Figure 3.33 and Figure 3.34. SRIM validation is shown in Table 3.8.

Table 3.8. SRIM validation of range of Alpha and Triton particle inde the scintillator

Particle	Ion energy (MeV)	Mean projected range (μm)
Alpha	2.05	7.37
Triton	2.72	42.88

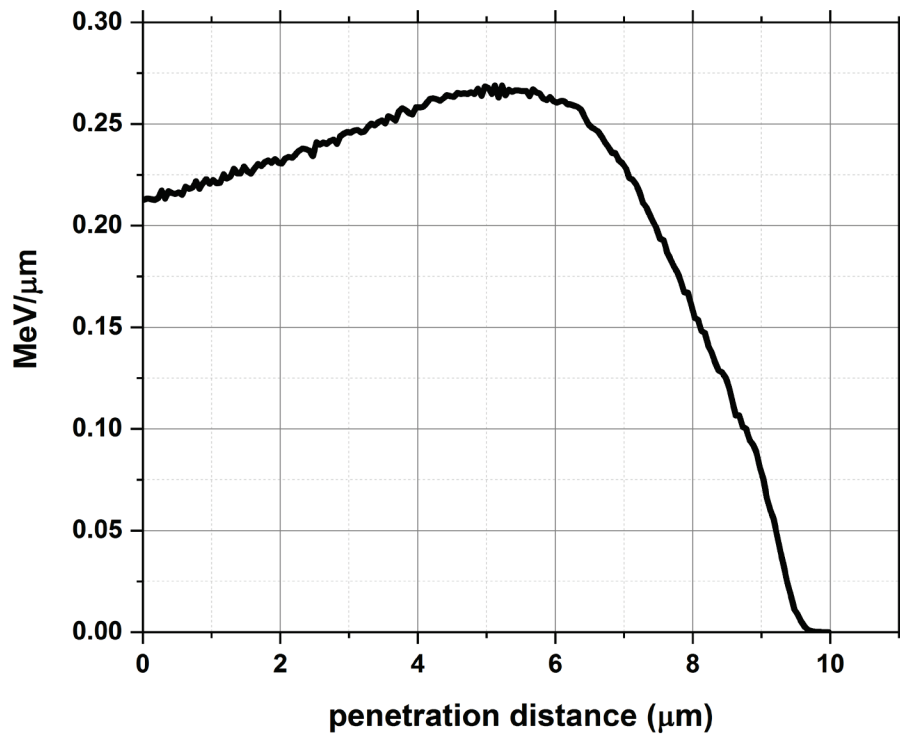


Figure 3.33. Range of Alpha particle with energy 2.05 MeV as obtained with Geant4 simulation.

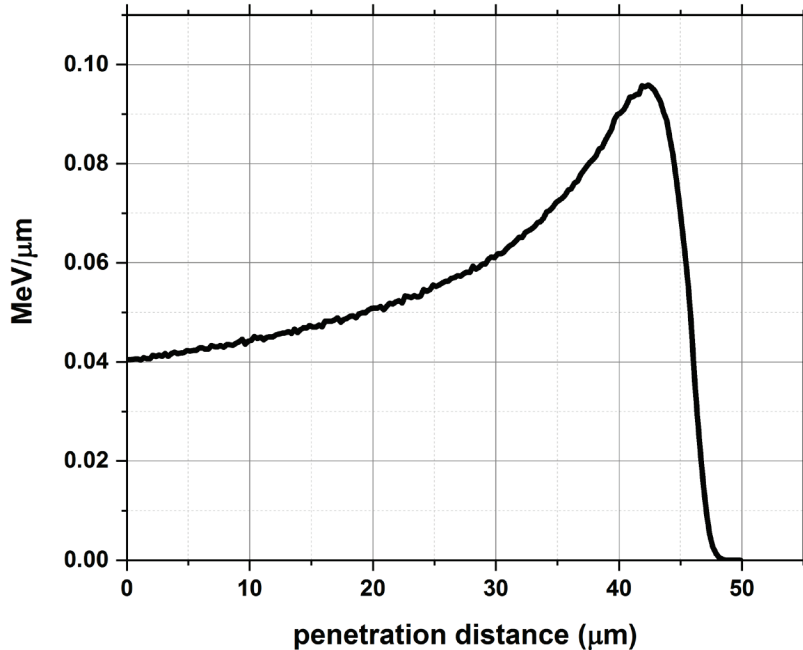


Figure 3.34. Range of Triton particle with energy 2.72 MeV as obtained with Geant4 simulation.

It can be observed from Figure 3.33 and Figure 3.34 that alpha particle has high stopping power but the range is around 12 μm , whereas Triton particle has comparatively lower stopping power but travels around five times as compared with an alpha particle. Since, the multi-physics phenomenon is involved in the scintillation process, the characterization of such scintillator requires an investigation of each occurrence. The physics process involved in the scintillation process can be listed as follows.

- Neutron transportation and absorption.
- Charge particle generation.
- Charge particle transportation and energy deposition.
- Optical photon generation.
- Optical photon transportation and absorption.

These events are explored next with different scintillator thickness to understand and characterize the resolution contribution of the scintillator with thickness varying between 25 μm and 400 μm .

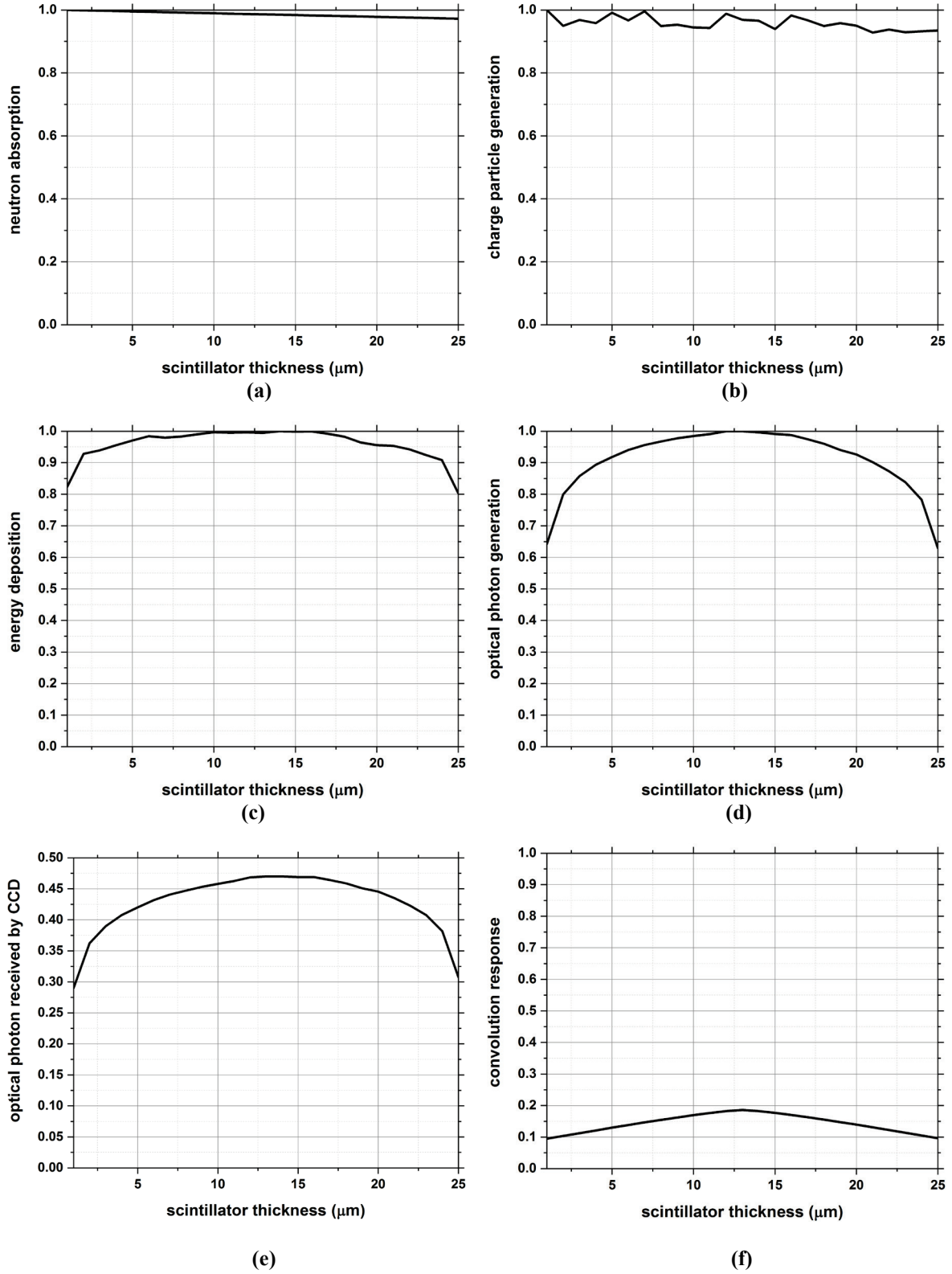


Figure 3.35. Profile plots for 25 μm scintillator showing, (a) neutron absorption, (b) charge particle generation, (c) energy deposition, (d) optical photon generation, (e) optical photon reception by CCD, and (f) convolution response of optical photon generation and reception (convolution profile is normalized with 400 μm thick scintillator for comparison).

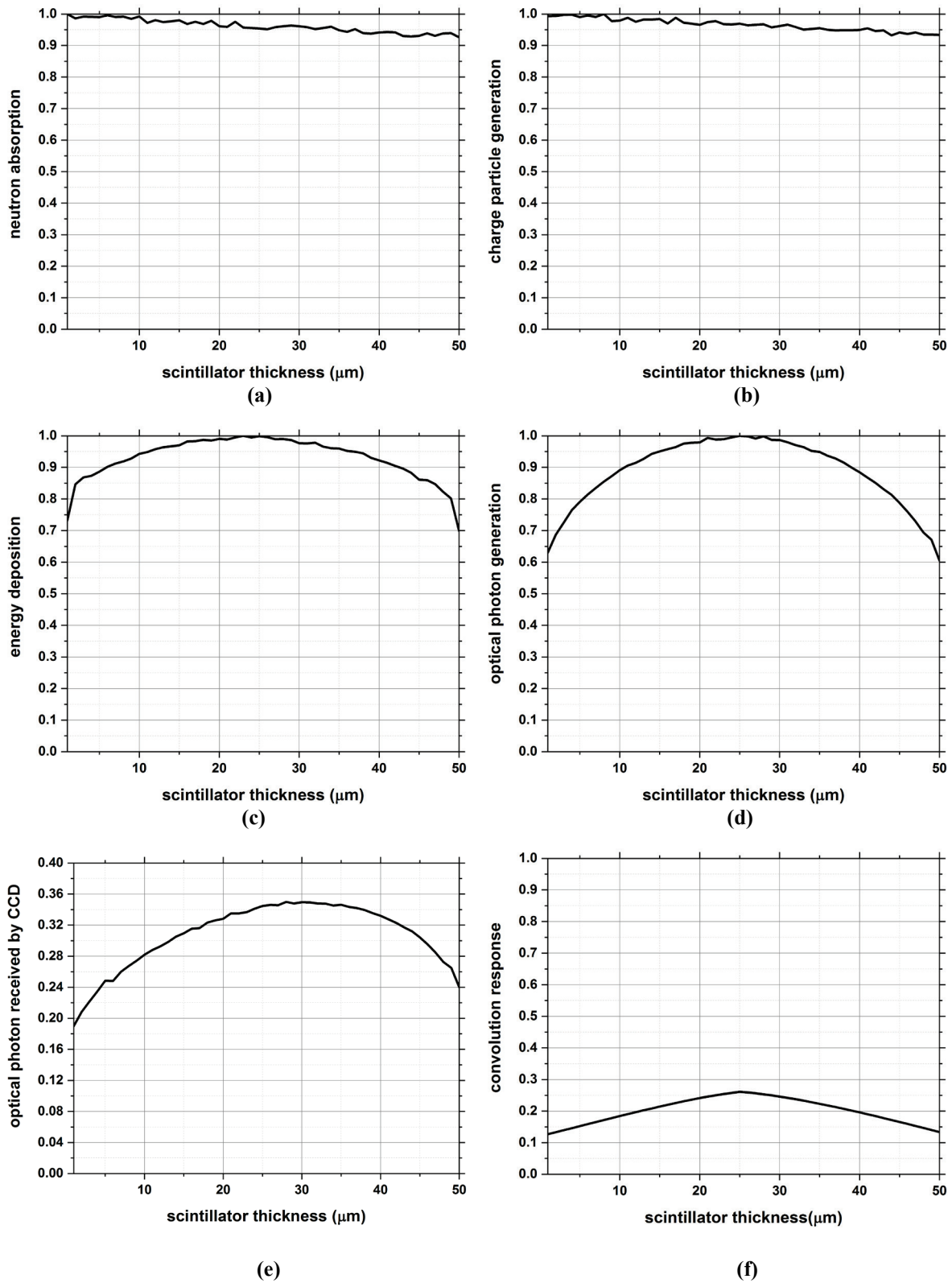


Figure 3.36. Profile plots for 50 μm scintillator showing, (a) neutron absorption, (b) charge particle generation, (c) energy deposition, (d) optical photon generation, (e) optical photon reception by CCD, and (f) convolution response of optical photon generation and reception (convolution profile is normalized with 400 μm thick scintillator for comparison).

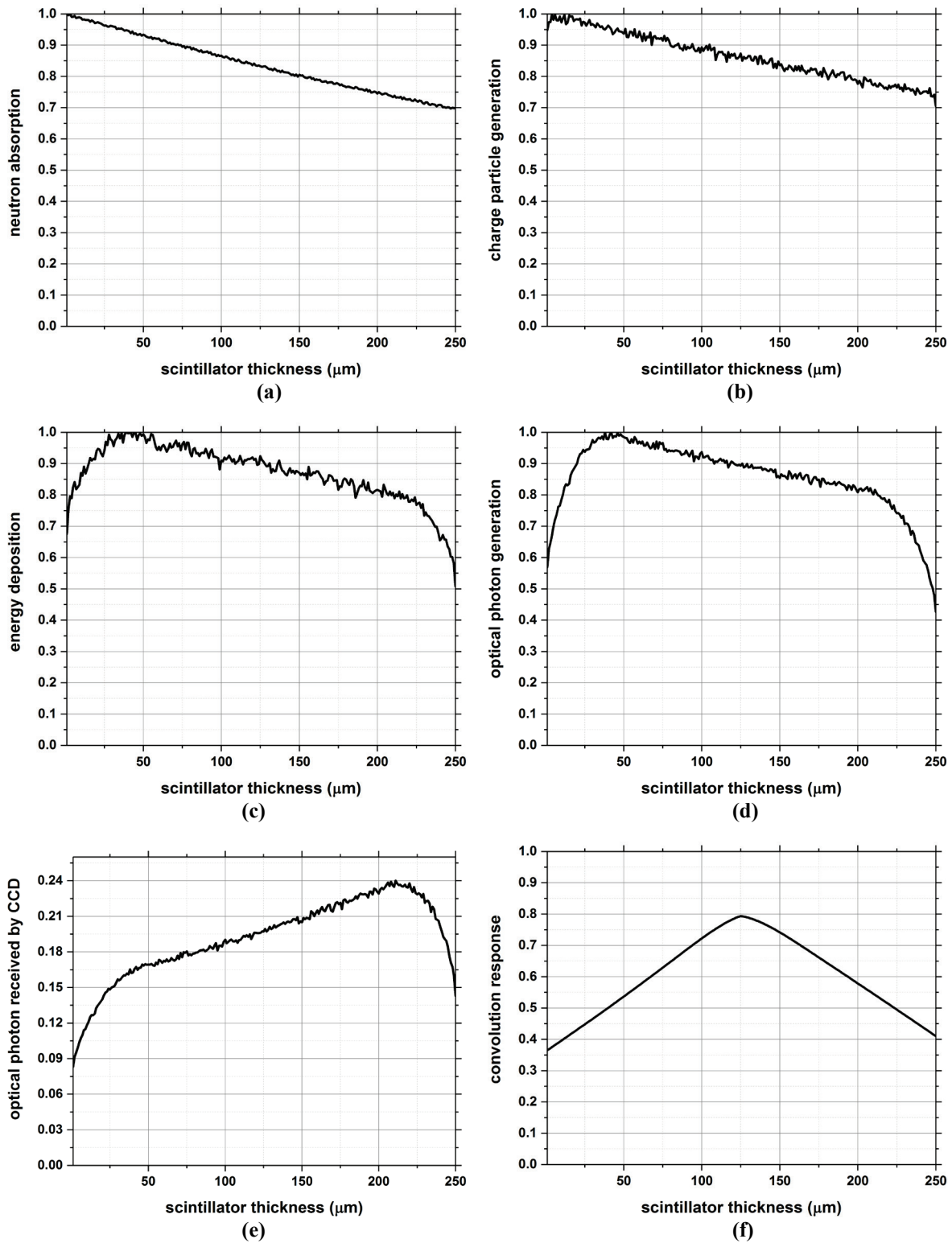


Figure 3.37. Profile plots for 250 μm scintillator showing, (a) neutron absorption, (b) charge particle generation, (c) energy deposition, (d) optical photon generation, (e) optical photon reception by CCD, and (f) convolution response of optical photon generation and reception (convolution profile is normalized with 400 μm thick scintillator for comparison).

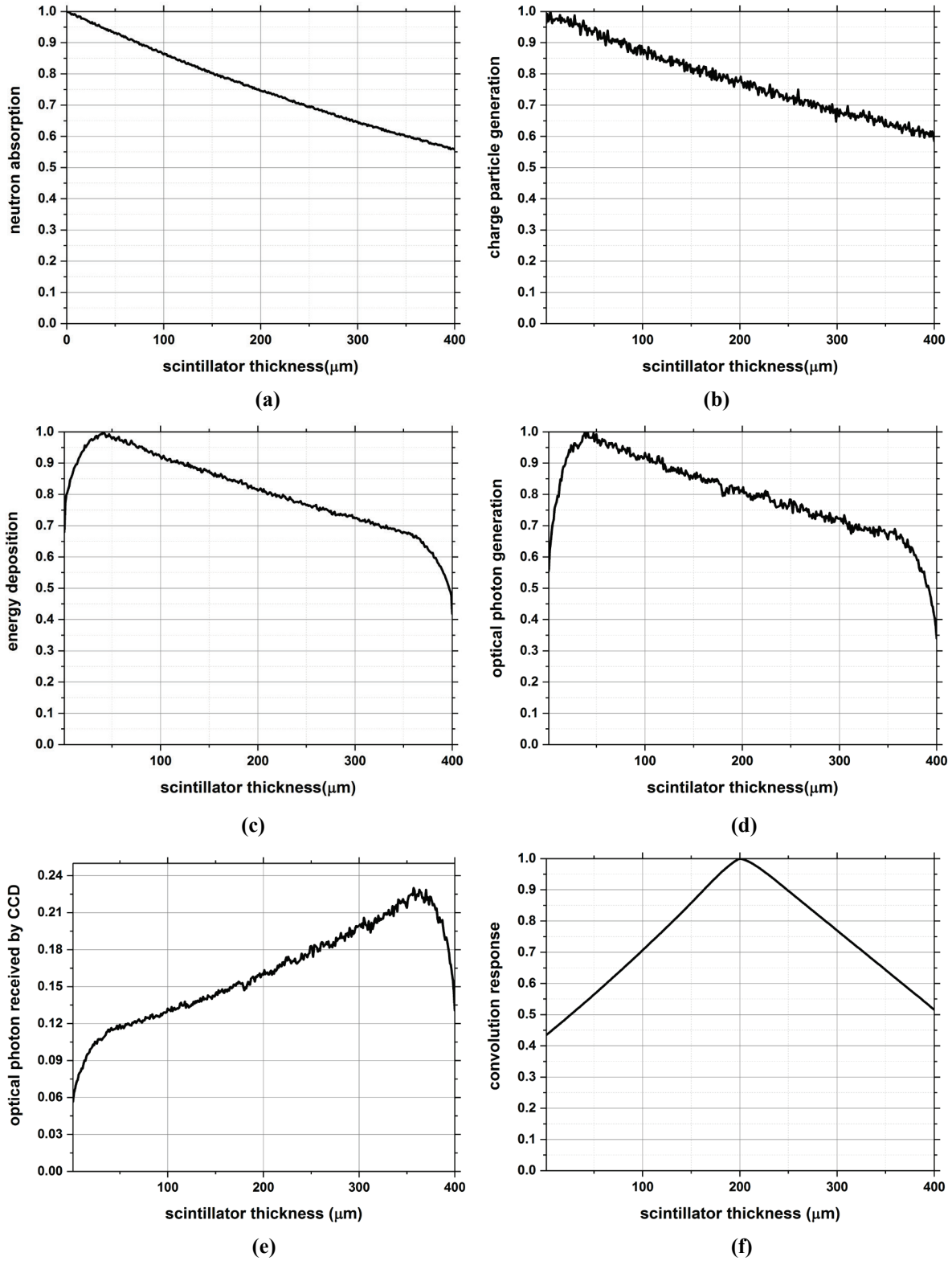


Figure 3.38. Profile plots for 400 μm scintillator showing, (a) neutron absorption, (b) charge particle generation, (c) energy deposition, (d) optical photon generation, (e) optical photon reception by CCD, and (f) convolution response of optical photon generation and reception (normalized).

It can be observed that the neutron attenuation profile is exponential because neutrons absorption follows the exponential Beer-Lambert law. In case of very thin scintillator like 25 μm , the profile looks like a straight line but as the thickness increases the exponential profile is clearly visible. When neutrons are absorbed inside the scintillator screen, Alpha and Triton particles are generated. So, the charge particle generation profile follows the neutron absorption profile as shown in (b) of Figure 3.35 - Figure 3.38. Charged particles deposit their energy along the tracks inside scintillator. But near the edge of the scintillator screen charge particle may escape the scintillator without depositing the entire energy. This results, incomplete energy deposition around the scintillator edge as illustrated by (c) of Figure 3.35 - Figure 3.38. Optical photons are generated following the energy deposition of the charged particle and the profile is similar as compared with the energy deposition profile as illustrated by (d) of Figure 3.35 - Figure 3.38. Optical photons are self-absorbed and scattered as they are transported inside scintillator. Thinner scintillator have low absorption probability resulting similar shape as generation profile. But for thick scintillator screen, optical photons those are generated closer to the edge of the scintillator screen and CCD have a higher probability to escape the scintillator and reach CCD. The optical photon profile received by CCD are illustrated by (e) of Figure 3.35 - Figure 3.38. Thus, it can be observed that, for a thin scintillator optical photon generation and reception profile by CCD is nearly uniform. For a thick scintillator most number of optical photons are generated in the first half of the scintillator. But, foremost number of the optical photons that are able to escape the scintillator and reach the CCD are generated in the second half. This observation can be further demonstrated by observing the convolution response profile between optical photon generation and reception by CCD profile as shown by (f) of Figure 3.35 - Figure 3.38. Thin scintillator have a more uniform response as compared with a thick scintillator. But, convolution profile of thick scintillator have a

peak near the half thickness of the scintillator. This observation is useful to correlate the scintillator thickness with measured spatial resolution. For the measurement of spatial resolution, radiographs were obtained by placing a 200 μm thick Gadolinium edge on the scintillator screen. Top view of the simulation geometry is shown in Figure 3.39. The spatial resolution was obtained with the edge method as outlined earlier. A radiograph obtained with 50 μm thick ${}^6\text{LiF}:\text{ZnS}(\text{Ag})$ is shown in Figure 3.40. The spatial resolution of the scintillator along with the variable thickness is shown in Figure 3.41.

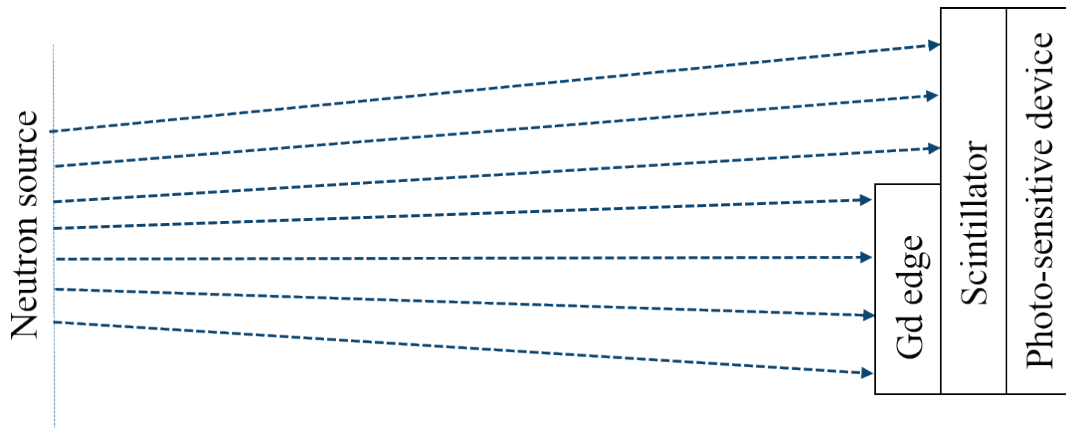


Figure 3.39. Illustration of the detector model (top view) used in the Geant4 simulation for the neutron radiograph generation.

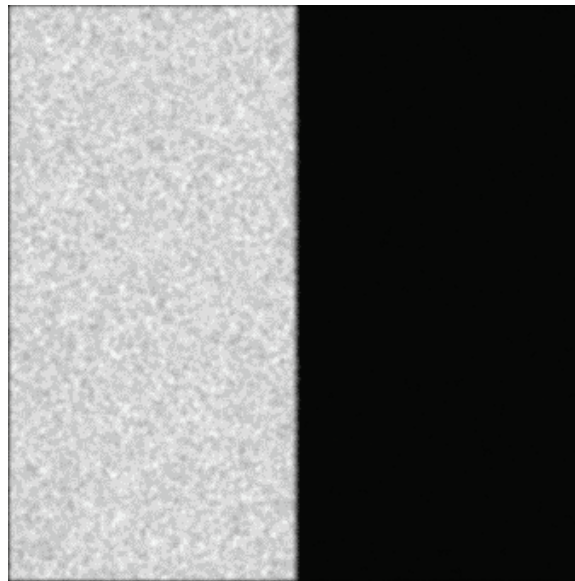


Figure 3.40. Edge radiograph as obtained with Geant4 simulation with 50 μm ${}^6\text{LiF}:\text{ZnS}(\text{Ag})$ scintillator for the calculation of the spatial resolution.

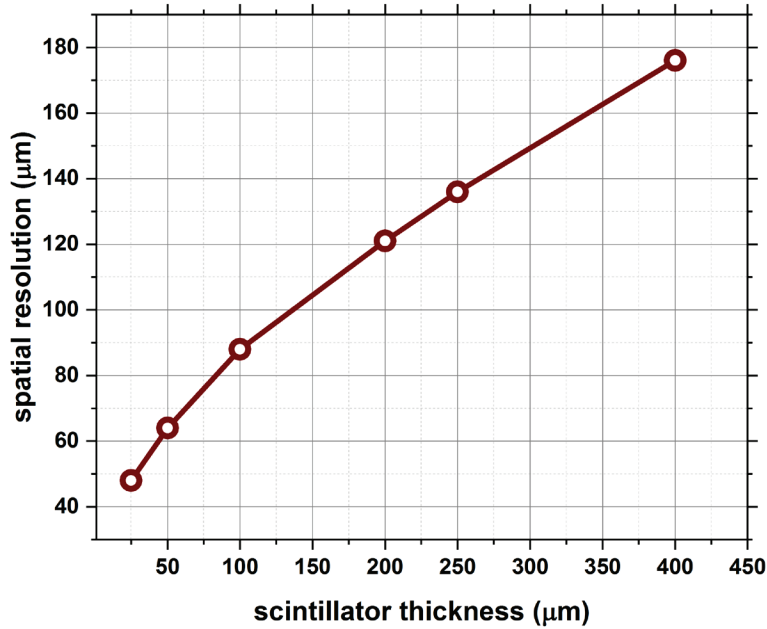


Figure 3.41. Spatial resolution of the scintillator with thickness showing the resolution contribution of the scintillator as obtained with Geant4 simulation.

The spatial resolution behavior of the scintillator screen with the thickness can be explained from the earlier discussion. For a thin scintillator, the optical photons travel the entire scintillator thickness before they are captured by CCD. Thus the spatial resolution approaches to the scintillator thickness. However, for a thick scintillator foremost number of optical photons travels around half of the scintillator thickness before they are captured at CCD, which limits the spatial broadening nearly half of the scintillator thickness. Thus for a thick scintillator, spatial resolution approach a value nearly the order of half thickness.

3.7 Experimental Results

Experiments were performed at PULSTAR neutron imaging facility to quantify the spatial resolution of the imaging system. For the measurement of the spatial resolution of each component, an edge image is obtained and calculated as outlined earlier. Assuming, a Gaussian distribution for the contribution of the various components of the imaging system, overall system response function R_T can be calculated as

$$R_T = \sqrt{R_G^2 + R_D^2}, \quad (3.27)$$

where R_G is the geometric component of the spatial resolution and R_D is the resolution contribution of the detection system. R_D can be expressed as

$$R_D = \sqrt{R_{Scintillator}^2 + R_{Lens+CCD}^2}, \quad (3.28)$$

where $R_{Scintillator}$ and $R_{Lens+CCD}$ are spatial resolution contribution of scintillator, lens and CCD. To quantify $R_{Lens+CCD}$, an image containing a sharp paper edge was obtained. The arrangement is shown in Figure 3.42 and the edge images are shown in Figure 3.43 and spatial resolution are tabulated in Table 3.9.



Figure 3.42. Experimental arrangement to calculate the spatial resolution contribution of lens and CCD by measuring an edge image with light.

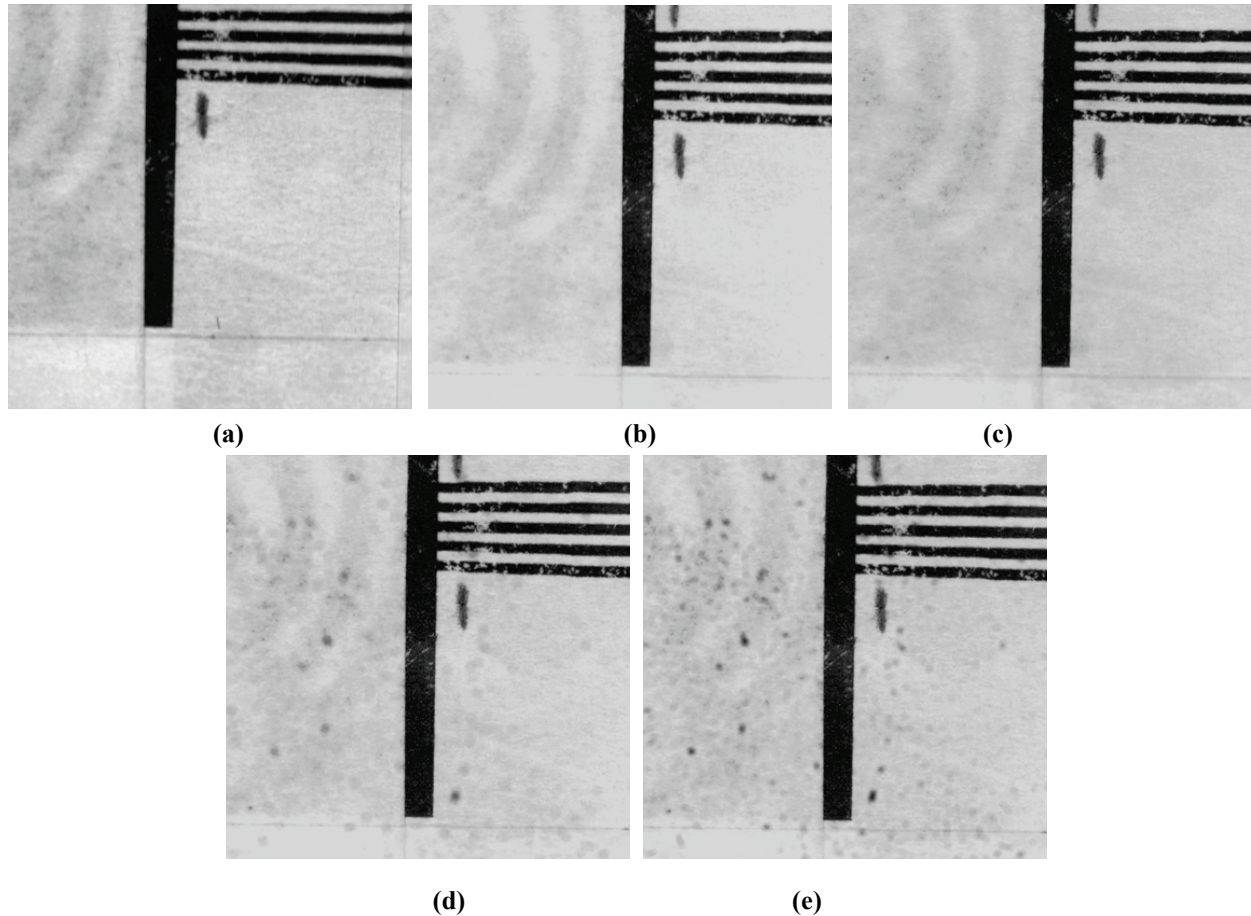


Figure 3.43. Edge images to calculate $R_{Lens+CCD}$ obtained with, (a) $f/4$, (b) $f/8$, (c) $f/16$, (d) $f/22$, and (e) $f/32$

Table 3.9. The spatial resolution of Lens and CCD

Lens	Pixel size (μm)	Aperture	Spatial Resolution (μm)
Nikon $f/4$ ED 200 mm	13	$f/4$	55 ± 1
		$f/8$	48 ± 1
		$f/16$	43 ± 1
		$f/22$	48 ± 1
		$f/32$	54 ± 2

Spatial resolution components of Lens and CCD system is illustrated in Figure 3.44. The combined spatial resolution of Lens and CCD system was measured as discussed earlier. Spatial resolution

of CCD was calculated assuming 3 pixel size as discussed earlier. The spatial resolution of Lens was calculated as,

$$R_{Lens} = \sqrt{R_{Lens+CCD}^2 - R_{CCD}^2}, \quad (3.29)$$

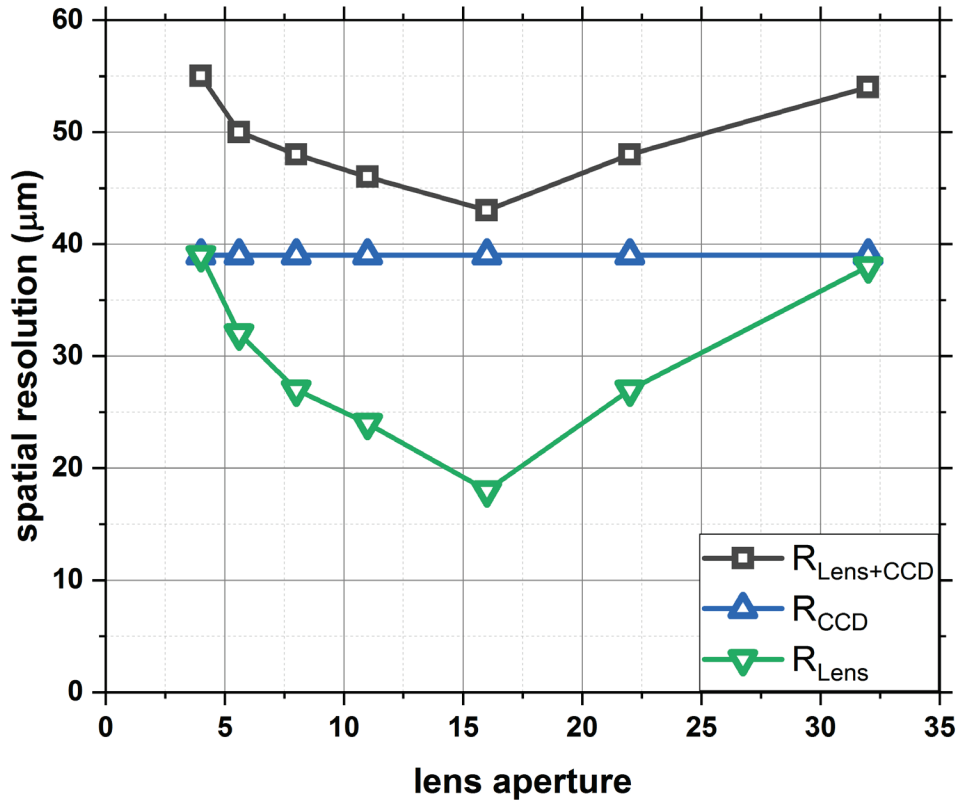
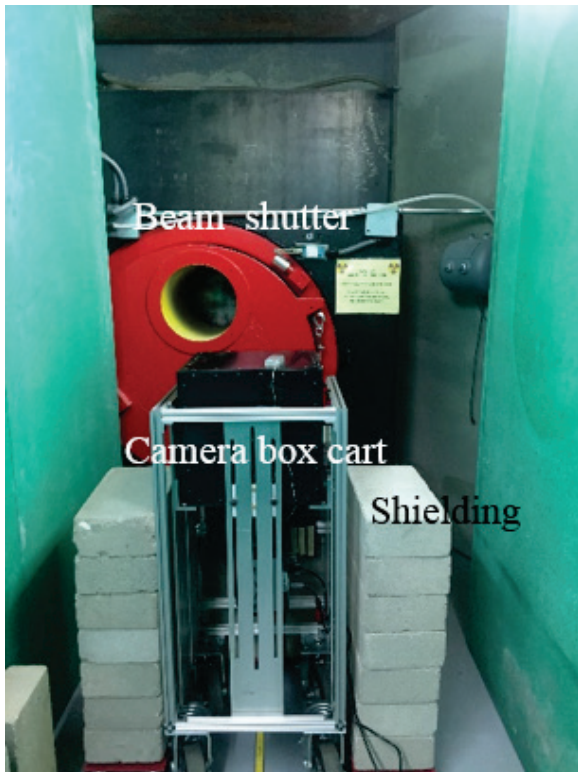
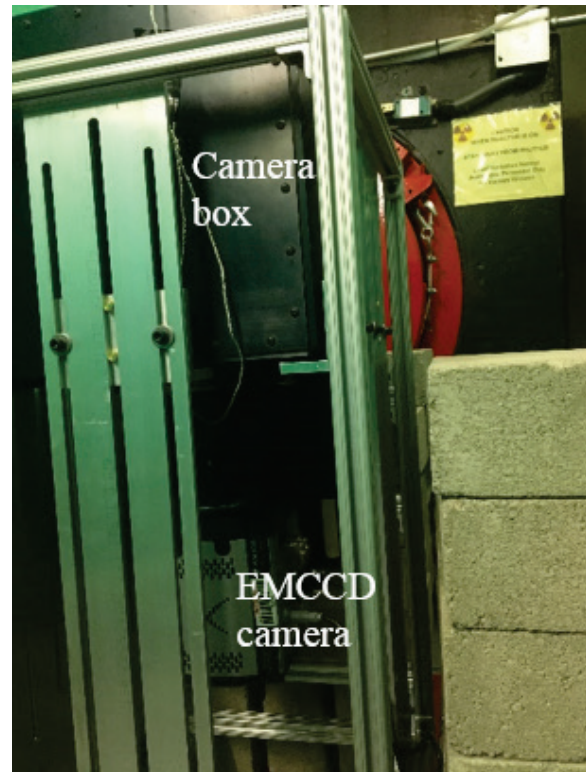


Figure 3.44. Spatial resolution components of the Lens and CCD system showing total measured spatial resolution of the Lens and CCD combined ($R_{Lens+CCD}$), theoretical contribution of CCD (R_{CCD}), and calculated spatial resolution contribution of Lens (R_{Lens}).

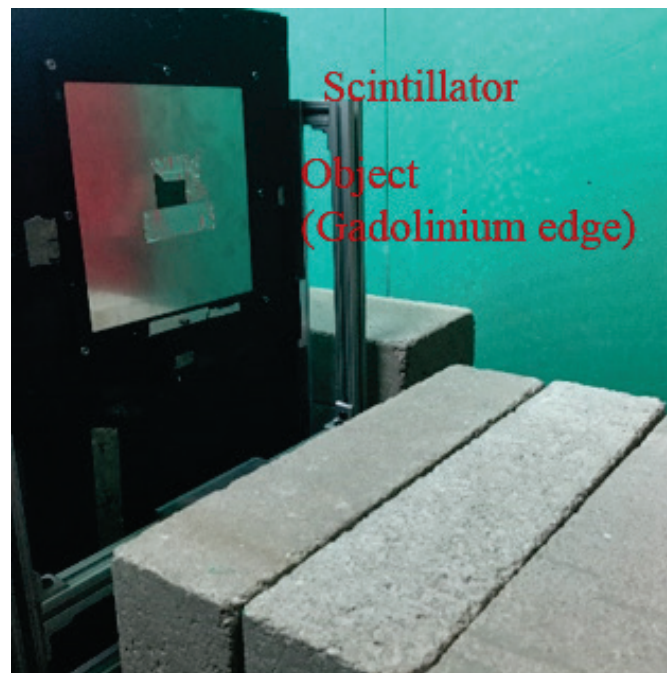
It can be observed that Lens has an optimum operating region at $f/16$ where best spatial resolution can be obtained. Next, a neutron radiograph was obtained, attaching a gadolinium edge on the scintillator screen as shown in Figure 3.45, (c). This arrangement makes the geometric contribution (R_G) negligible by reducing the distance between the object and the detector ($d \approx 0$), thus effectively quantify R_D . The edge neutron radiographs are shown in Figure 3.47, MTF and spatial resolution are shown in Figure 3.48 tabulated in Table 3.10. The neutron radiographs are obtained at lens aperture $f/16$ and spatial resolution components are shown in Figure 3.49.



(a)

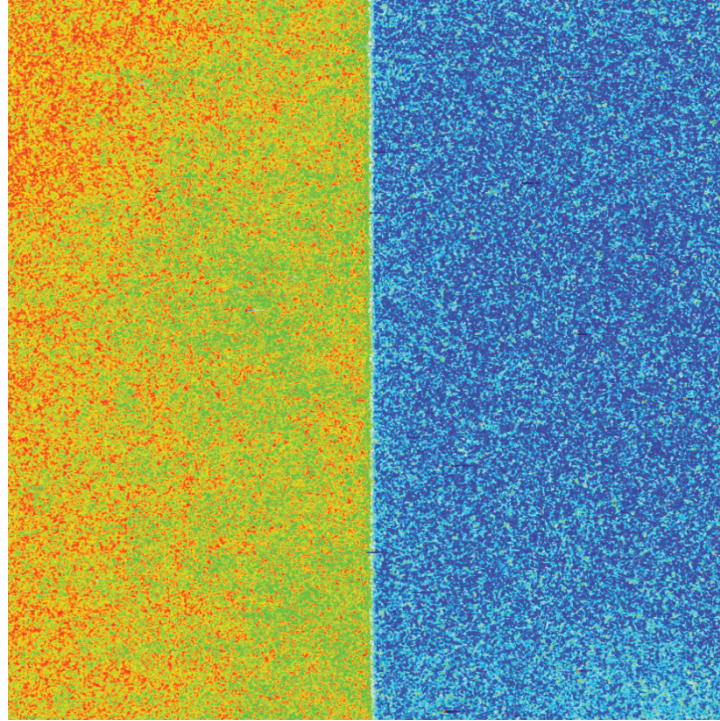


(b)

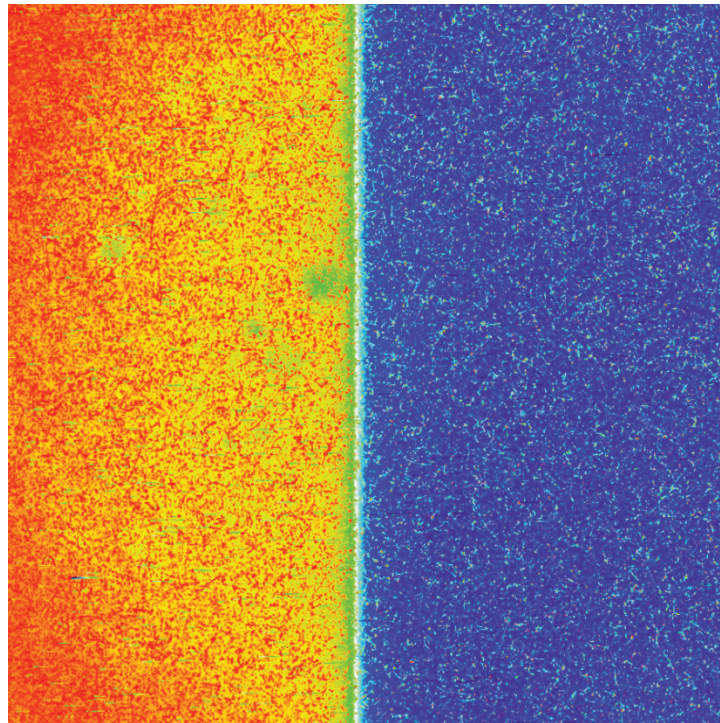


(c)

Figure 3.45. Experimental arrangement to calculate the spatial resolution of the detector R_D , (a)-(b) neutron imaging equipment, and (c) gadolinium edge as an object.



(a)



(b)

Figure 3.46. The neutron radiographs for the calculation of R_D obtained with ${}^6\text{LiF}:\text{ZnS}$ scintillator of thickness (a) 50 μm , and (b) 250 μm (colour representation of grey scale image for enhanced illustration).

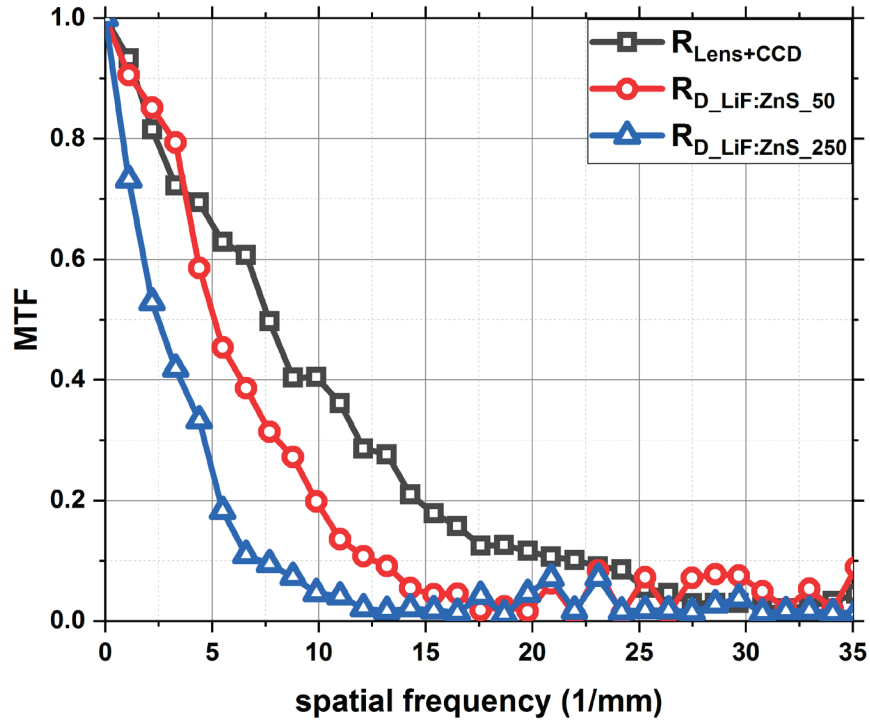


Figure 3.47. Illustration of the Modulation transfer function of the neutron imaging system with 50 μm , 250 μm $^6\text{LiF:ZnS(Ag)}$ thick scintillator screen and Lens- CCD system.

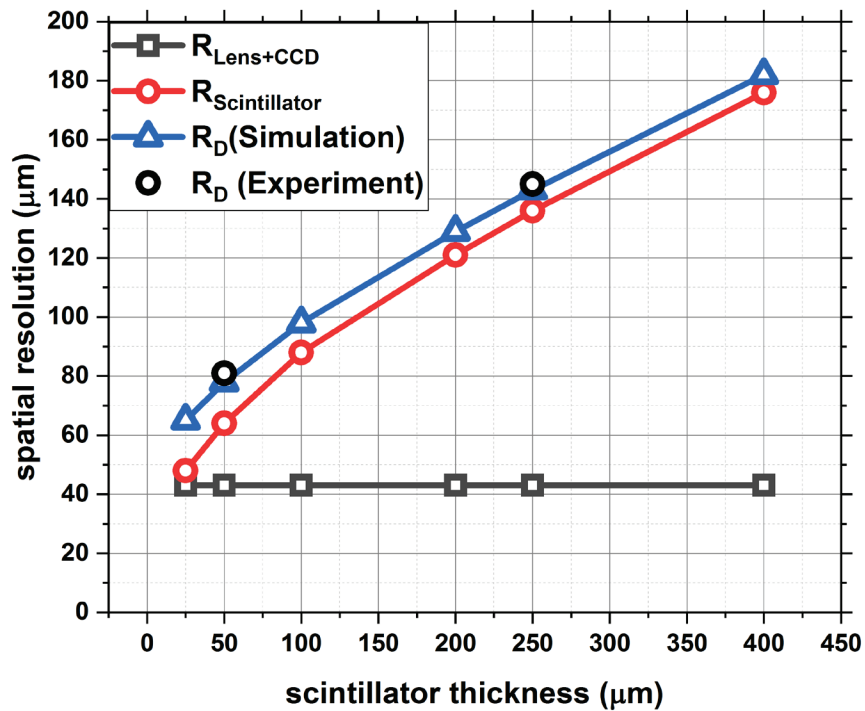


Figure 3.48. Spatial resolution components of the imaging system showing the resolution contribution of lens-CCD, scintillator, total spatial resolution and compared it with the experimental result for 50 μm and 250 μm scintillator.

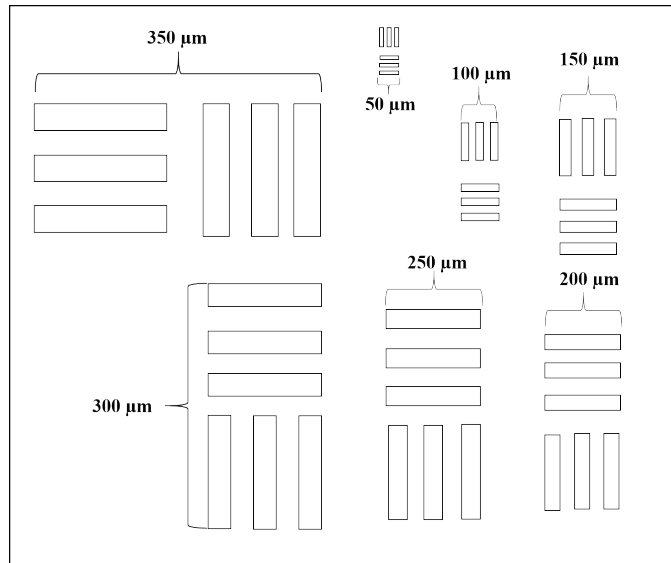


Figure 3.49. Sketch of resolution bar pattern used in the validation of calculated spatial resolution.

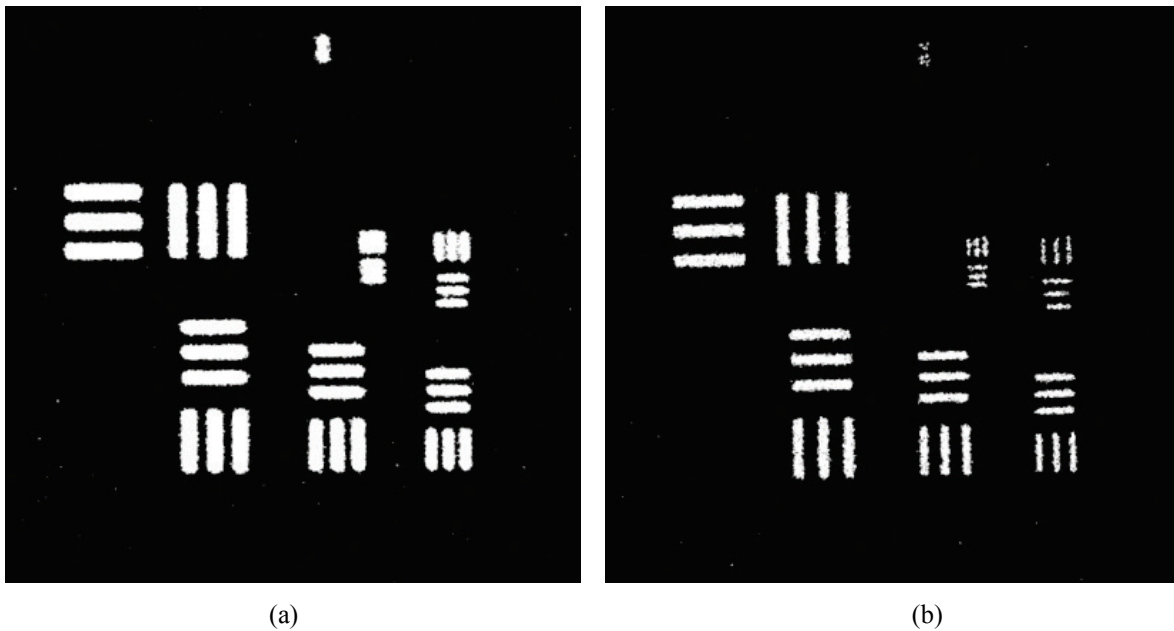


Figure 3.50. Radiograph of the resolution pattern measured with (a) 250 μm , and (b) 50 μm thick scintillator screen validating the spatial resolution qualitatively with the quantitative measurement.

Table 3.10. Spatial resolution comparison of the neutron imaging system

Scintillator thickness (μm)	R_D (μm) (experiment)	R_D (μm) (simulation)
250	145 ± 2	143 ± 1
50	81 ± 2	78 ± 1

Calculated spatial resolution from MTF can be validated by qualitative measurement with the bar radiograph. It can be observed from Figure 3.51, (a) that 100 μm bar is not resolvable and 150 μm bar is just resolvable in the radiograph obtained with 250 μm thick scintillator screen. However, in Figure 3.51, (b) the 100 μm bar pattern is resolvable with the 50 μm thick scintillator screen. This qualitative measurement can be corroborated by the quantitative spatial resolution of $145 \pm 2 \mu\text{m}$ and $81 \pm 2 \mu\text{m}$ for 250 μm and 50 μm scintillator screen.

Thus, it has been observed computationally and experimentally that thinner scintillator screens have a higher spatial resolution. Geant4 simulations revealed that spatial resolution behavior can be correlated with the range of the neutron absorption reaction products. If the range of the products covers scintillator screen thickness then spatial resolution will approach a value on the order of thickness, which motivates the use of thinner screens for imaging. However, use of thin screens will reduce neutron absorption probability and the overall efficiency of signal generation. Consequently, an optimum thickness should be chosen that should be facility dependent. Imaging facilities with high thermal neutron fluxes (and possibly using cold neutrons) can compensate for low detection efficiency and achieve high spatial resolution using thin screens.

Chapter 4 Development and Characterization of Neutron Tomography System

4.1 Introduction

In the previous chapter, we have seen that scintillator-CCD based real-time neutron radiography provides a useful insight of an object at high resolution. Characterization of such high resolution system were performed. However, two dimensional retrieval of three dimensional object in radiographs yields limited information recovery. Computed tomography (CT) is a technique to overcome such limitation where multiple radiographs are obtained and processed to reconstruct and retrieve such information. CT is an extension of the radiography where multiple radiographs or projections are processed to reconstruct the two-dimensional cross-section of an object. The mathematics to obtaining the cross-sectional image is called CT reconstruction. Typically, CT requires projection images to be acquired over 360° of arc acquiring several radiographs at equal angular intervals (see Appendix C).

Original mathematical framework of CT reconstruction was proposed by Radon in 1917 but it was first implemented by Hounsfield with first X-ray scanner at 1972. Since then, CT is evolved and used regularly all over the world for a wide range of non-destructive investigation in medical, science and engineering applications [133]. Apart from transmission CT, other forms of emission CT reconstruction techniques, like Positron Emission Tomography (PET) and Single Photon Emission Computed Tomography (SPECT) can be used to investigate different properties of an object [134]. The CT reconstruction can be performed on the data acquired by non-radiative imaging modalities like optical tomography, electrical impedance tomography and ionospheric tomography [135], [136].

In neutron tomography, neutrons are used for obtaining the radiographs or the projections. In this work, a high-resolution neutron CT imaging system was developed at the PULSTAR neutron imaging facility. The performance was characterized by experiment and multi-physics simulation. Different image reconstruction techniques including analytical and iterative methods were implemented and their performances were characterized. Additionally, an advanced model-based reconstruction technique was developed and implemented to improve the spatial resolution of such a tomography system. In the next section, we will briefly discuss the theory of tomography reconstruction techniques.

4.2 CT Reconstruction Techniques

CT is an advanced imaging technique to find the distribution of attenuation coefficients within the scanned object from the projection data. Typically, CT reconstruction techniques can be divided into three categories as shown in Figure 4.1. The analytical technique uses Fourier slice theorem to obtain a solution to the problem of finding the attenuation coefficients. Unlike analytical methods where projections are filtered and back-projected for the reconstruction, in iterative method, reconstructed image is estimated, compared and modified iteratively [137]. The iterative method can further be classified into algebraic reconstruction technique and statistical reconstruction technique. The algebraic technique can be expressed as an iterative method of solving a system of linear equation whereas, the statistical technique incorporates optimization some likelihood function during the iterative update of the reconstruction process [138], [139]. The assumption of ideal data acquisition settings in traditional approach can be overcome by model-based reconstruction, thus improving the spatial resolution of the reconstructed images.

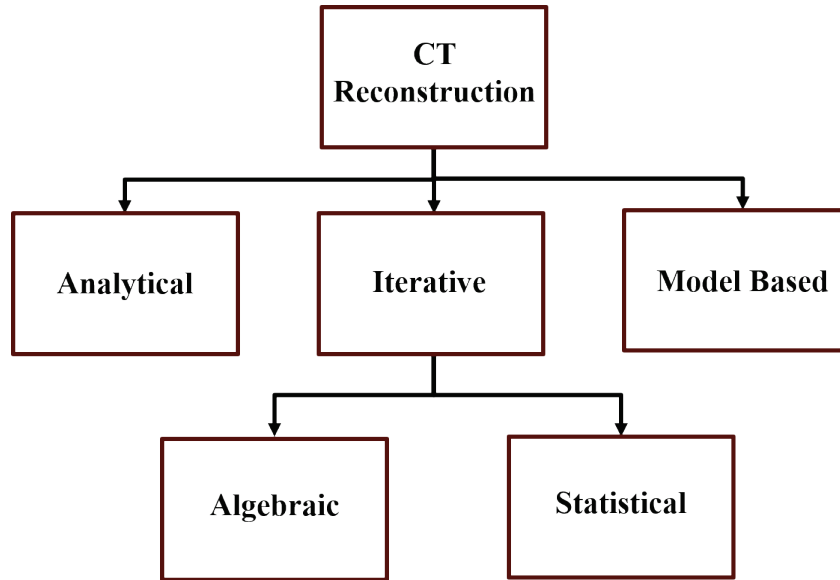


Figure 4.1. Computed tomography reconstruction methods showing analytical, iterative and model-based technique.

4.2.1 Analytical Reconstruction Method

In the analytical reconstruction technique, attenuation function can be related with projection data through analytical mapping. The Fourier slice theorem or central slice theorem is the governing proposition for the analytical reconstruction technique. The theorem states that one dimensional Fourier transformation of a parallel beam projection $f(x, y)$ at a certain angle is the same as the slice through the two dimensional Fourier transformation $F(u, v)$ of the scanned object [137]. Thus, analytical Fourier inversion of the projection data can be used to reconstruct the attenuation coefficient of the object as shown in Figure 4.2. The theorem is discussed in the next section and illustrated in Figure 4.3.

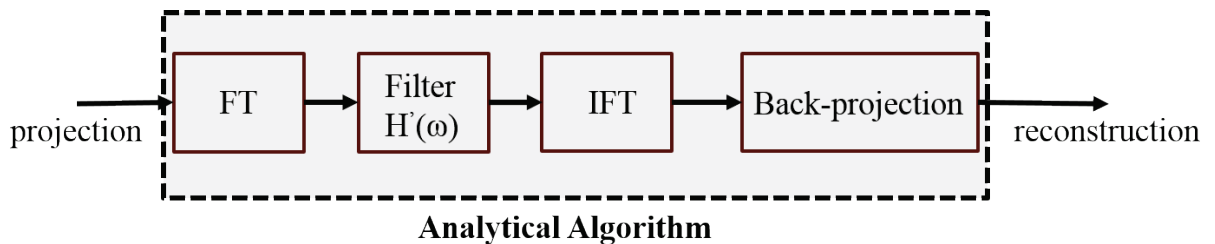


Figure 4.2. Block diagram of analytical CT reconstruction technique showing the direct application of the technique on the projection data for reconstruction.

4.2.1.1 Fourier Slice Theorem:

The Fourier transform of a parallel projection of an object obtained at an angle equals a line in a two-dimensional Fourier transform of the object taken at a same angle.

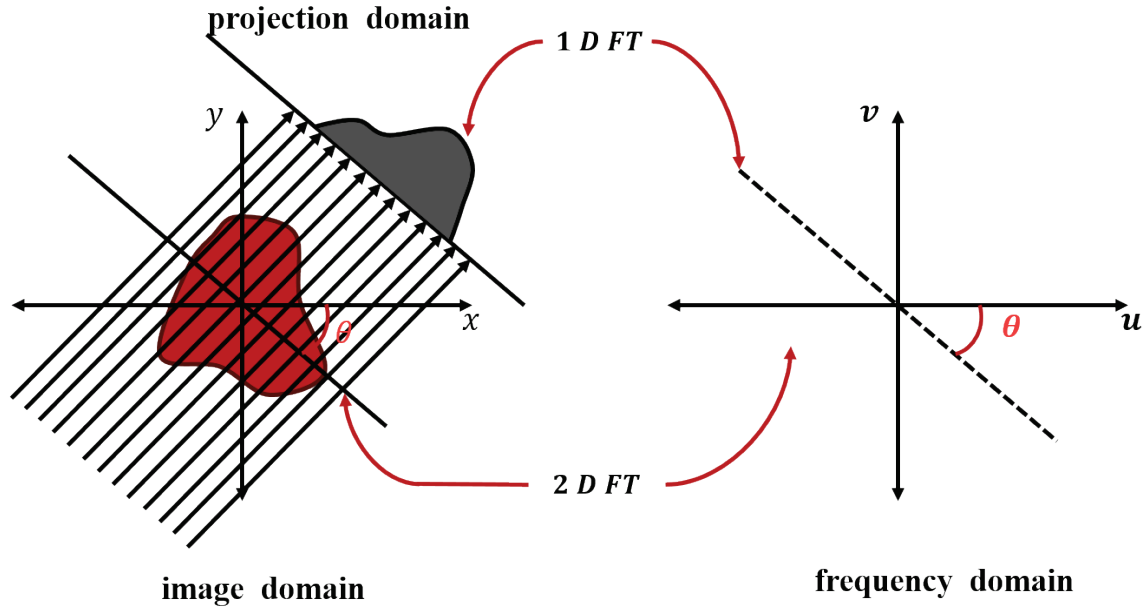


Figure 4.3. Illustration of Fourier Slice Theorem showing 1D Fourier transformation of projection data is equivalent with 2D Fourier transformation of function for the same angle.

The proof of the Fourier slice theorem is straightforward when the projection is taken parallel to y -axis. Projection take at $\theta=0$ can be written as

$$p(x, 0) = \int_{-\infty}^{\infty} f(x, y) dy \quad (4.1)$$

Taking the Fourier transformation with respect to x on both sides,

$$P(u) = \int_{-\infty}^{\infty} p(x, 0) e^{-j2\pi ux} dx \quad (4.2)$$

$$P(u) = \int_{-\infty}^{\infty} \int_{-\infty}^{\infty} f(x, y) e^{-2\pi ux} dx dy \quad (4.3)$$

The 2D Fourier transformation of the original function $f(x,y)$ evaluated at $v=0$:

$$F(u, v)|_{v=0} = \int_{-\infty}^{\infty} \int_{-\infty}^{\infty} f(x, y) e^{-j2\pi(ux+vy)} dx dy|_{v=0} \quad (4.4)$$

$$F(u, v)|_{v=0} = \int_{-\infty}^{\infty} \int_{-\infty}^{\infty} f(x, y) e^{-2\pi ux} dx dy \quad (4.5)$$

$$F(u, v)|_{v=0} = P(u) \quad (4.6)$$

Thus, it can be observed, that the 1D Fourier transform of the parallel projection of an object $f(x, y)$ is a slice in the 2D Fourier transform of the object, when the slice is taken at the same angle as the projection.

Although Fourier slice theorem provides a useful framework for the tomographic reconstruction, it has some limitation to implement directly. The Fourier transformation of the projection for a particular angle is a straight line in the Fourier space. When, we perform the Fourier transformation of multiple angles the Fourier space is shown in Figure 4.4

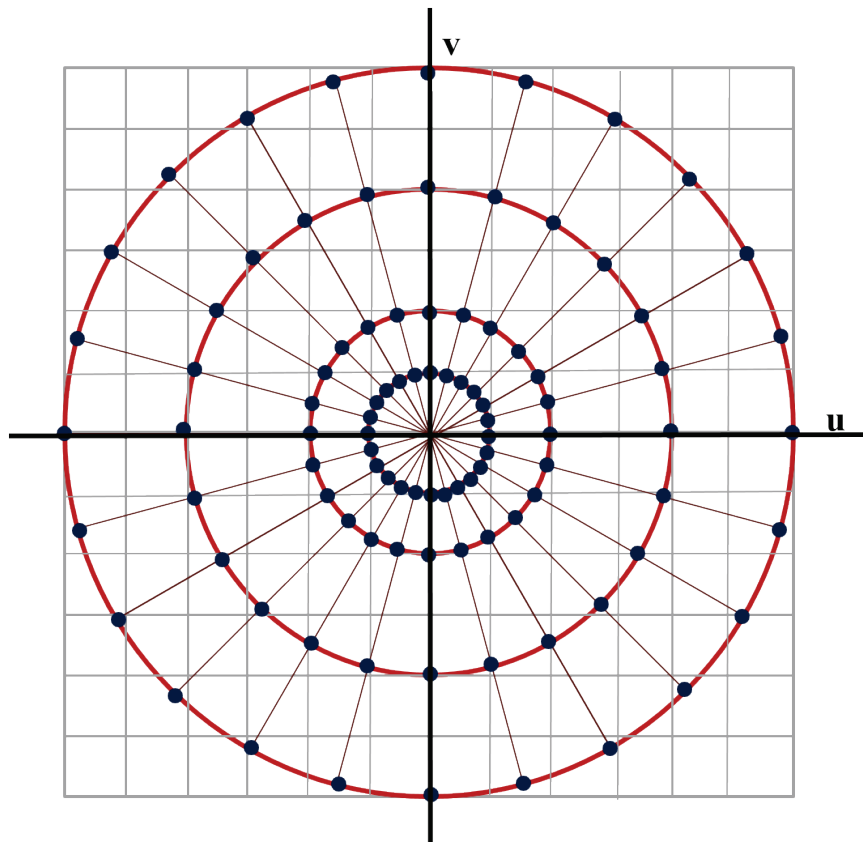


Figure 4.4. Fourier space of multiple projections where each line in the polar coordinate represents the 1D Fourier transformation of projection.

It can be observed that, samples of the projections fall on a polar grid. The tomography reconstruction requires 2D Fourier inversion, which requires a continuum space points. So, interpolation must be performed before the inversion. However, interpolation in the Fourier space

is difficult to perform. In image space, the interpolation error is confined within a localized region. However, an interpolation error in the frequency domain, affect the entire image space.

Targeted reconstruction is difficult to perform with analytical technique. Targeted reconstruction is often required in the clinical CT, where a small portion of the entire image is required for analysis. Direct Fourier approach will require to pad a large number of zeros to perform frequency domain interpolation and the size of the inverse Fourier transformation is inversely proportional to the size of the reconstruction area. Thus, for small reconstruction area, data size will be increased significantly making it difficult to implement.

4.2.1.2 Filtered Back Projection (FBP)

An alternative analytical method eases the problem by multiplying a weighted window near the origin to produce more densely sampled points in Fourier space. The popular analytical method is known as Filtered Back Projection (FBP). The reconstruction method is based on the following analytical formula [137]:

$$f(x, y) = \int_0^\pi \left\{ \int_{-\infty}^{\infty} P(\omega, \theta) |\omega| e^{j2\pi\omega t} d\omega \right\} d\theta \quad (4.7)$$

Here, $P(\omega, \theta)$ is the Fourier transform of the projection at angle θ . The inside integral is the inverse Fourier transform of the quantity $(\omega, \theta)|\omega|$. In spatial domain, it represents a projection filtered by a function whose frequency domain response is $|\omega|$, and is therefore called a “filtered projection”. The two-dimensional (2D) Fourier transformation can be expressed as,

$$f(x, y) = \int_{-\infty}^{\infty} \int_{-\infty}^{\infty} F(u, v) e^{j2\pi(ux+vy)} du dv \quad (4.8)$$

Since, projection data are collected in polar coordinate (ω, θ) , transforming the Cartesian coordinate (u, v) as,

$$u = \omega \cos \theta, v = \omega \sin \theta \quad (4.9)$$

$$du dv = \begin{vmatrix} \partial u / \partial \omega & \partial u / \partial \theta \\ \partial v / \partial \omega & \partial v / \partial \theta \end{vmatrix} = \omega d\omega d\theta \quad (4.10)$$

Substituting these in Eqn. 4.8,

$$f(x, y) = \int_0^{2\pi} d\theta \int_0^{\infty} F(\omega \cos \theta, \omega \sin \theta) e^{j2\pi\omega(x \cos \theta + y \sin \theta)} \omega d\omega \quad (4.11)$$

Using the Fourier slice theorem,

$$f(x, y) = \int_0^{2\pi} d\theta \int_0^{\infty} P(\omega, \theta) e^{j2\pi\omega(x \cos \theta + y \sin \theta)} \omega d\omega \quad (4.12)$$

$$f(x, y) = \int_0^{\pi} d\theta \int_0^{\infty} P(\omega, \theta) e^{j2\pi\omega(x \cos \theta + y \sin \theta)} \omega d\omega + \int_0^{\pi} d\theta \int_0^{\infty} P(\omega, \theta + \pi) e^{-j2\pi\omega(x \cos \theta + y \sin \theta)} \omega d\omega \quad (4.13)$$

Using the symmetry property,

$$P(\omega, \theta + \pi) = P(-\omega, \theta) \quad (4.14)$$

Substituting above relation,

$$f(x, y) = \int_0^{\pi} d\theta \int_0^{\infty} P(\omega, \theta) e^{j2\pi\omega(x \cos \theta + y \sin \theta)} |\omega| d\omega \quad (4.15)$$

If we express the above equation in the rotated coordinate system, we will arrive the following equation,

$$f(x, y) = \int_0^{\pi} \left\{ \int_{-\infty}^{\infty} P(\omega, \theta) |\omega| e^{j2\pi\omega t} d\omega \right\} d\theta \quad (4.16)$$

It can be observed that the inside integral represents a projection filtered by a function whose frequency domain response is $|\omega|$. Outside integral represents the values of the filtered projections are back projected along the straight line. Thus this reconstruction process known as filtered back projection. To ensure aliasing free reconstruction, the number of projection should be roughly the same as the number of rays per projection and can be described as follows [133],

$$\frac{M_{proj}}{N_{ray}} \approx \frac{\pi}{2} \quad (4.17)$$

where, M_{proj} is the number of projection, and N_{ray} is the number of rays per projection. However, reduced number of projection may be sufficient as shown in Appendix C.

It can be observed from Figure 4.4, that the center low frequency region is densely sampled whereas outer regions are under-represented. A ramp filter acts as a weight function which compensates the sparsely sampled high frequency region with raised weight as compared with the centralized low frequency region. The frequency domain representation of the ramp filter is shown in Figure 4.5.

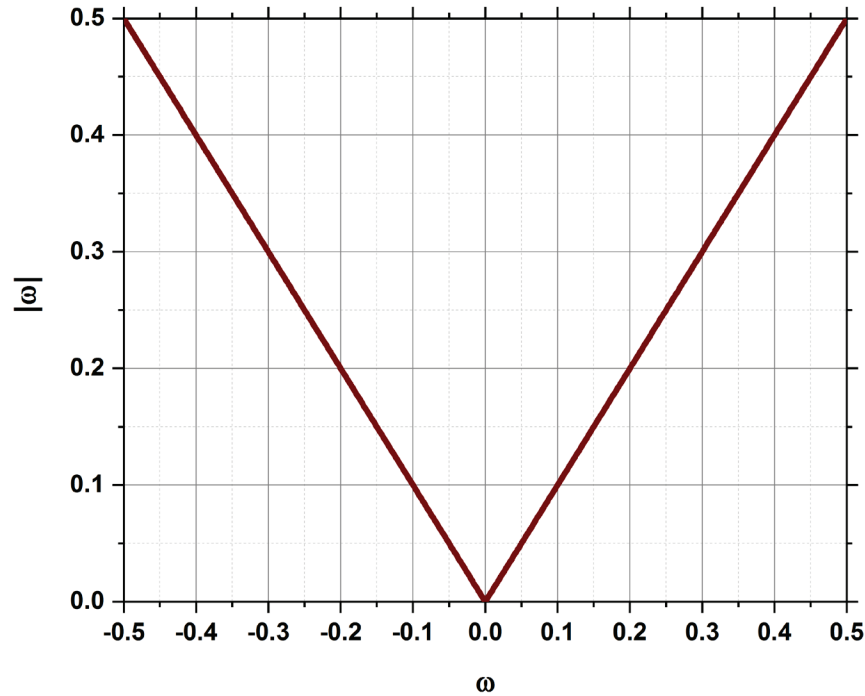


Figure 4.5. Frequency domain representation of a band-limited ramp filter showing the linear increase in the weight as the spatial frequency increases.

An application of ramp filter compensates for artificially enhanced center region at low frequency and underrepresented outer region in high frequency domain. Since, a ramp filter also enhances high frequency noise, low pass smoothing filter is often used with the ramp filter to improve reconstruction. Effective filter response function can be represented as the following equation.

$$H(\omega) = |\omega|F(\omega) \quad (4.18)$$

In this work, Hanning, Hamming, Cosine and Shepp-Logan filters were implemented to investigate the performance of the FBP reconstruction algorithm. The filter functions for Hanning,

Hamming, Cosine, and Shepp-Logan filters are described below [133]. The response function of these filters and $H(\omega)$ are shown in Figure 4.6 and Figure 4.7 respectively.

Hanning Filter:

$$F(\omega) = \begin{cases} 0.50 + 0.50 \cos\left(\frac{\pi\omega}{\omega_c}\right), & 0 \leq |\omega| \leq \omega_c \\ 0, & \textit{otherwise} \end{cases} \quad (4.19)$$

Hamming Filter

$$F(\omega) = \begin{cases} 0.54 + 0.46 \cos\left(\frac{\pi\omega}{\omega_c}\right), & 0 \leq |\omega| \leq \omega_c \\ 0, & \textit{otherwise} \end{cases} \quad (4.20)$$

Cosine Filter

$$F(\omega) = \begin{cases} \cos\left(\frac{\pi\omega}{2\omega_c}\right), & 0 \leq |\omega| \leq \omega_c \\ 0, & \textit{otherwise} \end{cases} \quad (4.21)$$

Shepp-Logan Filter

$$F(\omega) = \begin{cases} \frac{1}{\pi\omega/\omega_c} \sin\left(\frac{\pi\omega}{\omega_c}\right), & 0 \leq |\omega| \leq \omega_c \\ 0, & \textit{otherwise} \end{cases} \quad (4.22)$$

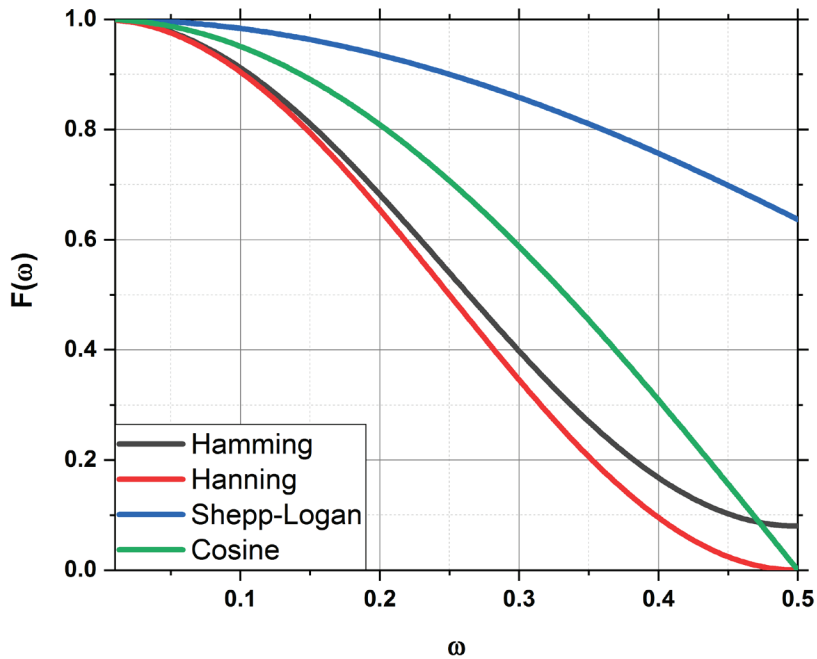


Figure 4.6. Frequency response function of the low pass filter used in filtered back projection Shepp-Logan, Hamming, Hann, Cosine.

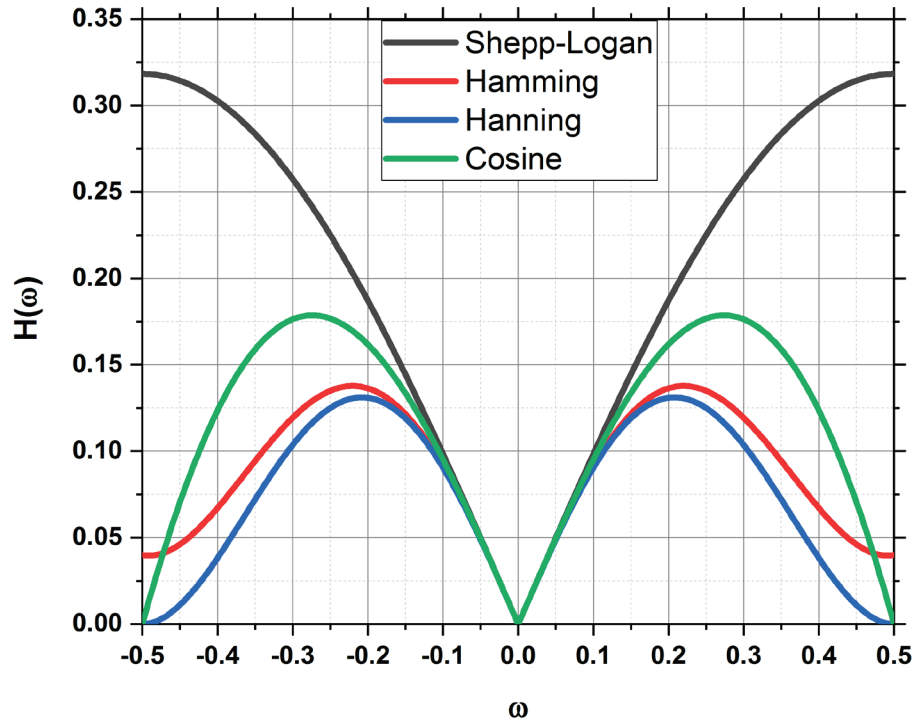


Figure 4.7. Frequency response function of the filtered back projection filters showing the different weight as the spatial frequency increases.

4.2.2 Iterative Reconstruction Method

An analytical method such as FBP assumes continuum and ideal data acquisition process. However, in real world this assumption may not be possible to achieve, thus limiting the applicability of such techniques. In algebraic approach, object's attenuation coefficients are modeled by a discrete representation of the object function $f(x, y)$, typically on a pixel grid. Additionally, assumption of analytical method further results streaking artifacts, noisy reconstruction. In iterative method, reconstructed image is estimated, compared and modified iteratively [140]. In certain circumstances, iterative reconstruction method is only viable option as few projection are available for reconstruction, where analytical method is not applicable. Unlike analytical methods where projections are filtered and back projected, iterative methods converges to solutions on iterative fashion where initial image is refined and modified iteratively until stopping criteria has been reached as shown in Figure 4.8.

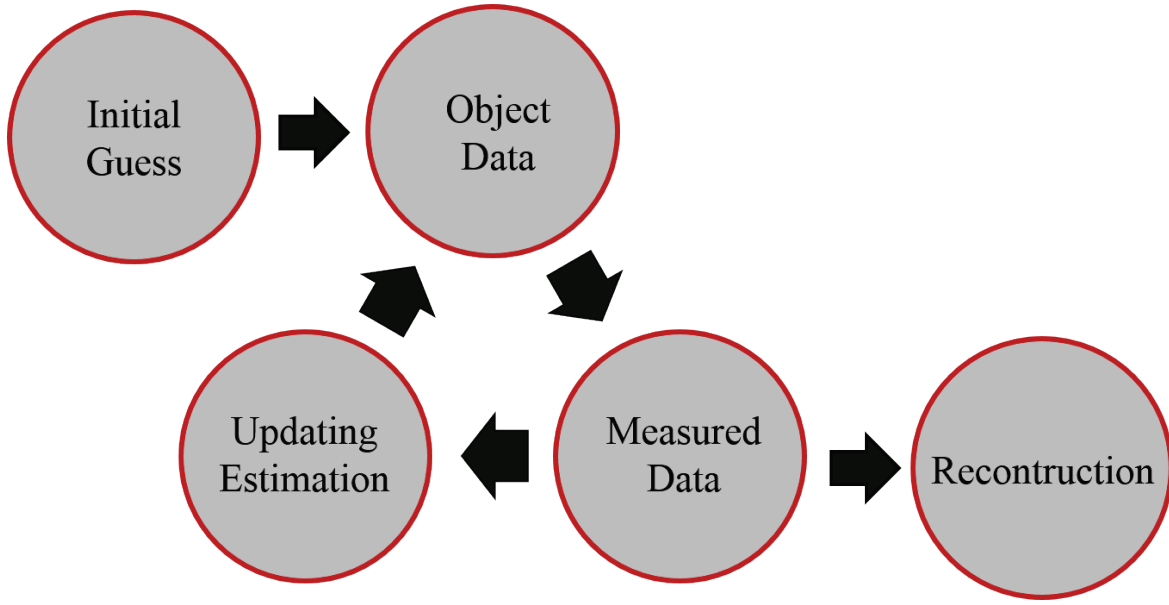


Figure 4.8. Workflow of iterative CT reconstruction technique showing the iterative update scheme between the measured projection and calculated forward projection data.

Iterative reconstruction technique can be classified into algebraic and statistical reconstruction technique. Typically, algebraic technique solves a system of linear equation to minimize projection distance for some norm, whereas statistical methods incorporate underlying physics and solve to minimize some likelihood function. The pixel grid within reconstructed object is assumed to have a constant attenuation value. Assuming pixel grid consists of N pixels, the objective function $f(x, y)$ can be approximated as,

$$f(x, y) \sim \sum_{j=1}^N x_j \phi_j \quad (4.23)$$

Where ϕ_j is the pixel basis function. Since an object is modelled by a finite number of attenuation values, it can be represented with a column vector $\mathbf{x} = (x_j) \in \mathbb{R}^N$.

4.2.2.1. Algebraic Reconstruction Technique

The law of Beer-Lambert relates attenuation of a passing particle to the properties of a material through which it is propagating. The law states that a monochromatic ray with intensity I_0 that propagates a distance w through a material with attenuation coefficient μ has remaining intensity

I as it passes through the material. It is illustrated in Figure 4.9. and can be expressed by following equations.

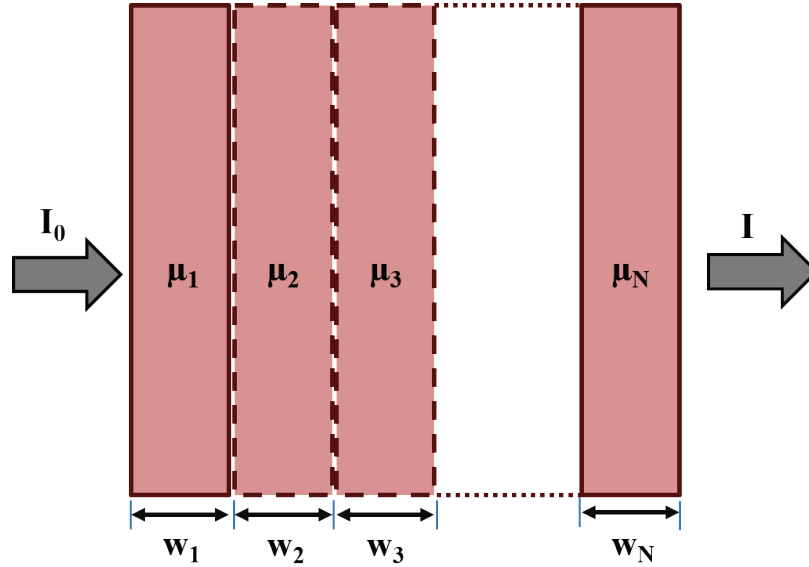


Figure 4.9. Illustration of Beer-Lambert attenuation law illustrating the reduction in neutron flux as it travels through materials of different attenuation coefficients.

$$I(x) = I_0 e^{-\mu_1 w_1} e^{-\mu_2 w_2} e^{-\mu_3 w_3} \dots e^{-\mu_n w_n} \quad (4.24)$$

$$I(x) = I_0 e^{-\sum_{n=1}^N \mu_n w_n} \quad (4.25)$$

$$p = -\ln\left(\frac{I(x)}{I_0}\right) = \sum_{n=1}^N \mu_n w_n \quad (4.26)$$

Where, μ_n is attenuation coefficient of n -th material, w_n is the width of the n -th material and p is a projection value. The objective of the tomographic reconstruction is to calculate a distribution of attenuation coefficients μ from the measured projections p . It is not possible to calculate a one dimensional data acquisition geometry as illustrated in Figure 4.9 as there is one measurement for the projection and n unknown. However, one dimensional data acquisition model can be extended to two dimension where multiple projection data can be obtained as illustrated in Figure 4.10. The equation 4.26 can be extended for two dimensional geometry as,

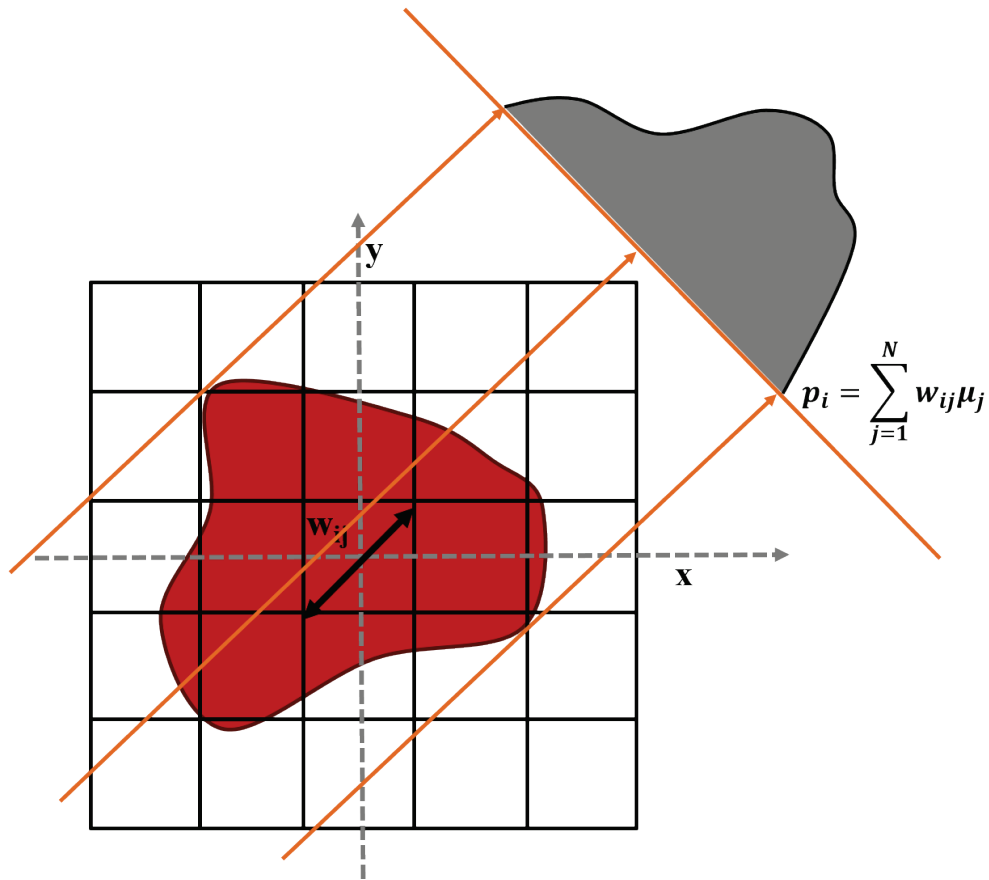


Figure 4.10. Illustration of data acquisition geometry for computed tomography showing the formation of projection data.

$$w_{11}\mu_1 + w_{12}\mu_2 + w_{13}\mu_3 + \dots + w_{1N}\mu_N = p_1$$

$$w_{21}\mu_1 + w_{22}\mu_2 + w_{23}\mu_3 + \dots + w_{2N}\mu_N = p_2$$

$$w_{31}\mu_1 + w_{32}\mu_2 + w_{33}\mu_3 + \dots + w_{3N}\mu_N = p_3$$

.
.
.

$$w_{M1}\mu_1 + w_{M2}\mu_2 + w_{M3}\mu_3 + \dots + w_{MN}\mu_N = p_M \tag{4.27}$$

Where, M is the total number of projections, N is the total number of pixel and $w_{i,j}$ represents the weight of the j^{th} pixel for the i^{th} ray. The forward projection model can be approximated by $p_i \approx \sum_{j=1}^N w_{ij}\mu_j$, where, w_{ij} represents the contribution of pixel j to the projection value with index i .

A precise calculation of weight function involves a strip kernel, where the weight w_{ij} is equal to the fractional area of the j^{th} pixel intercepted by i^{th} ray as shown in Figure 4.11.

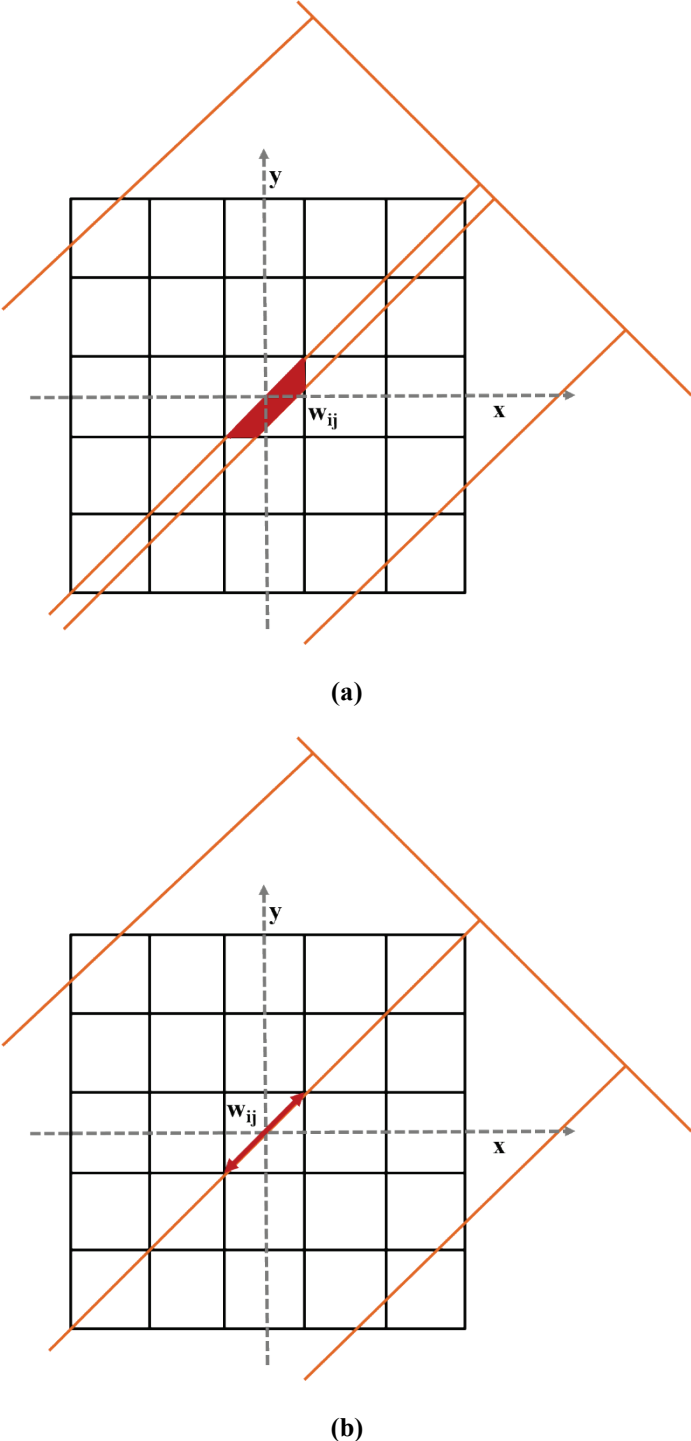


Figure 4.11. Kernel used for calculating forward projection during each iteration of the reconstruction, (a) strip kernel, and (b) line kernel.

A line-kernel is a computationally faster approximation, where the weight w_{ij} equals the ray-intersection length of the i^{th} ray with j^{th} pixel, or by a linear kernel. An intersection length is calculated linearly interpolating between the two nearest pixels of the intersection of the ray and the row column. Linear kernel is also known as Joseph's method [141]. Direct solution to determine attenuation coefficients is not feasible as inversion \mathbf{W} is impossible as \mathbf{W} is large, sparse and ill posed. The algebraic methods typically try to minimize the projection distance $\|\mathbf{W}\mathbf{x} - \mathbf{p}\|$. Iteration may be terminated if certain convergence condition has been encountered. The reconstruction process can be summarized as follows:

- Create an initial image array with N elements parameterized j . Usually the initial guess can be FBP reconstruction or zero.
- Calculate weight matrix W_{ij}
- Calculation of forward projections $p_i = \sum_{j=1}^N w_{ij}\mu_j$
- For each ray i , calculate the difference between the original projection p and estimated projection p_i
- Updating the estimation. Based upon the reconstruction algorithm the update will be unique.
- Check the criteria for convergence.

The estimation can be updated after each pixel per projection, after each projection or after all of the projections as shown in the following equations [133].

- ART (Algebraic Reconstruction Method) [142]

$$\mu_j^{(k+1)} = \mu_j^{(k)} + w_{ij} \frac{(p_i - \sum_{h=1}^N w_{ih}\mu_h^{(k)})}{\sum_{j=1}^N w_{ij}^2} \quad (4.28)$$

- SART (Simultaneous Algebraic Reconstruction Method) [143]

$$\mu_j^{(k+1)} = \mu_j^{(k)} + \frac{1}{\sum_{i \in I_\theta} w_{ij}} \sum_{i \in I_\theta} \left(\frac{w_{ij} (p_i - \sum_{h=1}^N w_{ih} \mu_h^{(k)})}{\sum_{h=1}^N w_{ih}} \right) \quad (4.29)$$

- SIRT (Simultaneous Iterative Reconstruction Method) [144]

In this technique, correction term is similar to SART. However, iteration is updated after calculation of full forward projections. It can be expressed as,

$$\mu_j^{(k+1)} = \mu_j^{(k)} + \frac{\lambda}{\sum_{i=1}^M w_{ij}} \sum_{i=1}^M \left(\frac{w_{ij} (p_i - \sum_{h=1}^N w_{ih} \mu_h^{(k)})}{\sum_{h=1}^N w_{ih}} \right) \quad (4.30)$$

Where, λ is the regularization parameter. Apart from an additive update scheme, multiplicative correction are also used in the algebraic technique [145]. A variant of SIRT is known as Conjugate Gradient Least Square (CGLS) technique, where L2 norm is minimized between the actual projection and calculated one [146]. It can be expressed as,

$$\mu(x, y) = \operatorname{argmin}_{\mu(x, y)} (\|W\mu - p\|_{norm L2}^2) \quad (4.31)$$

Additionally, regularization methods along with the prior knowledge can be used for faster convergence and better reconstruction, where minimization problem can be expressed as,

$$\mu(x, y) = \operatorname{argmin}_{\mu(x, y)} (\|Wx - p\|_{norm L2}^2) + \lambda\psi(x, y) \quad (4.32)$$

Where, $\psi(x, y)$ is the prior knowledge about the reconstructed object [139].

4.2.3 Statistical Reconstruction Method

The statistical nature of the data acquisition process can be incorporated into the statistical reconstruction process. The number of photons counted by the scintillator-CCD detector is assumed to be an independent process. Data acquisition process of a single detector pixel can be modeled by a Poisson distribution as shown as,

$$P(I_i | I_i^*) = \frac{(I_i^*)^{I_i}}{I_i!} e^{-I_i^*} \quad (4.33)$$

where, I_i and I_i^* is the measured and expected photon at i^{th} detector pulse, and $P(I_i|I_i^*)$ represents the probability of measuring I_i at the given expectation of I_i^* [147]. Overall process for M detector pixel can be expressed as,

$$P(\mathbf{I}|\mathbf{I}^*) = \prod_{i=1}^M \frac{(I_i^*)^{I_i}}{I_i!} e^{-I_i^*} \quad (4.34)$$

4.2.3.1 Expectation Maximization Reconstruction

In expectation maximization (EM) algorithm, the objective is to maximize the likelihood of acquiring the observed data while varying the expectation values of attenuation coefficients of a object [148]. Substituting the Beer-Lambert formula into equation 4.33,

$$P(\mathbf{I}|\boldsymbol{\mu}^*) = \prod_{i=1}^M \frac{\left(I_0 e^{-\sum_{j=1}^N w_{ij}\mu_j^*}\right)^{I_i}}{I_i!} e^{-I_0 e^{-\sum_{j=1}^N w_{ij}\mu_j^*}} \quad (4.35)$$

Defining a log-likelihood function $l(\boldsymbol{\mu}^*)$, by taking natural logarithm $P(\mathbf{I}|\boldsymbol{\mu}^*)$ of we get,

$$l(\boldsymbol{\mu}^*) = \ln(P(\mathbf{I}|\boldsymbol{\mu}^*)) = \sum_{i=1}^M \left[I_i \ln(I_0) - I_i \sum_{j=1}^N w_{ij}\mu_j^* - I_0 e^{-\sum_{j=1}^N w_{ij}\mu_j^*} - I_i \ln(I_i!) \right] \quad (4.36)$$

The reconstruction is performed by solving the following optimization problem,

$$\boldsymbol{\mu}^* = \arg \max(l(\boldsymbol{\mu}^*)) \quad (4.37)$$

The global maximum of the log-likelihood function exists due to concavity, thus Karush-Kuhn-Tucker (KKT) condition can be applied [149]. Using the dual feasibility and complementary slackness condition, we get

$$\mu^* = \mu^* \frac{\sum_{i=1}^M w_{ik} e^{-\sum_{j=1}^N w_{ij}\mu_j^*}}{\sum_{i=1}^M w_{ik} e^{-p_i}} \quad (4.38)$$

Where, $i = 1, \dots, N$ and $p_i = -\ln\left(\frac{I_i}{I_0}\right)$. For a fixed point iteration scheme, the EM algorithm can be expressed as,

$$\mu^{(n+1)} = \mu^n \frac{\sum_{i=1}^M w_{ik} e^{-\sum_{j=1}^N w_{ij}\mu_j^n}}{\sum_{i=1}^M w_{ik} e^{-p_i}} \quad (4.39)$$

Usually, direct implementation of EM often results numerically unstable solution. Thus, the regularization technique is used to stabilize the solution. Maximum a posteriori (MAP) reconstruction is one such technique.

4.2.4 Model-Based Reconstruction Method

As discussed earlier traditional CT reconstruction techniques such as analytical and iterative techniques are unable to consider actual data acquisition settings, resulting in spatial resolution loss in reconstructed images. In model-based reconstruction technique, an accurate data acquisition model can be incorporated. There has been an interest to improve the reconstruction quality by reducing the artifacts by pre or post processing or developing a staged reconstruction process to de-blur the projection data before reconstruction [150], [151]. The workflow of the model based CT reconstruction technique is shown in Figure 4.12.

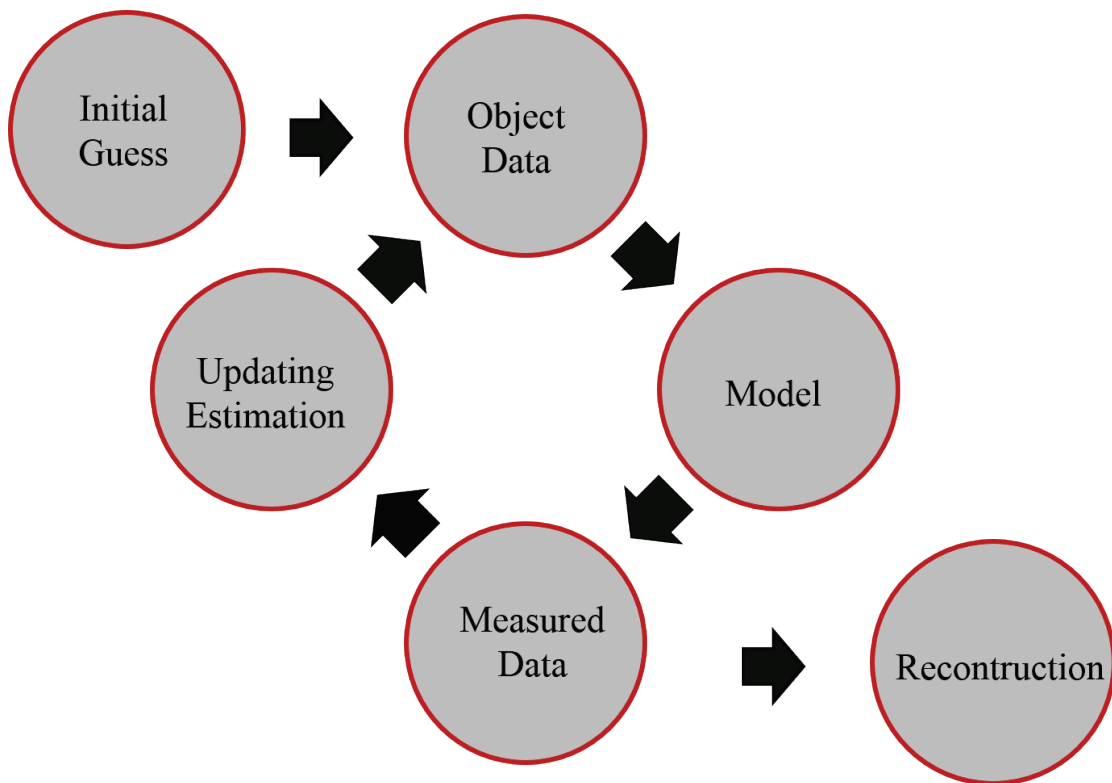


Figure 4.12. Workflow of model-based CT reconstruction technique showing the iterative update scheme between the measured projection and calculated forward projection data.

In this work, a model-based reconstruction technique was developed by including the system response function in the reconstruction process. The system response function is modeled as the point spread function (PSF) of the neutron imaging system. The PSF is included in the forward projection step of the iterative reconstruction process. Simplified CT data acquisition model can be represented as,

$$p = W\mu \quad (4.40)$$

where, p is log transformed data, W is the forward projection operator, μ is the unknown attenuation coefficients to be reconstructed. A direct solution of computing μ might be infeasible because of the ill-posed nature of the problem. An iterative method, perform the solution by calculating a forward projection with $W\mu$ and update the current solution by comparing with the actual projection. However, calculated forward projection, actually represents the projection data obtained with idealized data acquisition settings as represented by Figure 4.13.

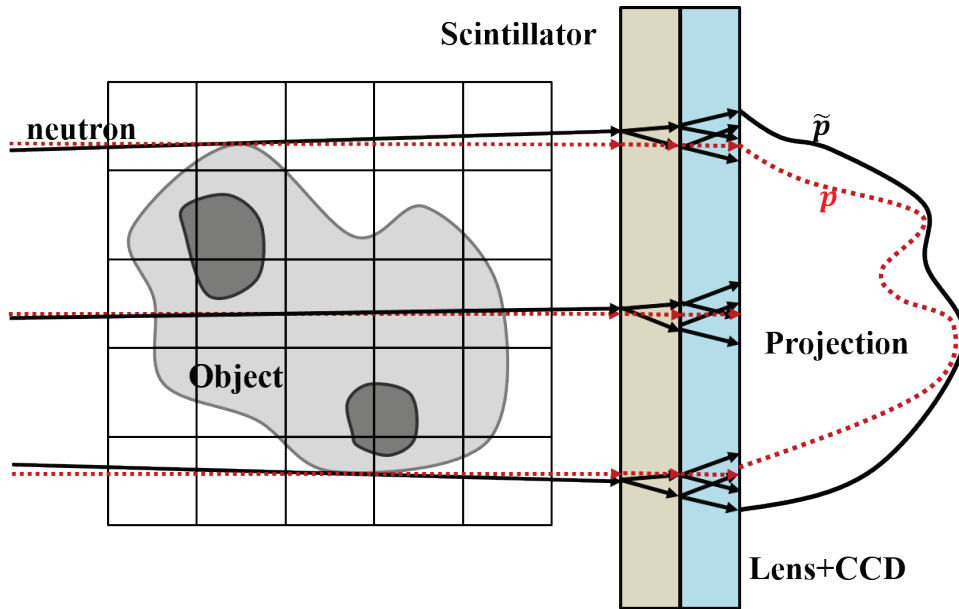


Figure 4.13. Illustration of the object detector model used for a neutron CT system showing the ideal and actual data acquisition geometry for neutron tomography.

The actual data acquisition model can be represented as,

$$\tilde{p} = Hp = HW\mu \quad (4.41)$$

where, H is the system response function and \tilde{p} is the actual projection.

A simultaneous iterative reconstruction technique (SIRT) iteration scheme was adapted for the solution, which converges towards a least square solution [144]. It expressed as,

$$\mu^* = \arg \min \|HW\mu - \tilde{p}\|_R^2. \quad (4.42)$$

Preconditioning the equation with $CA^T R$,

$$CA^T RHW\mu = CA^T R\tilde{p}, \quad (4.43)$$

where, R and C are the inverse row sum and the column sum of the system matrix A . Using, matrix splitting,

$$I - (I - CA^T RW\mu) = CA^T R\tilde{p}. \quad (4.44)$$

Re-arranging the term the iterative update scheme can be expressed as,

$$\mu^{(k+1)} = \mu^k + CA^T R(\tilde{p} - HW\mu^k). \quad (4.45)$$

The system response function, H was convolved with the calculated projection $W\mu$ and compared with actual projection \tilde{p} . Difference was weighted with $CA^T R$ and added with the estimated μ for k^{th} iteration.. The model based technique is shown in Figure 4.14 and the regular SIRT is illustrated in Figure 4.15.

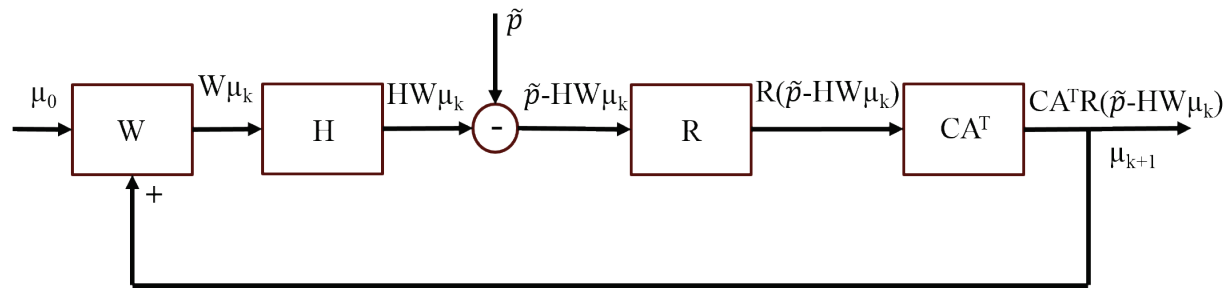


Figure 4.14. Workflow of model-based reconstruction method showing the inclusion of the system response function within the iterative reconstruction technique.

One dimensional system response function, H was convolved with each view of the calculated projection $W\mu$ and compared with the actual projection \tilde{p} . The system response function is illustrated in Figure 4.16. The difference was weighted with $CA^T R$ and added with the estimated

μ for k^{th} iteration. By convolving the projection data with system response of an imaging system, calculated projection provides a better estimate of the actual projections, thus improving the spatial resolution of the reconstructed images. The iteration is stopped when residual 2-norm is smaller than the tolerance ε or a maximum number of iteration is reached. We have selected the value of ε as 8×10^{-4} and 400 as maximum iteration value. The pseudocode of the model based technique and traditional SIRT is illustrated in Table 4.1. and Table 4.2. It can be observed that the model based technique is equivalent to regular SIRT when the system response function is delta function.

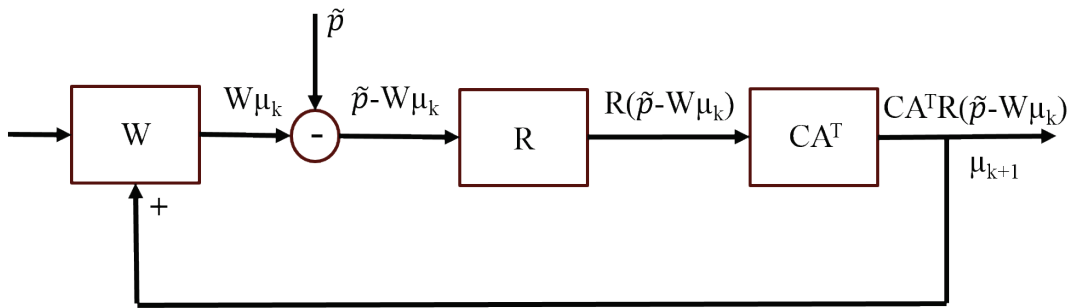


Figure 4.15. Workflow of regular simultaneous iterative reconstruction technique (SIRT) for computed tomography reconstruction.

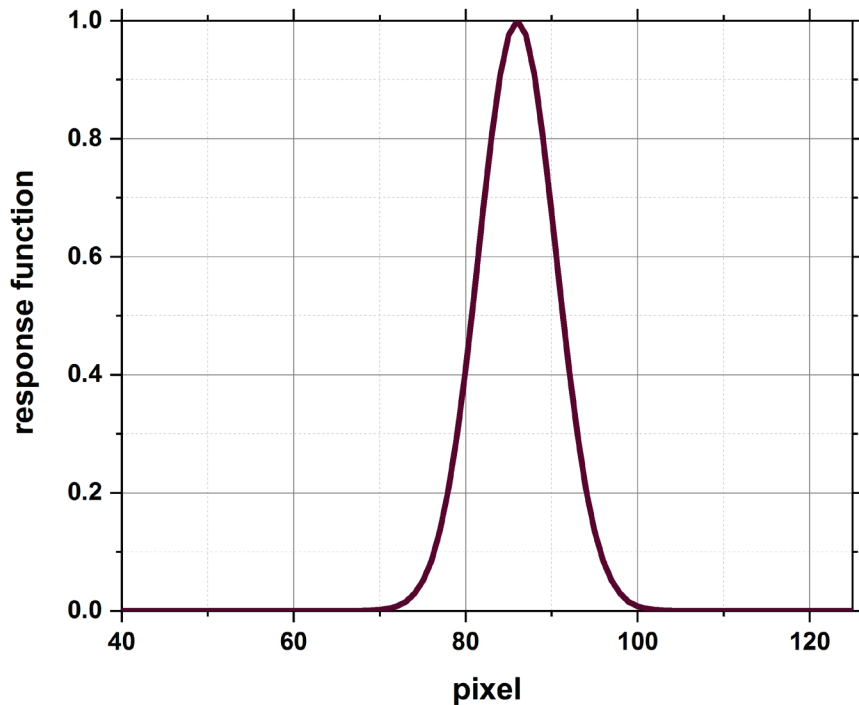


Figure 4.16. Illustration of system response function used for the model-based computed tomography reconstruction.

Table 4.1. Pseudo-code for the model-based reconstruction algorithm

```

1: initialize  $H$ ,  $\varepsilon$ , view, iteration
2:  $x^0 \leftarrow$  initial value set as zero
3: for  $k = 1, \dots$  # iteration
4:   do
5:      $T \leftarrow Ax$ 
6:     for  $i = 1, \dots$  # view
7:        $T \leftarrow 1D \text{ convolution}[T(:, \text{view}), H]$ 
8:     end for
9:      $x^{k+1} \leftarrow x^k + CA^T R(\tilde{p} - T)$ 
10:  end do
11:  if  $\|x^{k+1} - x^k\| \leq \varepsilon$ 
12:    break loop;
13:  end if
14: end for

```

Table 4.2. Pseudo-code for the regular SIRT

```

1: initialize  $\varepsilon$ , view, iteration
2:  $x^0 \leftarrow$  initial value set as zero
3: for  $k = 1, \dots$  # iteration
4:   do
5:      $T \leftarrow Ax$ 
6:     for  $i = 1, \dots$  # view
7:        $x^{k+1} \leftarrow x^k + CA^T R(\tilde{p} - T)$ 
8:     end for
9:   end do
10:  if  $\|x^{k+1} - x^k\| \leq \varepsilon$ 
11:    break loop;
12:  end if
13: end for

```

4.3 Implementation of CT Reconstruction

In all the iterative reconstruction algorithm, calculation of system matrix \mathbf{W} is essential for computation of the forward projection. However, implementation impose major computational and memory demands as system matrix is difficult to store beforehand because of large memory

requirement and mostly computed on the fly. Size of the system matrix increases with grid size of tomographic reconstruction. Memory requirements of such matrixes are illustrated in Figure 4.17.

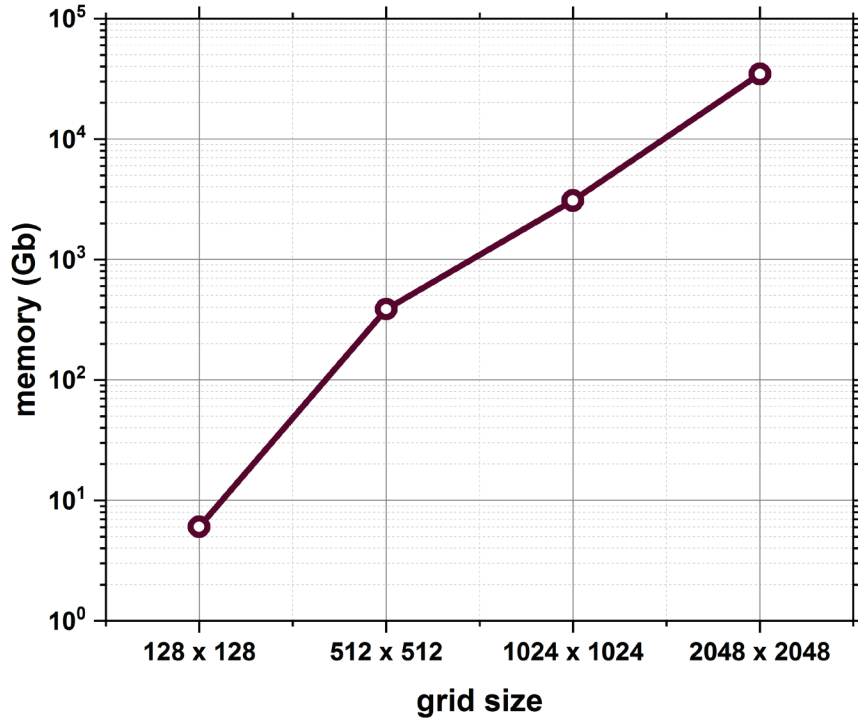


Figure 4.17. Memory requirements of the system matrix with different grid size for iterative CT reconstruction.

In this work, we have used ASTRA tomography toolbox for the implementation of the algorithm [152]. The toolbox uses spot mathematical operators, which are optimized for the faster and efficient calculation in the MATLAB framework [153]. Forward and backward projection operations were implemented and accelerated with multi core processor of graphical processing unit (GPU) for faster reconstruction. The simulations are performed on a Linux cluster available in the high-performance computing (HPC) center at NCSU and the tomographic reconstruction was performed in MATLAB. A work station was configured with 24 cores of Intel Xenon CPU E5-2643, 64 Gb of random access memory (RAM) and NVIDIA Quadro M4000 GPU unit for processing and reconstruction of tomographic data.

4.4 Calculation of Spatial Resolution of CT Reconstruction

Similar to the radiographs, spatial resolution in CT reconstructed images is defined as closest distinguishable points in the plane of interest. Spatial resolution is defined as the closest distinguishable points in the plane of interest. For measurement of spatial resolution in tomography, profiles are plotted through the center of the reconstructed cylinder slice of R-phantom to obtain the edge spread function (ESF). Line spread function (LSF) is obtained by differentiating the ESF. Fast Fourier Transform of LSF was performed to calculate the modulation transfer function (MTF) and the spatial resolution is calculated at 10% of the MTF value. This process is illustrated in Figure 4.18.

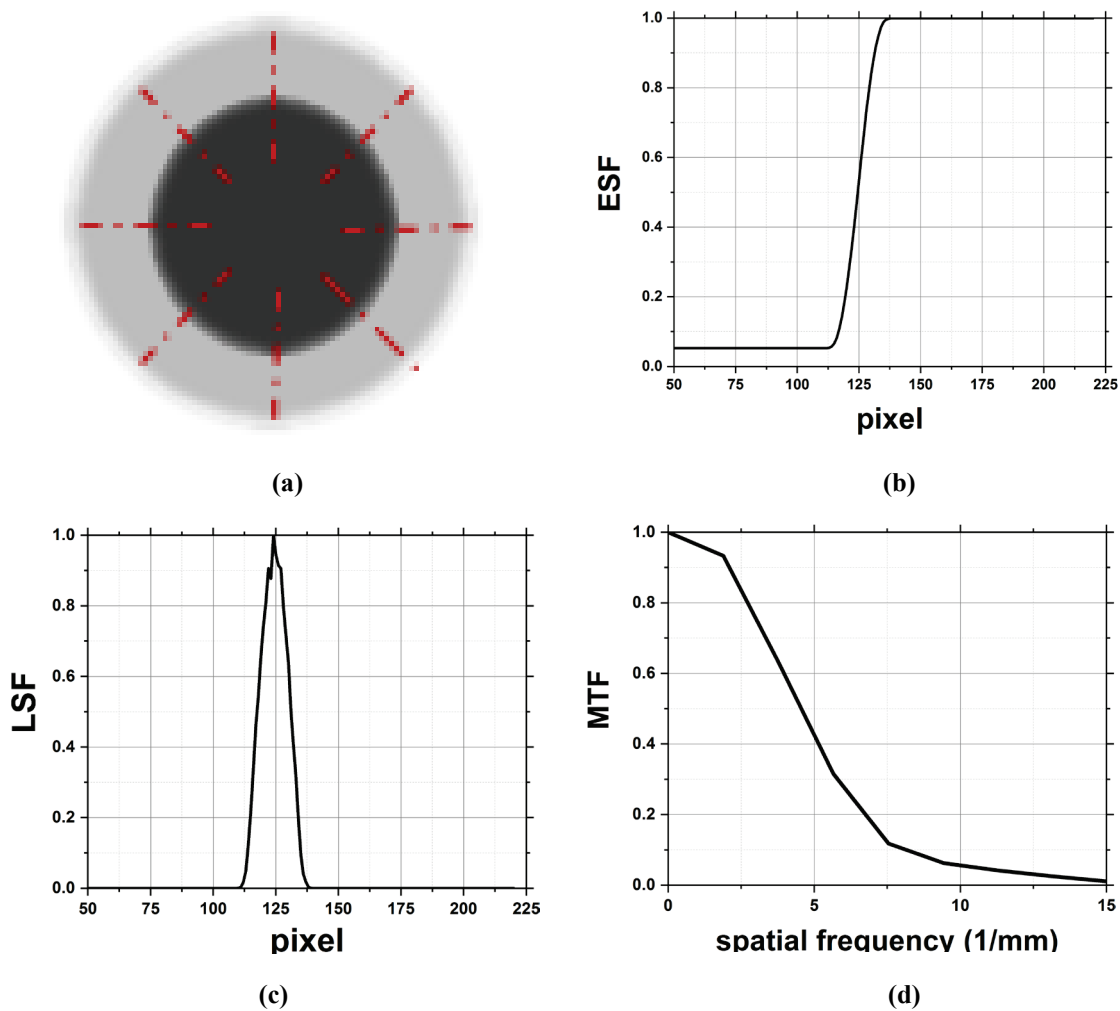


Figure 4.18. Calculation process of the spatial resolution from the reconstructed images of R-phantom (a) Reconstructed image, (b) ESF, and (c) LSF.

4.5 Phantom Design for CT Performance Evaluation

A phantom design is an important aspect of measuring performance of a CT system. Materials and dimensions of phantoms have been selected to eliminate the beam hardening effect and the needed correction that affects the spatial resolution of the reconstructed object. Two types of phantom are designed to evaluate the performance. First one is a resolution phantom (R-phantom) to quantify the performance of CT reconstruction method and second one is a validation phantom (V-phantom) to validate results with measurements with R phantom. Phantoms are illustrated in Figure 4.19 and Figure 4.20.

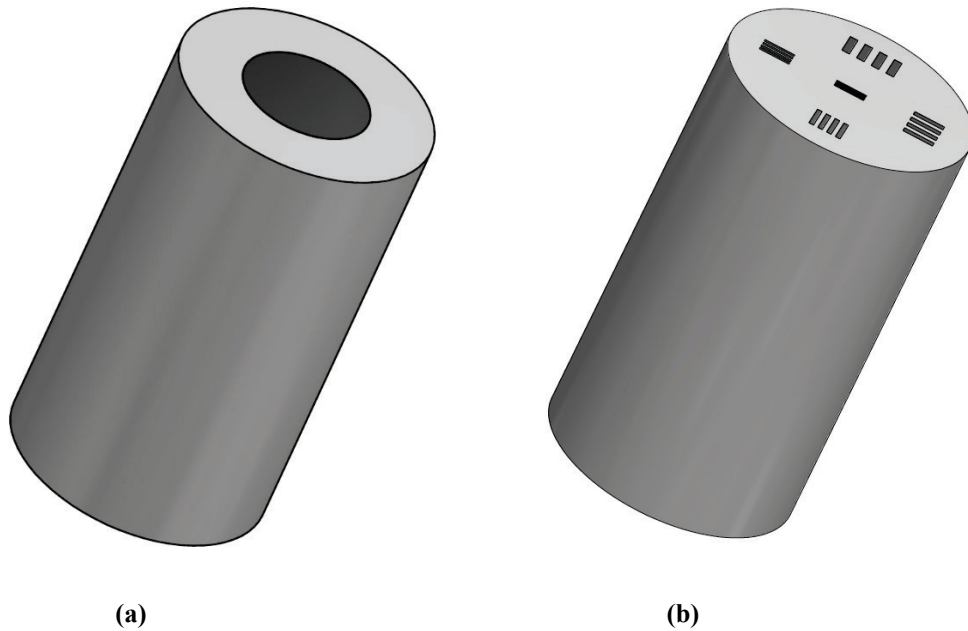


Figure 4.19. CAD drawings of (a) R-phantom for the quantitative calculation of the spatial resolution, and (b) V-phantom for validating the spatial resolution qualitatively.

Both phantoms are 8 mm in diameter. Outer cylinder of R-phantom is made of Nickel and inner cylinder is made of Aluminum with thickness of 4 mm each. The bar pattern of the V-phantom is made of Platinum and the cylinder is made of Aluminum. Details of the bar pattern are shown in Figure 4.20. Total cross section (Σ_T) of Nickel and Aluminum is shown in Figure 4.21 and neutron absorption probability is shown in Figure 4.22.

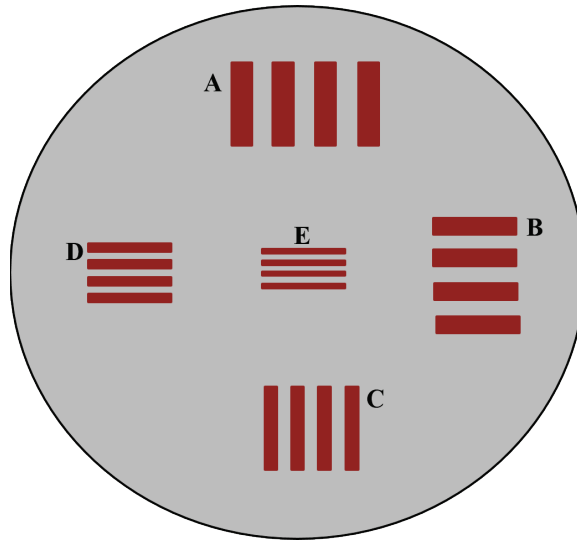


Figure 4.20. Sketch of the resolution bar pattern used in V-phantom. The bar pattern measures the spatial resolution (A) 250 μm , (B) 200 μm , (C) 150 μm , (D) 100 μm , and (E) 50 μm .

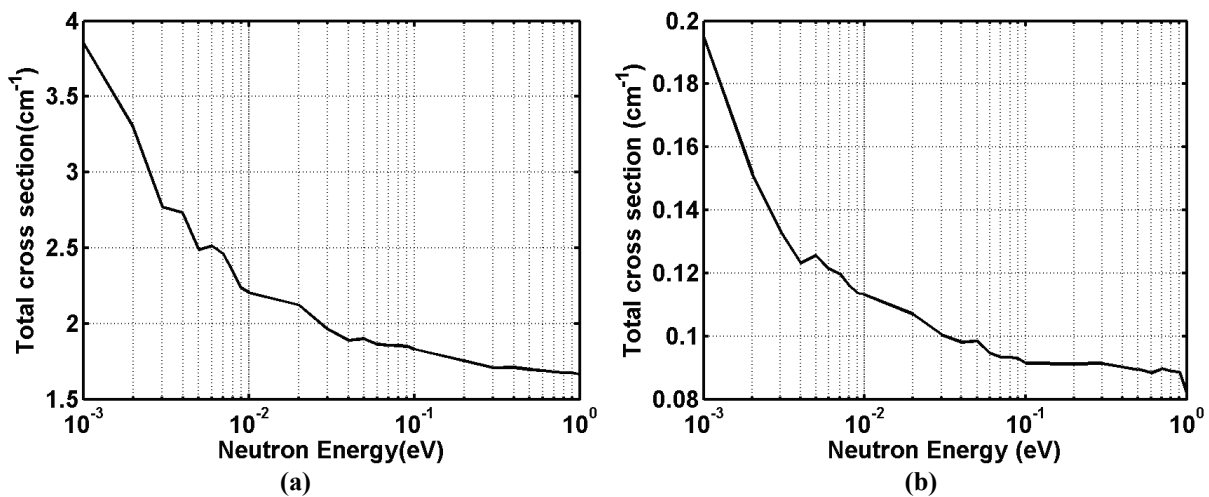


Figure 4.21. Total cross section of the phantom material as obtained by Geant4 simulation (a) Nickel, and (b) Aluminum.

The peak of filtered neutron energy spectrum of NCSU imaging facility is in the range of 0.02 eV to 0.1 eV. Figure 4.21 illustrates that the total macroscopic cross section (Σ_T) has a smaller variation in between that energy range. It will minimize the beam hardening artifacts and no further corrections are required in projection data. Figure 4.22 illustrates neutron absorption probability of Nickel and Aluminum. Dimension of the phantoms ensures that a sufficient number of neutrons

reach to the detector, reducing the photon starvation artifacts. Selection of the correct materials and their dimensions are important to produce artifacts free CT reconstruction [154].

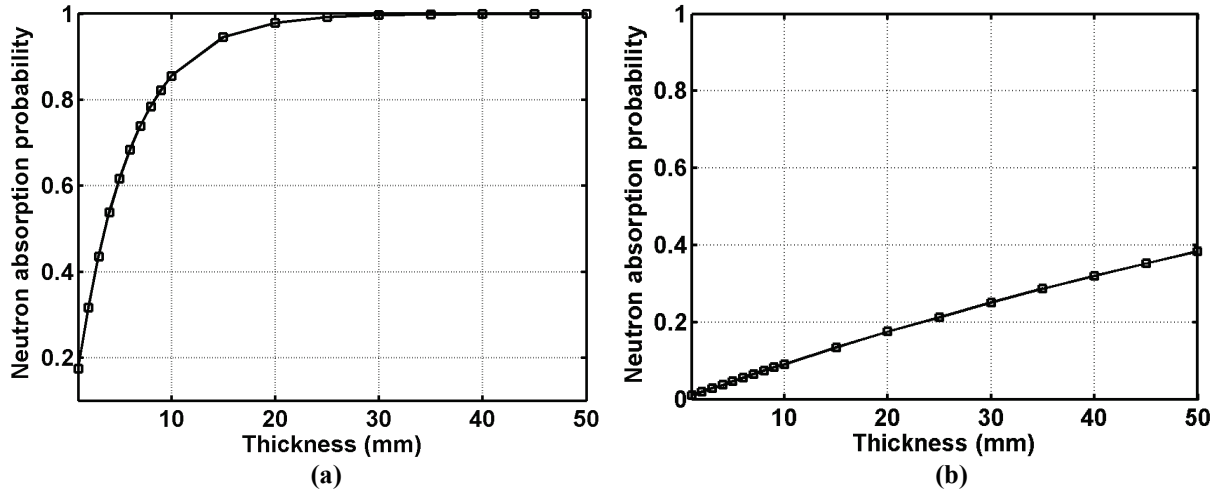


Figure 4.22. Neutron absorption probability with the thickness as obtained by Geant4 simulation (a) Nickel, and (b) Aluminum.

4.6 Monte Carlo Simulation Model of CT System

The developed Geant4 multi-physics simulation model was extended to simulate data acquisition for tomography reconstruction. The phantom and the detector system is shown in Figure 4.23. The center of the phantom is placed 1 cm from the detector. Beam aperture size is shown by D , object to detector distance is shown by d and aperture to object distance is shown by L . Detector system is made of Aluminum, ${}^6\text{LiF:ZnS(Ag)}$ scintillator and a photosensitive device. Neutrons are transmitted through object reaching the scintillator get absorbed in ${}^6\text{Li}$ and consequently, alpha and triton particles are emitted. These charged particle transports within the scintillator and cause scintillation event. Generated optical photons are transported within a scintillator and escaped optical photons are captured by the pixilated photosensitive device. The simulation parameters are illustrated in Table 4.3. Simulations were performed with 25 μm , 50 μm and 250 μm thick ${}^6\text{LiF:ZnS}$ scintillator screen with L/D ratio 73 and 142 to characterize the performance of the CT system.

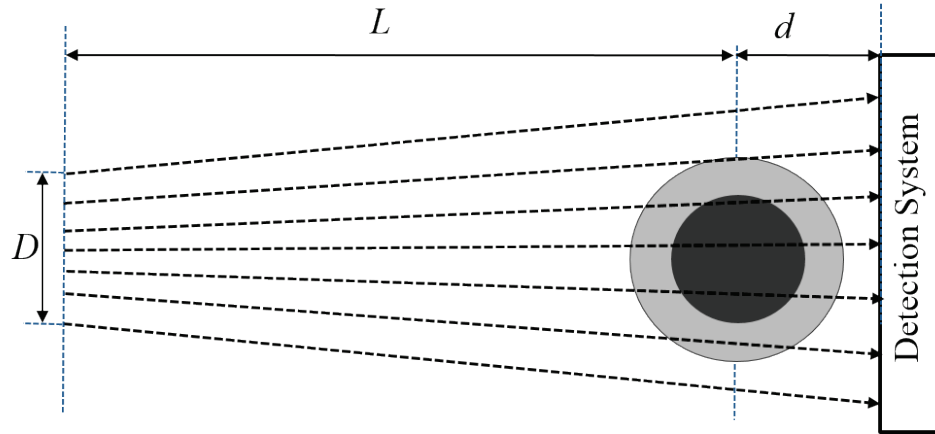


Figure 4.23. Illustration of the object detector model used in the simulation.

Table 4.3. Simulation parameters for the generation of projection data

Properties	Specification
${}^6\text{LiF:ZnS}$	1:2
Scintillator thickness (μm)	25, 50, 250
Beam aperture to object distance (cm)	292, 568
L/D	73, 142
Pixel size of photo sensitive device (μm)	13
Size of the scintillator (mm x mm)	13.312 x 13.312

4.7 Simulation Result

In the present simulation, performance of a neutron tomography system is evaluated for 25 μm , 50 μm and 250 μm thick scintillator screen. Each of the simulation performed at L/D of 73 and 142 and 360 views are accumulated. Escaped optical photons from a scintillator create a two-dimensional distribution of the gray levels at photosensitive device. These radiographs are normalized to 16-bit grayscale images. Open beam image is produced without an object and shown in Figure 4.24, (a), radiograph for R-phantom is shown in Figure 4.24, (b). Radiograph for V-

phantom generated with 50 μm thick scintillator screen at 0° , 45° , 90° , and 135° angle are shown in Figure 4.25 and Figure 4.26 respectively.

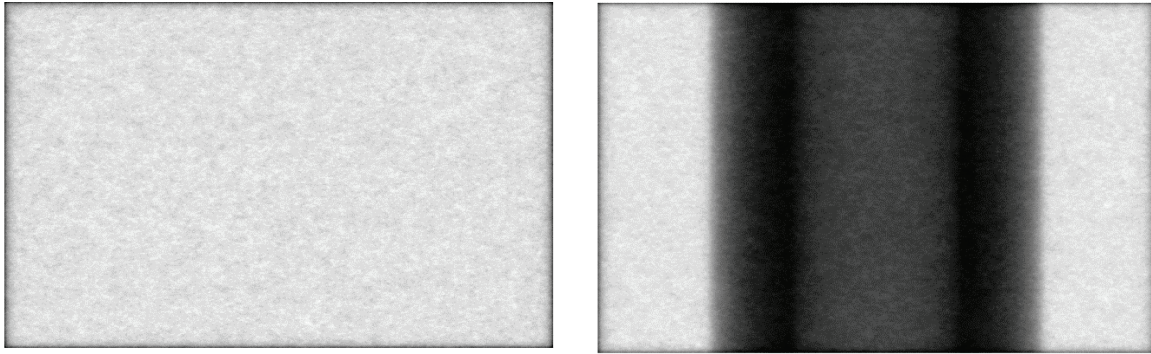


Figure 4.24. (a) Open beam image, and (b) Radiograph of R-phantom, as obtained from Geant4 simulation.

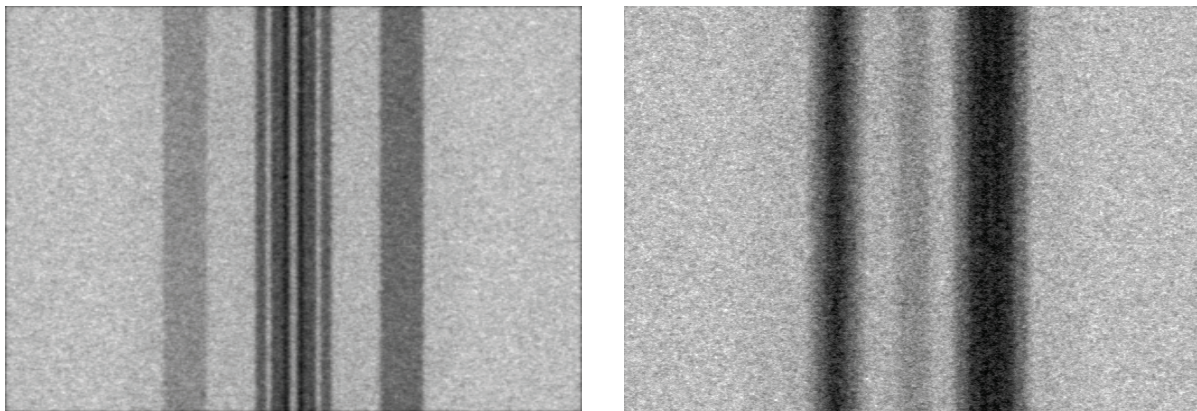


Figure 4.25. Radiographs of V-phantom as obtained from Geant4 simulation for angle (a) 0° , and (b) 45° .

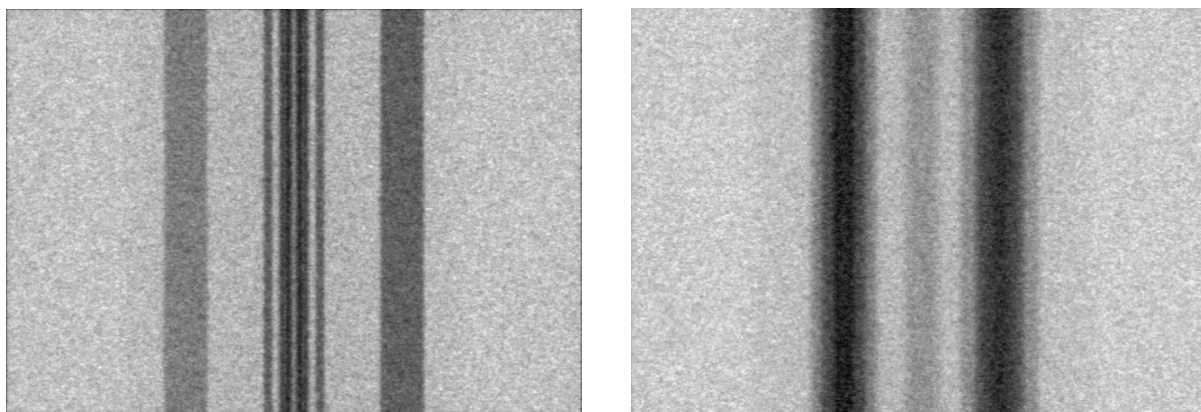


Figure 4.26. Radiographs of V-phantom as obtained from Geant4 simulation for angle (a) 90° , and (b) 135° .

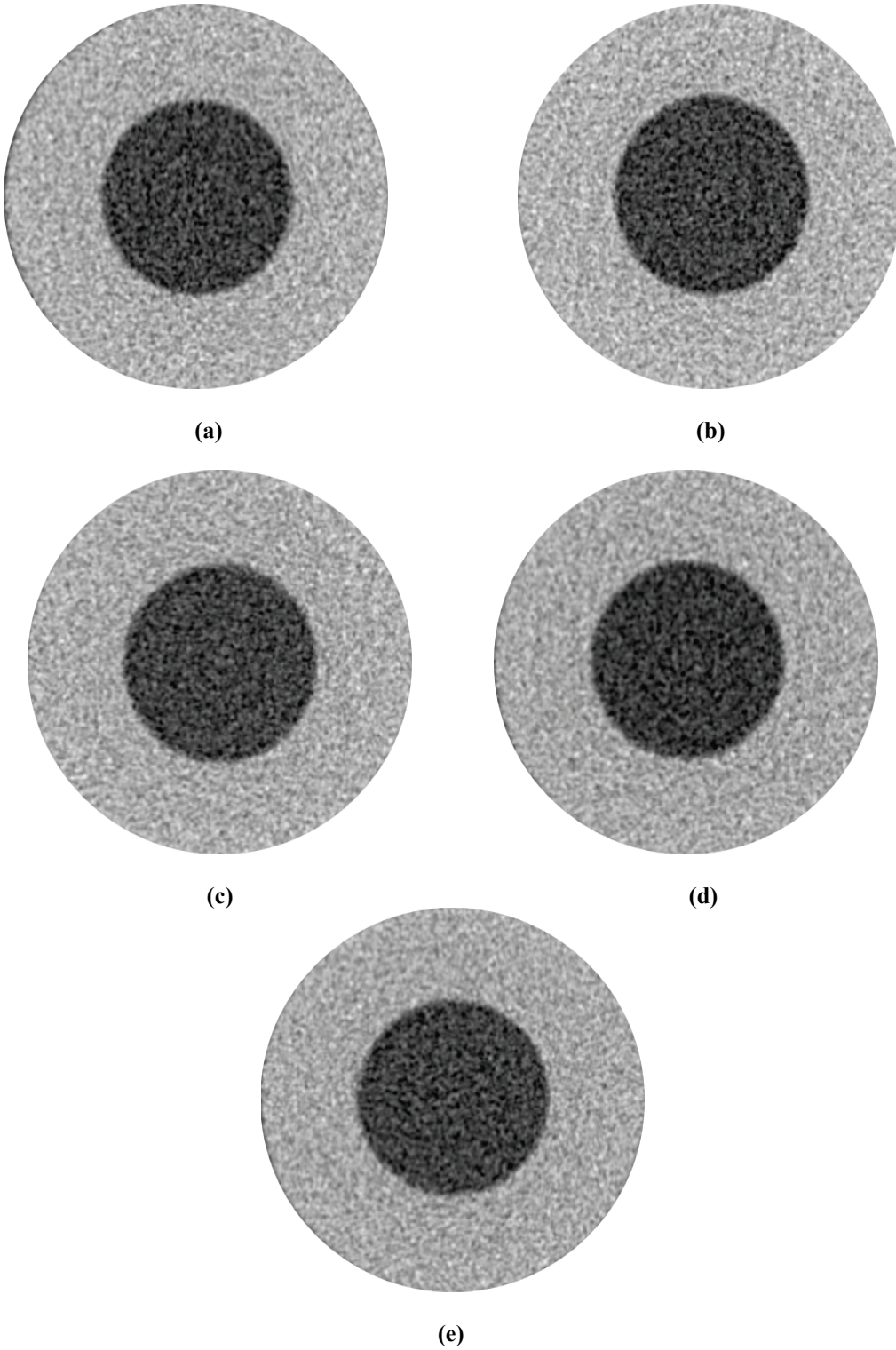


Figure 4.27. FBP reconstruction of R-phantom for scintillator thickness $50 \mu\text{m}$ and L/D 142 obtained with (a) Ramp, (b) Hamming, (c) Cosine, (d) Hanning, and (e) Shepp-Logan.

FBP reconstruction of R-phantom with different filters is shown in Figure 4.27. These reconstructions were performed with projection data simulated with 50 μm thick scintillator for L/D 142. MTF is calculated as outlined earlier and shown in Figure 4.28 and spatial resolution is shown in Table 4.4.

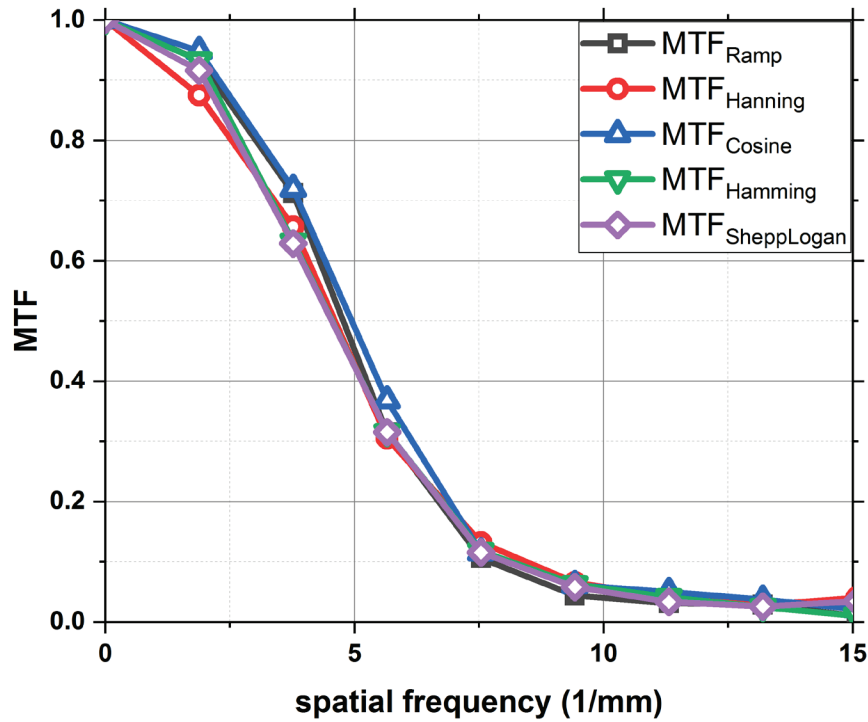


Figure 4.28. MTF of the FBP reconstruction showing the performance of different filters. (Simulation results obtained with 50 μm scintillator screen with L/D 142).

Table 4.4. Spatial resolution of CT reconstruction with different FBP filters (simulation results)

FBP filter	Spatial resolution(μm)
Ramp	131 \pm 2
Hamming	126 \pm 2
Cosine	122 \pm 2
Hanning	119 \pm 2
Shepp-Logan	130 \pm 2

It can be observed that the resolution performance, Hanning filter performs better as compared with the other filters. These performances can be correlated with the filter weight as illustrated in

Figure 4.7. As the weight of the filters increases towards high spatial frequency, noise also increases which reduces spatial resolution. Next, projections data are simulated with 25 μm , 50 μm , and 250 μm thick scintillator screen for L/D 142 and 73. FBP reconstruction was performed with a Hanning filter and illustrated in Figure 4.29 and Figure 4.30. The MTF is illustrated in Figure 4.31 spatial resolutions are tabulated in Table 4.5. In addition to the spatial resolution of the CT reconstruction (R_{CT}), total spatial resolution of the radiography system (R_{NR}) also obtained. A Gadolinium edge was placed at the 1 cm from the scintillator screen and radiograph was obtained to calculate R_{NR} .

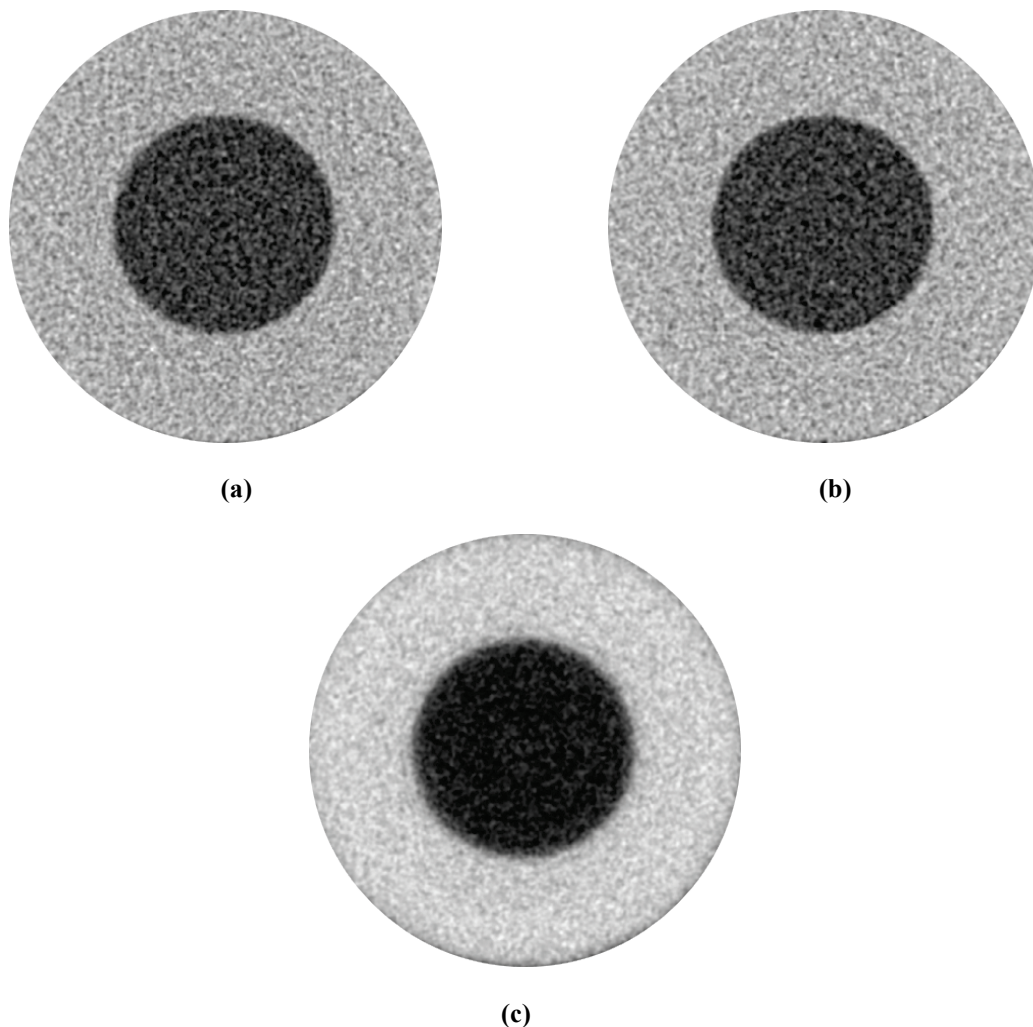


Figure 4.29. FBP reconstruction of R-phantom for scintillator screen thickness (a) 25 μm , (b) 50 μm , and (c) 250 μm at L/D 142.

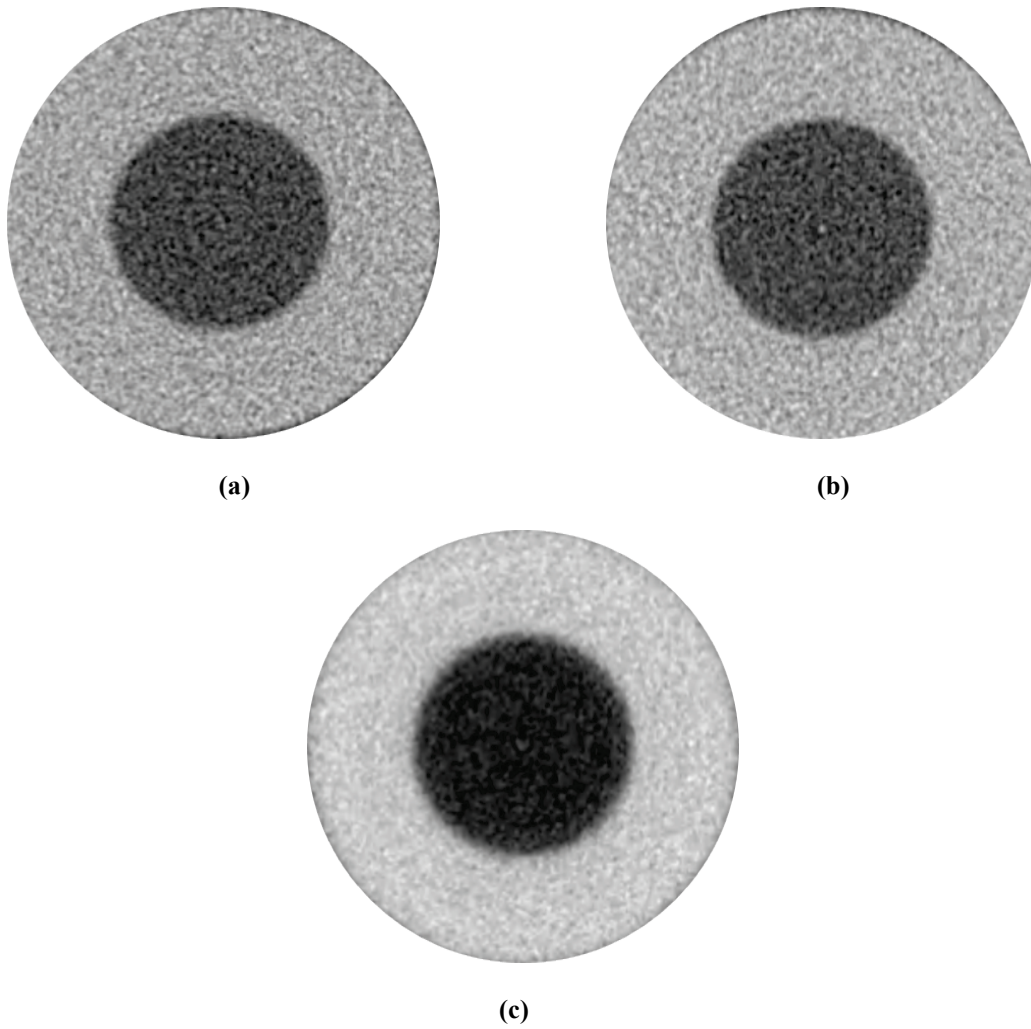


Figure 4.30. FBP reconstruction of R-phantom for scintillator screen thickness (a) 25 μm , (b) 50 μm , and (c) 250 μm at L/D 73.

Table 4.5. Spatial resolution components of the CT system

Scintillator thickness (μm)	L/D	R_G (μm)	$R_{Scintillator}$ (μm)	R_{NR} (μm)	R_{CT_FBP} (μm)
250	73	137	133 ± 1	209 ± 1	236 ± 1
	142	71		167 ± 2	186 ± 2
50	73	137	64 ± 2	166 ± 2	182 ± 2
	142	71		110 ± 2	119 ± 2
25	73	137	48 ± 2	157 ± 2	168 ± 2
	142	71		103 ± 2	115 ± 3

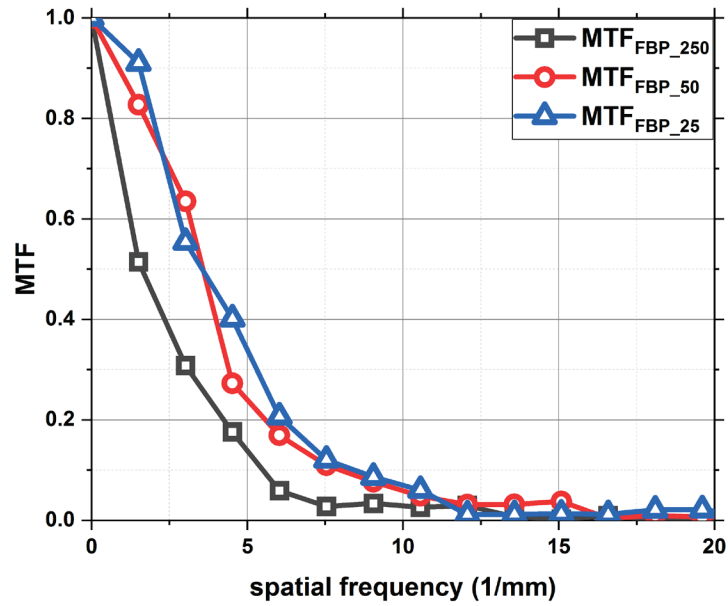


Figure 4.31. MTF of the FBP reconstruction for L/D 142 showing spatial resolution of CT reconstruction with 25 μm , 50 μm , and 250 μm scintillator.

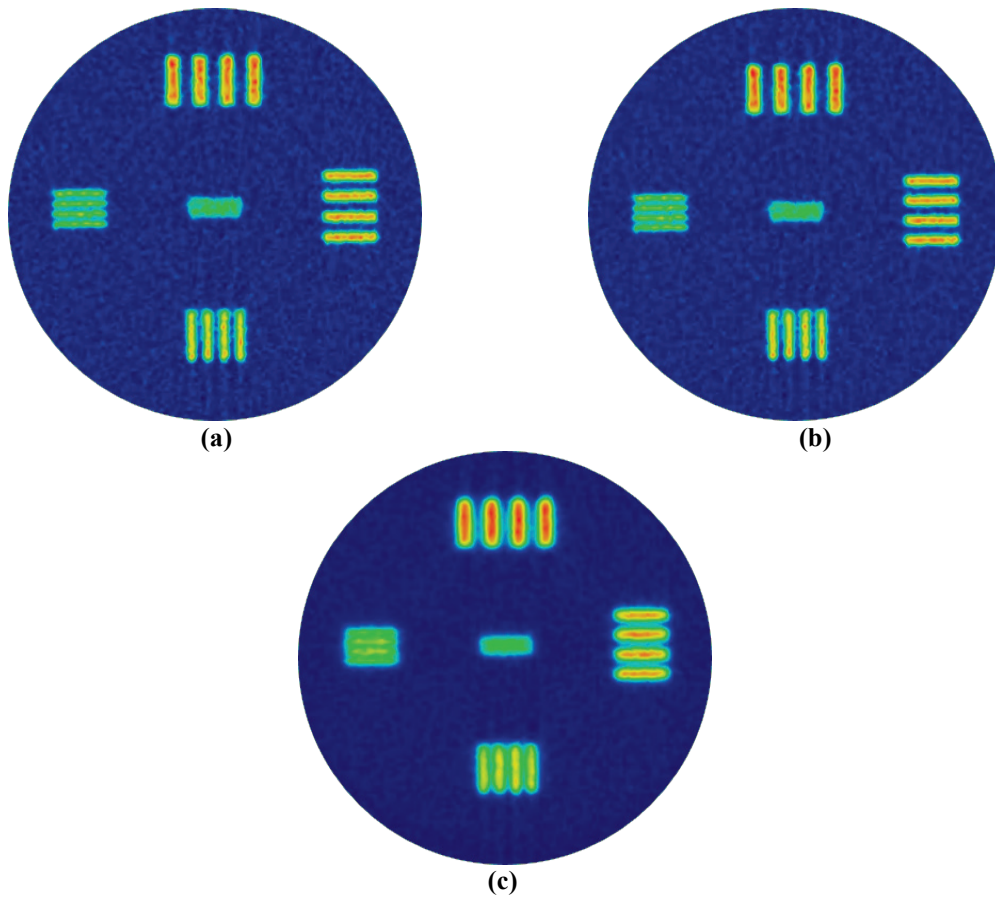


Figure 4.32. FBP reconstruction of V-phantom for scintillator thickness (a) 25 μm , (b) 50 μm , and (c) 250 μm . at L/D 142 (color representation for the enhanced illustration of the bar pattern for validation of the spatial resolution).

It can be observed from Figure 4.29 and Figure 4.30 that the inner cylinder edge is blurred as scintillator thickness increases. Additionally, it can be observed that for a fixed scintillator thickness, spatial resolution of reconstructed images improves as L/D increases. As L/D increases, neutron beam gets more parallel which reduces geometrical contribution. This observation is validated by the radiographic resolution R_{NR} from Table 4.6.

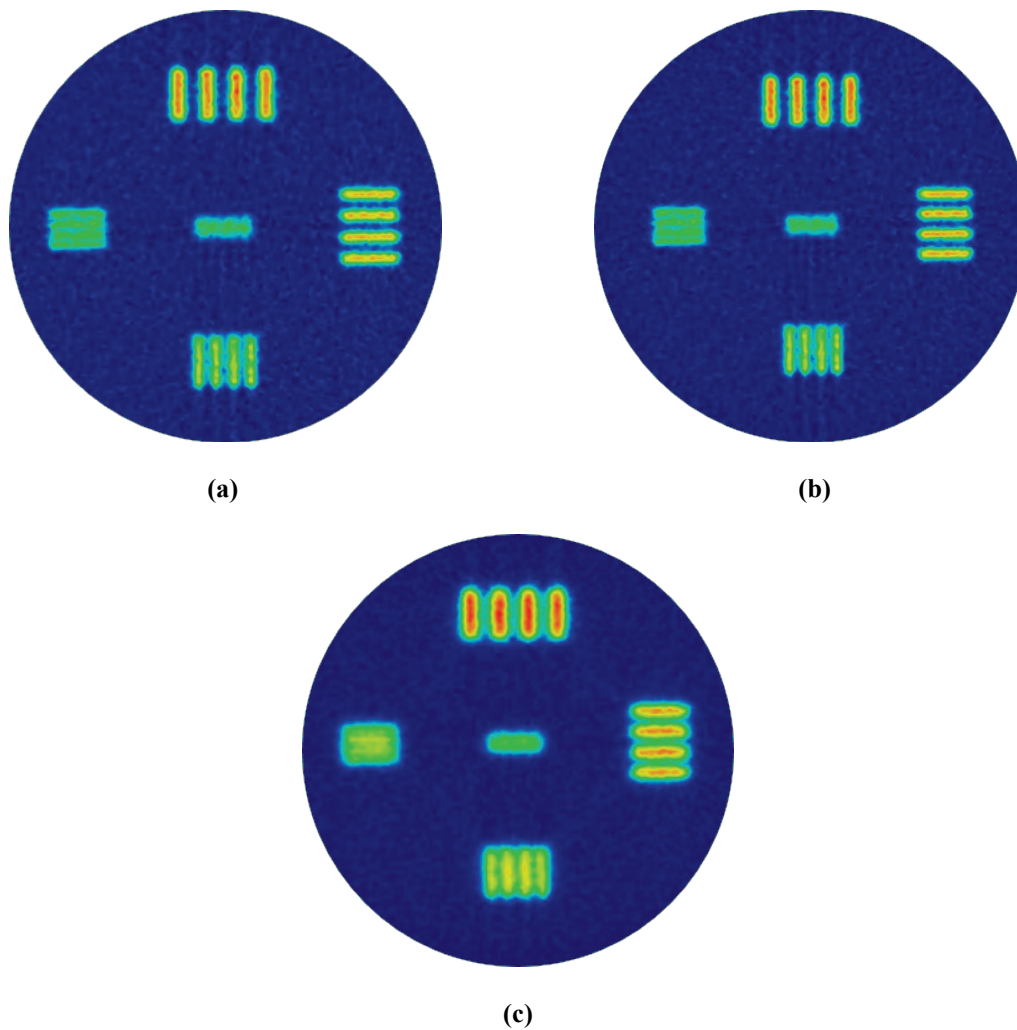


Figure 4.33. FBP reconstruction of V-phantom for scintillator thickness (a) 25 μm , (b) 50 μm , and (c) 250 μm . at L/D 73 (color representation for the enhanced illustration of the bar pattern for validation of the spatial resolution).

Tomographic resolution with FBP reconstruction, R_{CT_FBP} is further validated with CT reconstruction of V-phantom as shown in Figure 4.32 and Figure 4.33. It can be observed that 150 μm bar pattern is clearly visible in Figure 4.32 (a) and Figure 4.32 (b) indicating that spatial resolution is better than 150 μm . But the pattern is not visible in Figure 4.32 (c) which suggests that spatial resolution is more than 150 μm thus validating the quantitative resolution of 186 μm with 250 μm scintillator. To investigate and evaluate the performance of other iterative methods, reconstruction of R-phantoms were performed with algebraic SIRT and statistical MLEM techniques as shown in Figure 4.34 and Figure 4.35.

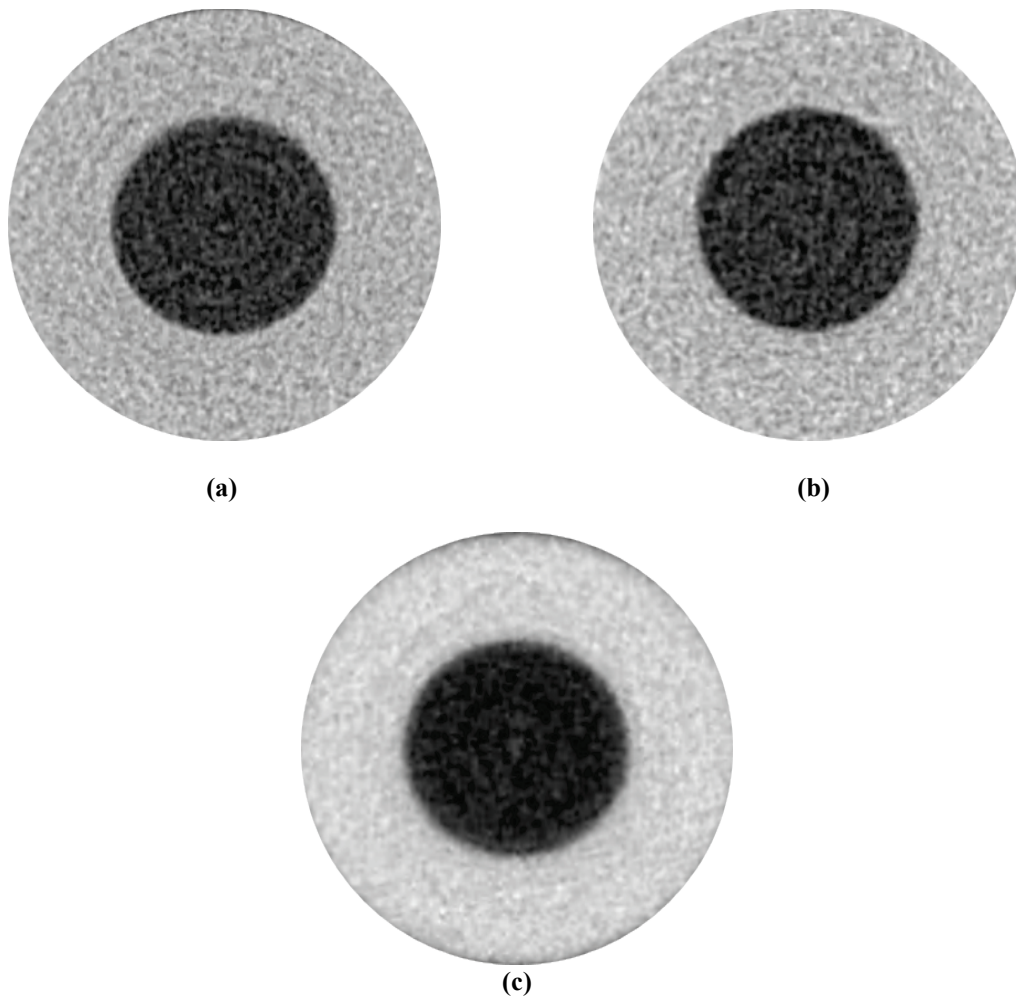


Figure 4.34. Algebraic CT reconstruction (simultaneous iterative reconstruction technique) of R-phantom for scintillator thickness (a) 25 μm , (b) 50 μm , and (c) 250 μm at L/D 142.

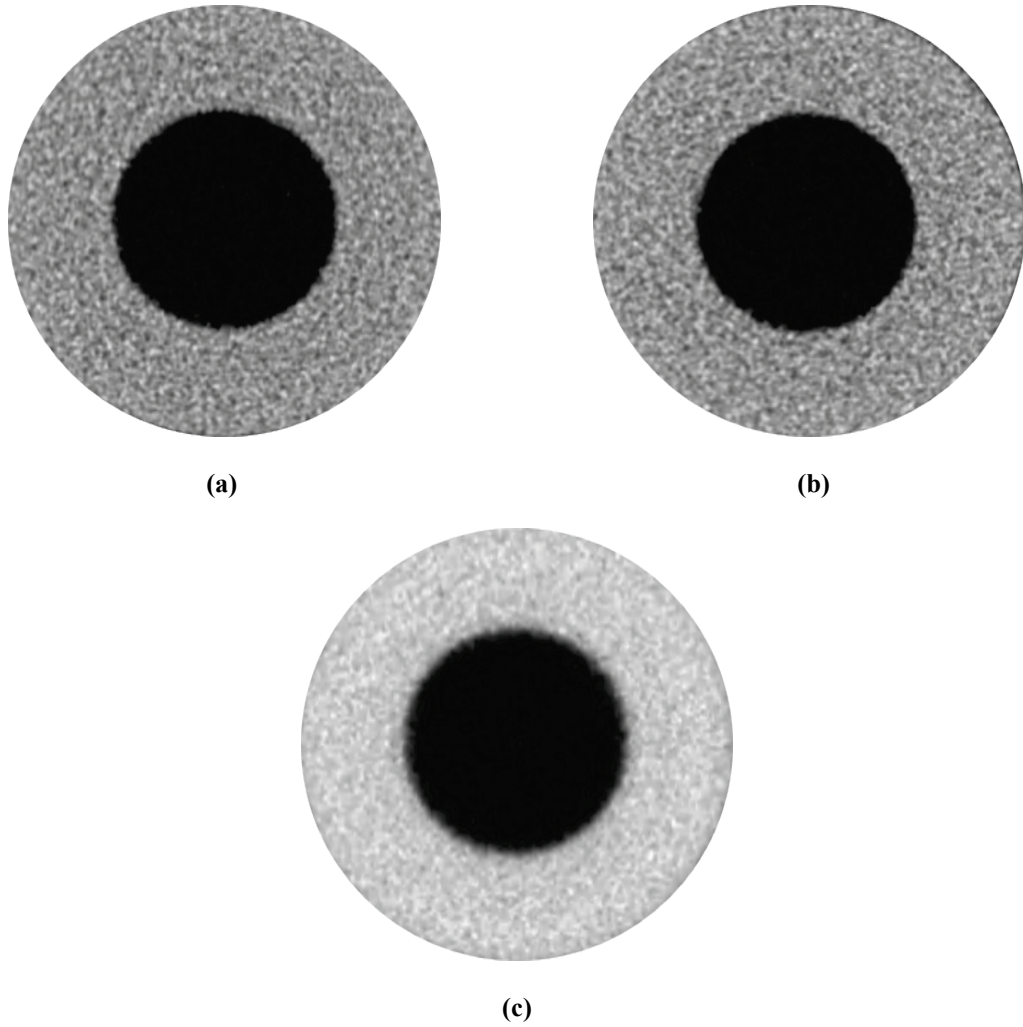


Figure 4.35. Statistical CT reconstruction (maximum likelihood expectation maximization) of R-phantom for scintillator thickness (a) 25 μm , (b) 50 μm , and (c) 250 μm at L/D 142.

Table 4.6. Spatial resolution comparison of FBP, SIRT, and MLEM

Scintillator thickness (μm)	L/D	R_{CT_FBP} (μm)	R_{CT_SIRT} (μm)	R_{CT_MLEM} (μm)
250	73	236 ± 1	224 ± 1	231 ± 2
	142	186 ± 2	180 ± 2	184 ± 2
50	73	182 ± 2	175 ± 2	170 ± 1
	142	120 ± 2	115 ± 1	112 ± 2
25	73	168 ± 2	162 ± 2	163 ± 2
	142	115 ± 3	111 ± 2	114 ± 1

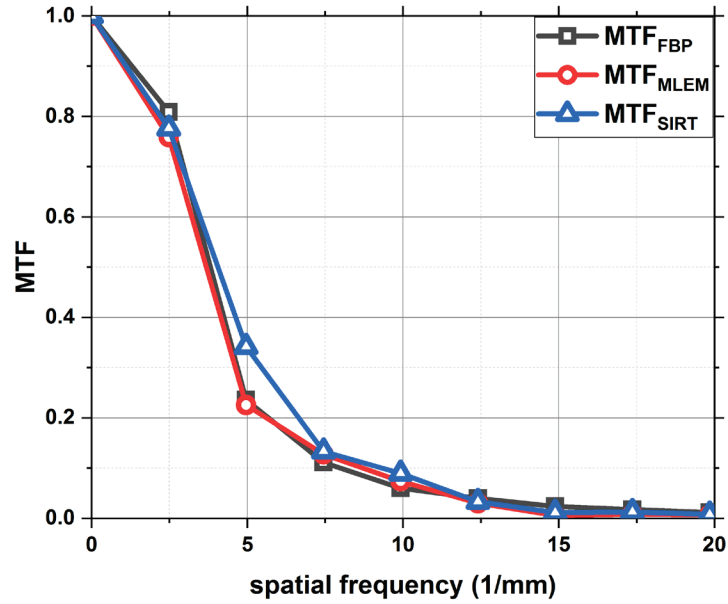


Figure 4.36. MTF comparison of the analytical (FBP), algebraic (SIRT) and statistical (MLEM) CT reconstruction.(project data simulated with 50 μm thick scintillator screen and L/D 142).

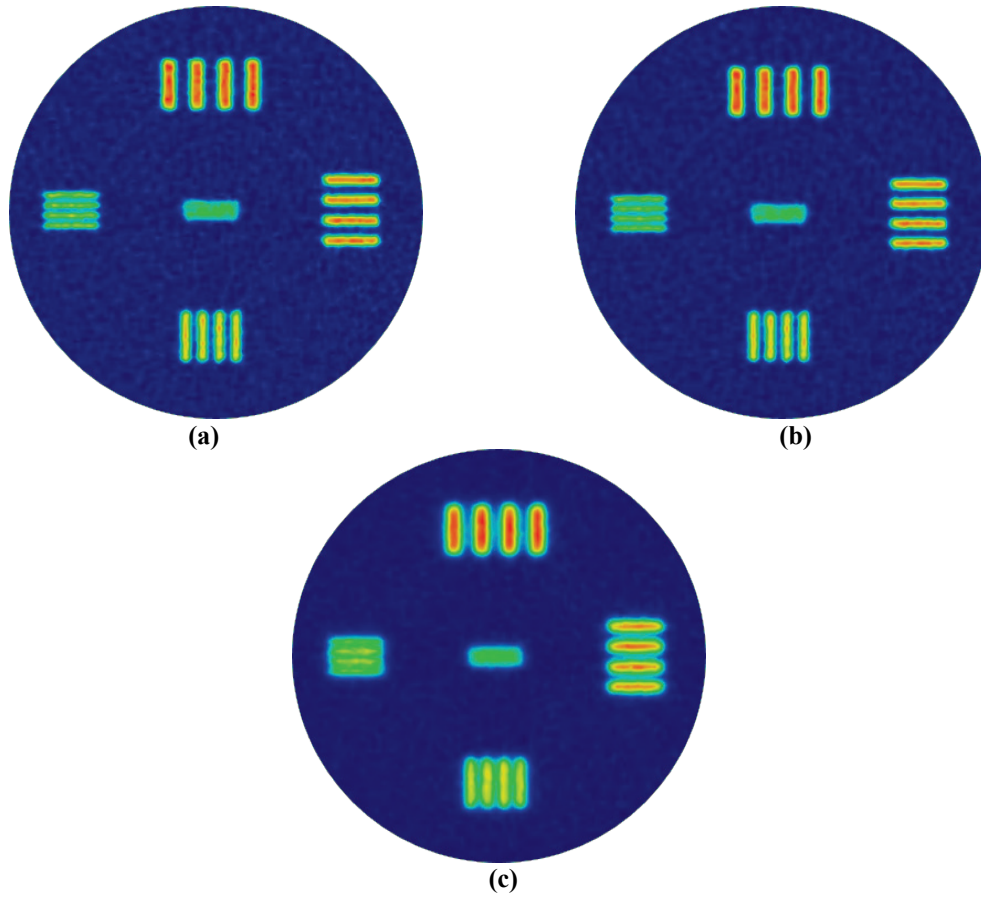


Figure 4.37. Algebraic CT reconstruction (simultaneous iterative reconstruction technique) of V-phantom for scintillator thickness (a) 25 μm , (b) 50 μm , and (c) 250 μm . at L/D 142 (color representation for the enhanced illustration of the bar pattern for validation of the spatial resolution).

It can be observed from Table 4.6 that iterative methods produce better reconstruction results as compared with the analytical FBP reconstruction method. Performances of algebraic SIRT, statistical MLEM and FBP is shown in Figure 4.36 and tabulated in Table 4.5. Validations were performed with V-phantom and shown in Figure 4.37 and Figure 4.38.

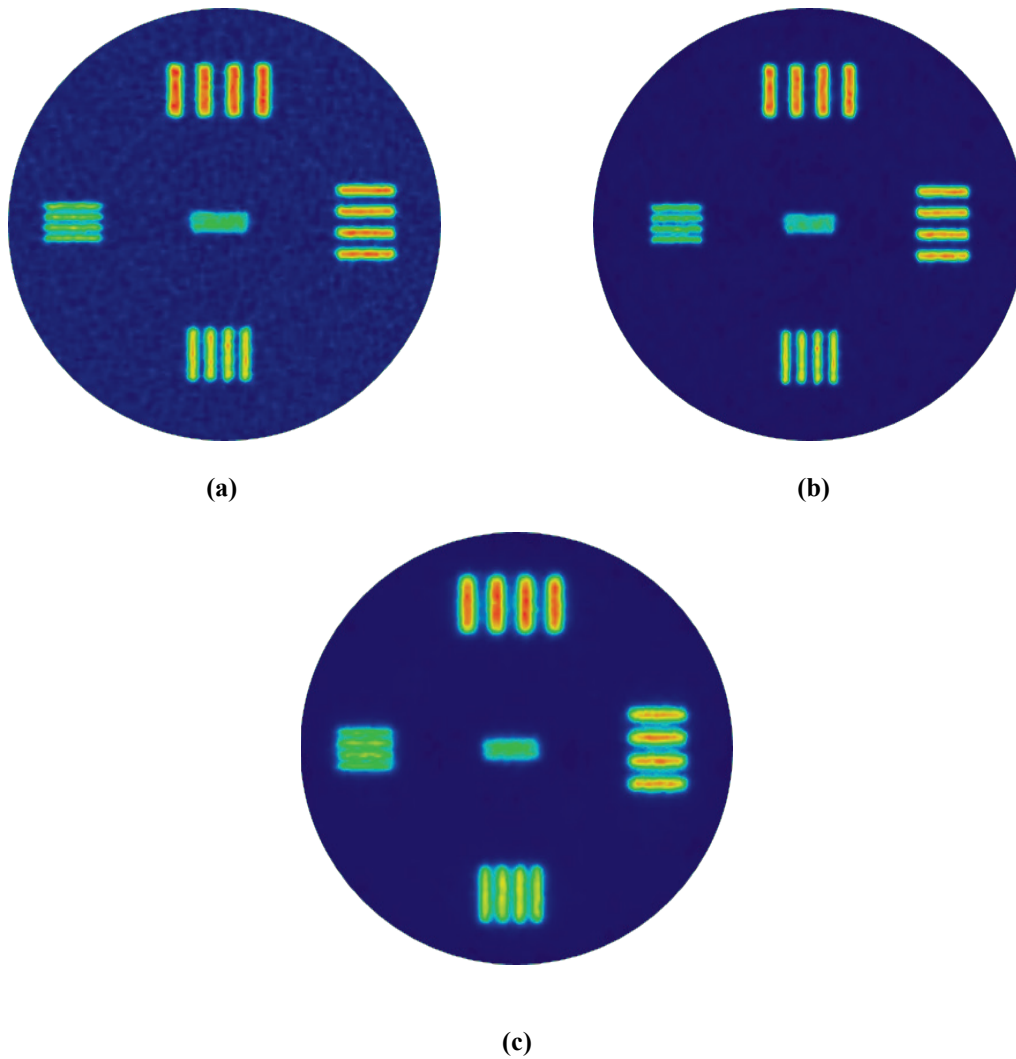


Figure 4.38. Statistical CT reconstruction (maximum likelihood expectation maximization) of V-phantom for scintillator thickness (a) 25 μm, (b) 50 μm, and (c) 250 μm. at L/D 142 (color representation for the enhanced illustration of the bar pattern for validation of the spatial resolution).

It can be observed that 150 μm bar pattern is clearly visible in Figure 4.37 (a, b) and Figure 4.38 (a, b) indicating that spatial resolution is better than 150 μm . But the pattern is not visible in Figure 4.37 (c) and Figure 4.38 (c) which suggests that spatial resolution is more than 150 μm thus validating the quantitative resolution of 186 μm with 250 μm scintillator. The qualitative difference between 250 μm bar patterns is clearly visible for L/D 73 and 142. A similar pattern can be observed with SIRT and EM methods for fixed L/D, thus validating the quantitative spatial resolution calculation as shown in Table 4.6.

Previous investigation shows that spatial resolution limitation in neutron tomography is contributed by neutron beam collimation and detection system. Additionally, it can be observed that for a fixed scintillator thickness, spatial resolution of reconstructed images improves as L/D increases. As L/D increases, beam gets more parallel which reduces the geometrical contribution. High beam collimation makes a neutron beam more parallel which restricts the spatial spread of object point onto the image plane, thus providing better spatial resolution. However, this may limit available neutron flux at a image plane, which limits practical implementation. Additionally, a thin scintillator may not always be a viable option due to the diminished neutron absorption efficiency. In typical neutron imaging facilities, the spatial resolution for tomography is reported to be in the range of 200 μm – 500 μm [41], [155]. This performance is based on using traditional image reconstruction techniques that do not account for the performance characteristics of the imaging system. In the model based reconstruction approach, we have included a system response function in forward projection model to provide a better estimation of the actual projection, thus improving spatial resolution of the reconstructed images.

The response function is a Gaussian point spread function with FWHM equals the obtained spatial resolution of the system as illustrated in Figure 4.16. The system response function was

convolved with each view of the calculated projection and compared with the actual projection. The difference was weighted with and added with the current estimation of the reconstruction process. Reconstruction results of the model-based technique with R-phantom is shown in Figure 4.39. Spatial resolution performance is compared with the analytical FBP and iterative SIRT and MLEM technique. MTF is compared shown in Figure 4.40 and spatial resolution are tabulated in Table 4.7. Additionally, quantitative spatial resolution of R-phantoms were validated qualitatively with reconstruction result of the V-phantom, as shown in Figure 4.41.

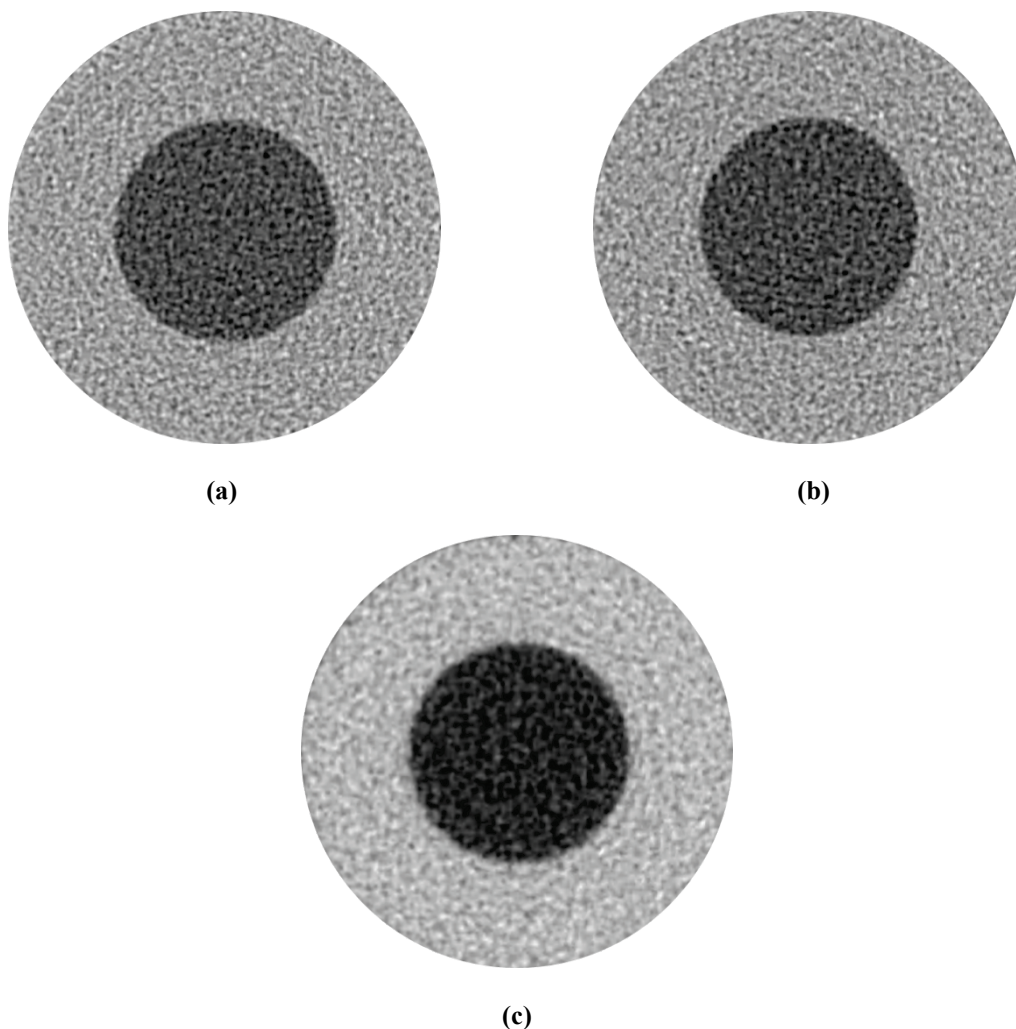


Figure 4.39. Model-based reconstruction of R-phantom for scintillator thickness (a) 25 μm , (b) 50 μm , and (c) 250 μm at L/D 142.

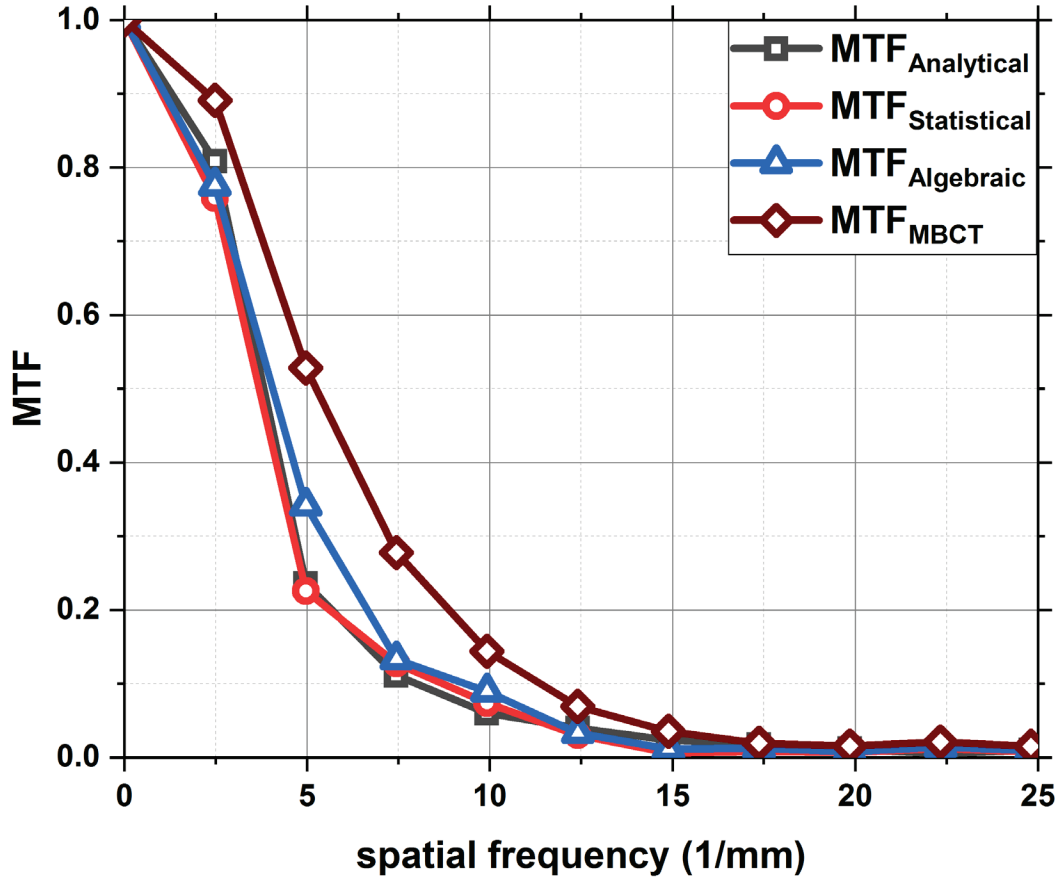


Figure 4.40. MTF comparison of the analytical (FBP), algebraic (SIRT) and statistical (MLEM), and model-based (MBCT) CT reconstruction.(project data simulated with 50 μm thick scintillator screen and L/D 142).

Table 4.7. Spatial resolution comparison of model-based technique with FBP, MLEM, and SIRT

Scintillator thickness (μm)	L/D	R_{CT_FBP} (μm)	R_{CT_SIRT} (μm)	R_{CT_MLEM} (μm)	R_{CT_MB}
250	73	236 \pm 1	224 \pm 1	231 \pm 2	172 \pm 1
	142	186 \pm 2	180 \pm 2	184 \pm 2	131 \pm 2
50	73	182 \pm 2	175 \pm 2	170 \pm 1	145 \pm 2
	142	120 \pm 2	115 \pm 1	112 \pm 2	86 \pm 1
25	73	168 \pm 2	162 \pm 2	163 \pm 2	138 \pm 2
	142	115 \pm 3	111 \pm 2	114 \pm 1	82 \pm 2

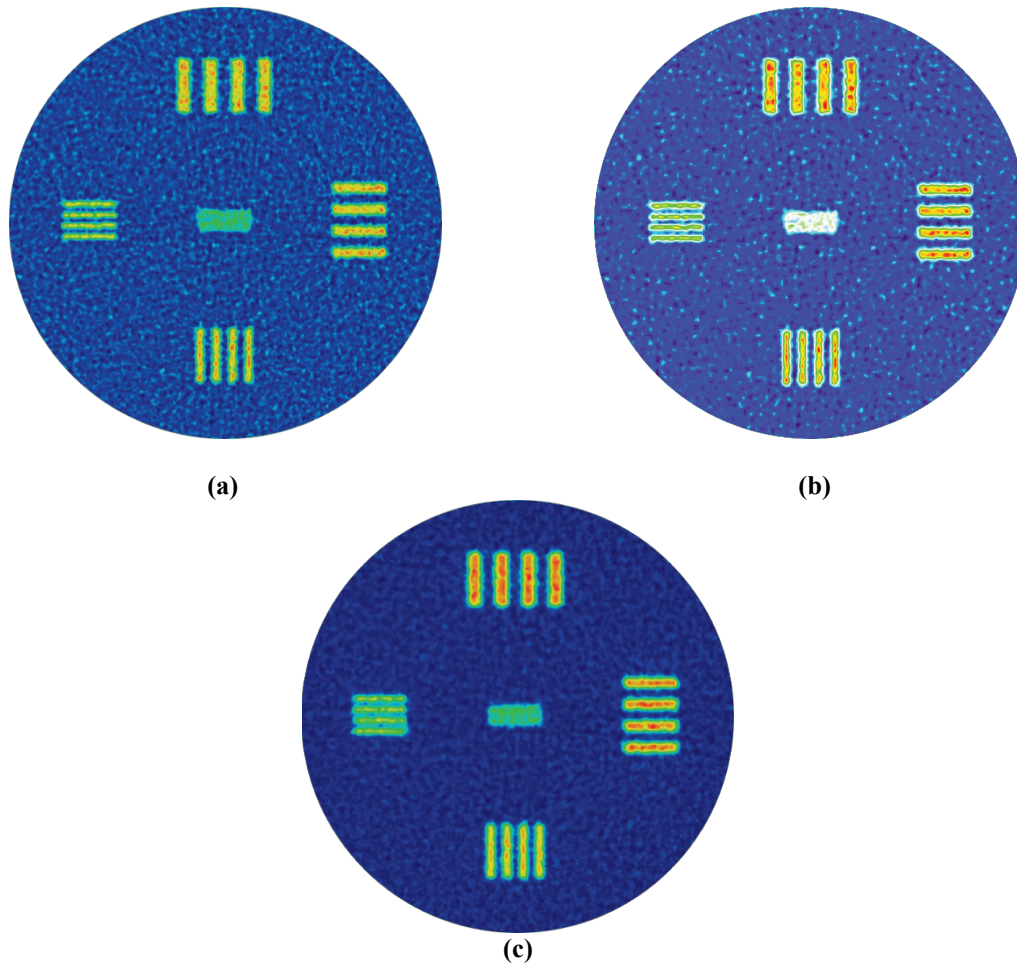


Figure 4.41. Model based reconstruction of R-phantom for scintillator thickness (a) 25 μm , (b) 50 μm , and (c) 250 μm at L/D 142 (color representation for the enhanced illustration of the bar pattern for validation of the spatial resolution).

It can be observed quantitatively from R-phantom and qualitatively from V-phantom that spatial resolution is improved. It can be illustrated further with a profile through the 100 μm bar pattern as shown in Figure 4.41. It can be observed that the 100 μm bar pattern is not distinguishable while 150 μm bar is visible with 50 μm scintillator screen with traditional FBP, SIRT and MLEM. Thus, validating the spatial resolution more than 100 μm . However, inclusion of system response function shows the improvement in spatial resolution of the model-based technique and can be observed with the discern visibility of 100 μm bar pattern. To illustrate it further a profile is plotted through the 100 μm bar of the reconstructed images with SIRT and model based technique and shown in Figure 4.42.

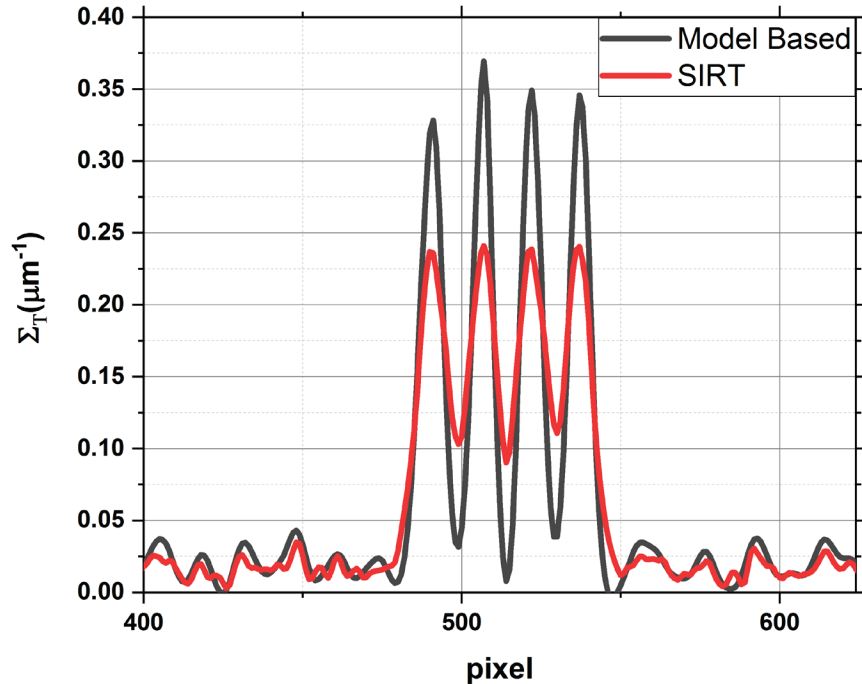


Figure 4.42. Comparison of profile plot through 100 μm bar pattern showing the improvement in the spatial resolution with the model-based reconstruction technique.

4.8 Experimental Results

Experiments were performed at the PULSTAR Neutron Imaging Facility to characterize performance of neutron CT system and validate the model based CT reconstruction technique experimentally. As discussed earlier, two types of two types of the phantoms were designed. The concentric cylinder phantom (R-phantom) was used to calculate the tomography spatial resolution and the bar phantom (V-phantom) was used to validate reconstruction results qualitatively. Both phantoms are 8 mm in diameter. The outer cylinder of R-phantom is made of Nickel and the inner cylinder is made of Aluminum as shown in Figure 4.43. Bar pattern of the V-phantom is made of Platinum and cylinder is made of Aluminum. Platinum and Aluminum bars were stacked top of each other and positioned in the assembly to form the bar pattern and illustrated in Figure 4.44 and Figure 4.45. The bar pattern of the V-phantom is shown in Figure 4.46. A positioning system was designed to move the sample or collect neutron radiography data for different angular position during a tomography experiment.



(a)



(b)

Figure 4.43. R-phantom for tomography performance characterization, (a) side view, and (b) top view.



(a)



(b)

Figure 4.44. V-phantom for tomography performance characterization, (a) side view, and (b) top view.



Figure 4.45. V-phantom assembly during manufacturing process.

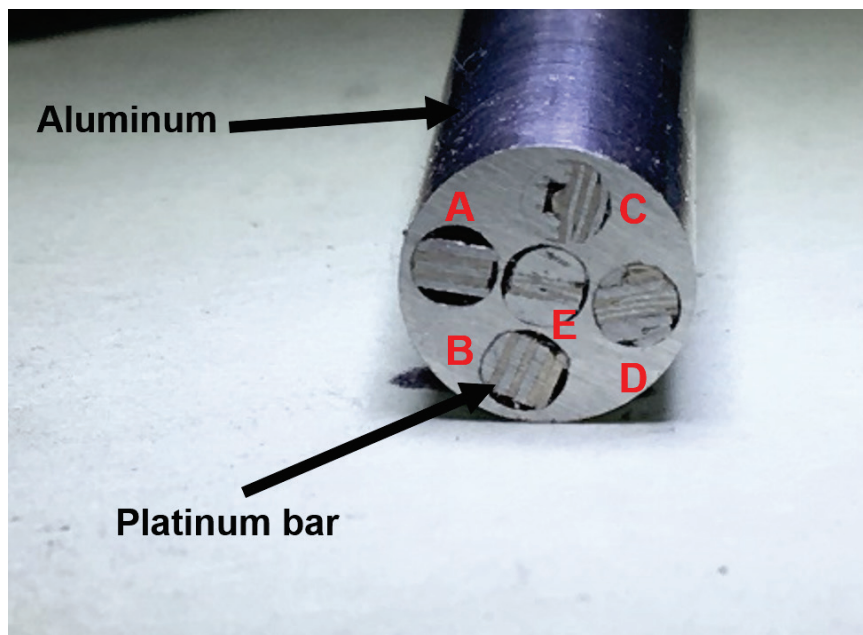


Figure 4.46. Magnified bars of V-phantom validates the spatial resolution [A] 250 μm , [B] 200 μm , [C] 150 μm , [D] 100 μm , and [E] 50 μm .

To facilitate automated data acquisition during tomography experiment, a control software was designed with the LabVIEW platform to rotate a sample and obtain a neutron radiograph as

discussed earlier. A user can specify the data acquisition parameters like exposure time, CCD gain, CCD temperature, angular incremental value etc. through a user interface (UI) as illustrated in Figure 2.23. The experimental arrangement for the tomography experiment is shown in Figure 4.47 and acquisition parameters are shown in Table 4.8. Tomography experiment was performed with a electron-multiplying CCD (EMCCD) camera. The camera has an internal gain mechanism that can reduce exposure time to obtain each radiograph. Gain was selected as 25 and 20 for 50 μm and 250 μm thick scintillator respectively. The exposure time was 50 sec and 20 sec for 50 μm and 250 μm scintillator respectively. The EMCCD camera is equipped with a thermo-electric Peltier cooling system and operated at -70°C to reduce dark current noise.

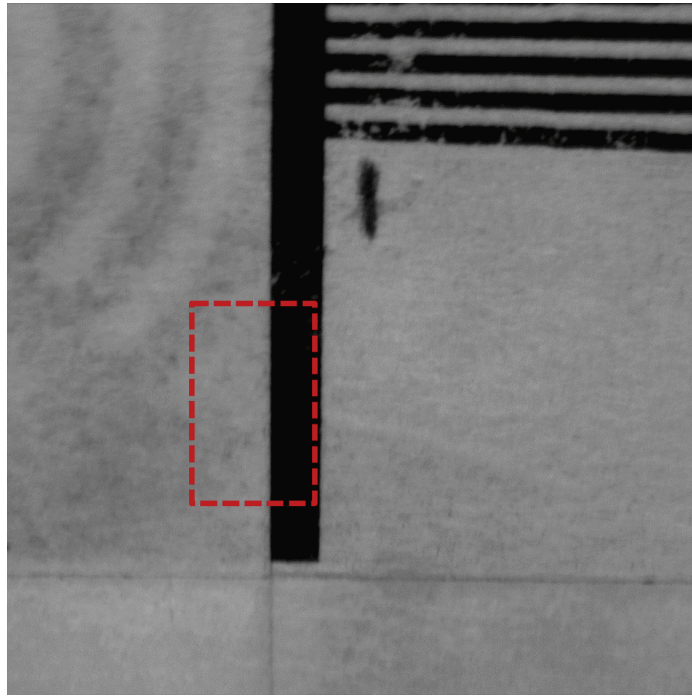


Figure 4.47. Experimental arrangement for tomography showing camera cart, camera box, scintillator, positioning system, and phantom.

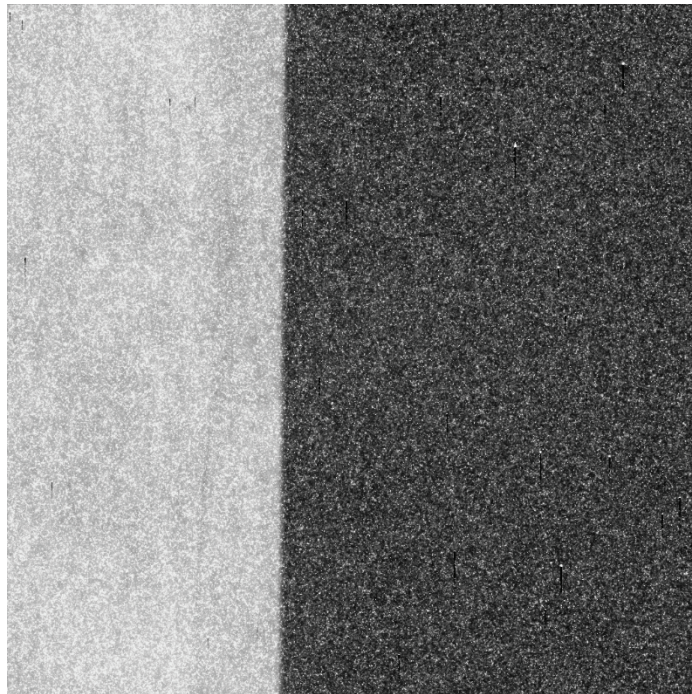
Table 4.8. Data acquisition settings for CT experiment at PULSTAR neutron imaging facility

Properties	Specification
Scintillator type	${}^6\text{LiF:ZnS}$
${}^6\text{LiF:ZnS}$ ratio	1:2
Scintillator thickness (μm)	50, 250
d (cm)	1
L/D	142
Lens	Nikon 200 mm Nikkor
Lens aperture	$f/4$
Lens Magnification	1:1
EMCCD pixel size(μm)	13
Field of view (mm x mm)	13.312 x 13.312
Angular increment	1°
Number of projection obtained	360

Spatial resolution is calculated as discussed earlier. To quantify $R_{Lens+CCD}$, an image containing a sharp paper edge was obtained. The highlighted area in Figure 4.48(a) is used for analysis. Next, a neutron radiograph was obtained, attaching a gadolinium edge on the scintillator screen as shown in Figure 4.48(b). This arrangement makes R_G negligible by reducing $d \approx 0$, thus effectively quantify R_D . In addition, a gadolinium edge was placed 1 cm from the scintillator and a radiograph was obtained to calculate R_{NR} . Edge neutron radiograph is obtained with 50 μm thick scintillator and corresponding MTF are shown in Figure 4.49 and spatial resolutions are tabulated in Table 4.9. It can be observed categorically, spatial resolution contribution from the Lens-CCD, Scintillator and geometry. For the tomography, 360 radiographs were obtained with the R-phantom and V-phantom. Each of the experiments were performed with the 50 μm and 250 μm ${}^6\text{LiF:ZnS}$ (Ag) scintillator. Neutron radiographs of R-phantom obtained with 50 μm and 250 μm thick scintillator are shown in Figure 4.50.



(a)



(b)

Figure 4.48. The edge images for the calculation of (a) the spatial resolution contribution from lens and CCD, (b) the detector system.

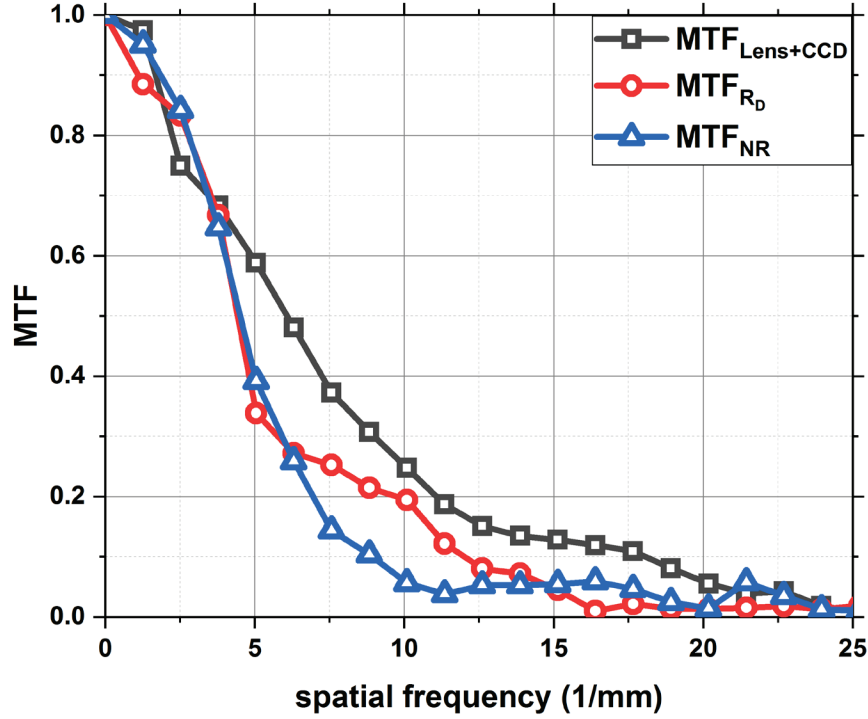


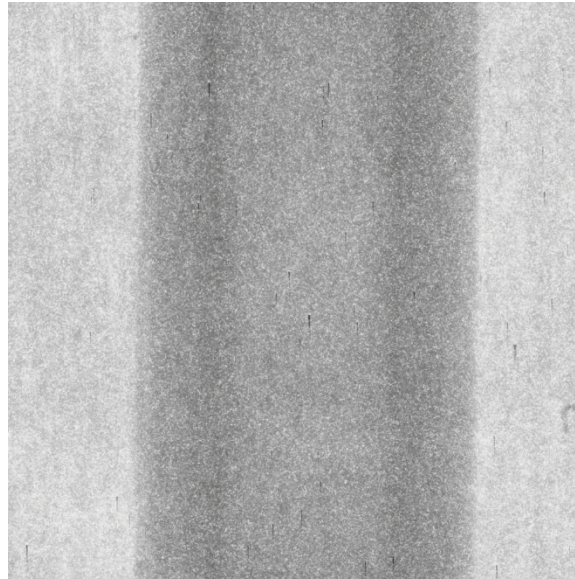
Figure 4.49. MTF of the imaging system as obtained with 50 μm thick ${}^6\text{LiF: ZnS}$ scintillator showing the contribution of lens and CCD, detector and total spatial resolution.

Table 4.9. Spatial resolution components of the neutron imaging system

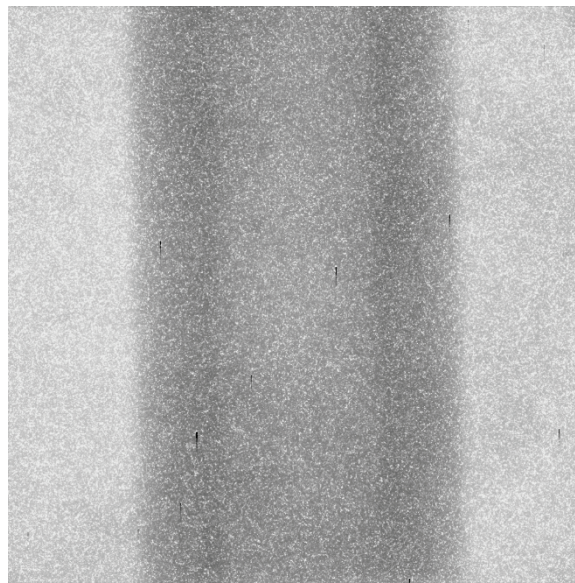
Scintillator thickness (μm)	$R_{Lens+CCD}$ (μm)	R_D (μm)	R_{NR} (μm)
50	55 ± 1	86 ± 2	116 ± 2
250		145 ± 2	173 ± 2

Tomography reconstruction was performed with FBP and model-based technique and resolution calculated as outlined earlier. Tomography reconstruction of the R-phantom for 50 μm thick scintillator with traditional and the model-based techniques are shown in Figure 4.51. The R_{NR} value from Table 4.9 was used for system response function in the model based reconstruction technique. A Gaussian system response function is generated with the full width at half maximum (FWHM) equal to R_{NR} . MTF of the traditional and model based CT reconstructions are illustrated

in Figure 4.52 and spatial resolutions are shown in Table 4.10. Reconstruction result for the V-phantoms are shown in Figure 4.53 and Figure 4.54.



(a)



(b)

Figure 4.50. Neutron radiograph of R-phantom obtained with $^6\text{LiF}:\text{ZnS}(\text{Ag})$ scintillator of thickness, (a) 50 μm , and (b) 250 μm .

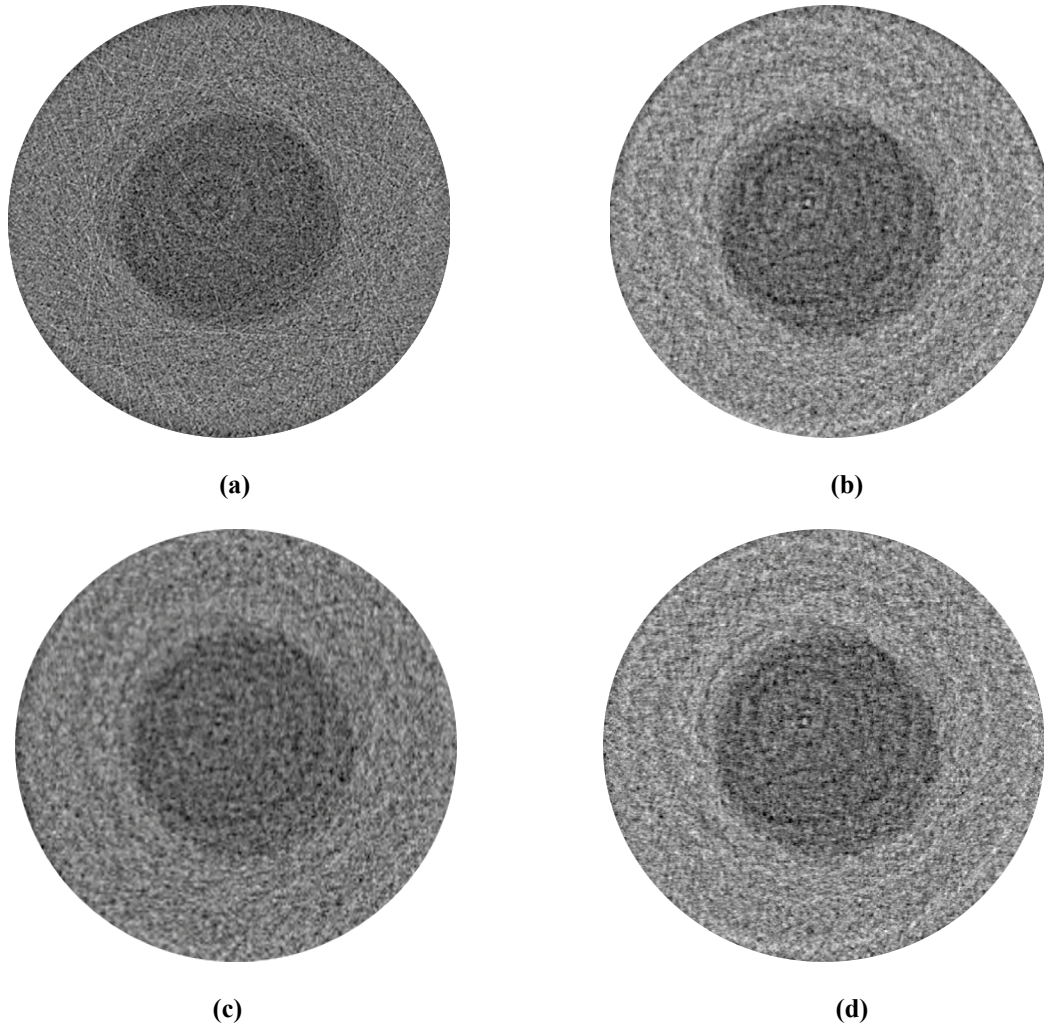


Figure 4.51. CT reconstruction of R-phantom with (a) analytical FBP, (b) algebraic SIRT, (c) statistical MLEM, and (d) model based technique obtained with 50 μm scintillator at L/D 142.

Table 4.10. Spatial resolution comparison of CT reconstruction (experimental result)

Scintillator thickness (μm)	Spatial resolution (μm)			
	Analytical (FBP)	Algebraic (SIRT)	Statistical (MLEM)	Model based reconstruction
50	124 ± 4	120 ± 4	124 ± 4	87 ± 3
250	194 ± 3	186 ± 3	190 ± 3	141 ± 2

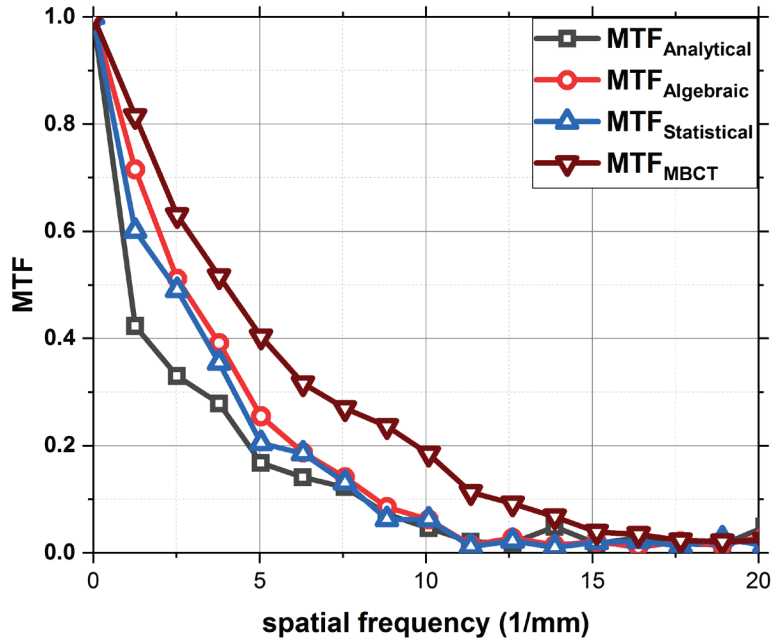


Figure 4.52. MTF comparison of the analytical (FBP), algebraic (SIRT) and statistical (MLEM), and model-based (MBCT) CT reconstruction.(experimental data obtained with 50 μ m thick scintillator screen and L/D 142).

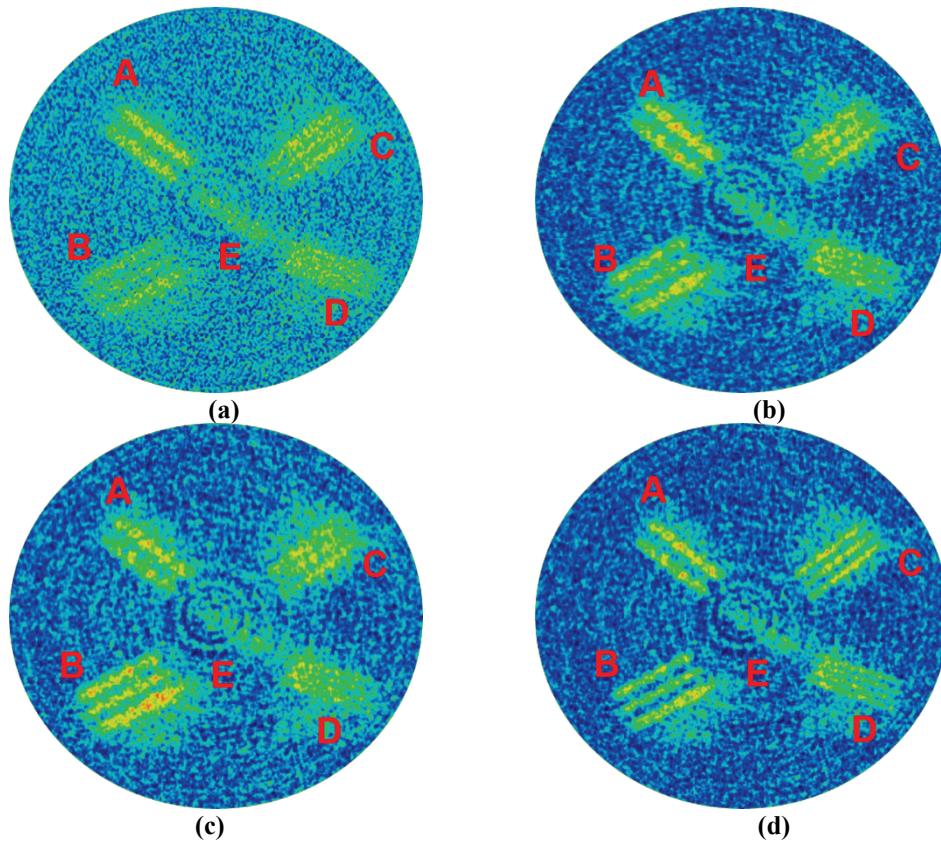


Figure 4.53. CT reconstruction of R-phantom with (a) analytical FBP, (b) algebraic SIRT, (c) statistical MLEM, and (d) model based technique obtained with 250 μ m scintillator at L/D 142 (color representation for the enhanced illustration of the bar pattern for validation of the spatial resolution).

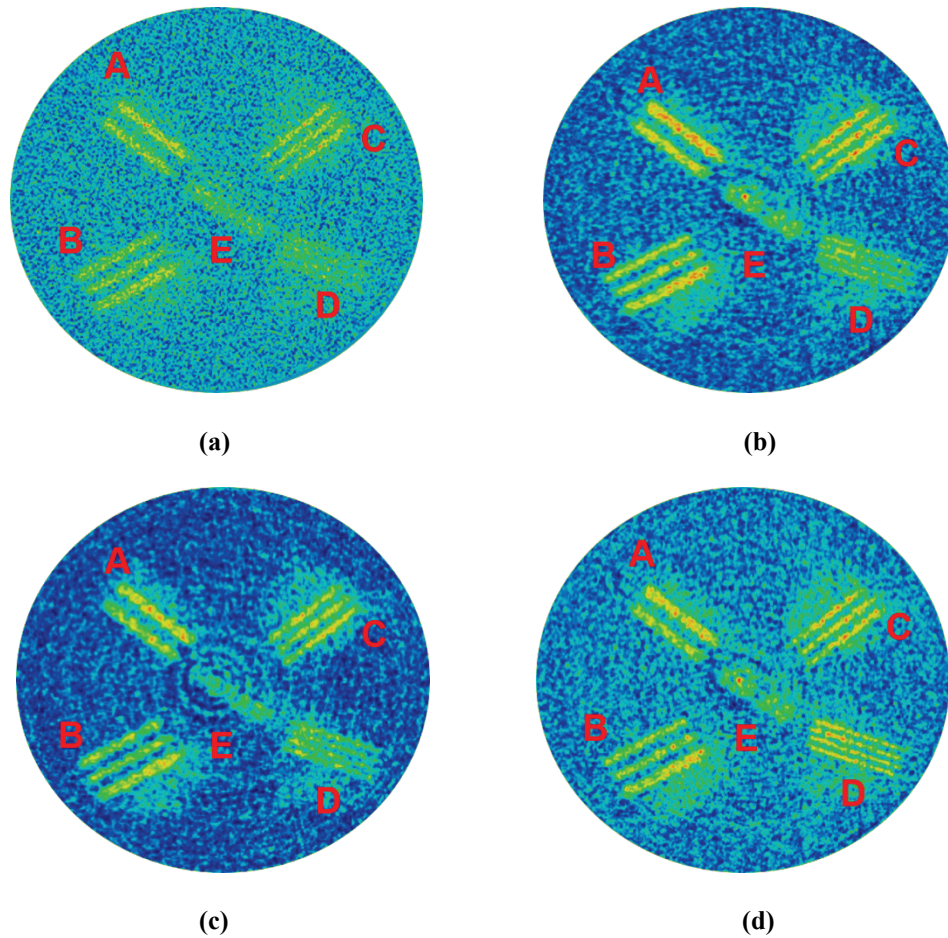


Figure 4.54. CT reconstruction of R-phantom with (a) analytical FBP, (b) algebraic SIRT, (c) statistical MLEM, and (d) model based technique obtained with 50 μm scintillator at L/D 142 (color representation for the enhanced illustration of the bar pattern for validation of the spatial resolution).

It can be quantitatively observed from the MTF data in Figure 4.52 that spatial resolution is improved with the model-based technique as compared to when using the traditional CT reconstruction techniques. Qualitative validation was performed with the V-phantom. It can be observed that, in Figure 4.53, (a-c) the 250 μm bar pattern is visible while 200 μm bar pattern is marginally distinguishable. Which suggests that the spatial resolution is closer to 200 μm . In Figure 4.54, (a-c) 150 μm bar pattern is clearly discernable while 100 μm bar is not, suggesting the spatial resolution is more than 100 μm . The improvement in spatial resolution can be clearly seen in 150 μm bar pattern of Figure 4.53, (d) and 100 μm bar pattern of Figure 4.54, (d) These

results are attributed due to the inclusion of system response function in forward projection model during reconstruction process, which provides a better estimate of the projection data, thus improving spatial resolution.

Chapter 5 Characterization and Implementation of a Dynamic Radiography System

5.1 Introduction

In the previous chapters, discussion was limited to a static neutron radiography where the state of an object was static in nature with time. Most real-time applications involve time scales that are much shorter than typical exposure time for static imaging like films or IP. However, these dynamic events can be explored in real time at high resolution with a scintillator-CCD based system non-invasively. In this work, capability of dynamic imaging was demonstrated by visualizing microbubbles in real time. Computational fluid dynamics simulation was performed to estimate the bubble diameter and behavior. A phantom was designed and manufactured to generate such bubbles. A neutron imaging system was characterized and optimized for such investigation. Additionally, radiographs were processed and segmented to quantify the bubble diameter.

5.2 Dynamic Neutron Radiography

Neutron imaging can be easily extended for the study of the dynamic occurrence as it develops in real-time. Non-destructive examination of dynamic events may help us to understand, explore and model the important prospect of kinematic actions. Sensitivity of neutrons toward the hydrogenous material, together with capability to observe dynamic events opened up a plethora of applications where neutron imaging can be used as an investigation probe. Often, requirement arises to observe these phenomena when covered with visually opaque metal enclosures, thus making it impossible to obtain information by non-invasive techniques. Non-invasive techniques like neutron imaging can be used to obtain the necessary information in such circumstances. These applications may include characterizing the structure, morphology, and hydrogen dynamics inside a fuel cell for the development of efficient cell devices [156]. Movement of water and other fluids

in rocks or concrete for the purpose of reservoir characterization in petroleum engineering or preservation of building strength respectively [157]. Sorptivity and diffusivity of a sandstone can be also characterized by visualizing the water imbibition [158]. Hydraulic parameters are important for petro-physical investigation in geology and petroleum engineering studies [159]. Dynamic neutron imaging has also been applied for an investigation of the water flows in soil and water interface movement for the geothermal applications [160]. Spatial and temporal resolution are interconnected and limited by neutron flux and imaging system. Using the recent developed sCMOS technology along with the high neutron flux, neutron imaging has been used to observe chemical reactions, liquid metal flow and two phase flow [161-163]. In this work, a system characterization were performed to study spatial and temporal resolution performance. Simulation were performed to predict bubble behavior. In addition to visualization of the bubbles, image segmentation were performed to characterize and quantify the generated bubbles.

5.3 Nucleate Boiling and Micro Bubble Formation

Nucleate boiling is an efficient heat transfer process that is utilized in many industrial application including nuclear reactors. When a solid surface is superheated and in contact with liquid, bubbles can be formed from a location known as nucleation sites [164]. Nucleate boiling can occur in pool boiling and forced-convective boiling. Bubble dynamics is an important phenomenon in a nucleate boiling process, and it can affect the heat transfer coefficients. Thus, predicting an accurate heat transfer coefficient can be correlated with the measurement of precise bubble diameter during the process. In general, bubble generation process can be divided into three steps as shown below:

1. Formation of nucleation sites on the heating surface.

2. The growth of the bubbles at the nucleation sites up-to-the moment of departure from the heating surface
3. Detachment from the nucleation sites and further growth through the layer of the liquid.

Nucleation can be classified into homogeneous and heterogeneous modes. In homogeneous nucleation, the unstable nuclei from which the bubble starts growing are formed by random fluctuations in local energy in the superheated liquid. Heterogeneous nucleation occurs when pre-existing vapor spontaneously grows and generates vapor bubbles. The presence of trapped gas or vapor in small cavities on heating surface starts a heterogeneous nucleation process. The heat transfer mechanism and bubble activity specifically bubble departure diameter on a heated surface can be correlated. Thus empirical relations that are used to predict heat transfer coefficients are related to bubble departure diameter. An effort to predict bubble departure diameter can be seen as early as 1935. Fritz derived simple correlations for bubble departure diameter with surface tension and buoyancy force. Cole and Rohsenow correlated bubble departure diameter for various fluids at low pressure, whereas Kacamura and Ishii developed a correlation at high pressure. A pressure dependent correlation for bubble departure diameter was proposed by Unal. Kiper described a method for determining the bubble departure diameter in saturated nucleate pool boiling [68], [165], [166]. Diameter of such bubbles depends on heat flux and mixture constituents and usually are in between 1 mm and 3.5 mm [165], [167]. It can be observed that, although many empirical correlations exist to predict the heat transfer coefficients, they are often conflicting [165], [168], [169]. Thus, capability of visualization of these micro-bubbles with high resolution by neutron imaging system would be beneficial for such investigations. In this work, we will generate and visualize similar size bubbles to demonstrate the feasibility of such study and capability of the developed high-resolution neutron imaging system to visualize dynamic phenomenon.

5.3.1 Micro Bubble Generation

Bubble formation in a submerged liquid has a wide variety of application including nuclear reactor as it can mimic bubble departure in nucleate boiling phenomenon. Thus, controlling an accurate bubble size is important for simulating such events. Bubble columns are usually used for multi-phase research studies. Numerous experimental and numerical studies have been developed to characterize bubble formation and growth [170-172]. Liquid properties including density, surface tension and viscosity can affect bubble size, growth, and departure [173]. When a bubble is generated from the submerged orifice within a liquid, primary force that contributes to detach bubble from the orifice is the buoyancy force. Other forces that affect bubble dynamics are surface tension force, drag force, and liquid inertia force. A surface tension force acts along the edges of the orifice, viscous drag force and liquid inertia force acts against the buoyancy force and tries to restrain the growth of the bubble at the orifice. When quasi-steady bubble formation occurs, surface tension is the only restraining force, while viscous drag and the inertial forces gradually become dominant with the increase in the rate of gas flow into a bubble. Thus, bubble diameter should be greater than that of the orifice diameter by a significant amount to overcome these forces at the time of the de-attachment as shown in Figure 5.1.

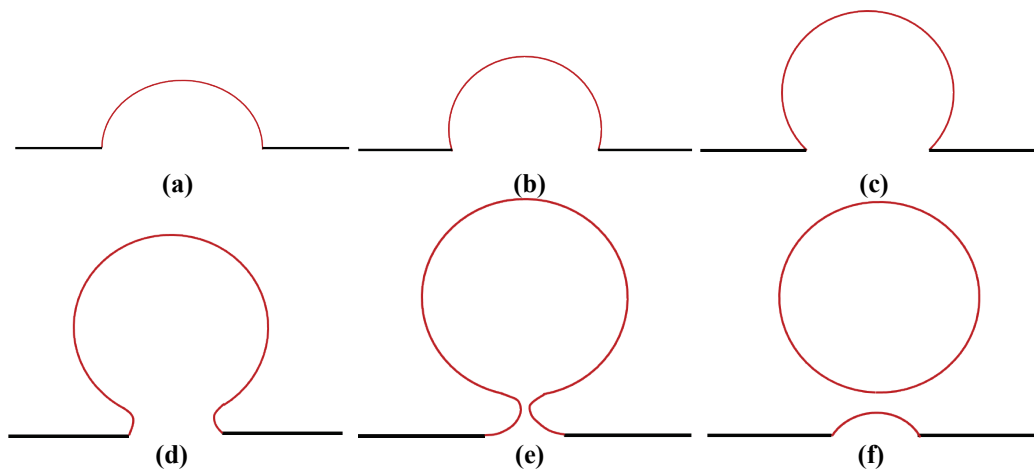


Figure 5.1. Illustration of bubble formation stages, (a) bubble birth, (b, c) bubble expansion, (d) neck formation, (e) bubble lift-off, and (f) bubble de-attachment [174].

The bubble forms at the tip of orifice increase in size until the buoyancy force equals with surface tension force that holds the bubble on tip [175]. At this condition, equating the two forces we get,

$$\frac{4}{3}\pi R_b^3(\rho_w - \rho_a)g = 2\pi R_o\gamma \quad (5.1)$$

Where, R_o and R_b are the radius of the orifice and the bubble respectively, ρ_w and ρ_a is the density of water and air respectively, g is the gravitational acceleration constant and γ is the surface tension. The value of the parameters are,

$$\rho_w = 997 \text{ kg/m}^3, \rho_a = 0.98 \text{ kg/m}^3, \gamma = 71.97 \times 10^{-3} \text{ dynes/cm}$$

Using, the values

$$R_b = R_o^{1/3} \left[\frac{3}{2} \times \frac{71.97 \times 10^{-3}}{997 \times 9.8} \right]^{1/3} m \quad (5.2)$$

$$R_b = R_o^{1/3} \times 2.2271 \times 10^{-4} m \quad (5.3)$$

$$R_b = 223 \times R_o^{1/3} \mu m \quad (5.4)$$

Thus, it can be observed that the generated bubble size is much bigger than the orifice size. For example, a 50 μm diameter orifice can generate 1.3 mm diameter bubble, which is illustrated in Figure 5.2.

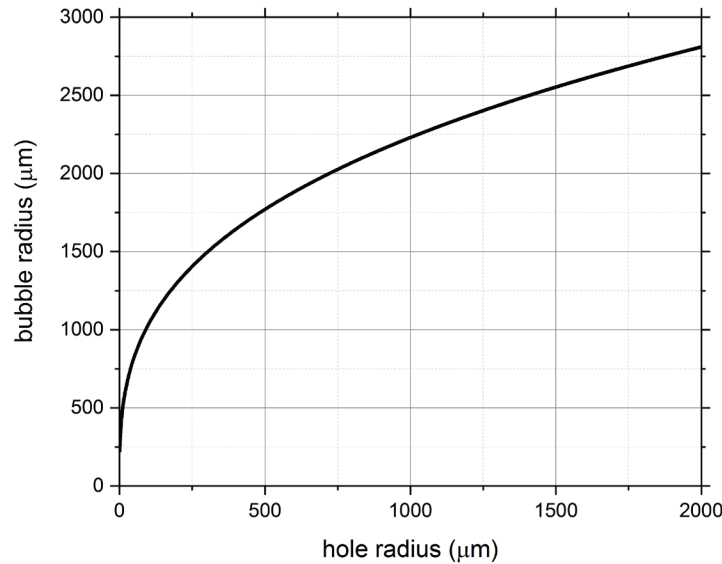


Figure 5.2. Bubble radius with orifice radius 0 μm - 2000 μm .

5.4 CFD Simulation Model for Micro-Bubble Generation

Computational fluid dynamics (CFD) is a technique that allows modeling and simulation two-phase flows to estimate and characterize different properties. Numerical simulations were performed with the CFD module of COMSOL Multiphysics package to visualize bubble formation process. Numerical simulations were necessary for designing of a phantom specifically to determine the orifice size and separation length between them. Orifice separation size was a necessary parameter to prevent bubble coalescence and to generate a predetermined bubble size.

The model is implemented in COMSOL Multiphysics CFD module which uses Navier-Stokes theorem along with the level set method for the simulation of micro-bubble generation [176]. The simulation geometry is 50 mm in height, 20 mm in width and 10 mm in depth. Three-dimensional geometry is shown in Figure 5.3 (a) and a two-dimensional slice obtained at center of the geometry is shown in Figure 5.3 (b). Container material was made of aluminum and holds water and air. Material used in the simulation and their dimensions are shown in Table 5.1. Laminar two-phase flow along with the level set method was used for the study. First step of simulation is phase initialization process which initializes level set function and then a time-dependent step simultaneously solves the Navier-Stokes equations and the level set equations. Linear P1+P1 discretization is used for the level set and laminar flow variables. The wetted wall is used for all the surface that may come into contact with the water or air. The inlet is selected as a surface of the hole and outlet is defined as an outer surface of air. Description of the mesh used in the simulation geometry is shown in Table 5.2.

The simulation was performed for varying distance between the holes. Up to 1 second and 1 *ms* time steps were selected. Meshed geometries are shown in Figure 5.4. The holes are located at the bottom of geometry and air was injected through a hole. Holes are shown in Figure 5.5.

Injection profile of the air is a smoothed step function as shown in Figure 5.6. It can be observed that, air supply is gradually increased to 9 μs and reached the maximum velocity at 11 μs . The smoothed function is required to prevent numerical stability. The simulations were performed in Fission High-Performance computer (HPC) cluster. Each simulation were parallelized in 80 cores and average runtime was 22 hours.

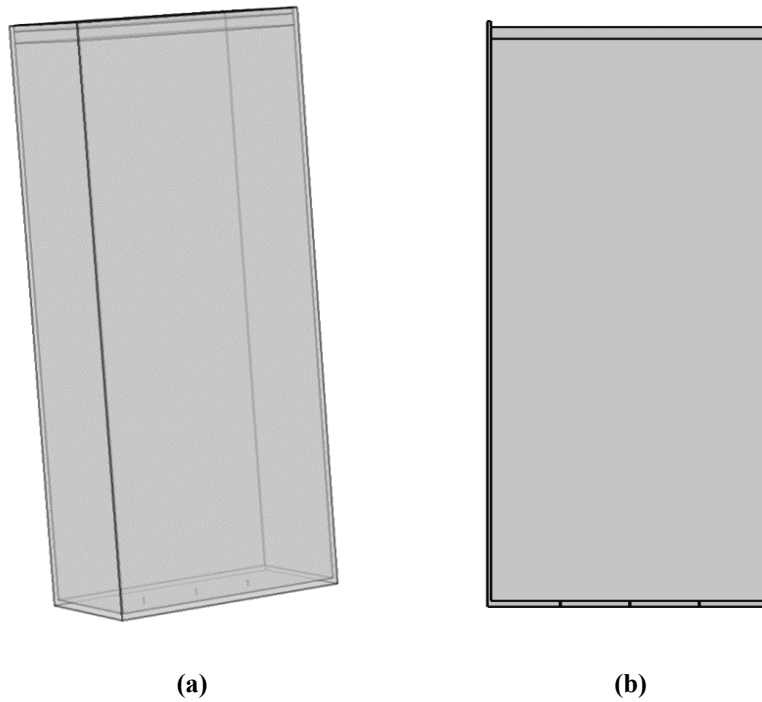


Figure 5.3. COMSOL simulation model (a) 3D phantom, and (b) 2D central slice.

Table 5.1. Dimension of the simulation phantom

Material	Dimensions (height x width x depth)
Water	45 x 20 x 10 (mm x mm x mm)
Air	5 x 20 x 10 (mm x mm x mm)
Aluminum	50 x 25 x 15 (mm x mm x mm)

Table 5.2. Mesh description used for the COMSOL CFD simulation

Mesh attributes	Description
Maximum element size (mm)	0.05
Minimum element size (mm)	0.02
Maximum element growth rate	1.15
Curvature factor	0.3
Resolution of narrow region	2

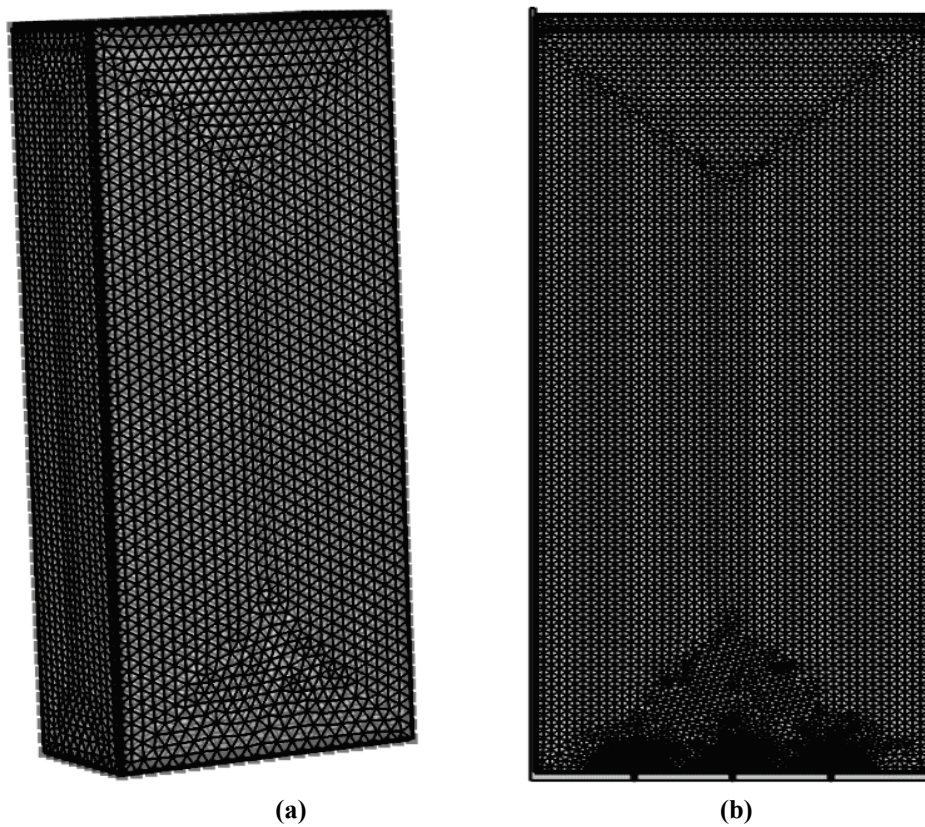


Figure 5.4. Mesh of the geometry (a) 3D phantom, and (b) 2D central slice.

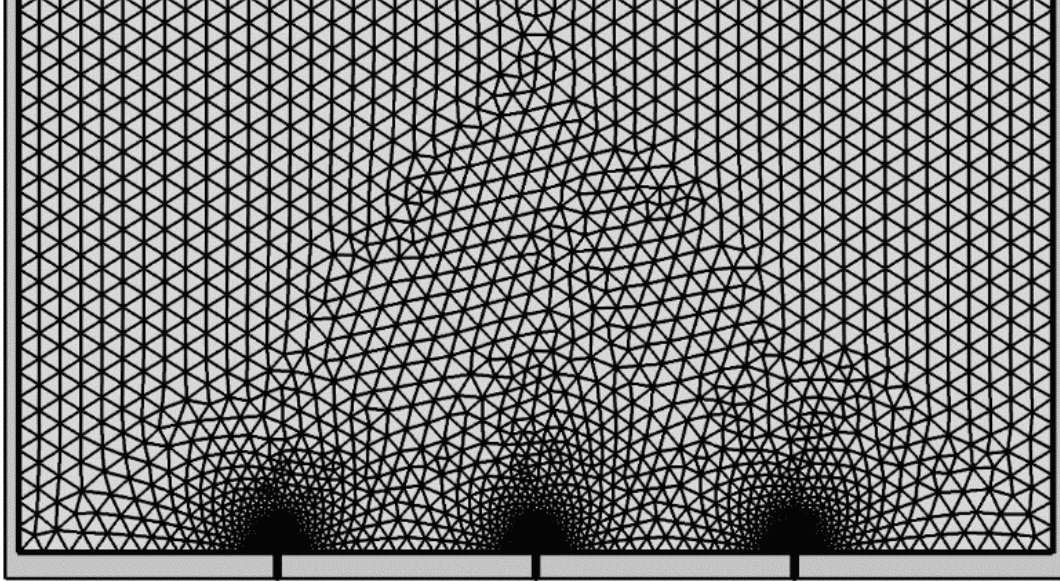


Figure 5.5. Meshed geometry illustrating the hole.

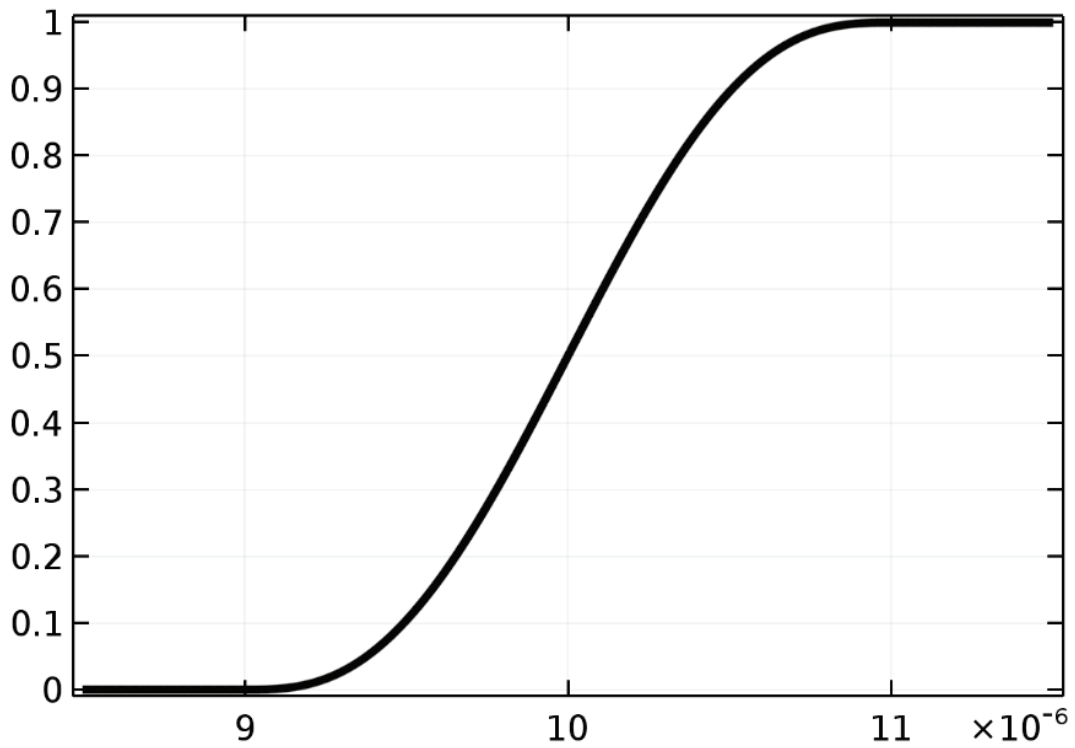


Figure 5.6. Bubble injection profile (horizontal axis is in microsecond).

5.4.1 CFD Simulation Results

In the first simulation, air is injected through a single 50 μm diameter orifice to observe bubble growth process. Snapshot of a single bubble growth process is shown in Figure 5.7.

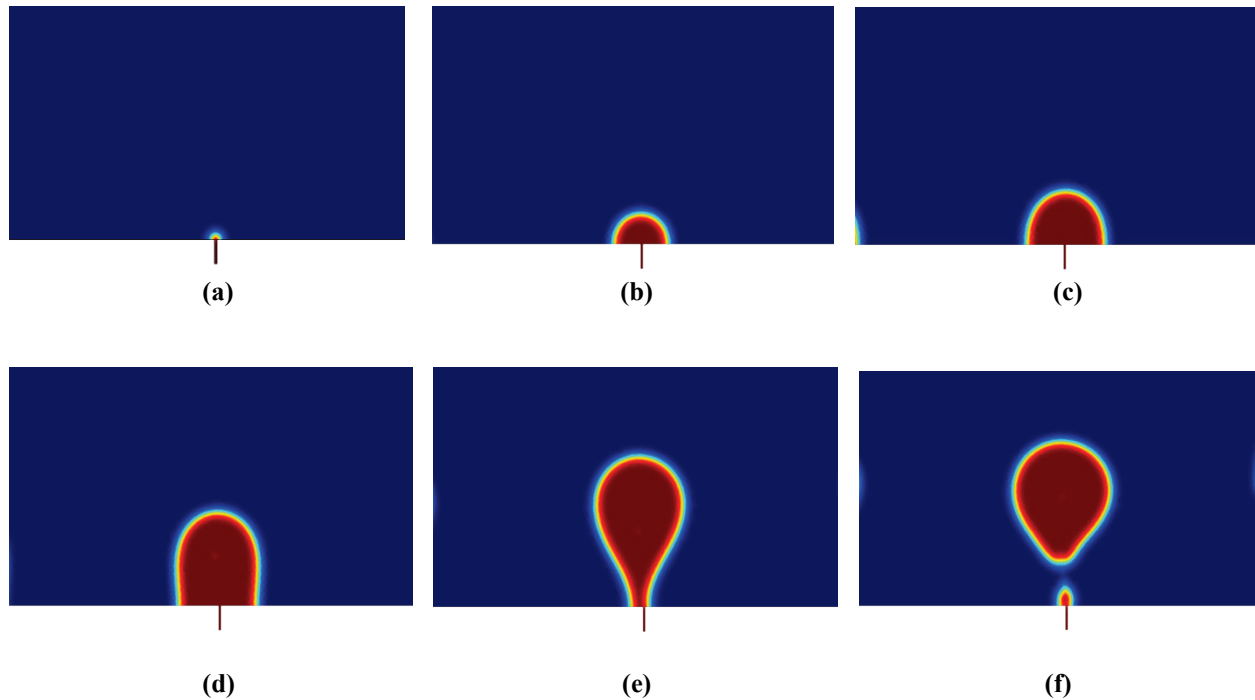


Figure 5.7. Illustration of bubble growth process for time (a) 0.001 s, (b) 0.025 s, (c) 0.075 s, (d) 0.150 s, (e) 0.190 s, and (f) 0.196 s.

Next set of the simulation was performed with multiple 50 μm holes separated by 1 mm, 2 mm, 3 mm, 4 mm and 5 mm distance to illustrate merging phenomenon during the growth. Simulation results are presented to illustrate bubble behavior. It can be observed from Figure 5.8, Figure 5.9, Figure 5.10, Figure 5.11, and Figure 5.12 that bubbles are merged when separation distance is 4 mm or less. It can be observed from Figure 5.8 that when holes are 1 mm apart, all of them are merged to form only one bubble of larger size and continued to grow as a large bubble. As the separation between the holes are increased, it can be observed the bubbles are merged at 0.25 s, 0.48 s and 0.79 s for separation distance 2mm, 3 mm and 4 mm respectively.

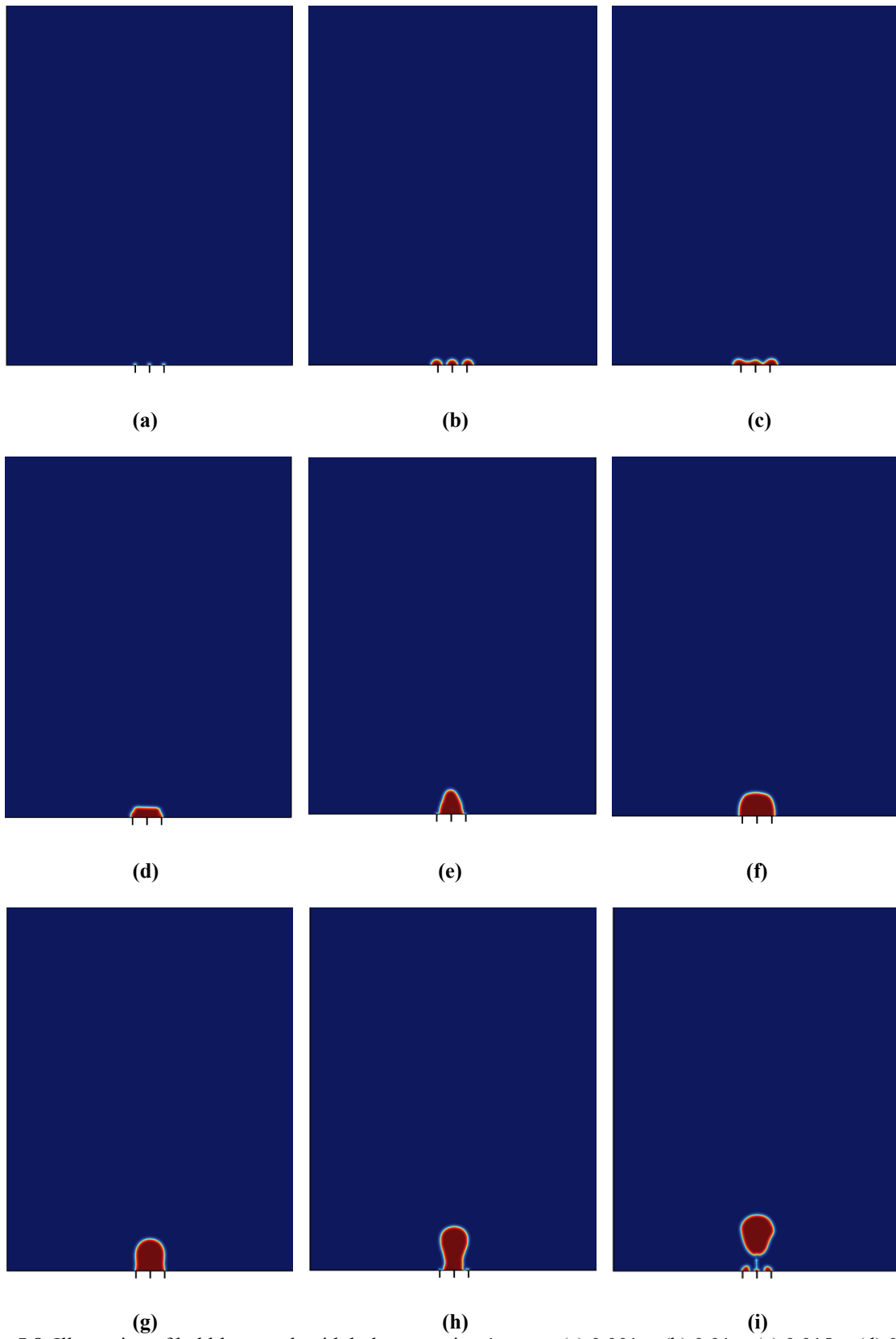


Figure 5.8. Illustration of bubble growth with hole separation 1 mm at (a) 0.001 s, (b) 0.01 s, (c) 0.015 s, (d) 0.021 s, (e) 0.03 s, (f) 0.05 s, (g) 0.06 s, (h) 0.07 s, and (i) 0.08 s.

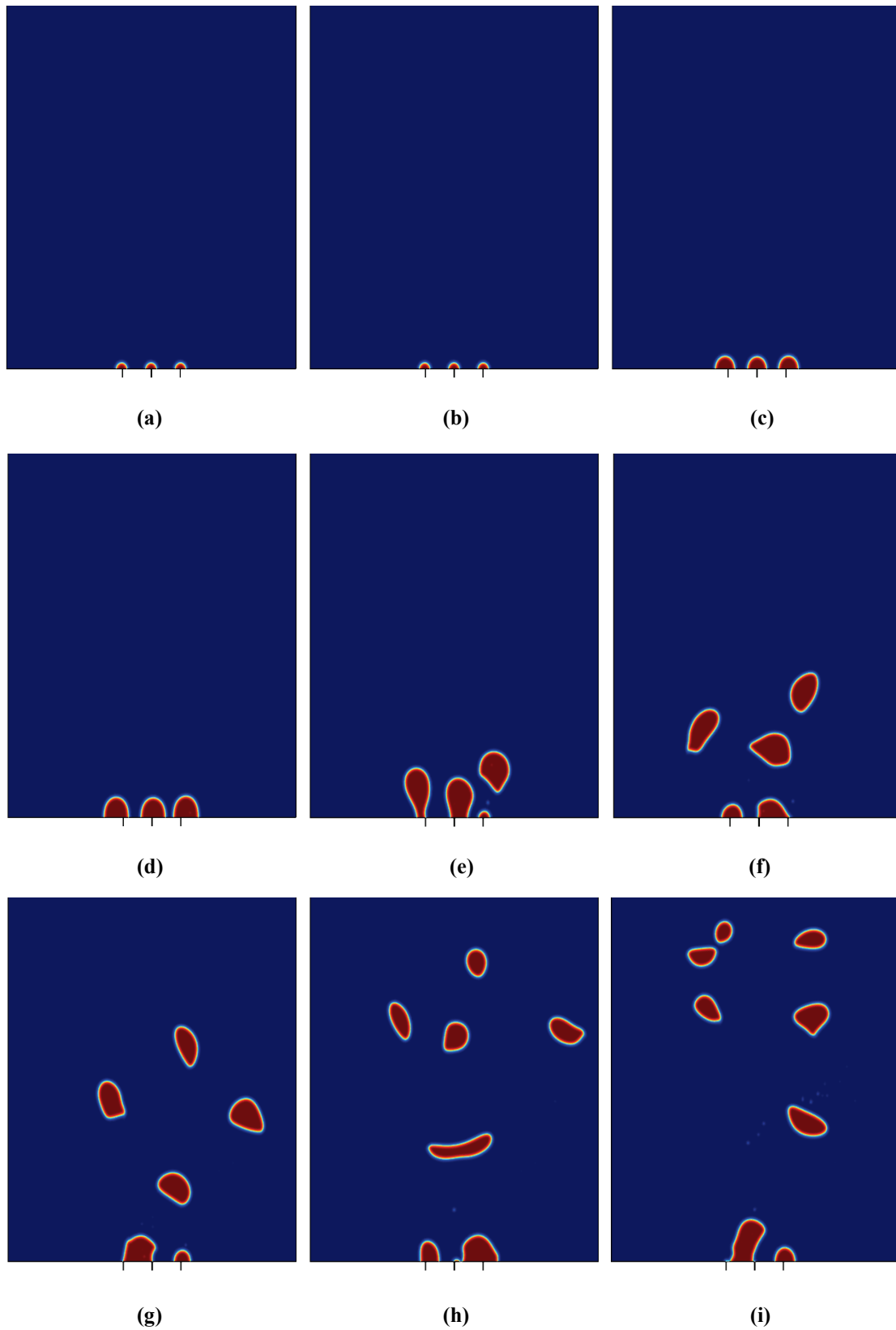


Figure 5.9. Illustration of bubble growth with hole separation 2 mm at (a) 0.01 s, (b) 0.02 s, (c) 0.05 s, (d) 0.1 s, (e) 0.2 s, (f) 0.25 s, (g) 0.31 s, (h) 0.39 s, and (i) 0.45 s.

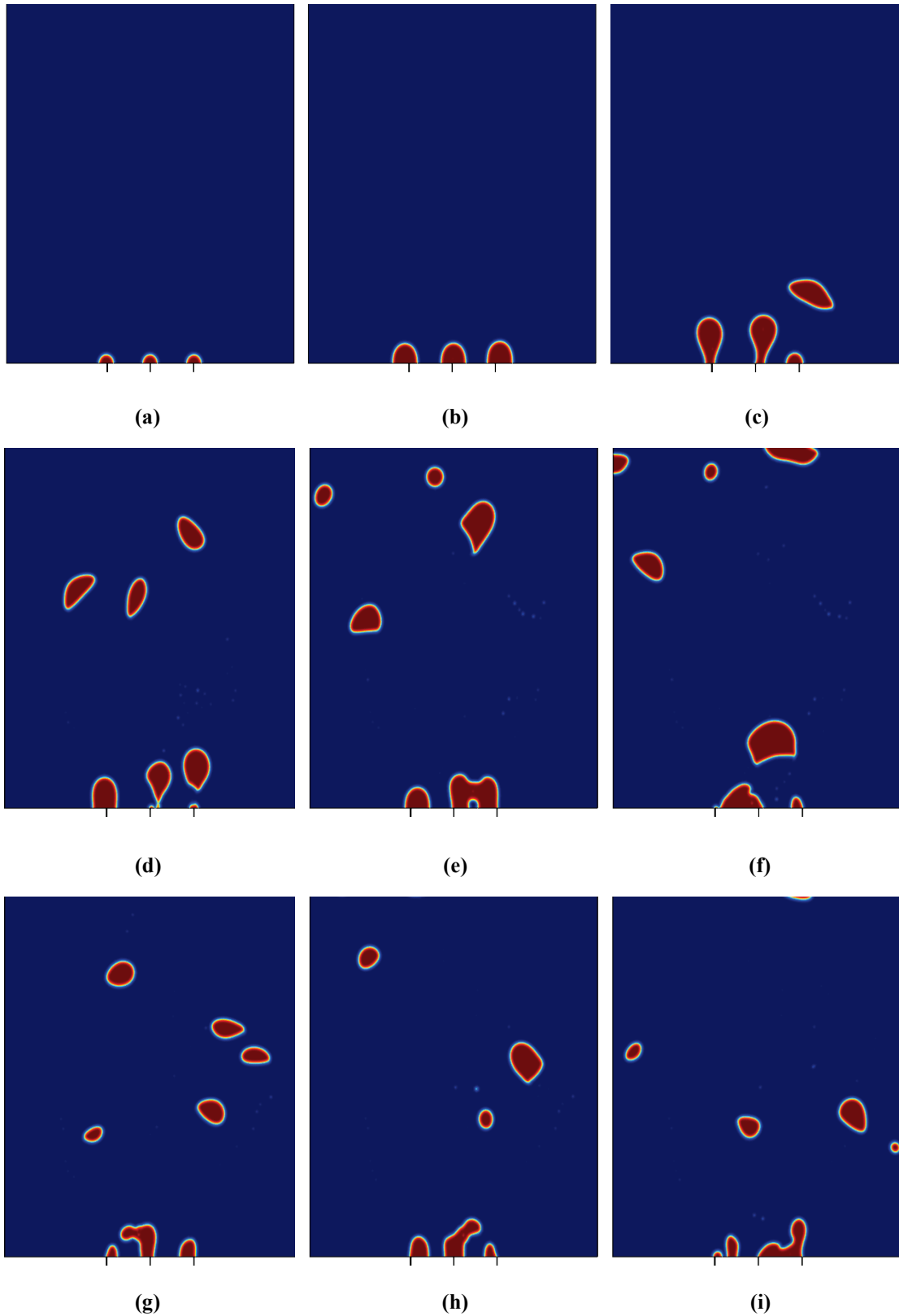


Figure 5.10. Illustration of bubble growth with hole separation 3 mm at (a) 0.02 s, (b) 0.1 s, (c) 0.2 s, (d) 0.35 s, (e) 0.48 s, (f) 0.52 s, (g) 0.75 s, (h) 0.85 s, and (i) 0.93 s.

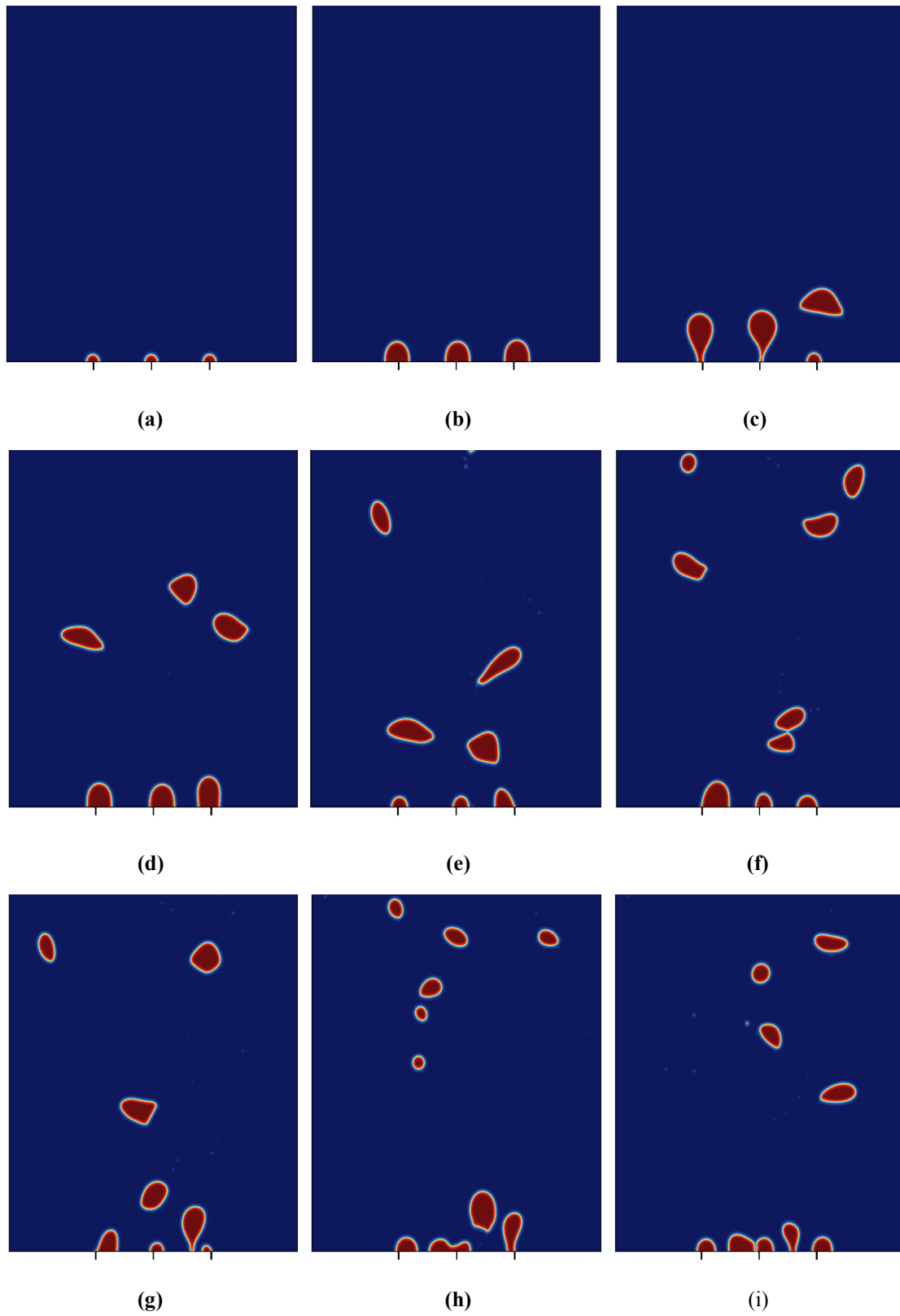


Figure 5.11. Illustration of bubble growth with hole separation 4 mm at (a) 0.01 s, (b) 0.1 s, (c) 0.2 s, (d) 0.3 s, (e) 0.4 s, (f) 0.5 s, (g) 0.6 s, (h) 0.79 s, and (i) 0.97 s.

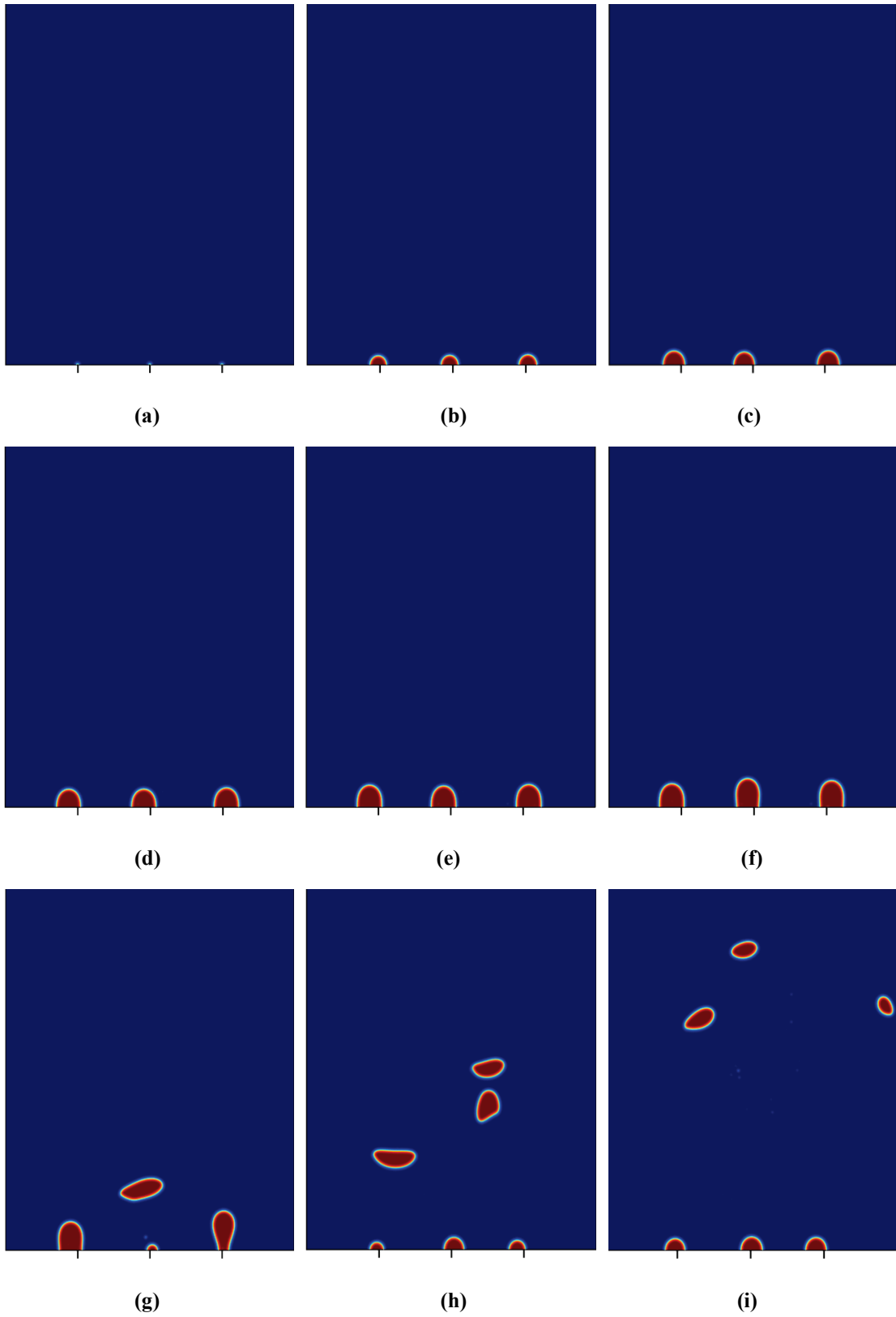


Figure 5.12. Illustration of bubble growth with hole separation 5 mm at (a) 0.001 s, (b) 0.1 s, (c) 0.2 s, (d) 0.3 s, (e) 0.4 s, (f) 0.5 s, (g) 0.6 s, (h) 0.7 s, and (i) 0.8 s.

5.5 Phantom Design

A phantom was designed to generate bubble in a water column. The phantom was made of aluminum and bubbles were generated by injecting air through 50 μm diameter holes. It has been observed that 5 mm separation were required to generate unmerged bubble. Size of the water column was 150 mm x 150 mm x 10 mm and each hole was separated by 5 mm. Aluminum tube and magnified sectional view of the holes is shown in Figure 5.13. The design of the phantom is illustrated in Figure 5.14. Designed phantom was manufactured and shown in Figure 5.15. The holes were magnified for the illustration and arrangement is shown in Figure 5.16. Magnified 50 μm holes are illustrated in Figure 5.17 (a). Grayscale threshold was performed for better visualization of holes as shown in Figure 5.17 (b).

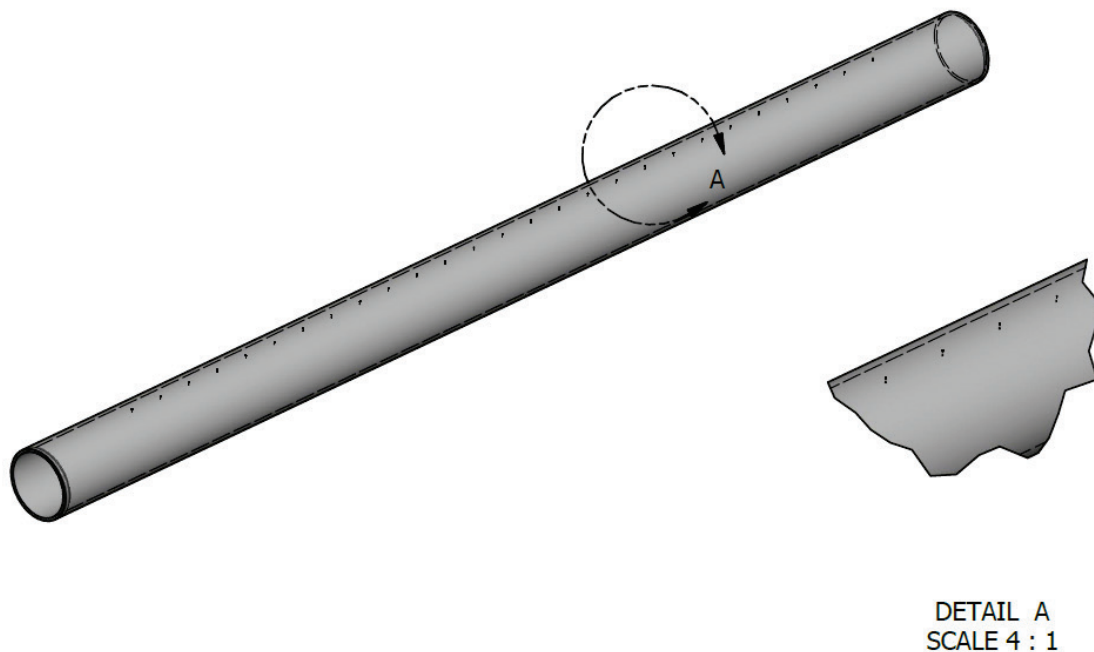
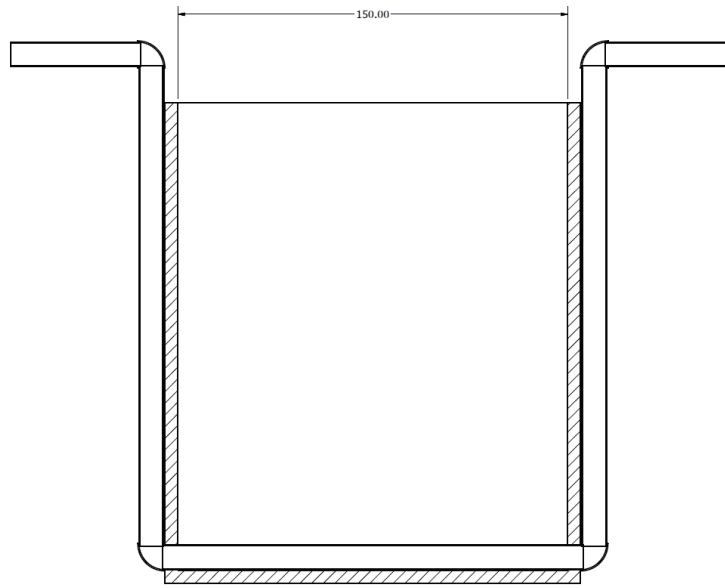
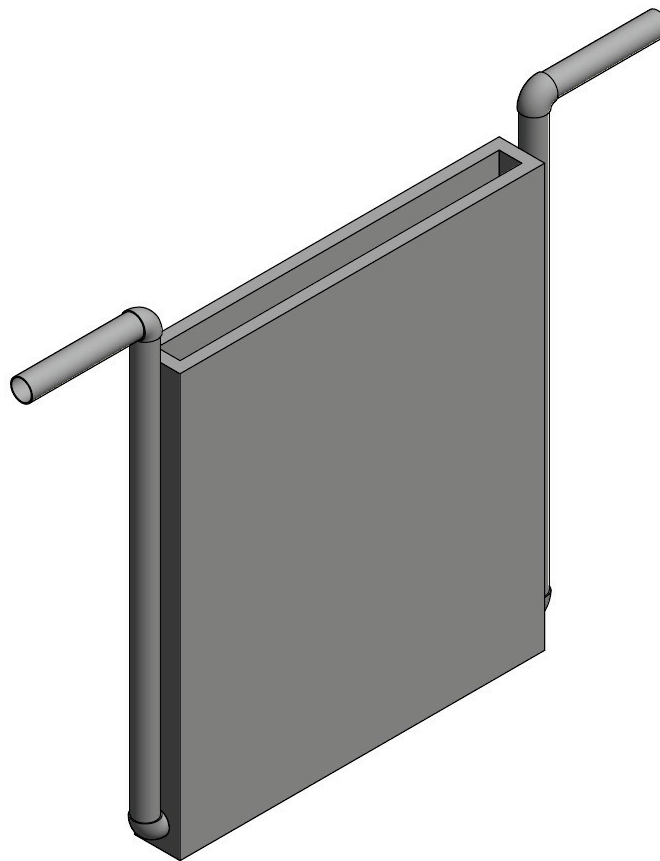


Figure 5.13. CAD drawing of the aluminum tube with 50 μm holes. The detail view illustrates the holes and the distances between them at 4:1 magnification scale.



(a)



(b)

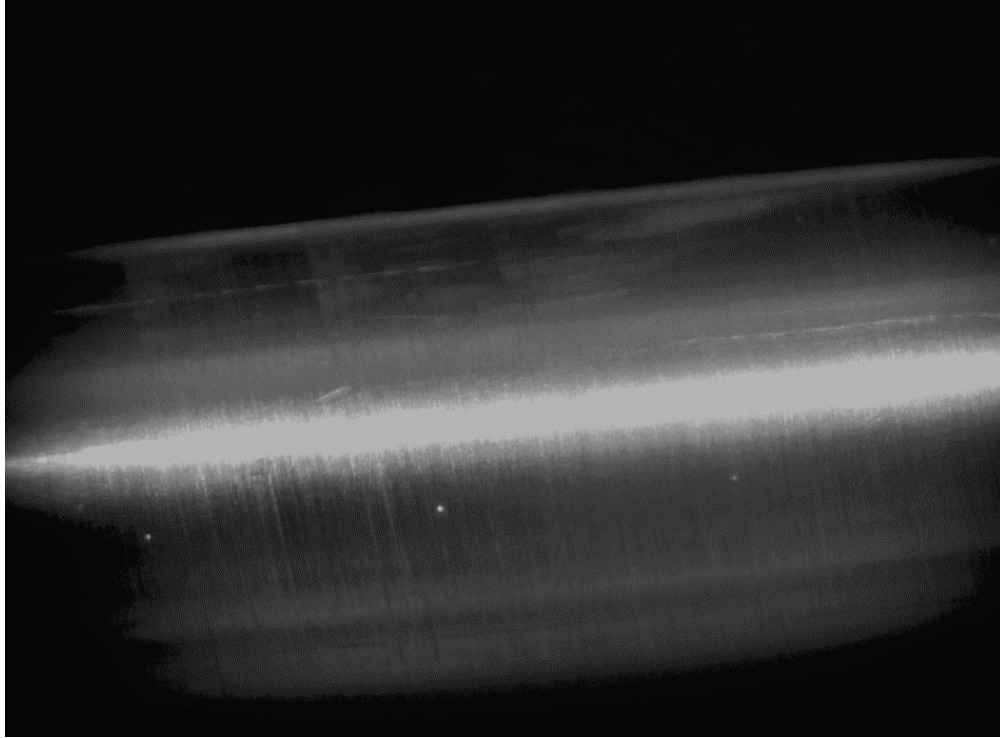
Figure 5.14. CAD drawing of the phantom showing air inlet and outlet and aluminum container for the water column, (a) 3-D drawing of the phantom, and (b) 2-D cross-section of the phantom along the center line.



Figure 5.15. Designed phantom for dynamic experiment showing air inlet, aluminum body, and an air outlet.



Figure 5.16. Experimental arrangement to view the 50 μm hole through magnifying lens and camera system.



(a)



(b)

Figure 5.17. Visualization of 50 μm hole for air injection into the water column, (a) magnified photographic view, and (b) grayscale threshold for better visualization of the holes.

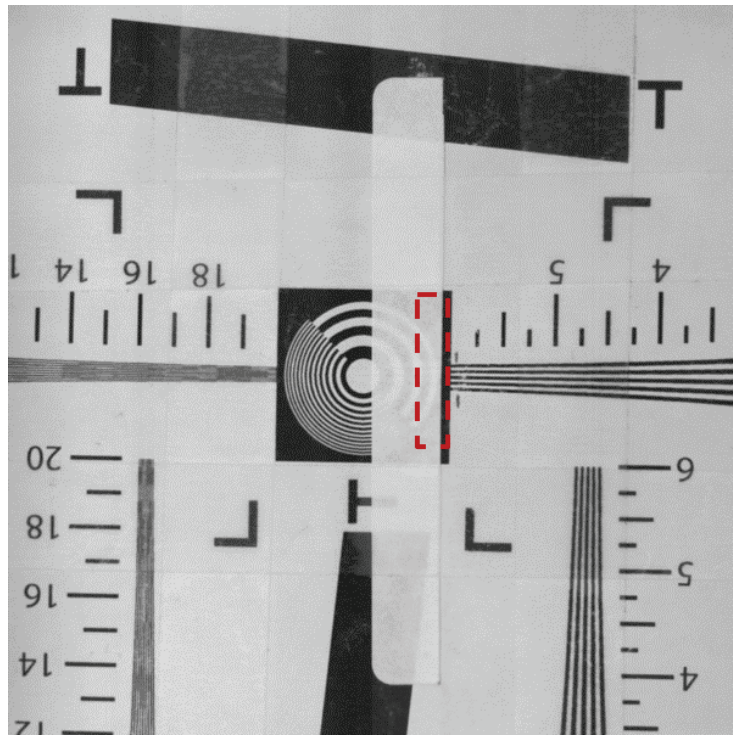
5.6 Experimental Results

Experiments were performed at the PULSTAR Neutron Imaging Facility to demonstrate the capability of dynamic radiography. Each component of the imaging system was characterized to determine optimum parameters for such dynamic study. Two types of lenses were selected and their performances are characterized by a light image obtained with normal condition outside neutron beam. Lenses are shown in Figure 2.14 and described in Table 5.3.

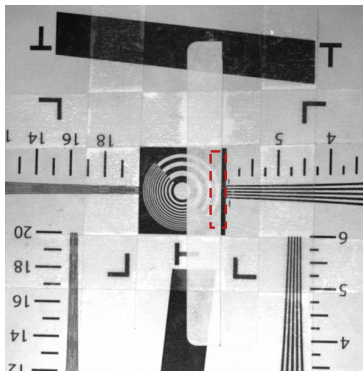
Table 5.3. Lens characteristics

Characteristics	Lens	
	Micro-NIKKOR 55mm	Micro-NIKKOR 200 mm
Focal length (mm)	55	200
Maximum aperture	f/2.8	f/4
Minimum aperture	f/32	f/32
Minimum focus distance	0.9 ft	1.6 ft
Focus mode	Manual	Manual/Auto
Lens groups	5	8
Maximum reproduction ratio	1:2	1:1

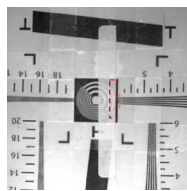
These two lenses were selected for their maximum aperture to achieve higher temporal resolution while maintaining better spatial resolution. Spatial resolution of these two lenses was characterized for different bin sizes 1x1, 2x2 and 4x4. The light images are shown in Figure 5.18 and Figure 5.19 with EMCCD binning 1x1, 2x2 and 4x4 respectively. These images are obtained with Nikkor 55mm and Nikkor 200 mm respectively. Highlighted area is used for calculation of spatial resolution and shown in Figure 5.20 and Figure 5.21.



(a)

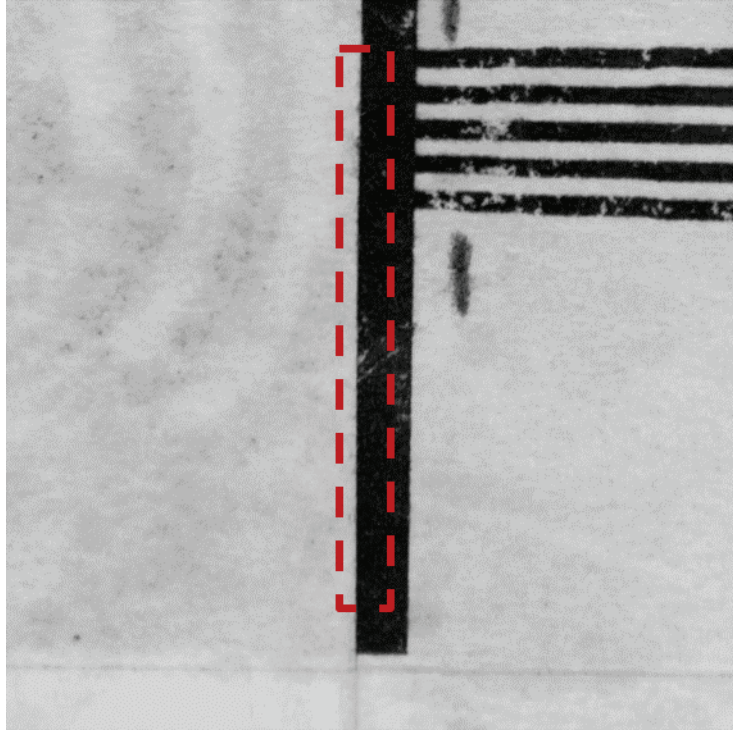


(b)

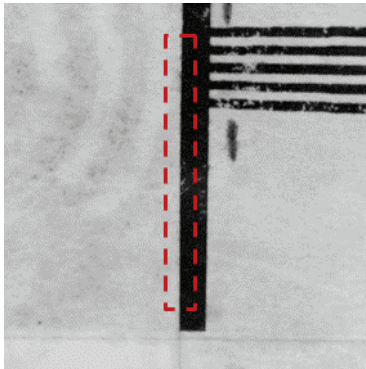


(c)

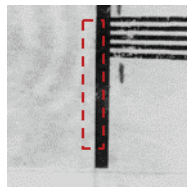
Figure 5.18. Light image obtained with Micro-NIKKOR 55 mm lens obtained with bin size (a) 1 x 1, (b) 2 x 2, and (c) 4 x 4 (image size shown is proportional to the pixel number).



(a)



(b)



(c)

Figure 5.19. Light image obtained with Micro-NIKKOR 200 mm lens obtained with bin size (a) 1 x 1, (b) 2 x 2, and (c) 4 x 4 (image size shown is proportional to the pixel number).

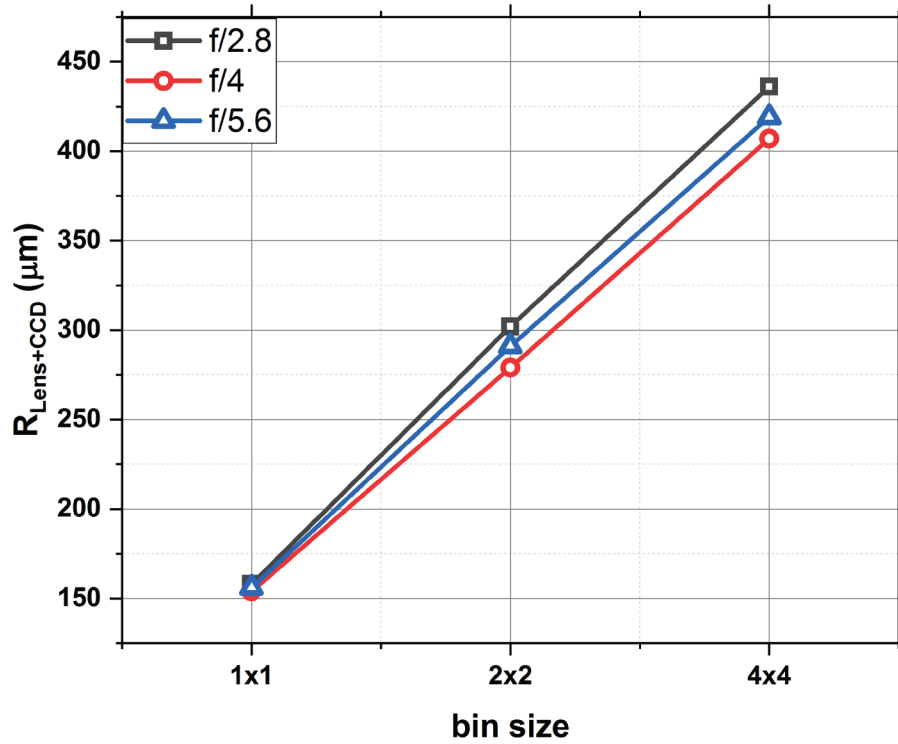


Figure 5.20. Spatial resolution of the Micro-NIKKOR 55 mm lens for EMCCD bin size 1x1, 2x2 and 4x4 as obtained from light images containing the paper edge.

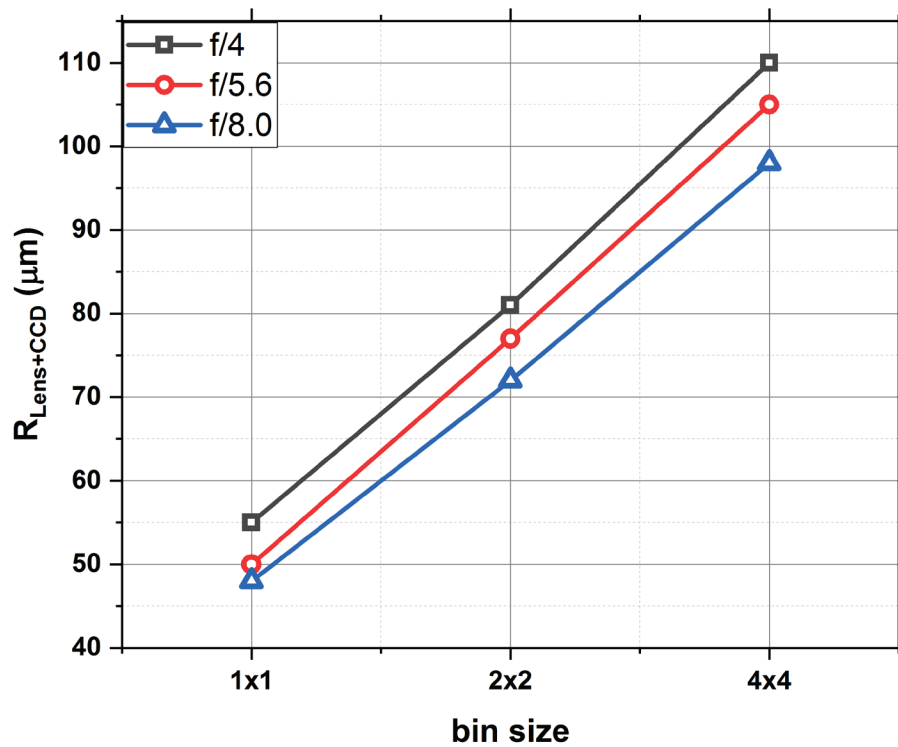


Figure 5.21. Spatial resolution of the Micro-NIKKOR 200 mm lens for EMCCD bin size 1x1, 2x2 and 4x4 as obtained from light images containing the paper edge.

Pixel size with Micro-NIKKOR 55 mm lens was $68 \pm 2 \mu\text{m}$ and Micro-NIKKOR 200 mm lens was $13 \pm 1 \mu\text{m}$ due to the achievable distance between the scintillator screen and focal plane of EMCCD. The system was then characterized with $50 \mu\text{m}$ and $250 \mu\text{m}$ scintillator. Total spatial resolution (R_T) as well as detector spatial resolution (R_D) was calculated from the radiograph image containing an edge. To calculate R_T , the edge was placed at same position where bubbles were generated. The R_T was characterized for L/D 142 and 73. Experimental arrangements are shown in Figure 5.22 and Figure 5.23.

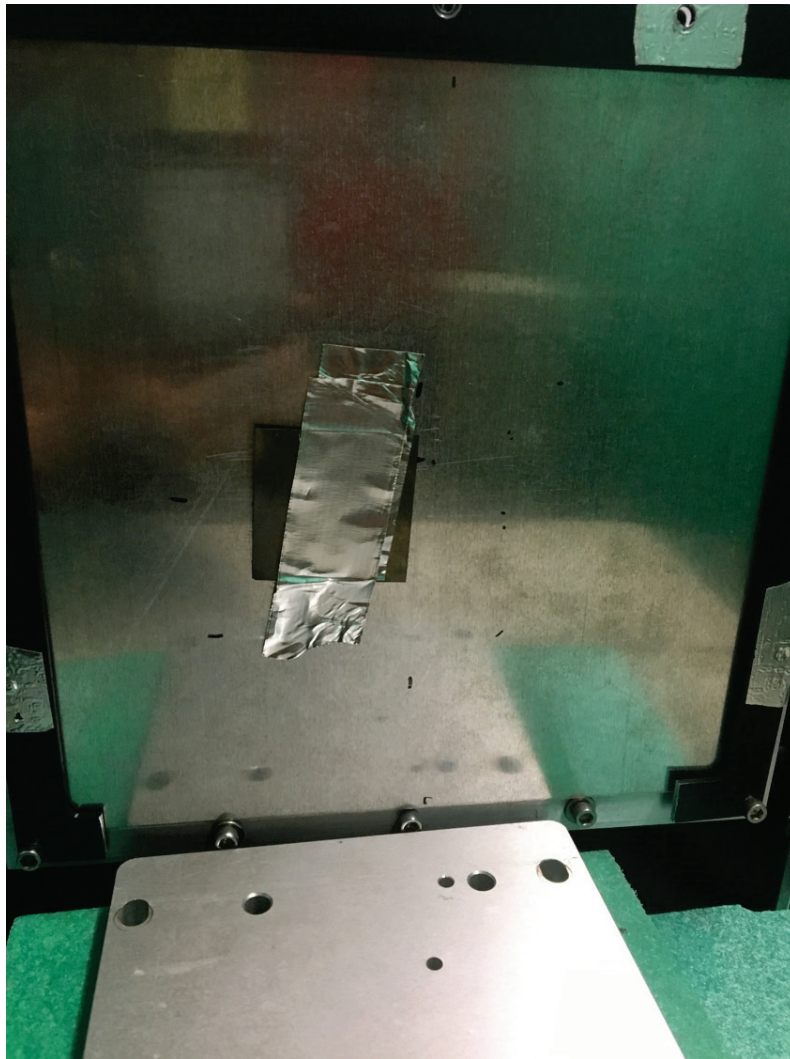


Figure 5.22. Experimental arrangement to calculate the detector spatial resolution by placing a Gadolinium edge on the scintillator.

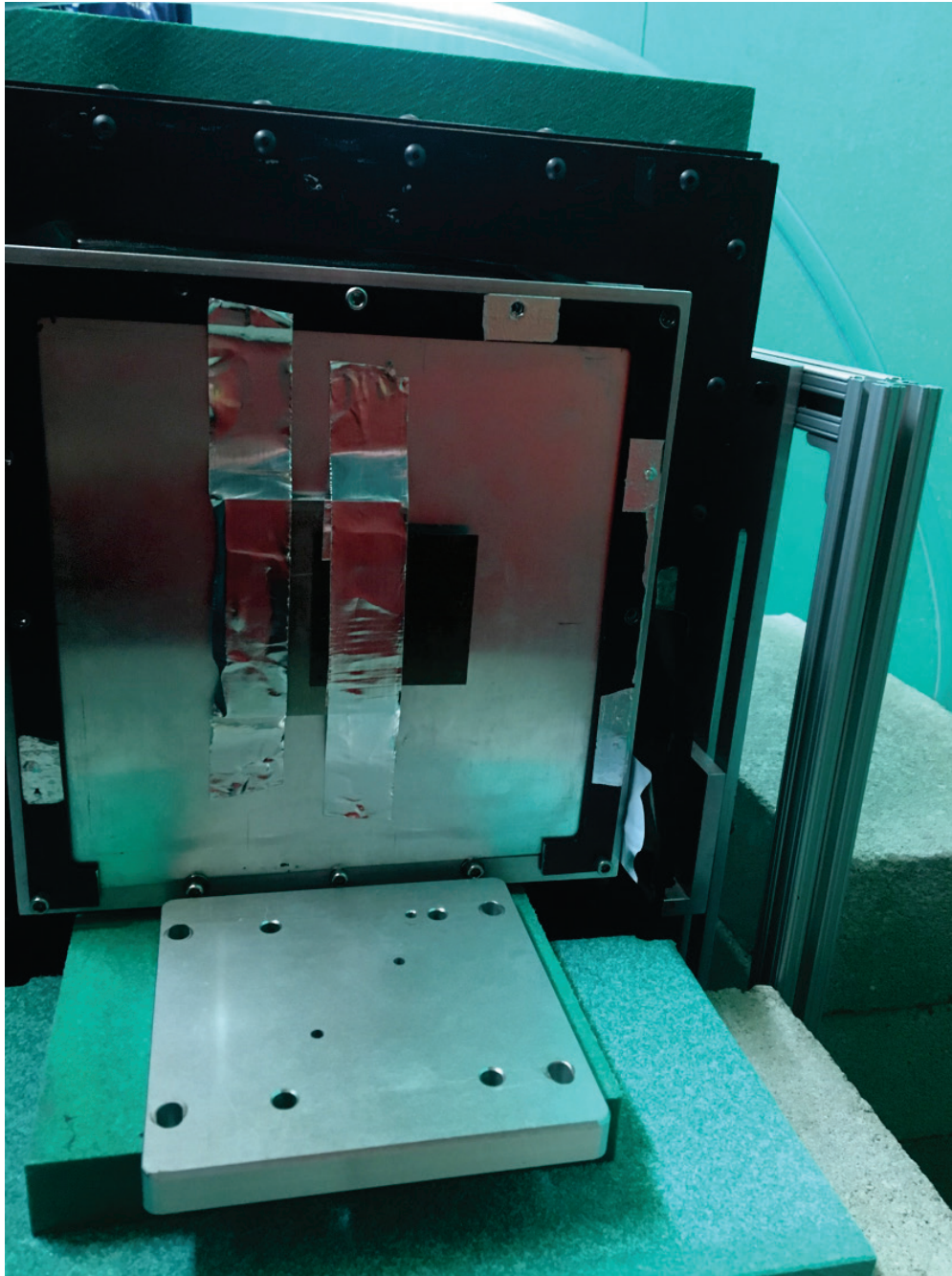
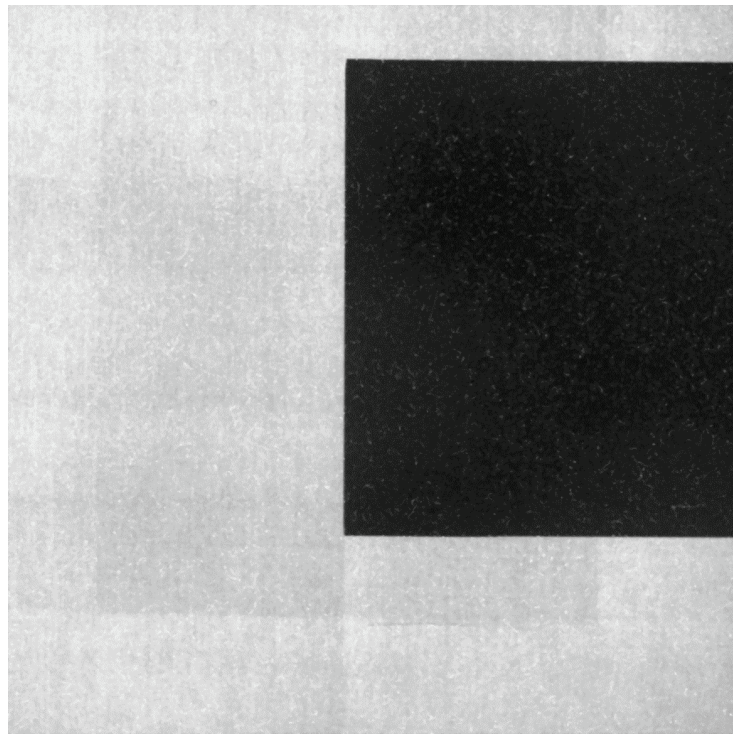
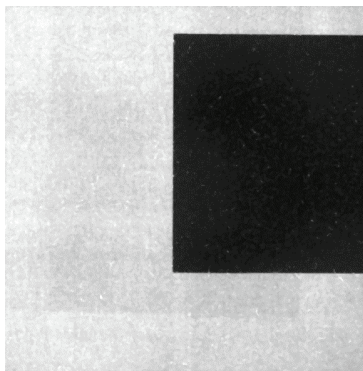


Figure 5.23. Experimental arrangement to calculate the total spatial resolution by placing the Gadolinium edge at 1 cm from the scintillator.

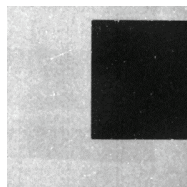
Obtained edge radiographs are shown in Figure 5.24 and Figure 5.25. These radiographs were obtained with 50 μm scintillator to calculate the total spatial resolution at L/D 73, 142 and detector resolution respectively. The calculated spatial resolution is shown in Figure 5.26 and Figure 5.27.



(a)

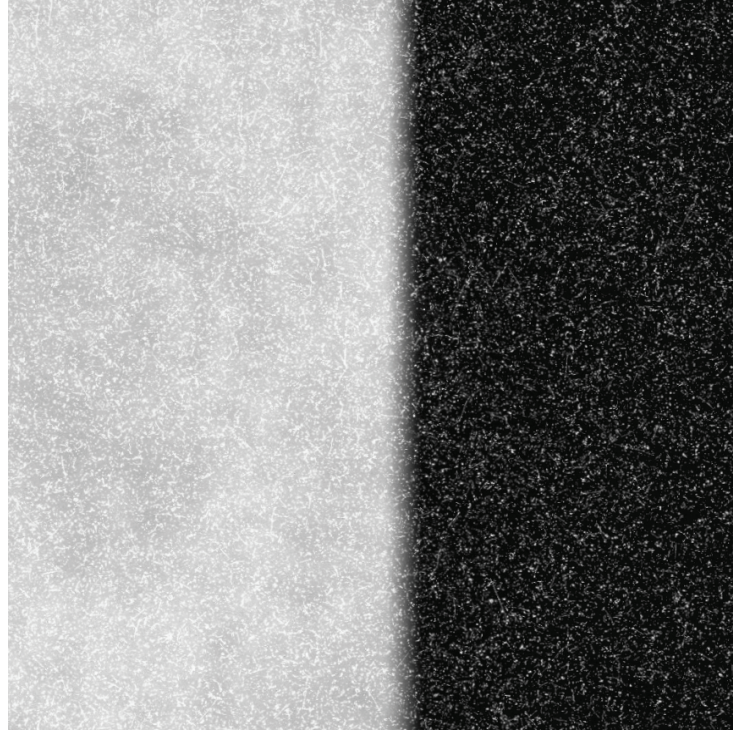


(b)

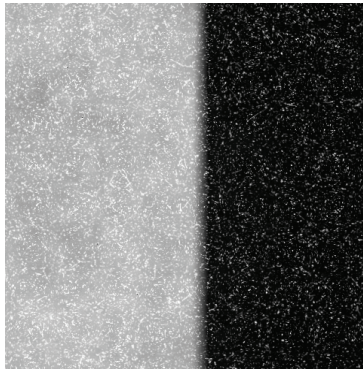


(c)

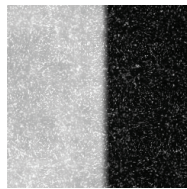
Figure 5.24. Edge radiographs obtained with $250\ \mu\text{m}$ ${}^6\text{LiF}:\text{ZnS}$ scintillator with Micro-NIKKOR 55 mm lens and aperture $f/2.8$ showing Gadolinium edge for $L/D\ 73$ and $d=1\ \text{cm}$ for bin size (a) 1×1 , (b) 2×2 , and (c) 4×4 . (image size shown is proportional to the pixel number).



(a)



(b)



(c)

Figure 5.25. Edge radiographs obtained with $250\ \mu\text{m}$ ${}^6\text{LiF}:\text{ZnS}$ scintillator with Micro-NIKKOR 200 mm lens and aperture $f/2.8$ showing Gadolinium edge for $L/D\ 73$ and $d=1\ \text{cm}$ for bin size (a) 1×1 , (b) 2×2 , and (c) 4×4 (image size shown is proportional to the pixel number).

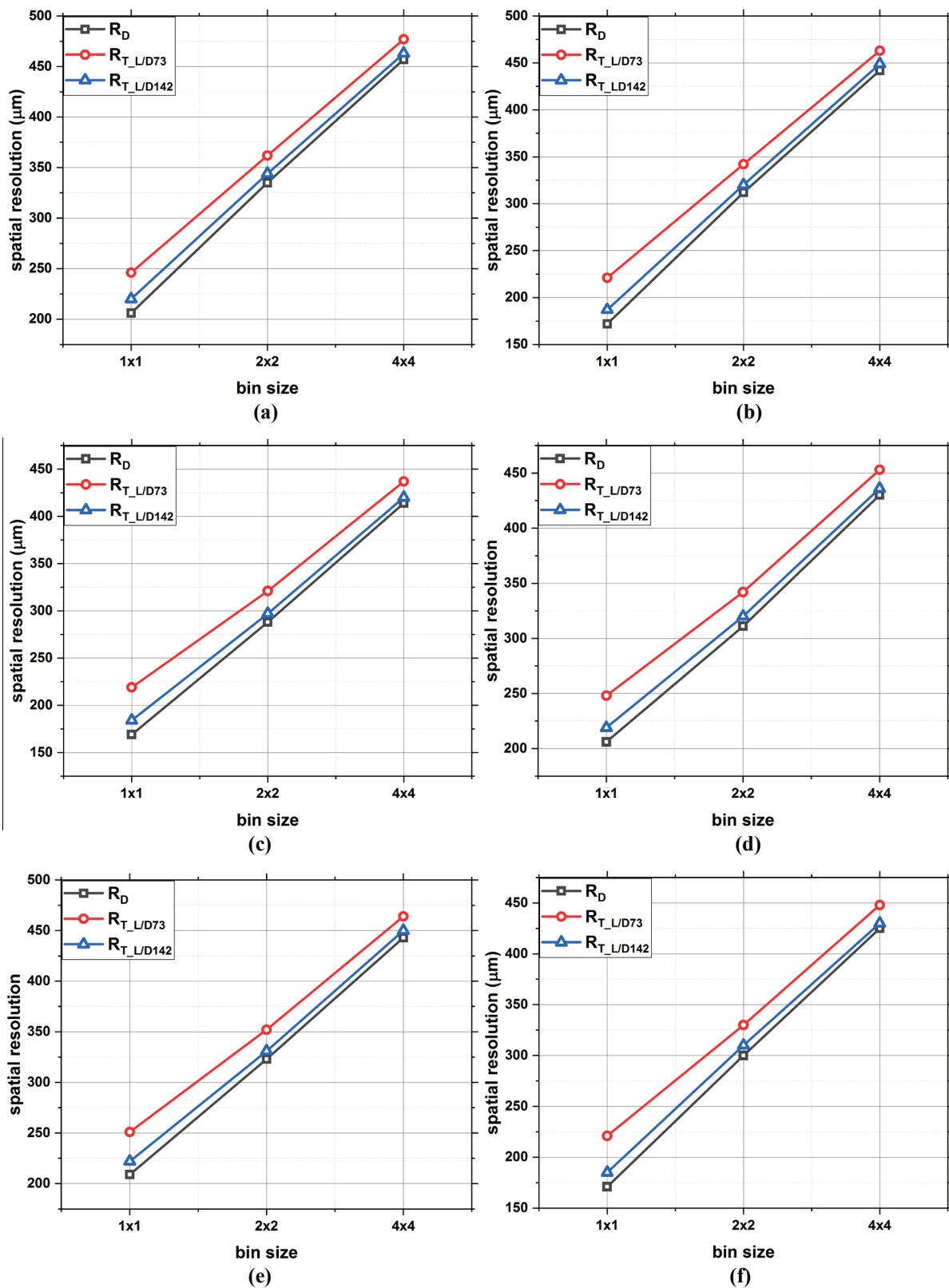


Figure 5.26. Spatial resolution of the neutron imaging system with Micro-NIKKOR 55 mm lens with 250 μm (left column) and 50 μm thick scintillator screen obtained with lens aperture (a, b) $f/2.8$, (c, d) $f/4$, and (e, f) $f/5.6$.

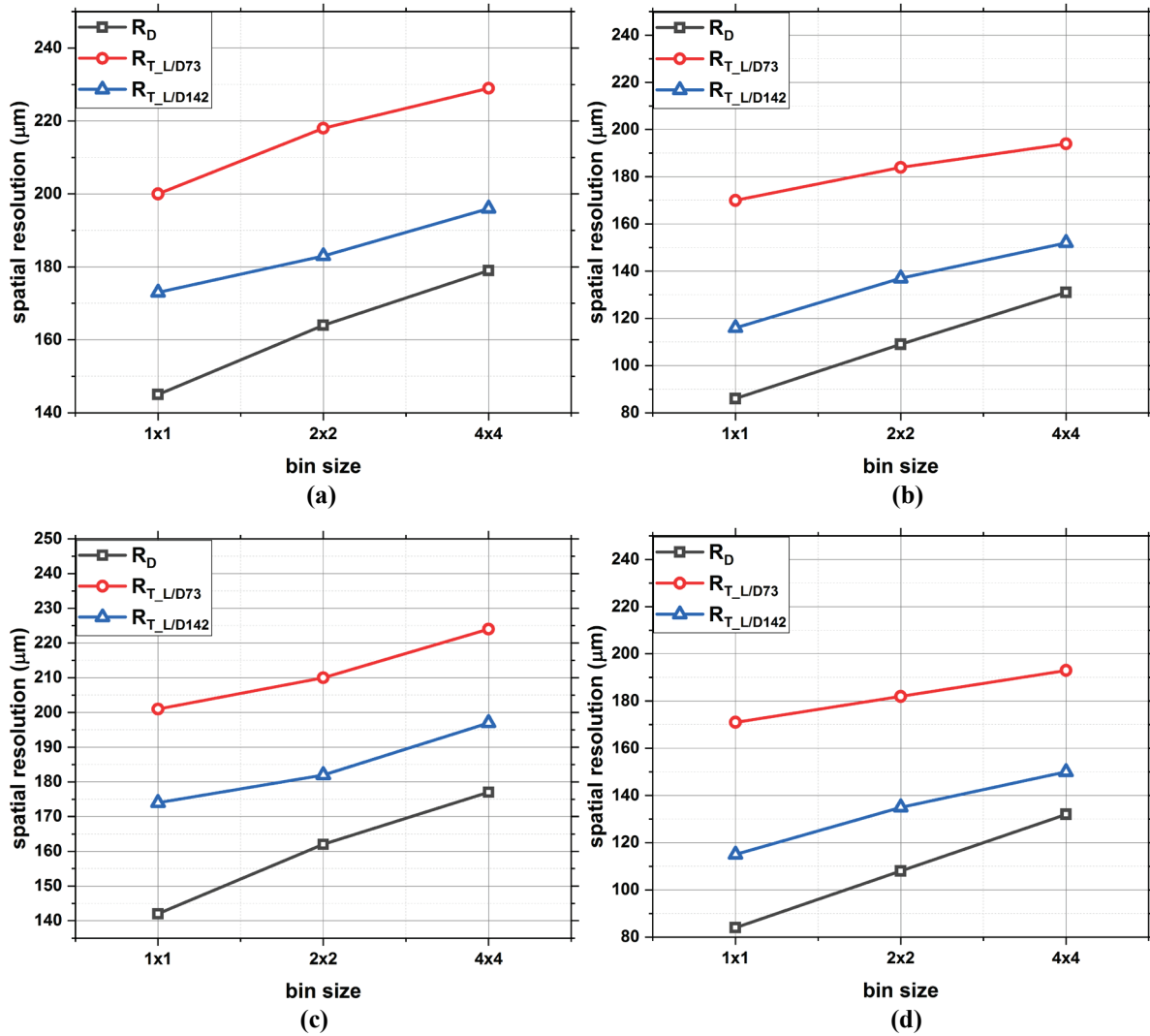


Figure 5.27. Spatial resolution of the neutron imaging system with Micro-NIKKOR 200 mm lens with 250 μm (left column) and 50 μm (right column) thick scintillator screen obtained with lens aperture (a, b) $f/4.0$, and (c, d) $f/5.6$.

It can be observed as the pixel size increases with the larger binning the spatial resolution degrades for both the Nikkor 55 mm and Nikkor 200 mm lens. Further, it can be observed that the spatial resolution degrades as the L/D increases for both the 50 μm and 250 μm scintillator. The spatial resolution is better with 50 μm scintillator as compared with 250 μm scintillator. Additionally, it can be observed that the slope of spatial resolution degradation with the larger bin is more for large pixel size. It can be explained as follows, when the pixel size is small, the scintillator contribution is dominant in total detector resolution. As the pixel size increases the

combined contribution of CCD and Lens become dominant as compared with a scintillator and the degradation is more prominent. The exposure time and the signal to noise ratio (SNR) are characterized to determine the optimum acquisition parameters for the dynamic experiment. The experimental arrangement is shown in Figure 5.28 and . The characterization of the imaging system were performed at L/D 73 and 142 as shown in Figure 5.29 and Figure 5.30

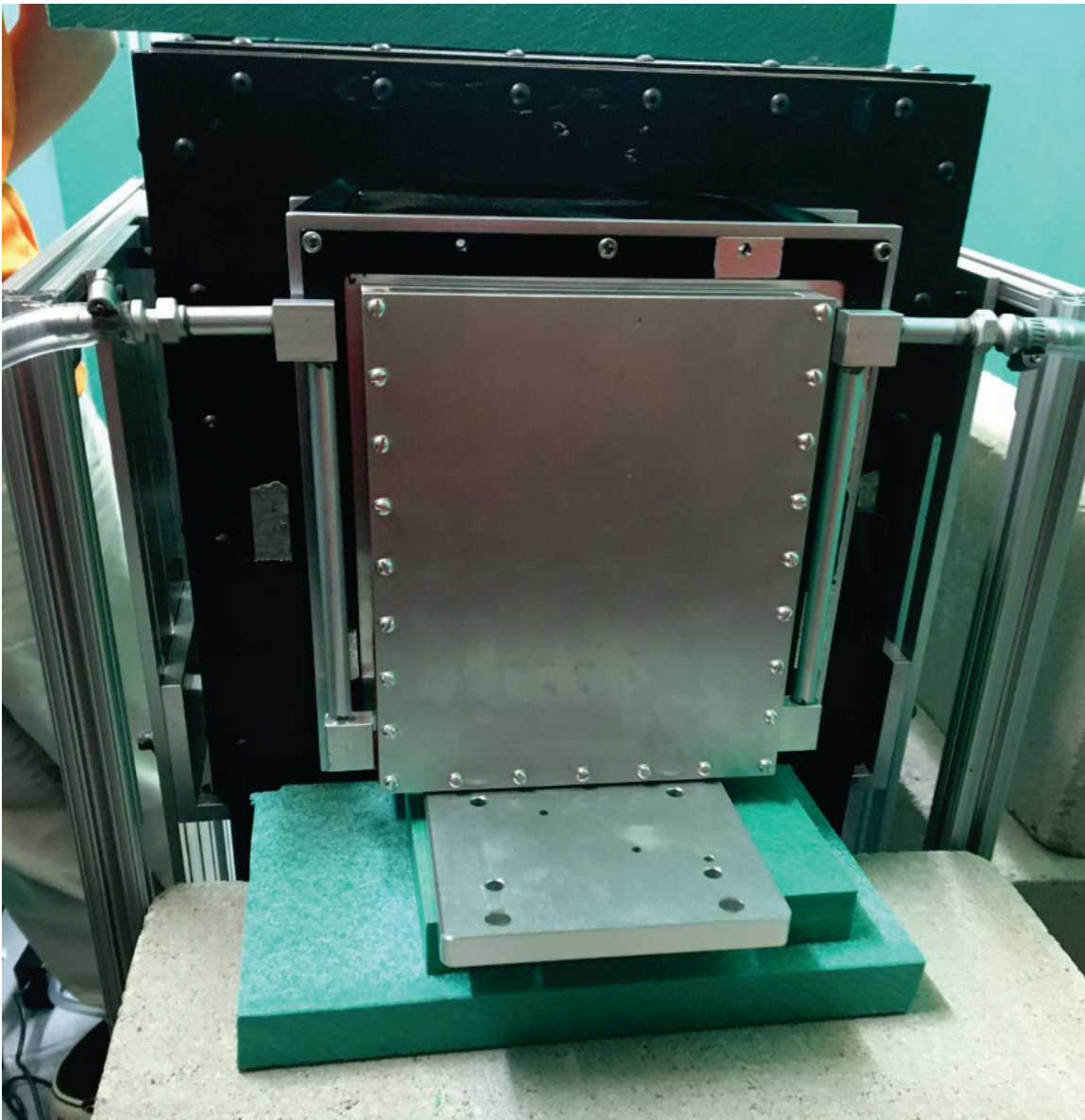


Figure 5.28. Experimental arrangement for dynamic neutron imaging showing, air-inlet, air-outlet, phantom, camera cart, camera box, shielding (front view).

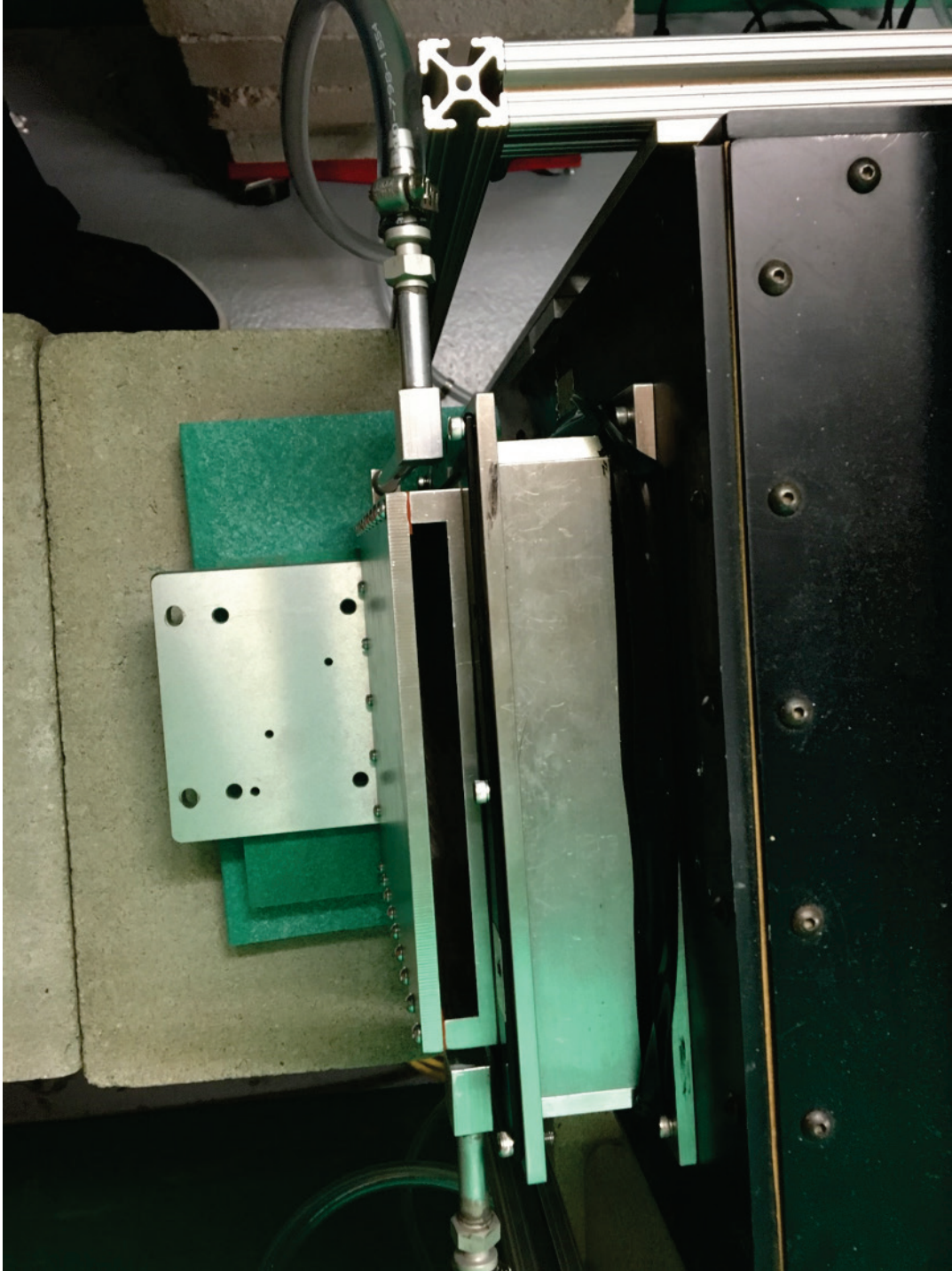


Figure 5.29. Experimental arrangement for dynamic neutron imaging showing, air-inlet, air-outlet, phantom, camera cart, camera box, shielding top view.

The radiographs are obtained with still water column (without air injection) and the highlighted area in Figure 5.31 is used for the calculation of exposure and the signal to noise ratio (SNR).



Figure 5.30. Experimental arrangement for the dynamic imaging showing the setup at two different positions from the neutron beam yielding L/D ratio of 73.



Figure 5.31. Experimental arrangement for the dynamic imaging showing the setup at two different positions from the neutron beam yielding L/D ratio of 142.

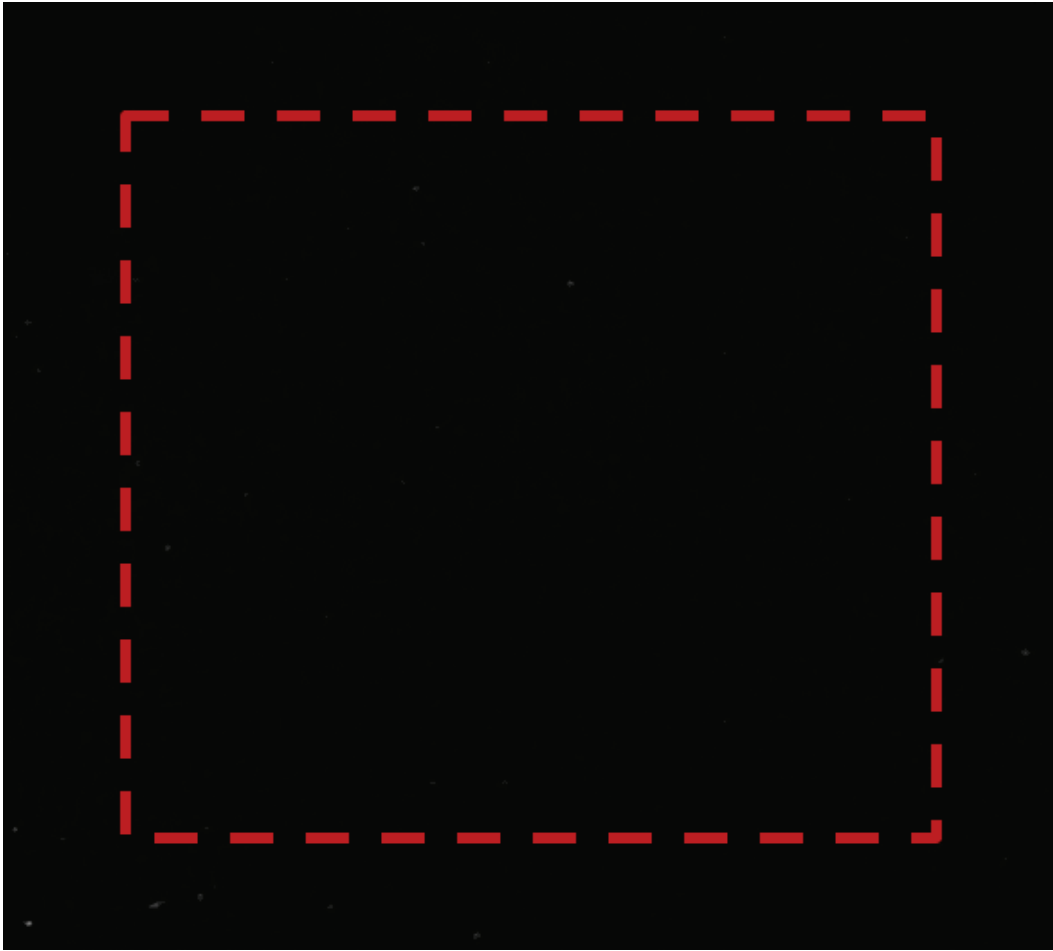


Figure 5.32. Radiograph obtained with still water column (without air injection) to calculate the exposure and SNR (the highlighted area is used for the calculation).

Exposure time and SNR were characterized for different EM gain and CCD bin size. Radiographs were obtained with increasing EM gain from 100 to 900 for a different bin size of 1x1, 2x2 and 4x4. Performances were quantified with 50 μm and 250 μm $^6\text{LiF}:\text{ZnS}$ scintillator and different position from the neutron beam aperture yielding L/D of 73 and 142. To improve temporal resolution EM gain and bin size can be increased. However, increasing bin size degrades spatial resolution and can be seen in Figure 5.26 and Figure 5.27. Exposure time was determined by the time required to reach the mean gray level at highest EM gain without saturating the CCD pixel. Exposure time with EM gain is plotted in Figure 5.32 and Figure 5.33 for bin 1x1, 2x2 and 4x4 respectively. SNR with EM gain is plotted in Figure 5.34 and Figure 5.35.

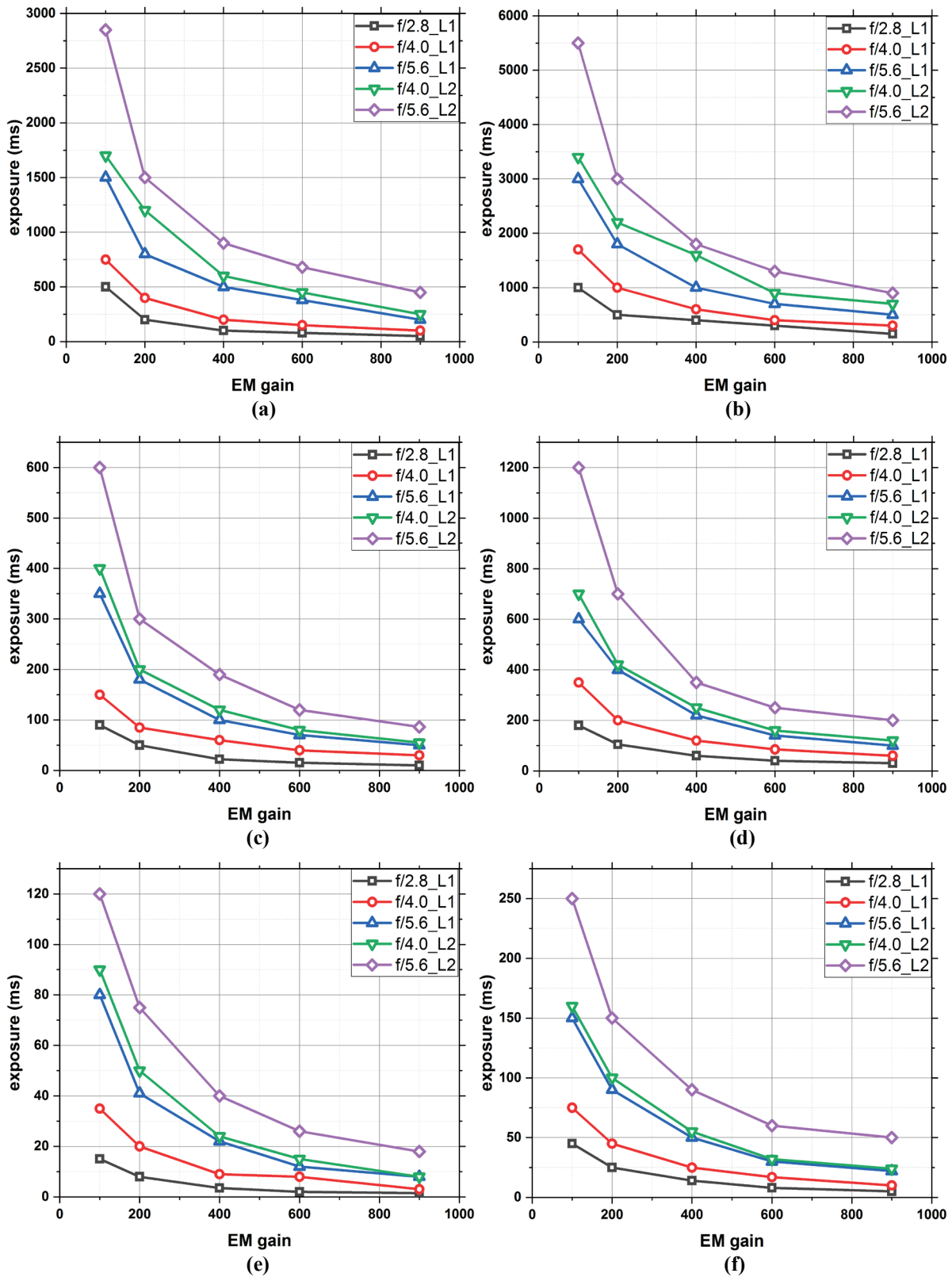


Figure 5.33. Exposure time of EMCCD obtained with L/D 73 Nikkor 55 mm lens (L1) and Nikkor 200 mm lens (L2) 250 μm (left column) and 50 μm (right column) thick scintillator for different EM gain and pixel bin (a, b) 1 x 1, (c, d) 2 x 2, and (e, f) 4 x 4.

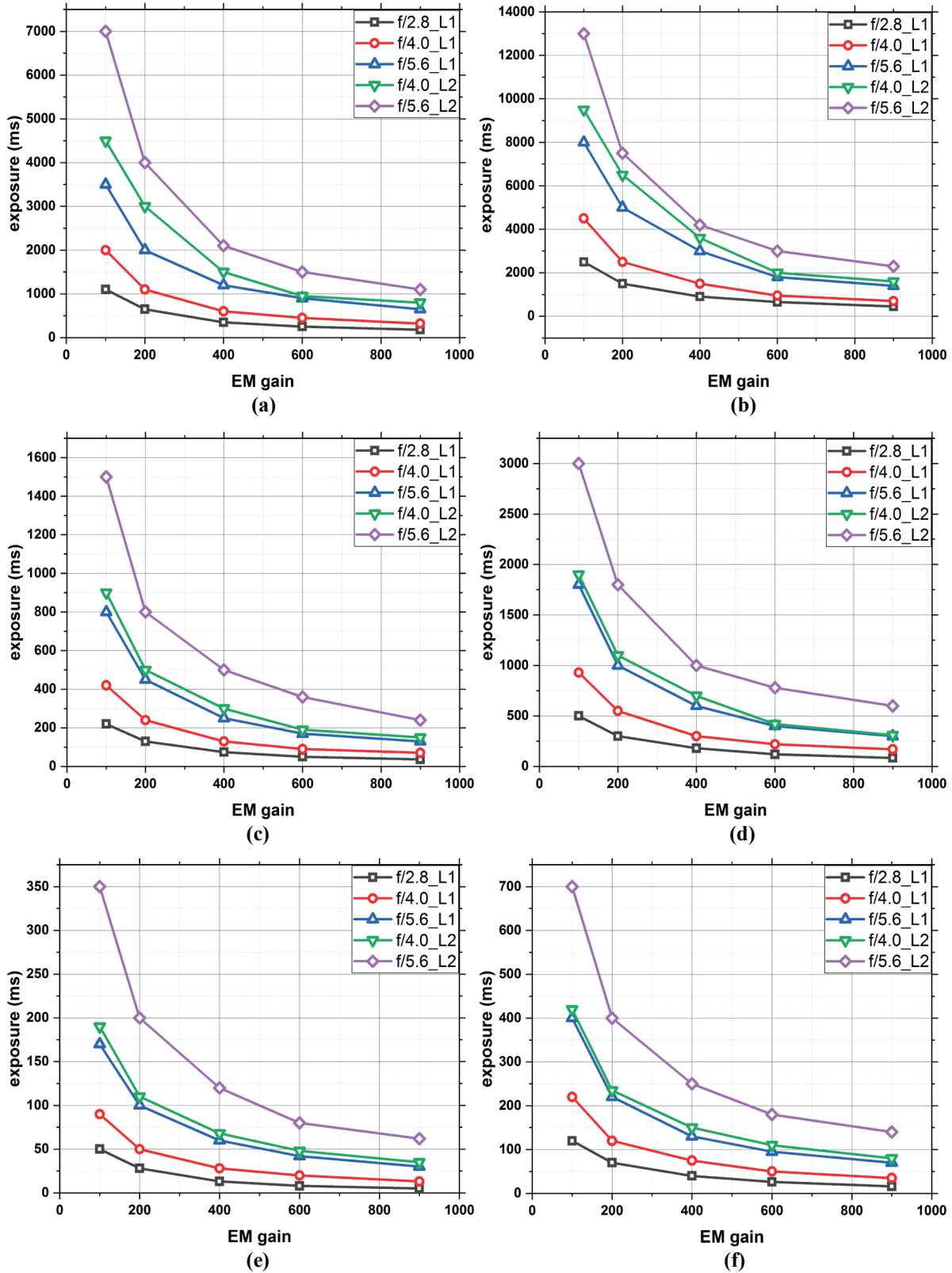


Figure 5.34. Exposure time of EMCCD obtained with L/D 142 Nikkor 55 mm lens (L1) and Nikkor 200 mm lens (L2) 250 μm (left column) and 50 μm (right column) thick scintillator for different EM gain and pixel bin (a, b) 1 x 1, (c, d) 2 x 2, and (e, f) 4 x 4.

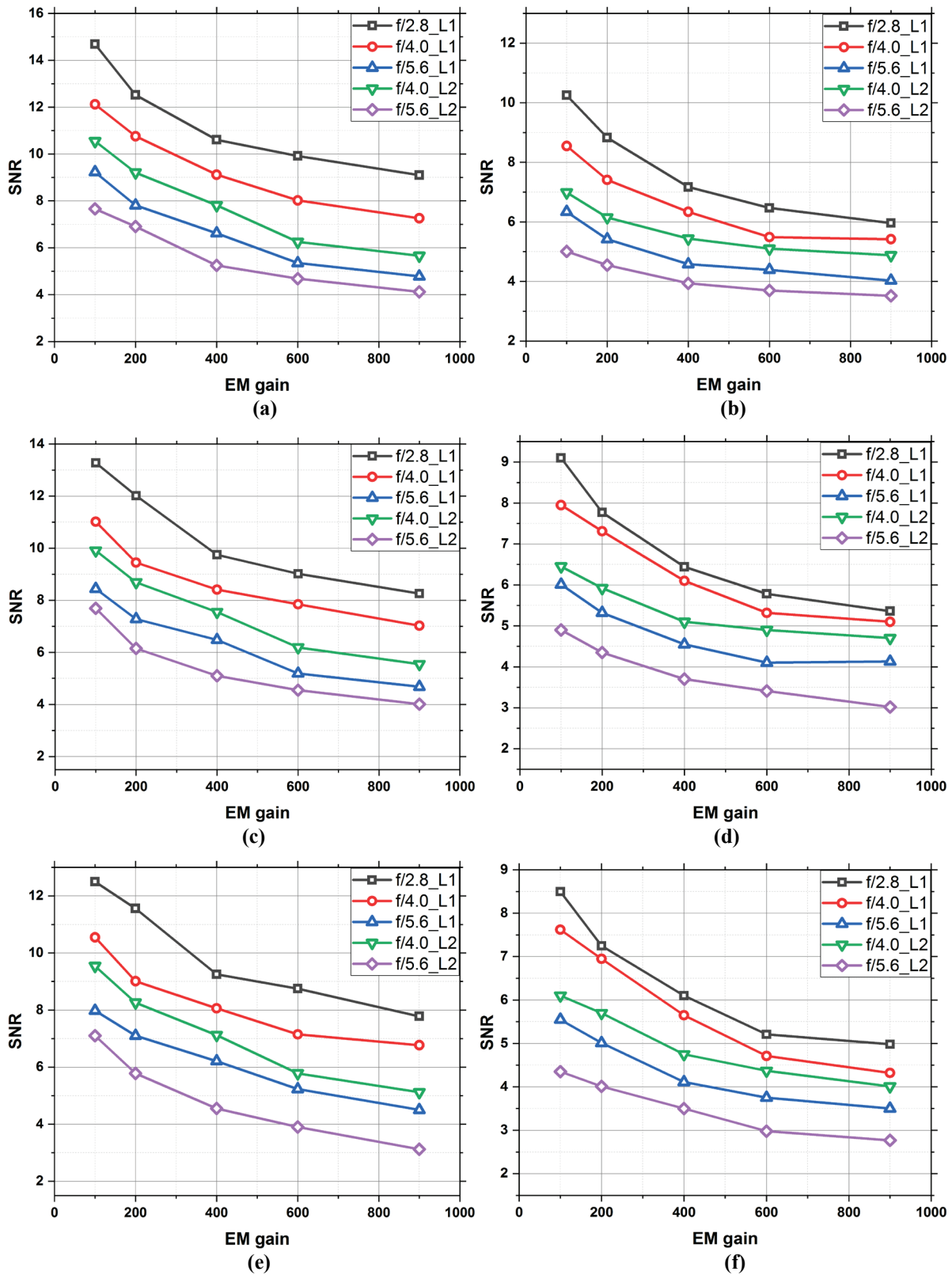


Figure 5.35. SNR of EMCCD obtained with L/D 73 Nikkor 55 mm lens (L1) and Nikkor 200 mm lens (L2) 250 μm (left column) and 50 μm thick scintillator (right column) for different EM gain and pixel bin (a, b) 1 x 1, (c, d) 2 x 2, and (e, f) 4 x 4.

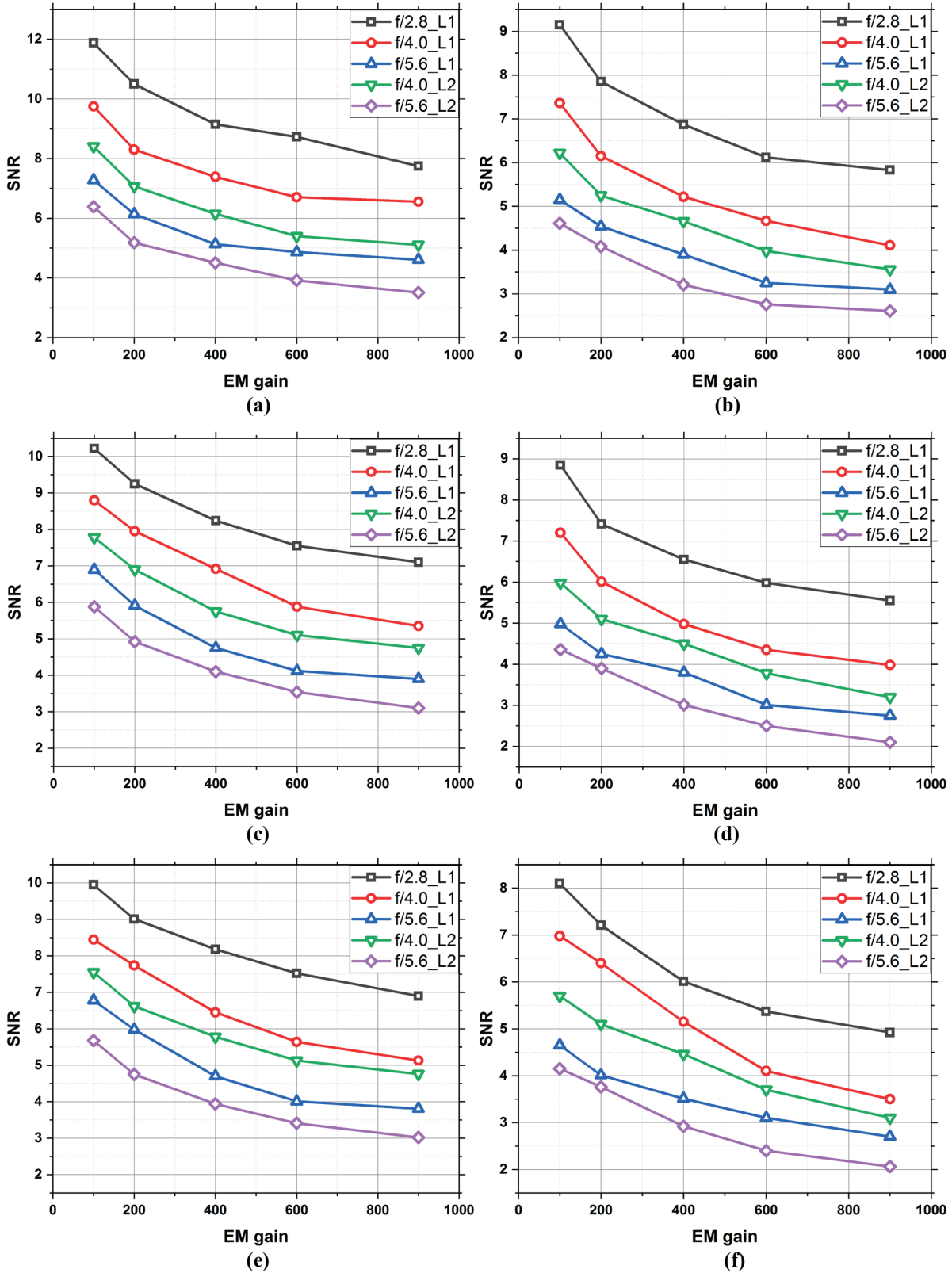


Figure 5.36. SNR of EMCCD obtained with L/D 142 Nikkor 55 mm lens (L1) and Nikkor 200 mm lens (L2) 250 μm (left column) and 50 μm thick scintillator (right column) for different EM gain and pixel bin (a, b) 1 x 1, (c, d) 2 x 2, and (e, f) 4 x 4.

It can be observed in Figure 5.32 and Figure 5.33 that exposure time decreases with gain as high EM gain increases the signal level. Exposure time is maximum for the Nikkor 200 mm lens (L2) at $f/5.6$ aperture and minimum with Nikkor 55 mm lens at the $f/2.8$ aperture (L1). The field of view of the L1 lens is more than the L2, thus increases optical photon input onto the CCD sensor which reduces the exposure time. Additionally, $f/2.8$ aperture increases optical photon input as lens opening with $f/2.8$ is bigger than $f/5.6$. Now, if we compare 250 μm and 50 μm scintillator at same L/D, it can be observed that exposure time is high for 50 μm scintillator as compared with 250 μm scintillator as optical photon output from 50 μm scintillator is lower than 250 μm scintillator. Further, it can be observed from Figure 5.32 and Figure 5.33 that exposure time is high as we move the detector system from the close proximity of the beam shutter (L/D, 73) to furthest distance within the imaging facility. Neutron flux in the imaging plane reduces as we increase distance from beam shutter, which diminishes the number of optical photon onto the CCD sensor, thus increasing exposure time. Also, by comparing image rows (a, b), (c, d) and (e, f) of Figure 5.32 and Figure 5.33, it can be observed that an increase in bin size reduces the exposure time. Higher bin size combines multiple pixels together, thus achieving a similar signal at lower exposure.

Signal to noise ratio is calculated as follows. The highlighted area in Figure 5.33 is selected and the SNR is calculated as,

$$SNR = \frac{\bar{p}}{\sigma_p} . \quad (5.5)$$

Where, \bar{p} is mean gray value and σ_p is the standard deviation. It can be observed from Figure 5.34 and Figure 5.35 that, higher SNR can be achieved with a thicker scintillator, larger field of view and large lens aperture opening as these conditions yield larger optical photon input onto CCD sensor. It can be observed that, the larger SNR can be obtained with 250 μm thick scintillator,

Nikkor 55 mm lens (L1) and $f/2.8$ aperture. Also, it can be observed that for the same position, the SNR obtained with 50 μm scintillator is lower than 250 μm scintillator. Additionally, it can be observed that SNR of radiographs degrades with distance from the beam aperture. Also, by comparing image rows (a, b), (c, d) and (e, f) of Figure 5.34 and Figure 5.35, it can be observed that, SNR is also deteriorating with pixel bin size. Higher bin size compensate low exposure time to achieve similar mean grayscale, however, lower neutron flux at the scintillator screen increases standard deviation, thus reducing the SNR. The acquisition parameter for the dynamic imaging are illustrated in Table 5.4.

Table 5.4. Acquisition parameters for dynamic neutron imaging

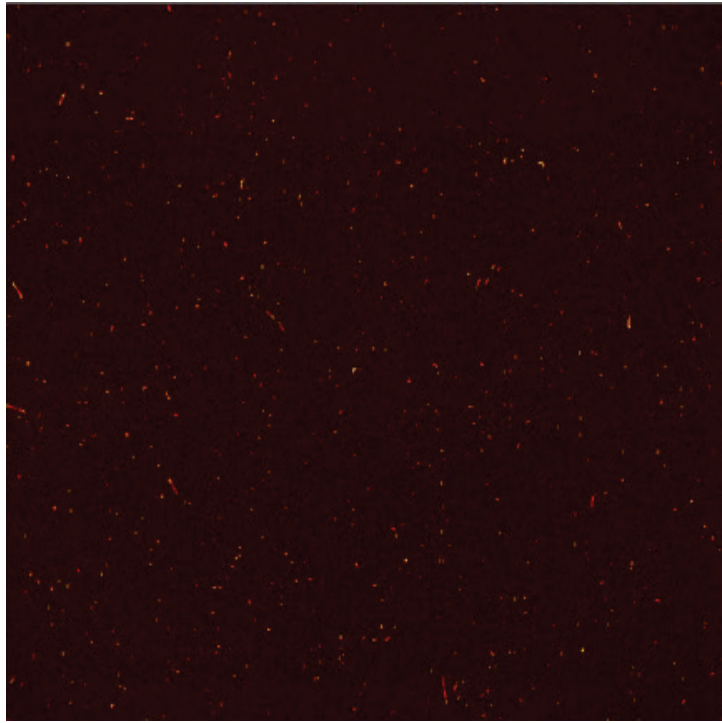
Properties	Specification
Scintillator type	LiF:ZnS
Scintillator thickness (μm)	250
L/D	73
Lens	Nikkor 55 mm
Lens aperture	$f/2.8$
EM gain	900
CCD bin size	1x1
Field of view (cm x cm)	6.96 x 6.96
Spatial resolution (μm)	245 ± 5
Temporal resolution (ms)	50

Thus from the characterized performance of the detector system, it can be observed that thinner scintillator or higher L/D provide better spatial resolution but lower temporal resolution. High temporal resolution can be achieved with a thicker scintillator and the close proximity of beam

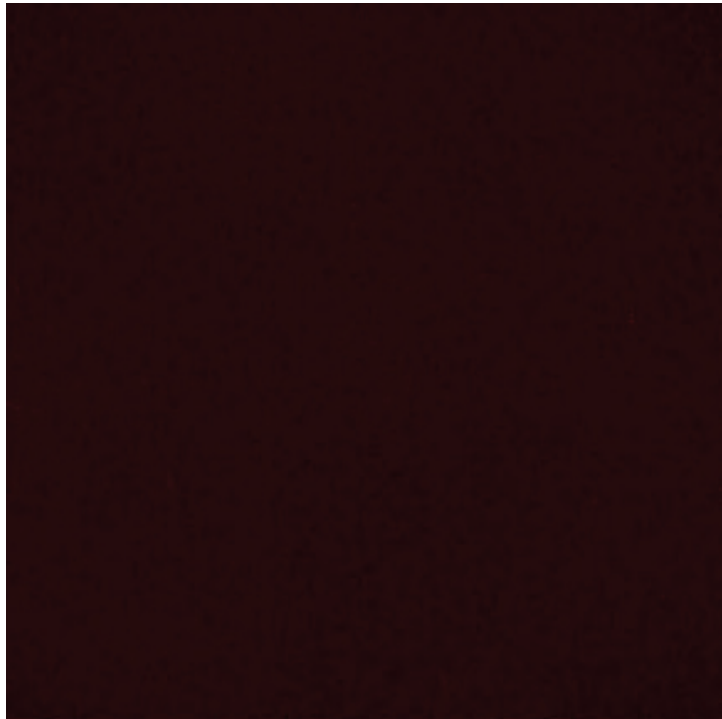
aperture. Additionally, the EM gain and the CCD pixel binning improves the temporal resolution. However, pixel binning also decreases the spatial resolution. From the characterization, it can be observed that it is possible to achieve the temporal resolution of 50 ms with a spatial resolution of 245 μm , which is adequate to observe 1300 μm bubbles.

5.7 Bubble Quantification

Radiographs were obtained with the specified settings and processed to quantify bubble size. Hot pixels were removed by median of the surrounding pixel value if the grey value of certain pixel deviates more than the $2\sigma_p$ from the mean gray level of the radiograph as illustrated in Figure 5.36. The bubbles were identified by using a Sobel edge operator. The edge operator highlights the changes in intensity of radiograph as shown in Figure 5.37. Identified bubbles were magnified and shown in Figure 5.38 for better visualization. Grayscale images were converted to binary images using Otsu's optimum local thresholding method [177]. Binarization of the image was obtained by normalizing the image first, then replacing all the pixel with the value 1 if the pixel value is greater than a threshold and with the value 0 for rest of the pixels. Isolated pixels were removed by examining a connectivity between adjacent pixels along horizontal, vertical or diagonal direction. Binary images are shown in Figure 5.39. Further, to quantify the bubble diameter, area of individual segmented bubbles were calculated for each 8-connected component within the image. Diameter of the bubbles were calculated from the area and size distribution was plotted as shown in Figure 5.40. The algorithm was developed and implemented using MATLAB image processing toolbox framework [178]. It can be observed that average diameter of the segmented bubbles are around 1300 μm .



(a)



(b)

Figure 5.37. (a) Single frame of the neutron radiograph showing hot pixels, and (b) Processed radiographs to remove the hot pixels whose intensity deviates more than two standard deviations of the mean intensity level.

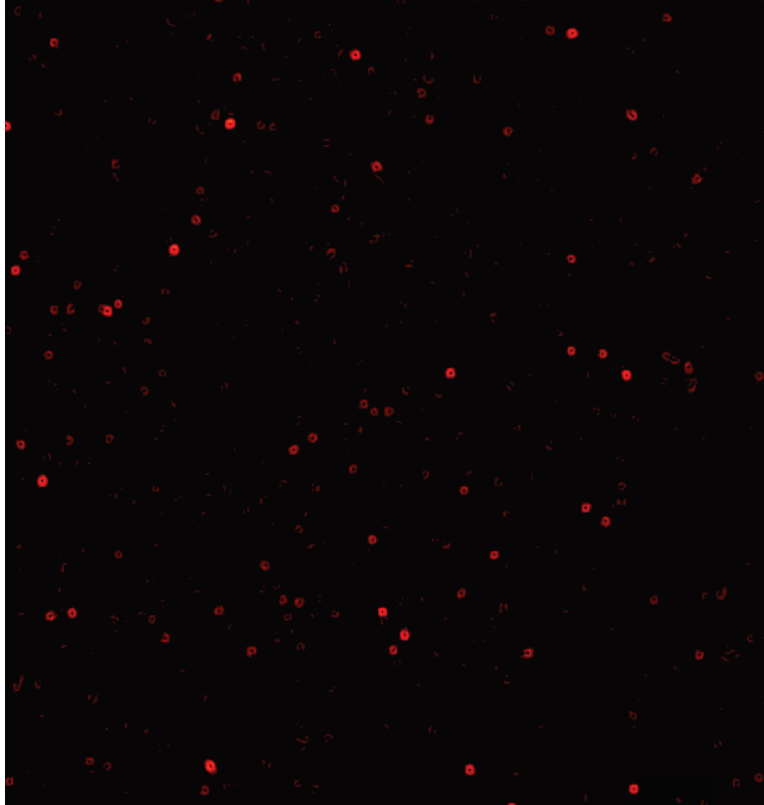


Figure 5.38. Bubble edges after applying Sobel edge filter to identify the bubbles within the radiograph and quantify the bubble diameter through subsequent image processing.

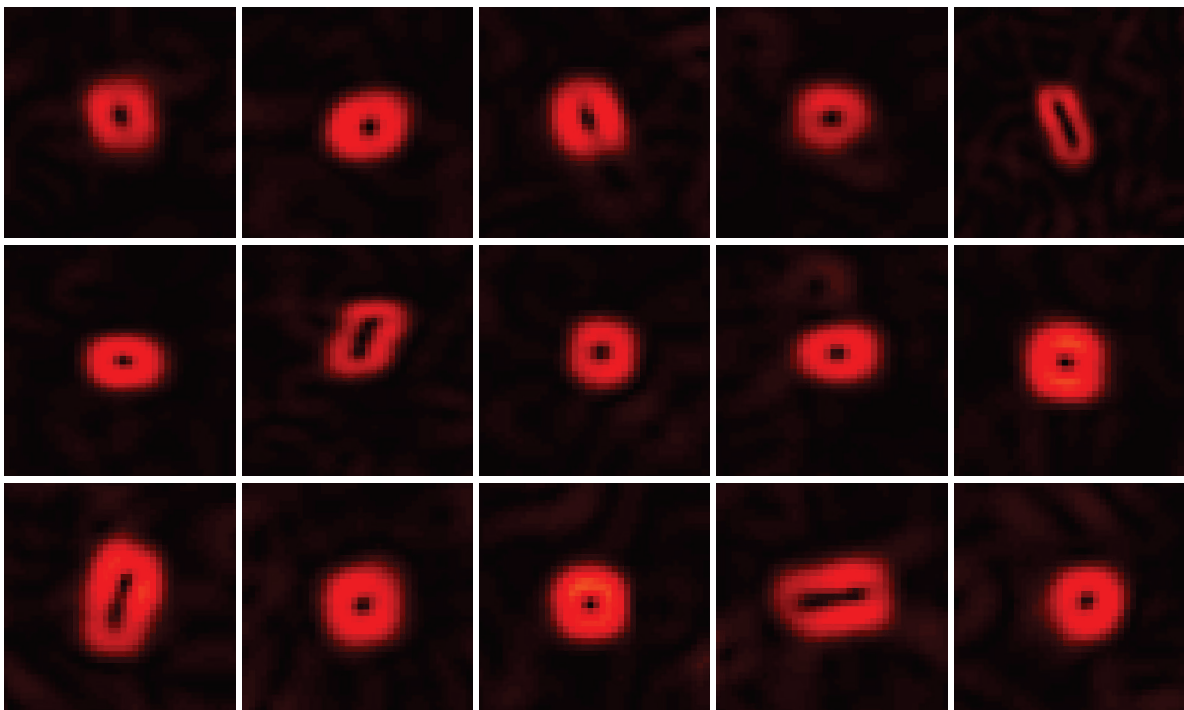


Figure 5.39. Close view of the individual detected bubbles in the radiograph after applying the Sobel edge filter showing the shape of the detected bubbles.

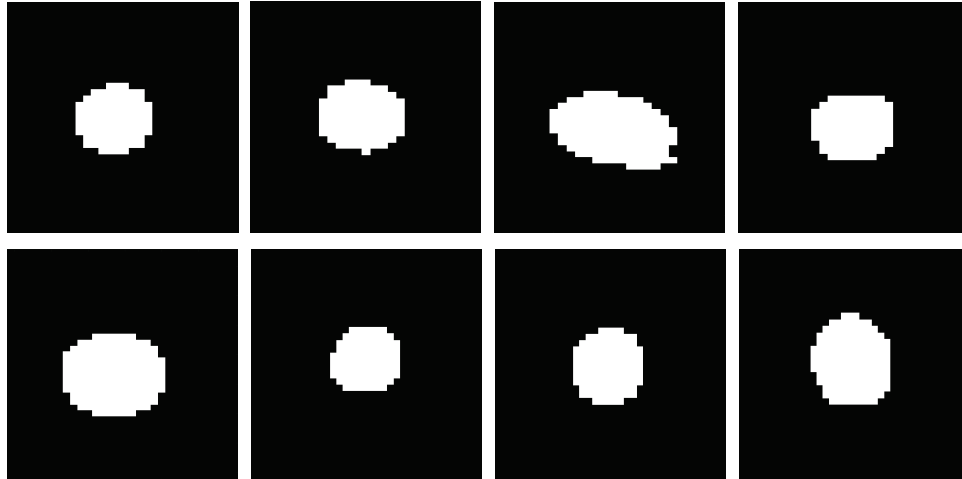


Figure 5.40. Segmented bubbles from the binary image for the calculation of the bubble diameter.

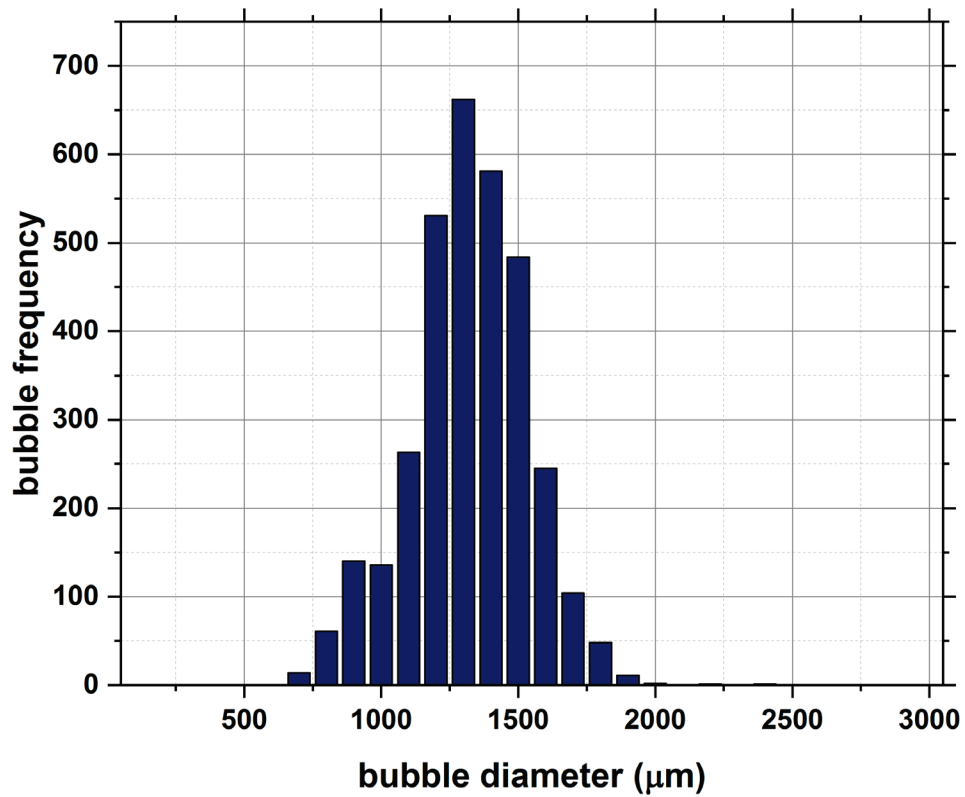


Figure 5.41. Distribution of bubble diameter from the segmented image showing Gaussian distribution of the bubbles with a mean diameter around 1300 μm .

Chapter 6 Conclusion and Future Work

6.1 Conclusion

In the present work, the components of a real-time neutron imaging system have been explored and quantified. The investigation includes the theoretical understanding of spatial resolution contribution of CCD, Lens and scintillator, simulation techniques, system design, and performance characterization as well as development of an image reconstruction technique that can be applied to the process of computed reconstruction to improve the spatial resolution.

A Geant4 simulation model of a real-time CCD-based neutron imaging system was developed. The model uses a multi-physics approach that treats explicitly the neutrons, charged particles and optical photons which are involved in the imaging process. Various aspects of the scintillator including efficiency and spatial resolution have been investigated. Experimental validation of the model was performed at the NCSU PULSTAR neutron imaging facility. The achievable spatial resolution of the imaging system was $81 \pm 2 \mu\text{m}$ with $50 \mu\text{m}$ thick ${}^6\text{LiF:ZnS}$ scintillator screen. It has been observed computationally and experimentally that thinner scintillator screens have a higher spatial resolution. The Geant4 simulations revealed that resolution behavior can be correlated with the range of the neutron absorption reaction products. If range of the secondary particles covers scintillator screen thickness then spatial resolution will approach a value on the order of thickness, which motivates the use of thinner screens for imaging. However, use of thin screens will reduce neutron absorption probability and the overall efficiency of signal generation. Consequently, an optimum thickness should be chosen which can be facility dependent. Imaging facilities with high thermal neutron fluxes (and possibly using cold neutrons) can compensate for low detection efficiency and can achieve high spatial resolution using thin screens.

Further, the developed simulation model was extended to develop and characterize the performance of a neutron computed tomography system. Projection data were obtained by simulating various scintillator thickness at two positions from the beam aperture, yielding different L/D ratio. The theoretical number of required projections to ensure aliasing free reconstruction is approximately 1600 for a 1.33 cm diameter area with 13 μm detector pixel. However, the theoretical calculation assumes that spatial resolution is contributed by detector pixel only. In neutron imaging, spatial frequency content of obtained radiographs is attributed by Gaussian contribution of CCD pixel, lens, scintillator and beam geometry. As the obtained detector spatial resolution with 50 μm scintillator was $116 \pm 2 \mu\text{m}$, the required number of projection can be calculated as 360. The reconstruction performance was characterized by algebraic, statistical and analytical reconstruction method. It has been observed that algebraic technique performs better and obtained spatial resolution was 120 ± 4 with 50 μm thick scintillator screen. However, the traditional reconstruction approach assumes an ideal data acquisition environment, in neutron tomography such techniques may assume that the projections are produced with highly collimated neutron beam and a high-resolution detector. In this work, a model based computed tomography (CT) reconstruction approach was developed and implemented to investigate the improvement of spatial resolution in neutron tomography. The quantified system response function was included in the forward projection model of the iterative reconstruction process to provide a better estimation of the actual projection, thus improving the spatial resolution of the reconstructed images. Experiments were performed at the neutron imaging facility of the PULSTAR research reactor to corroborate the performance of the developed model-based algorithm. The spatial resolution of model based technique was $87 \pm 3 \mu\text{m}$ with 50 μm thick scintillator screen, showing

an improvement of nearly 40% in achievable spatial resolution as compared with traditional reconstruction approach.

Further, feasibility of a dynamic neutron radiography was demonstrated with visualizing micro-bubbles in real-time. The neutron imaging system was characterized for spatial resolution, temporal resolution, and signal to noise ratio with different lens magnification, different scintillator, and different position along neutron beam. It is observed that although the spatial resolution improves with a thin scintillator, temporal resolution degrades as optical photon generation diminishes. Temporal resolution improves with high lens aperture but spatial resolution deteriorates due to increased lens aberration. Additionally, the temporal resolution can be improved with the electronic gain and CCD pixel binning. However, pixel binning increases the pixel size thus decreases the spatial resolution. The optimum parameters of the imaging system were determined with a spatial resolution of $245 \pm 5 \mu\text{m}$ and temporal resolution of 50 ms to demonstrate the dynamic imaging capability. Bubbles were generated by injecting air through orifice and radiographs were obtained as they move through a water column. Radiographs were processed further to segment and characterize the distribution of imaged bubble. Thus, the feasibility of the implementation of a dynamic neutron imaging system at PULSTAR neutron imaging facility is successfully demonstrated.

6.2 Future Work

In the future, a path can be envisioned to improve such neutron imaging system which may include hardware upgrades or advanced real-time image processing technique to enhance the quality of neutron radiography and tomography. In addition, the advanced system can be used for numerous non-destructive investigation in science and technology. The simulation model

developed in this work can be extended to predict the system performance for future improvements.

In addition with thin scintillator, the spatial resolution can be improved by a good lens. As thin scintillator is now commercially available, the spatial resolution of the imaging system is limited with lens contribution. An ideal lens should have zero aberration distortion at maximum aperture opening. Although it is impossible to manufacture such a perfect lens, usually aberration is low for high quality lenses. In near future, it would be interesting to characterize the neutron imaging system with advanced lenses like Canon MP-E 65 mm. Although, this lens can achieve 1:5 magnification, the focusing distance is limited to 23.8 cm. which makes it difficult to use directly. However, an infinity-corrected optical arrangement can be used to increase the focal length [179]. An in-house customization and manufacturing of a good quality lens can be implemented in near future.

Apart from EMCCD, CMOS camera can be explored as an alternative option for high-resolution imaging as the low pixel size can achieve. However, unlike EMCCD, CMOS sensor doesn't have an internal gain. Intensifier can be used to compensate the high exposure time of CMOS camera. Thus an alternative approach may consist of an infinity corrected optics coupled with intensifier and CMOS camera. In the future, the performance of the computed tomography system can be characterized by another reconstruction approach like maximum a posteriori (MAP) technique, conjugate gradient least square (CGLS) or multiplicative algebraic reconstruction technique (MART) [145], [180], [181]. In addition, it would be interesting to study the effect of regularization on reconstruction quality and convergence. In addition to the traditional technique, the advanced model-based technique can also be implemented with the statistical framework instead of algebraic SIRT structure. The technique can be further modified to include a

deconvolution step followed by a convolution approach. In addition, regularization and prior information about an object can be included which may further improve the spatial resolution. Although, GPU implementation may accelerate the reconstruction, additional processing may increase CT reconstruction time. It would be interesting to explore other hardware options like a reconfigurable field programmable gate array (FPGA) to implement computed tomography reconstruction algorithm to speed up the process further.

Temporal resolution for a dynamic study can be improved by selecting a lens with high aperture. Nikon NIKKOR Z 58 mm $f/0.95$ S Noct can be used to characterize the system for such dynamic study. In addition, EMCCD can be replaced with High-speed sCMOS to achieve high readout speed as compared with CCD camera. The stream of dynamic images may be processed in real-time to extract structural information from the image on the fly. Image processing algorithm can be implemented in reconfigurable FPGA device to achieve real-time processing. In addition to the dynamic radiography, a tomography system can be designed to observe a quasi-dynamic phenomenon. This approach can be possible to implement only when a dynamic event is occurring at very slow rate as compared to data acquisition time.

Last but not least, other advanced imaging technology can also be incorporated in neutron imaging to improve image quality in near future. With advancement of science and technology now it is possible to design a smart imaging system by incorporating artificial intelligence (AI). In medical imaging, AI has been integrated to identify malignant tissue, abnormalities in organs, common cancers etc. Recently, AI has also been used to improve spatial and temporal resolution in microscopic image [182]. Thus, in the future an advanced neutron system can be anticipated for real-time high-resolution non-destructive examination in numerous science and technology applications.

REFERENCES

- [1] I. S. Anderson, R. L. McGreevy and H. Z. Bilheux, "Neutron imaging and applications," *Springer Science Business Media*, vol. 200, (2209), pp. 987-980, 2009.
- [2] M. Strobl *et al*, "Advances in neutron radiography and tomography," *J. Phys. D*, vol. 42, (24), pp. 243001, 2009.
- [3] J. Banhart, *Advanced Tomographic Methods in Materials Research and Engineering*. 200866.
- [4] H. Kallmann, "Neutron radiography." *Research; a Journal of Science and its Applications*, vol. 1, (6), pp. 254, 1948.
- [5] J. Thewlis, "Neutron radiography," *British Journal of Applied Physics*, vol. 7, (10), pp. 345, 1956.
- [6] J. P. Barton, "Divergent Beam Collimator for Neutron Radiography," 1967.
- [7] H. Berger, *Neutron Radiography: Methods, Capabilities and Applications*. 1965.
- [8] H. Berger, "Characteristics of a thermal neutron television imaging system," *Materials Evaluation (US) Formerly Nondestr. Test.*, vol. 4, 1966.
- [9] S. Kawasaki, "A thermal neutron television system using a high yield neutron generator," *Nucl. Instrum. Methods*, vol. 62, pp. 311-315, 1968.
- [10] I. C. Hendry *et al*, "The display of neutron radiography results by direct viewing of a scintillating plate," *Journal of Physics E: Scientific Instruments*, vol. 2, (2), pp. 191, 1969.
- [11] J. P. Barton, "Neutron Radiography—An overview," in *Practical Applications of Neutron Radiography and Gaging* Anonymous 1976, .
- [12] "Track-etch neutron radiography," H. W. Alter, , July 22, 3,457,408 H. W. Alter, "Track-etch neutron radiography," 3,457,408, July 22, 1969.
- [13] G. A. Schlapper *et al*, "Neutron Tomography Investigations at the Missouri University Research Reactor," *Transactions of the American Nuclear Society. Supplement*, vol. 26, (1), pp. 39, 1977.
- [14] J. P. Barton and P. von der Hardt, *Neutron Radiography: Proceedings of the First World Conference San Diego, California, USA December 7–10, 1981*. Springer Science & Business Media, 1981.

- [15] M. Verat, H. Rougeot and B. Driard, "Neutron image intensifier tubes," in *Neutron Radiography* Anonymous 1983, .
- [16] R. H. Bossi, A. H. Robinson and J. P. Barton, "High frame-rate neutron radiography of dynamic events," in *Neutron Radiography* Anonymous 1983, .
- [17] N. Niimura *et al*, "An imaging plate neutron detector," *Nuclear Instruments and Methods in Physics Research Section A: Accelerators, Spectrometers, Detectors and Associated Equipment*, vol. 349, (2-3), pp. 521-525, 1994.
- [18] K. Takahashi *et al*, "Imaging performance of imaging plate neutron detectors," *Nuclear Instruments and Methods in Physics Research Section A: Accelerators, Spectrometers, Detectors and Associated Equipment*, vol. 377, (1), pp. 119-122, 1996.
- [19] H. Kobayashi and M. Satoh, "Basic performance of a neutron sensitive photostimulated luminescence device for neutron radiography," *Nuclear Instruments and Methods in Physics Research Section A: Accelerators, Spectrometers, Detectors and Associated Equipment*, vol. 424, (1), pp. 1-8, 1999.
- [20] M. Balasko and E. Svab, "Dynamic neutron radiography instrumentation and applications in Central Europe," *Nuclear Instruments and Methods in Physics Research Section A: Accelerators, Spectrometers, Detectors and Associated Equipment*, vol. 377, (1), pp. 140-143, 1996.
- [21] E. H. Lehmann, P. Vontobel and L. Wiesel, "Properties of the radiography facility NEUTRA at SINQ and its potential for use as European reference facility," *Nondestr. Test. Eval.*, vol. 16, (2-6), pp. 191-202, 2001.
- [22] D. S. Hussey *et al*, "New neutron imaging facility at the NIST," *Nuclear Instruments and Methods in Physics Research Section A: Accelerators, Spectrometers, Detectors and Associated Equipment*, vol. 542, (1-3), pp. 9-15, 2005.
- [23] F. C. De beer* and W. J. Strydom, "Neutron radiography at SAFARI-1 in South Africa," *Nondestr. Test. Eval.*, vol. 16, (2-6), pp. 163-176, 2001.
- [24] N. Kardjilov *et al*, "Three-dimensional imaging of magnetic fields with polarized neutrons," *Nature Physics*, vol. 4, (5), pp. 399, 2008.
- [25] N. Kardjilov *et al*, "Phase-contrast radiography with a polychromatic neutron beam," *Nuclear Instruments and Methods in Physics Research Section A: Accelerators, Spectrometers, Detectors and Associated Equipment*, vol. 527, (3), pp. 519-530, 2004.
- [26] K. K. Mishra and A. I. Hawari, "Investigating Phase Contrast Neutron Imaging for Mixed Phase-Amplitude Objects," *IEEE Trans. Nucl. Sci.*, vol. 56, (3), pp. 1629-1636, 2009.

- [27] W. Kockelmann *et al*, "Energy-selective neutron transmission imaging at a pulsed source," *Nuclear Instruments and Methods in Physics Research Section A: Accelerators, Spectrometers, Detectors and Associated Equipment*, vol. 578, (2), pp. 421-434, 2007.
- [28] E. T. H. Zurich and C. Grunzweig, "Neutron Grating Interferometry for Imaging Magnetic Structures in Bulk Ferromagnetic Materials," .
- [29] N. Kardjilov *et al*, "Neutron imaging in materials science," *Materials Today*, vol. 14, (6), pp. 248-256, 2011.
- [30] V. Sinha, A. Srivastava and H. K. Lee, "A novel method for NDT applications using NXCT system at the Missouri University of Science & Technology," *Nuclear Instruments and Methods in Physics Research Section A: Accelerators, Spectrometers, Detectors and Associated Equipment*, vol. 750, pp. 43-55, 2014.
- [31] E. Lehmann *et al*, "Recent Applications of Neutron Imaging Methods," vol. 88, pp. 5-12, 2017.
- [32] E. H. Lehmann and D. Ridikas, "Status of Neutron Imaging—Activities in a Worldwide Context," *Physics Procedia*, vol. 69, pp. 10-17, 2015.
- [33] F. Salvemini *et al*, "DINGO—the neutron imaging station at ANSTO: embracing material science, palaeontology, and cultural heritage," *Neutron News*, vol. 27, (2), pp. 14-19, 2016.
- [34] R. Pugliesi *et al*, "Neutron imaging at the IPEN-CNEN/SP and its use in technology," *Neutron News*, vol. 25, (4), pp. 40-43, 2014.
- [35] L. He *et al*, "Design of real-time neutron radiography at China advanced research reactor," *Physics Procedia*, vol. 43, pp. 48-53, 2013.
- [36] M. Schulz and B. Schillinger, "ANTARES: Cold neutron radiography and tomography facility," *Journal of Large-Scale Research Facilities JLSRF*, vol. 1, pp. 17, 2015.
- [37] M. J. Mühlbauer *et al*, "Neutron imaging with fission and thermal neutrons at NECTAR at MLZ," *Physica B: Condensed Matter*, 2017.
- [38] N. Kardjilov *et al*, "Imaging with cold neutrons at the conrad-2 facility," *Physics Procedia*, vol. 69, pp. 60-66, 2015.
- [39] Z. Kis, L. Szentmiklósi and T. Belgya, "NIPS—NORMA station—a combined facility for neutron-based nondestructive element analysis and imaging at the Budapest Neutron Centre," *Nuclear Instruments and Methods in Physics Research Section A: Accelerators, Spectrometers, Detectors and Associated Equipment*, vol. 779, pp. 116-123, 2015.
- [40] Y. Kiyonagi, "Neutron imaging at compact accelerator-driven neutron sources in Japan," *Journal of Imaging*, vol. 4, (4), pp. 55, 2018.

- [41] Y. Matsumoto *et al*, "Recent progress of radiography and tomography at the energy-resolved neutron imaging system RADEN," *Physics Procedia*, vol. 88, pp. 162-166, 2017.
- [42] S. Cheul-Muu *et al*, "Characterization of HANARO neutron radiography facility in accordance with ASTM standard E545-91/E803-91 for KOLAS/ISO17025," *Applied Radiation and Isotopes*, vol. 61, (4), pp. 631-638, 2004.
- [43] L. Shi, "Development of a Neutron Computed Tomography System at the Pennsylvania State University," 2016.
- [44] W. J. Richards *et al*, "Neutron radiography inspection of investment castings," *Applied Radiation and Isotopes*, vol. 61, (4), pp. 675-682, 2004.
- [45] A. J. Gilbert and M. R. Deinert, "Neutron tomography of axisymmetric flow fields in porous media," *Nuclear Instruments and Methods in Physics Research Section B: Beam Interactions with Materials and Atoms*, vol. 301, pp. 23-28, 2013.
- [46] D. J. Dorsey and W. S. Charlton, "Recent developments and applications for the University of Texas Thermal Neutron Imaging Facility," *Applied Radiation and Isotopes*, vol. 61, (4), pp. 525-528, 2004.
- [47] E. Perfect *et al*, "Neutron imaging of hydrogen-rich fluids in geomaterials and engineered porous media: A review," *Earth-Sci. Rev.*, vol. 129, pp. 120-135, 2014.
- [48] D. S. Hussey *et al*, "A New Cold Neutron Imaging Instrument at NIST," *Physics Procedia*, vol. 69, pp. 48-54, 2015.
- [49] N. Kardjilov *et al*, "Neutron imaging in materials science," *Materials Today*, vol. 14, (6), pp. 248-256, 2011.
- [50] I. Manke *et al*, "Fuel cell research with neutron imaging at Helmholtz Centre Berlin," *Physics Procedia*, vol. 69, pp. 619-627, 2015.
- [51] J. B. Siegel *et al*, "Neutron imaging of lithium concentration in LFP pouch cell battery," *J. Electrochem. Soc.*, vol. 158, (5), pp. A529, 2011.
- [52] M. Lanz *et al*, "In situ neutron radiography of lithium-ion batteries during charge/discharge cycling," *J. Power Sources*, vol. 101, (2), pp. 177-181, 2001.
- [53] J. Campbell, "The concept of net shape for castings," *Mater Des*, vol. 21, (4), pp. 373-380, 2000.
- [54] X. Yao and S. Shivkumar, "Mould filling characteristics in lost foam casting process," *Materials Science and Technology*, vol. 13, (10), pp. 841-846, 1997.

- [55] D. Penumadu, "Material science and engineering with neutron imaging," in *Neutron Imaging and Applications* Anonymous 2009, .
- [56] A. S. Tremsin *et al*, "Energy-Resolved Neutron Imaging for Reconstruction of Strain Introduced by Cold Working," *Journal of Imaging*, vol. 4, (3), pp. 48, 2018.
- [57] F. C. De Beer, W. J. Strydom and E. J. Griesel, "The drying process of concrete: a neutron radiography study," *Applied Radiation and Isotopes*, vol. 61, (4), pp. 617-623, 2004.
- [58] K. Mitton, A. Jones and M. J. Joyce, "Digital fast neutron radiography of steel reinforcing bar in concrete," *Journal of Instrumentation*, vol. 9, (12), pp. C12045, 2014.
- [59] F. C. De Beer, J. J. Le Roux and E. P. Kearsley, "Testing the durability of concrete with neutron radiography," *Nuclear Instruments and Methods in Physics Research Section A: Accelerators, Spectrometers, Detectors and Associated Equipment*, vol. 542, (1-3), pp. 226-231, 2005.
- [60] M. Cekanova *et al*, "Neutron imaging: Detection of cancer using animal model," in *Biomedical Science and Engineering Center Conference (BSEC), 2014 Annual Oak Ridge National Laboratory*, 2014, .
- [61] R. W. Metzke *et al*, "Neutron computed tomography of rat lungs," *Physics in Medicine & Biology*, vol. 56, (1), pp. N1, 2010.
- [62] A. J. Kapadia *et al*, "Neutron spectroscopy of mouse using neutron stimulated emission computed tomography (NSECT)," in *Nuclear Science Symposium Conference Record, 2006. IEEE*, 2006, .
- [63] A. C. Sharma *et al*, "Design and development of a high-energy gamma camera for use with NSECT imaging: Feasibility for breast imaging," *IEEE Trans. Nucl. Sci.*, vol. 54, (5), pp. 1498-1505, 2007.
- [64] T. Materna, "New neutron imaging techniques for cultural heritage purposes," in *Nuclear Science Symposium Conference Record, 2008. NSS'08. IEEE*, 2008, .
- [65] T. Materna and Ancient Charm Collaboration, "Combined neutron imaging techniques for cultural heritage purpose," in *AIP Conference Proceedings*, 2009, .
- [66] B. Schillinger *et al*, "Neutron Imaging in Cultural Heritage Research at the FRM II Reactor of the Heinz Maier-Leibnitz Center," *Journal of Imaging*, vol. 4, (1), pp. 22, 2018.
- [67] E. H. Lehmann, S. Hartmann and M. O. Speidel, "Investigation of the content of ancient Tibetan metallic Buddha statues by means of neutron imaging methods," *Archaeometry*, vol. 52, (3), pp. 416-428, 2010.

- [68] S. G. Kandlikar, "Bubble behavior and departure bubble diameter of bubbles generated over nucleating cavities in flow boiling," in *Pool and External Flow Boiling*, Eds. V. K. Dhir and AE Bergles, *Proceedings of the Engineering Foundaton Conference*, 1992, pp. 22-27.
- [69] C. Paz *et al*, "On the Application of Image Processing Methods for Bubble Recognition to the Study of Subcooled Flow Boiling of Water in Rectangular Channels," *Sensors*, vol. 17, (6), pp. 1448, 2017.
- [70] K. Mishima, T. Hibiki and H. Nishihara, "Visualization and measurement of two-phase flow by using neutron radiography," *Nucl. Eng. Des.*, vol. 175, (1-2), pp. 25-35, 1997.
- [71] J. Chang, A. J. Kelly and J. M. Crowley, *Handbook of Electrostatic Processes*. 1995.
- [72] L. Xu and L. Xu, "Ultrasound tomography system used for monitoring bubbly gas/liquid two-phase flow," *IEEE Trans. Ultrason. Ferroelectr. Freq. Control*, vol. 44, (1), pp. 67-76, 1997.
- [73] S. Sharaf *et al*, "Comparison between wire mesh sensor and gamma densitometry void measurements in two-phase flows," *Measurement Science and Technology*, vol. 22, (10), pp. 104019, 2011.
- [74] T. J. Heindel, "A review of X-ray flow visualization with applications to multiphase flows," *Journal of Fluids Engineering*, vol. 133, (7), pp. 074001, 2011.
- [75] A. Bieberle *et al*, "Validation of high-resolution gamma-ray computed tomography for quantitative gas holdup measurements in centrifugal pumps," *Measurement Science and Technology*, vol. 26, (9), pp. 095304, 2015.
- [76] F. Fischer *et al*, "An ultra fast electron beam x-ray tomography scanner," *Measurement Science and Technology*, vol. 19, (9), pp. 094002, 2008.
- [77] C. Gerardi *et al*, "Study of bubble growth in water pool boiling through synchronized, infrared thermometry and high-speed video," *Int. J. Heat Mass Transfer*, vol. 53, (19-20), pp. 4185-4192, 2010.
- [78] C. Paz *et al*, "On the Application of Image Processing Methods for Bubble Recognition to the Study of Subcooled Flow Boiling of Water in Rectangular Channels," *Sensors*, vol. 17, (6), pp. 1448, 2017.
- [79] Paul T. Callaghan, *Principles of Nuclear Magnetic Resonance Microscopy*. 1993.
- [80] R. W. Brown *et al*, *Magnetic Resonance Imaging: Physical Principles and Sequence Design*. 2014.

- [81] A. B. Tayler *et al*, "Applications of ultra-fast MRI to high voidage bubbly flow: measurement of bubble size distributions, interfacial area and hydrodynamics," *Chemical Engineering Science*, vol. 71, pp. 468-483, 2012.
- [82] H. Prasser, D. Scholz and C. Zippe, "Bubble size measurement using wire-mesh sensors," *Flow Meas. Instrum.*, vol. 12, (4), pp. 299-312, 2001.
- [83] S. C. Saxena *et al*, "An assessment of experimental techniques for the measurement of bubble size in a bubble slurry reactor as applied to indirect coal liquefaction," *Chem. Eng. Commun.*, vol. 63, (1), pp. 87-127, 1988.
- [84] A. I. Hawari, "Multidisciplinary Engagement at Research Reactors: The NCSU PULSTAR," 2017.
- [85] K. K. Mishra, A. I. Hawari and V. H. Gillette, "Design and performance of a thermal neutron imaging facility at the North Carolina State University PULSTAR reactor," *IEEE Trans. Nucl. Sci.*, vol. 53, (6), pp. 3904-3911, 2006.
- [86] A. I. Hawari, I. I. Al-Qasir and K. K. Mishra, "Accurate simulation of thermal neutron filter effects in the design of research reactor beam applications," *PHYSOR-2006: Advances in Nuclear Analysis and Simulation*, 2006.
- [87] K. K. Mishra, *Phase Contrast Neutron Imaging using Single and Multiple Pinhole Apertures*. 2010.
- [88] A. Datta and A. I. Hawari, "Geant4 Analysis of a Thermal Neutron Real-Time Imaging System," *IEEE Trans. Nucl. Sci.*, vol. 64, (7), pp. 1652-1658, 2017.
- [89] H. Kobayashi, "Design and Basic Character of Neutron Collimator on Radiography," *JAERI Conference Proceedings*, pp. 367-372, 1999.
- [90] A. K. Heller and J. S. Brenizer, "Neutron radiography," in *Neutron Imaging and Applications* Anonymous 2009, .
- [91] P. von der Hardt and H. Röttger, *Neutron Radiography Handbook: Nuclear Science and Technology*. 2012.
- [92] C. Rafael Gonzalez and R. Woods, "Digital image processing," *Pearson Education*, 2002.
- [93] R. Y. Rubinstein and D. P. Kroese, *Simulation and the Monte Carlo Method*. 201610.
- [94] S. Agostinelli *et al*, "GEANT4—a simulation toolkit," *Nuclear Instruments and Methods in Physics Research Section A: Accelerators, Spectrometers, Detectors and Associated Equipment*, vol. 506, (3), pp. 250-303, 2003.

- [95] X-5 Monte Carlo Team, "MCNP—A General Monte Carlo N-Particle Transport Code, Version 5," *La-Ur-03-1987*, vol. 1, 2003.
- [96] L. S. Waters, "MCNPX user's manual," *Los Alamos National Laboratory*, 2002.
- [97] S. M. Seltzer, "Electron-photon Monte Carlo calculations: the ETRAN code," *International Journal of Radiation Applications and Instrumentation. Part A. Applied Radiation and Isotopes*, vol. 42, (10), pp. 917-941, 1991.
- [98] J. Halbleib, "Structure and operation of the ITS code system," in *Monte Carlo Transport of Electrons and Photons* Anonymous 1988, .
- [99] W. R. Nelson, D. W. Rogers and H. Hirayama, "The EGS4 code system," *Stanford Linear Accelerator Center Report, SLAC-265.*, 1985.
- [100] R. D. Stewart *et al*, "Microdosimetric properties of ionizing electrons in water: a test of the PENELOPE code system," *Physics in Medicine & Biology*, vol. 47, (1), pp. 79, 2001.
- [101] R. Brun *et al*, "GEANT: detector description and simulation tool," *CERN Program Library Long Writeup W5013, Geneva.*, 1993.
- [102] J. Carrier *et al*, "Validation of GEANT4, an object-oriented Monte Carlo toolkit, for simulations in medical physics," *Med. Phys.*, vol. 31, (3), pp. 484-492, 2004.
- [103] G. Collaboration, "Geant4 user's guide for application developers," *Accessible from the GEANT4 Web Page [1] Version Geant4*, vol. 9, 2012.
- [104] J. Allison *et al*, "Recent developments in Geant4," *Nuclear Instruments and Methods in Physics Research Section A: Accelerators, Spectrometers, Detectors and Associated Equipment*, vol. 835, pp. 186-225, 2016.
- [105] G. Collaboration, "Physics reference manual," *Version: Geant4*, vol. 10, (9), 2016.
- [106] J. Perl, "HepRep: a generic interface definition for HEP event display representables," *Web Page: [Http://Www.Slac.Stanford.Edu/~ Perl/Heprep](http://www.Slac.Stanford.Edu/~Perl/Heprep)*, 2000.
- [107] K. K. Mishra, "Development of a thermal neutron imaging facility at the NC State University PULSTAR reactor," 2005.
- [108] Z. Xiao, *Development of Resolution-Enhanced Magnified Neutron Imaging at the PULSTAR Reactor*. 2016.
- [109] Y. Koba *et al*, "Scintillation efficiency of inorganic scintillators for intermediate-energy charged particles," *Prog Nucl Sci Technol*, vol. 1, (218.10), pp. 15669, 2011.

- [110] V. I. Tretyak, "Semi-empirical calculation of quenching factors for ions in scintillators," *Astroparticle Physics*, vol. 33, (1), pp. 40-53, 2010.
- [111] C. W. van Eijk, "Inorganic scintillators for thermal neutron detection," *Radiat. Measur.*, vol. 38, (4), pp. 337-342, 2004.
- [112] I. Kandarakis *et al*, "Evaluation of ZnS: Cu phosphor as X-ray to light converter under mammographic conditions," *Radiat. Measur.*, vol. 39, (3), pp. 263-275, 2005.
- [113] P. F. Liaparinos *et al*, "Modeling granular phosphor screens by Monte Carlo methods," *Med. Phys.*, vol. 33, (12), pp. 4502-4514, 2006.
- [114] S. W. Smith, "The scientist and engineer's guide to digital signal processing," 1997.
- [115] S. W. Smith, "The scientist and engineer's guide to digital signal processing," 1997.
- [116] C. C. Hu, "Modern Semiconductor Devices for Integrated Circuits," *Part I: Electrons and Holes in a Semiconductor*, 2011.
- [117] A. J. Theuwissen, *Solid-State Imaging with Charge-Coupled Devices*. 20061.
- [118] *ANDOR products specification*. Available: <https://andor.oxinst.com/products/>.
- [119] ANDOR, "CCD Spatial Resolution," 2018. Available: <https://andor.oxinst.com/learning/view/article/ccd-spatial-resolution>.
- [120] Scott G. Olenych *et al*, "Concepts in Digital Imaging Technology," Available: <http://hamamatsu.magnet.fsu.edu/articles/microscopyimaging.html>.
- [121] M. Nickola, R. Botha and W. L. Combrinck, "Investigation of techniques to determine astronomical seeing conditions at matjiesfontein," in *11th SAGA Biennial Technical Meeting and Exhibition*, 2009.
- [122] W. J. Smith, *Image Formation: Geometrical and Physical Optics*. 1978.
- [123] W. J. Smith, *Modern Optical Engineering*. Tata McGraw-Hill Education, 1966.
- [124] A. Lipson, S. G. Lipson and H. Lipson, *Optical Physics*. Cambridge University Press, 2010.
- [125] M. Bass *et al*, *Handbook of Optics*. 19952.
- [126] M. Bass, C. DeCusatis and J. Enoch, *Handbook of Optics*. McGraw-Hill New York, 20012.
- [127] M. Nikl, "Scintillation detectors for x-rays," *Measurement Science and Technology*, vol. 17, (4), pp. R37, 2006.

- [128] G. F. Knoll, *Radiation Detection and Measurement*. 2010.
- [129] J. B. Birks, *The Theory and Practice of Scintillation Counting: International Series of Monographs in Electronics and Instrumentation*. 201327.
- [130] C. W. van Eijk, "Inorganic scintillators for thermal neutron detection," *IEEE Trans. Nucl. Sci.*, vol. 59, (5), pp. 2242-2247, 2012.
- [131] V. V. Nagarkar *et al*, "New Structured Scintillators for Neutron Radiography," *Physics Procedia*, vol. 69, pp. 161-168, 2015.
- [132] P. Liaparinos *et al*, "Investigating the particle packing of powder phosphors for imaging instrumentation technology: an examination of Gd₂O₂S: Tb phosphor," *Journal of Instrumentation*, vol. 11, (10), pp. P10001, 2016.
- [133] Avinash C.. Kak and M. Slaney, *Principles of Computerized Tomographic Imaging*. 1988.
- [134] M. N. Wernick and J. N. Aarsvold, *Emission Tomography: The Fundamentals of PET and SPECT*. 2004.
- [135] D. S. Holder, *Electrical Impedance Tomography: Methods, History and Applications*. 2004.
- [136] C. A. Puliafito *et al*, "Imaging of macular diseases with optical coherence tomography," *Ophthalmology*, vol. 102, (2), pp. 217-229, 1995.
- [137] J. Hsieh, *Computed Tomography: Principles, Design, Artifacts, and Recent Advances*. SPIE press, 2003114.
- [138] K. J. Batenburg and L. Plantagie, "Fast approximation of algebraic reconstruction methods for tomography," *IEEE Trans. Image Process.*, vol. 21, (8), pp. 3648-3658, 2012.
- [139] A. Chambolle, "An algorithm for total variation minimization and applications," *Journal of Mathematical Imaging and Vision*, vol. 20, (1-2), pp. 89-97, 2004.
- [140] G. T. Herman and A. Lent, "Iterative reconstruction algorithms," *Comput. Biol. Med.*, vol. 6, (4), pp. 273-294, 1976.
- [141] P. M. Joseph, "An improved algorithm for reprojecting rays through pixel images," *IEEE Trans. Med. Imaging*, vol. 1, (3), pp. 192-196, 1982.
- [142] R. Gordon, R. Bender and G. T. Herman, "Algebraic reconstruction techniques (ART) for three-dimensional electron microscopy and X-ray photography," *J. Theor. Biol.*, vol. 29, (3), pp. 471-481, 1970.

- [143] A. H. Andersen and A. C. Kak, "Simultaneous algebraic reconstruction technique (SART): a superior implementation of the ART algorithm," *Ultrason. Imaging*, vol. 6, (1), pp. 81-94, 1984.
- [144] J. Gregor and T. Benson, "Computational analysis and improvement of SIRT," *IEEE Trans. Med. Imaging*, vol. 27, (7), pp. 918-924, 2008.
- [145] D. Mishra, K. Muralidhar and P. Munshi, "A robust MART algorithm for tomographic applications," *Numerical Heat Transfer: Part B: Fundamentals*, vol. 35, (4), pp. 485-506, 1999.
- [146] C. C. Paige and M. A. Saunders, "LSQR: An algorithm for sparse linear equations and sparse least squares," *ACM Transactions on Mathematical Software (TOMS)*, vol. 8, (1), pp. 43-71, 1982.
- [147] T. M. Buzug, *Computed Tomography: From Photon Statistics to Modern Cone-Beam CT*. 2008.
- [148] A. J. Rockmore and A. Macovski, "A maximum likelihood approach to transmission image reconstruction from projections," *IEEE Trans. Nucl. Sci.*, vol. 24, (3), pp. 1929-1935, 1977.
- [149] K. Lange and R. Carson, "EM reconstruction algorithms for emission and transmission tomography," *J. Comput. Assist. Tomogr.*, vol. 8, (2), pp. 306-316, 1984.
- [150] S. Tilley II, J. H. Siewerdsen and J. W. Stayman, "Model-based iterative reconstruction for flat-panel cone-beam CT with focal spot blur, detector blur, and correlated noise," *Phys. Med. Biol.*, vol. 61, (1), pp. 296, 2015.
- [151] P. J. La Rivière, J. Bian and P. A. Vargas, "Penalized-likelihood sinogram restoration for computed tomography," *IEEE Trans. Med. Imaging*, vol. 25, (8), pp. 1022-1036, 2006.
- [152] F. Bleichrodt *et al*, "Easy implementation of advanced tomography algorithms using the ASTRA toolbox with Spot operators," *Numerical Algorithms*, vol. 71, (3), pp. 673-697, 2016.
- [153] E. Van den Berg and M. P. Friedlander, "Spot-a linear-operator toolbox," *URL <Http://Www.Cs.Ubc.Ca/Labs/Scl/Spot>*, 2014.
- [154] W. Dewulf, Y. Tan and K. Kiekens, "Sense and non-sense of beam hardening correction in CT metrology," *CIRP Annals-Manufacturing Technology*, vol. 61, (1), pp. 495-498, 2012.
- [155] R. M. Schoueri *et al*, "The new facility for neutron tomography of IPEN-CNEN/SP and its potential to investigate hydrogenous substances," *Applied Radiation and Isotopes*, vol. 84, pp. 22-26, 2014.

- [156] P. Boillat *et al*, "Neutron imaging of fuel cells—Recent trends and future prospects," *Current Opinion in Electrochemistry*, vol. 5, (1), pp. 3-10, 2017.
- [157] M. Yehya *et al*, "Neutron imaging of hydraulic flow within structural concrete," *S25-Comportements Mécaniques Et Propriétés De Transport Des Matériaux De Génie Civil*, 2017.
- [158] M. Kang *et al*, "Diffusivity and sorptivity of Berea sandstone determined using neutron radiography," *Vadose Zone Journal*, vol. 12, (3), 2013.
- [159] M. F. Middleton, I. Pázsit and M. Solymar, "Petrophysical applications of neutron radiography," *Nondestr. Test. Eval.*, vol. 16, (2-6), pp. 321-333, 2001.
- [160] P. Bingham *et al*, "Neutron radiography of fluid flow for geothermal energy research," *Physics Procedia*, vol. 69, pp. 464-471, 2015.
- [161] J. Terreni *et al*, "Observing Chemical Reactions by Time-Resolved High-Resolution Neutron Imaging," *The Journal of Physical Chemistry C*, vol. 122, (41), pp. 23574-23581, 2018.
- [162] M. Sarma *et al*, "Neutron radiography visualization of solid particles in stirring liquid metal," *Physics Procedia*, vol. 69, pp. 457-463, 2015.
- [163] R. Zboray and P. Trtik, "800 fps neutron radiography of air-water two-phase flow," *MethodsX*, vol. 5, pp. 96-102, 2018.
- [164] D. Kenning, "NUCLEATE BOILING," *Two-Phase Flow and Heat Transfer*, 1977.
- [165] S. Hamzekhani, M. M. Falahieh and A. Akbari, "Bubble departure diameter in nucleate pool boiling at saturation: pure liquids and binary mixtures," *Int. J. Refrig.*, vol. 46, pp. 50-58, 2014.
- [166] N. I. Kolev, "Bubble departure diameter," in *Multiphase Flow Dynamics 2* Anonymous Springer, 2007, pp. 417-438.
- [167] S. M. Peyghambarzadeh *et al*, "Photographic study of bubble departure diameter in saturated pool boiling to electrolyte solutions," *Chemical Industry and Chemical Engineering Quarterly*, vol. 20, (1), pp. 143-153, 2014.
- [168] M. Matkovic and B. Koncar, "Bubble departure diameter prediction uncertainty," *Science and Technology of Nuclear Installations*, vol. 2012, 2012.
- [169] J. Du, C. Zhao and H. Bo, "Investigation of bubble departure diameter in horizontal and vertical subcooled flow boiling," *Int. J. Heat Mass Transfer*, vol. 127, pp. 796-805, 2018.

- [170] M. Jamialahmadi *et al*, "Study of bubble formation under constant flow conditions," *Chem. Eng. Res. Design*, vol. 79, (5), pp. 523-532, 2001.
- [171] V. K. Badam, V. Buwa and F. Durst, "Experimental investigations of regimes of bubble formation on submerged orifices under constant flow condition," *The Canadian Journal of Chemical Engineering*, vol. 85, (3), pp. 257-267, 2007.
- [172] E. Delnoij, J. Kuipers and van Swaaij, Willibrordus Petrus Maria, "Computational fluid dynamics applied to gas-liquid contactors," *Chemical Engineering Science*, vol. 52, (21-22), pp. 3623-3638, 1997.
- [173] P. Hanafizadeh *et al*, "The effect of gas properties on bubble formation, growth, and detachment," *Particul. Sci. Technol.*, vol. 33, (6), pp. 645-651, 2015.
- [174] N. W. Geary and R. G. Rice, "Bubble size prediction for rigid and flexible spargers," *AIChE J.*, vol. 37, (2), pp. 161-168, 1991.
- [175] D. C. Blanchard and L. D. Syzdek, "Production of air bubbles of a specified size," *Chemical Engineering Science*, vol. 32, (9), pp. 1109-1112, 1977.
- [176] COMSOL, "Comsol Multiphysics CFD User Guide," 2017.
- [177] N. Otsu, "A threshold selection method from gray-level histograms," *IEEE Trans. Syst. Man Cybern.*, vol. 9, (1), pp. 62-66, 1979.
- [178] O. Marques, *Practical Image and Video Processing using MATLAB*. 2011.
- [179] T. O. Charrett and R. P. Tatam, "Full-field interferometry using infinity corrected optics," *Measurement Science and Technology*, vol. 27, (1), pp. 015402, 2015.
- [180] T. Hsiao, A. Rangarajan and G. Gindi, "A new convergent MAP reconstruction algorithm for emission tomography using ordered subsets and separable surrogates," in *Biomedical Imaging, 2002. Proceedings. 2002 IEEE International Symposium On, 2002*, .
- [181] M. R. Hestenes and E. Stiefel, *Methods of Conjugate Gradients for Solving Linear Systems*. 195249(1).
- [182] W. Ouyang *et al*, "Deep learning massively accelerates super-resolution localization microscopy," *Nat. Biotechnol.*, 2018.

APPENDICES

Appendix A Neutron Interactions and Geant4 Neutron Data Library

A.1 Neutron Interactions

The neutron mainly interacts by elastic scattering, inelastic scattering, radiative capture and fission. When a neutron collides with a nuclei and loses its energy by nuclear recoil. The process of elastic scattering (n, n) obeys the conservation law of energy and momentum. The transferred energy by elastic scattering can be illustrated calculated as,

$$E_R = E_n \frac{4M_R M_n}{(M_R + M_n)^2} \cos^2 \theta, \quad (\text{A1. 1})$$

where, E_n is the energy of incoming neutron, E_R is the energy of the target nucleus, M_n is the mass of the neutron, M_R is the mass of the target nucleus, θ is the angle of the recoiled nucleus with respect to incident neutron direction as illustrated in Figure A1.1. Maximum energy transfer occurs when backscattering occurs at $\theta = 0^\circ$.

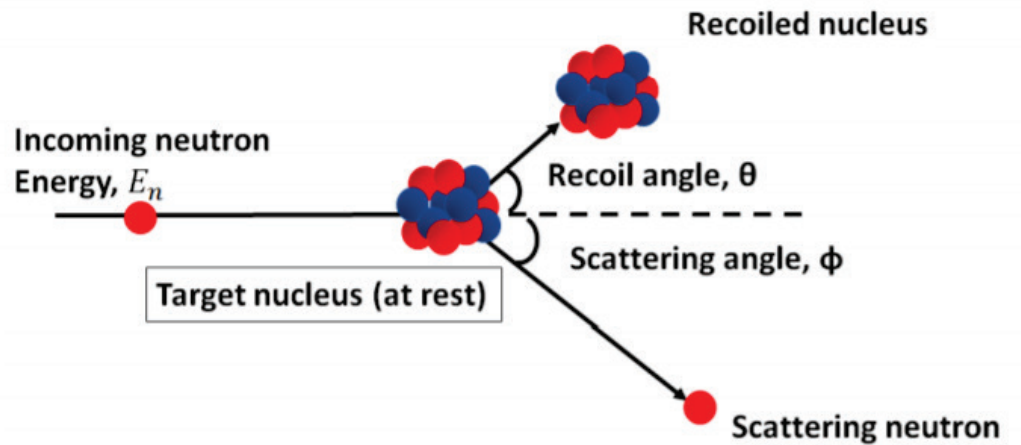


Figure A1.1. Elastic scattering illustration

In contrast, inelastic scattering (n, n') is an interaction process where a neutron with high energy collide with the target nucleus and formed a compound nucleus. The compound nucleus is in excited state and eventually emits the energy for stabilization. The inelastic scattering occurs

above a threshold energy. The threshold energy is higher than the first excited state of target nucleus and can be expressed as,

$$E_t = \left(\frac{A+1}{A}\right) \times \epsilon_1, \quad (\text{A1.2})$$

where, E_t is the threshold energy, A is the atomic number and ϵ_1 is the energy of the first excited state. It is difficult to express average energy loss due to inelastic scattering as it depends on the energy levels within the target nucleus. The inelastic process can be illustrated by Figure A.2.

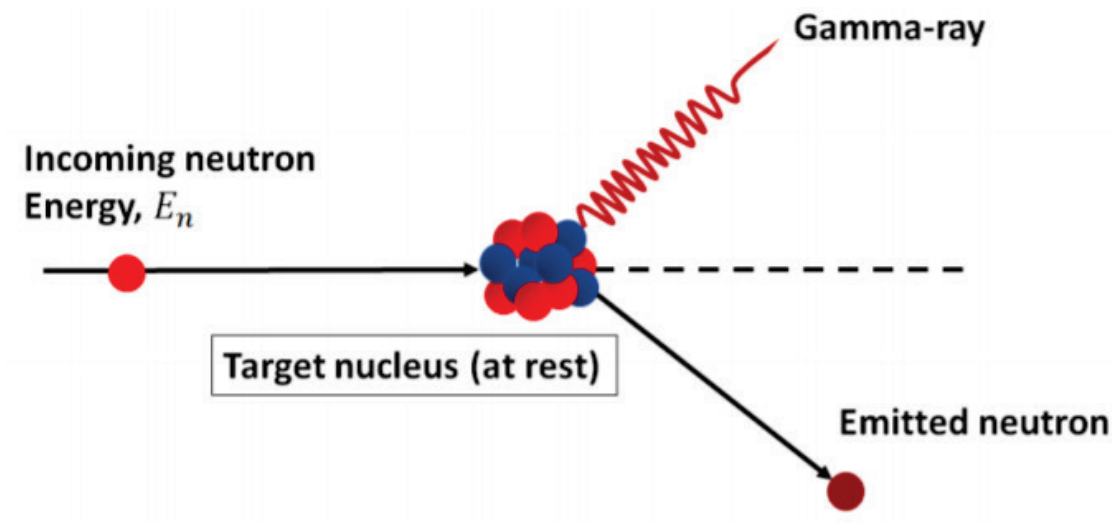


Figure A1. 2. Illustration of inelastic scattering

Unlike neutron scattering, when neutron interact with a nucleus it might be captured by the target nucleus to form a heavier isotope of the target element as shown in Figure A1.2. After the neutron capture, the nucleus may rearrange its internal structure and emit gamma ray and other particles like alpha, deuteron, protons etc. The excitation energy carries away by those particles. Fission (n, f) is a nuclear reaction process in which neutrons are collide with target nucleus releasing two fission fragment, neutrons and one or more prompt gamma ray.

A.2 Geant4 Neutron Data Library (G4NDL)

The probability of neutron interaction with target nuclei is characterized by the cross section of the target nuclei. All cross section is incorporated from ENDF/B-VI data libraries. All the cross section from evaluated data libraries have been processed and stored as point wise cross section rather than parameterization. The point wise data are further processed into linearly operated format, such that any intermediate point can be deduced by linear interpolation. The final state of the elastic scattering cross section can be described by sampling the differential scattering cross-section $\frac{d\sigma}{d\Omega}$. For elastic scattering two type of differential scattering cross sections are supported in Geant4 as describe as,

$$\frac{d\sigma}{d\Omega} = \frac{d\sigma}{d\Omega}(\cos \theta, E), \quad (\text{A2.1})$$

$$\frac{2\pi}{\sigma(E)} \frac{d\sigma}{d\Omega}(\cos \theta, E) = \sum_{l=0}^{n_l} \frac{2l+1}{2} a_l(E) P_l(\cos \theta), \quad (\text{A2.2})$$

where E is the energy of the incoming neutron, θ is the scattering angle, P_l is the legendre polynomial and a_l is the legendre coefficients. In both the representation the normalized differential cross sections are tabulated as the function of the incoming neutron energy. For inelastic scattering the Geant4 currently supports the following final states: np, nd, nt, n α , dt, t, α , p, pd. In case of radiative capture, the final state is described by photon production cross sections, discrete and continuous contribution of photon energy spectra with the angular distribution of the emitted photons. The normalized emission probability of the photon can be expressed as a weighted sum of the incoming neutron energy E and the photon energy E_γ as described as,

$$f(E \rightarrow E_\gamma) = \sum_i p_i(E) g_i(E \rightarrow E_\gamma), \quad (\text{A2.3})$$

where, p_i are tabulated weights as a function of energy of the incoming neutron and g are the tabulated function of the photon energy for each incoming neutron energy. The angular distribution for radiative capture are similar to the elastic scattering. The energy distribution for the fission neutrons are tabulated as a normalized function of incoming and outgoing neutron energy and can be represented as,

$$f(E \rightarrow E') \propto f\left(\frac{E'}{\Theta(E)}\right), \quad (\text{A2. 4})$$

where, E is the energy of the incoming neutron, E' is the energy of the outgoing neutron and $\Theta(E)$ is the effective temperature used to characterize the secondary neutron energy. Eqn. represents when the energy distribution is Maxwell spectrum.

$$f(E \rightarrow E') \propto \sqrt{E'} e^{\frac{E'}{\Theta(E)}}, \quad (\text{A2. 5})$$

The Monte-Carlo simulation of interaction of neutrons depends upon the physical model and data libraries. In case of Geant4 *G4NeutronHP* (high precision) model is the appropriate transport code for simulating neutron transport below 20 MeV and it relies on Geant4 Neutron Data Library (G4NDL). In general it contain similar information that is found in standard ENDF-VI data files but in different format. The conversion process of ENDF format to G4NDL was not straight forward and not documented. Thus makes it difficult to include cross-section for a new material, not existed in G4NDL library. One of such material in context of neutron imaging is sapphire filter. This filter is used extensively in neutron imaging to remove high energy neutrons while maintaining reasonable thermal neutron flux. But the cross section of the sapphire was not available in G4NDL library. For the complete development of the simulation model it was necessary to include the sapphire cross section into G4NDL library. Thermal neutron scattering cross section libraries for sapphire was processed from LEAPR calculation using the THERMR

module. An in-house code was developed in C++ platform to process the THERMR output and converted to G4NDL format. The generated data library for sapphire was zipped with *zlib* and imported in Geant4. The Geant4 source code needs to be compiled again for proper functionality after the addition. The G4NDL file format are described below and first few lines of the sapphire cross section library is shown in Figure B.1. Each file in the cross section directories has the following entries:

- First entry is identification of library (in this case G4NDL)
- Second entry original data library from which the file came
- Third entry is a dummy entry but the value usually corresponds to the MT number of reaction in ENDF formats (2: Elastic, 102: Capture, 18: Fission; files in the directory of inelastic cross section usually have 0 for this entry).
- Fourth entry is also a dummy
- Fifth entry represents the number of (energy, cross section) pairs (in eV, barn) to follow.

```

G4NDL          (1st entry)
ENDF/B-VII.1  (2nd entry)
      3        (3rd entry)          \\MF
      223      (4th entry)          \\MT
      296      (5th entry)          \\temperature
      2453     (6th entry)          \\number of E-XS pairs
1.000000e-5 3.456415e+2 1.125000e-5 3.272908e+2 ,,,,,
(1st pair of E and XS) (2nd pair of E and XS)

4.000040e+0 0.000000e+0 2.000000e+7 0.000000e+0
(2452nd pair of E and XS) (2453rd pair of E and XS)
      3        (MF)
      223      (MT)
      350      (temperature)
      2789     (Number of E-XS pair)
1.000000e-5 4.457232e+2 1.125000e-5 4.220525e+2 ,,,,,
(1st pair of E and XS) (2nd pair of E and XS)

```

FigureA2.1. General structure of Geant4 neutron data library

Appendix B Convolution of Gaussian PDF: A Brief Note

Let, $f(x)$ and $g(x)$ are two Gaussian PDFs with mean μ_f, μ_g and σ_f, σ_g respectively. The PDFs are illustrated following,

$$f(x) = \frac{1}{\sqrt{2\pi}\sigma_f} e^{-\frac{(x-\mu_f)^2}{2\sigma_f^2}}, \quad (\text{B.1})$$

$$g(x) = \frac{1}{\sqrt{2\pi}\sigma_g} e^{-\frac{(x-\mu_g)^2}{2\sigma_g^2}}. \quad (\text{B.2})$$

Using the convolution theorem,

$$F^{-1}[F(f(x))F(g(x))] = f(x) * g(x), \quad (\text{B.3})$$

where, F and F^{-1} is the Fourier transform and inverse Fourier transformation operator as expressed as,

$$F(f(x)) = \int_{-\infty}^{\infty} f(x) e^{-2\pi i k x} dx \quad (\text{B.4})$$

$$F^{-1}(F(k)) = \int_{-\infty}^{\infty} F(k) e^{2\pi i k x} dk \quad (\text{B.5})$$

Using the transformation, $x' = x - \mu_f$ the Fourier transformation of $f(x)$ is given by,

$$F(f(x)) = \frac{1}{\sqrt{2\pi}\sigma_f} \int_{-\infty}^{\infty} e^{-\frac{x'^2}{2\sigma_f^2}} e^{-2\pi i k(x'-\mu_f)} dx' \quad (\text{B.6})$$

$$F(f(x)) = \frac{e^{-2\pi i k \mu_f}}{\sqrt{2\pi}\sigma_f} \int_{-\infty}^{\infty} e^{-\frac{x'^2}{2\sigma_f^2}} e^{-2\pi i k x'} dx' \quad (\text{B.7})$$

Using, Euler's formula,

$$F(f(x)) = \frac{e^{-2\pi i k \mu_f}}{\sqrt{2\pi}\sigma_f} \int_{-\infty}^{\infty} e^{-\frac{x'^2}{2\sigma_f^2}} [\cos(2\pi k x') - i \sin(2\pi k x')] dx' \quad (\text{B.8})$$

The $\sin(2\pi k x')$ is odd function and integral over $(-\infty, \infty)$ will be zero. The remaining terms are,

$$F(f(x)) = \frac{e^{-2\pi i k \mu_f}}{\sqrt{2\pi}\sigma_f} \int_{-\infty}^{\infty} e^{-\frac{x'^2}{2\sigma_f^2}} \cos(2\pi k x') dx' \quad (\text{B.9})$$

Using the standard form of integral,

$$\int_0^{\infty} e^{-at^2} \cos(2xt) dt = \frac{1}{2} \sqrt{\frac{\pi}{a}} e^{-\frac{x^2}{a}} \quad (\text{B.10})$$

$$F(f(x)) = e^{-2\pi i k \mu_f} e^{-2\pi^2 \sigma_f^2 k^2} \quad (\text{B.11})$$

Using the value of $f(x)$ from Eqn,

$$F(f(x)) = F\left(\frac{1}{\sqrt{2\pi}\sigma_f} e^{-\frac{(x-\mu_f)^2}{2\sigma_f^2}}\right) = e^{-2\pi i k \mu_f} e^{-2\pi^2 \sigma_f^2 k^2} \quad (\text{B.12})$$

Similar expression can be obtained for $F(g(x))$, Therefore Eqn, can be expressed as,

$$[F(f(x))F(g(x))] = e^{-2\pi i k(\mu_f + \mu_g)} e^{-2\pi^2(\sigma_f^2 + \sigma_g^2)k^2} = e^{-2\pi i k(\mu_f + \mu_g)} e^{-2\pi^2\left(\sqrt{(\sigma_f^2 + \sigma_g^2)}\right)^2 k^2} \quad (\text{B.13})$$

So, it can be observed that, the convolution of Gaussian functions results a Gaussian function. The standard deviation of the resulting Gaussian function can be expressed as,

$$\sigma_{f*g} = \sqrt{\sigma_f^2 + \sigma_g^2}. \quad (\text{B.14})$$

The relation between FWHM and the variance of a Gaussian function can be expressed as,

$$FWHM = 2.35\sigma. \quad (\text{B.15})$$

If we assume FWHM of two imaging component as R_f and R_g . The total resolution after convolution can be expressed as,

$$FWHM_{f*g} = \sqrt{R_f^2 + R_g^2}. \quad (\text{B.16})$$

Appendix C Number of Projection Requirement for Neutron CT

Assuming detector consists of N_D pixel element with pixel pitch Δ . The highest resolvable spatial frequency can be expressed with Shannon theorem as [1], [133]

$$f_{max} = \frac{1}{2\Delta}. \quad (C.1)$$

The distance between two points on a radial line, can be expressed as,

$$\varepsilon_r = \frac{2 \times f_{max}}{N_D} = \frac{1}{N_D \Delta}, \quad (C.2)$$

where, ε_r is the radial resolution. The 1D Fourier transform of the projections acquired at any angle represents a radial line in Fourier space as shown in Figure C.1.

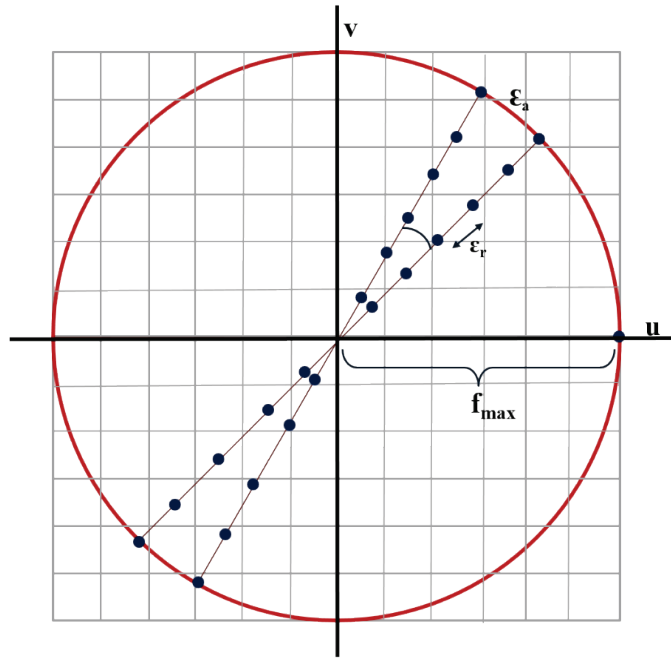


Figure C.1. Frequency domain representation of the parallel projection data showing radial resolution (ε_r), azimuthal resolution (ε_a) and maximum obtainable frequency (f_{max}).

The angle between two successive projections can be expressed as

$$\alpha = \frac{\pi}{N_p}, \quad (C.3)$$

where, N_p is the number of projection. The distance between two successive points on the periphery can be express as,

$$\varepsilon_a = f_{max} \times \alpha = \frac{1}{2\Delta} \times \frac{\pi}{N_p}, \quad (C.4)$$

where, ε_a is azimuthal resolution. For uniform sampling the azimuthal resolution should be similar with radial resolution. Therefore,

$$\varepsilon_a \approx \varepsilon_r \quad (C.5)$$

$$N_p \approx \frac{\pi N_D}{2}. \quad (C.6)$$

Further, the number of scanning points per projection can be expressed as

$$N_D = \frac{D}{\Delta x}, \quad (C.7)$$

where, D is the diameter of the object to be scanned and Δx is the difference between two points.

Substituting the value of N_D in Equation C.5,

$$N_p \approx \frac{\pi}{2} \times \frac{D}{R_{NR}/2}, \quad (C.8)$$

where, R_{NR} is spatial resolution of the imaging system. In real time neutron imaging system, this may include the spatial resolution contribution from CCD pixel, lens, scintillator and beam geometry. Thus, the number of projections required can be expressed as,

$$N_p \approx \pi \times \frac{D}{R_{NR}}. \quad (C.9)$$

In this work, D is 13.3 mm and R_{NR} is $116 \pm 2 \mu\text{m}$ with 50 μm thick scintillator. Thus,

$$N_p \approx \pi \times \frac{13.3 \times 1000}{116} \approx 360. \quad (C.10)$$